Chemical synthesis of switchable peptide-based nanopores: from ion channels to bio-inspired materials

TECHNISCHE UNIVERSITÄT DARMSTADT

Vom Fachbereich Chemie
der Technischen Universität Darmstadt

zur Erlangung des Grades
Doctor rerum naturalium
(Dr. rer. nat.)

Dissertation

von
Lena Karin Müller

Erstgutachterin: Asst. Prof. Dr. Alesia A. Tietze

Zweitgutachter: Prof. Dr. Gerhard Thiel

Darmstadt 2020

Mueller, Lena Karin: Chemical synthesis of switchable peptide-based nanopores: from ion channels to bio-inspired materials

Darmstadt, Technische Universität Darmstadt

Jahr der Veröffentlichung der Dissertation auf TUprints: 2020

URN: urn:nbn:de:tuda-tuprints-114951

Tag der Einreichung: 13.12.2019

Tag der mündlichen Prüfung: 27.02.2020

Das schönste Glück des denkenden Menschen ist, das Erforschliche erforscht zu haben und das Unerforschliche zu verehren

Johann Wolfgang von Goethe

The presented work is result of research accomplished by Lena Karin Müller from July 2016 to December 2019 at the Technical University of Darmstadt, Clemens-Schöpf-Institute for Organic Chemistry and Biochemistry under supervision of Asst. Prof. Alesia Tietze (now: Department of Chemistry and Molecular Biology at the University of Gothenburg, Sweden, a part of the Wallenberg Centre for Molecular and Translational Medicine)

Parts of this work have been presented at national and international conferences:

2019: Conferences with poster presentations

German Peptide Symposium, 18.03 – 21.03.2019, Cologne, Germany
Hybrid Nanopores as an Effective Sensing Tool with Numerous Perspectives

Wallenberg Centre for Molecular and Translational Medicine – yearly Event, 31.01.2019, Gothenburg, Sweden
Hybrid Nanopores as an Effective Sensing Tool with Numerous Perspectives

PhD day TU Darmstadt, 15.01.2019, Darmstadt, Germany
Development of a Strategic and Quantitative Route for the Chemical Synthesis of Membrane Associated Proteins

2018: Conferences with poster presentations

European Peptide Symposium, 26.08. – 31.08.2018, Dublin, Ireland
Development of a Strategic and Quantitative Route for the Chemical Synthesis of Membrane Associated Proteins
WILEY poster award

2018: Oral presentations

PhD day TU Darmstadt, 28.06.2018, Darmstadt, Germany
Hybrid Nanopores as an Effective Sensing Tool for Early Diagnostics in Alzheimer's Disease
Award for best oral presentation

2017: Conferences with poster presentations

Molecular basis of life – Herbsttagung der GBM, 24.09 – 27.09.2017 Bochum, Germany
Chemical Synthesis of Switchable Protein-Based Nanopores

WE-Heraeus-Seminar "Transport Mechanisms in Biological and Synthetic Nanopores and –channels", 16.07 – 21.07.2017 Bremen, Germany
Chemical Synthesis of Switchable Protein-Based Nanopores

iNAPO for sensors: Formation, Characterization and Modeling, 08.06 – 09.06.2017, Darmstadt, Germany
Chemical Synthesis of Switchable Protein-Based Nanopores

Parts of this work are published or are about to be published:

Baumruck, A.C., Tietze, D., Steinacker, L.K., Tietze, A.A.
Chemical synthesis of membrane proteins: a model study on the influenza virus B proton channel
Chem. Sci. 2018, 9, 2365-2375

Müller, L.K., Baumruck, A.C., Zhdanova, H., Tietze, A.A.
Challenges and Perspectives in Chemical Synthesis of Highly Hydrophobic Peptides
Front. Bioeng. Biotechnol. 2020, doi 10.3389/fbioe.2020.00162

Müller, L.K.#, Duznovic, I.#, Tietze, D., Weber, W., Ali, M., Stein, V., Tietze, D., Ensinger, W., Tietze, A.A.
Ultrasensitive and selective copper(II) detection: introducing a bioinspired and robust sensor
Chem. Eur. J. 2020, doi 10.1002/chem.202001160

Müller, L.K., Gräwe, A., Tietze, D., Stahl, J., Stein, V., Tietze, A.A.
DNA scission of non-His-containing ATCUN-like peptides
in preparation

Table of contents

1. Abstract

Vital and fundamental biological processes are executed by ion channels and other pore-forming structures spanning the membrane of the cell. Electrical signaling in the nervous system by potassium channels[1], the contraction of cardiac and smooth muscle cells by voltage gated Ca^{2+} channels[2] or the conduction of cellular responses to hormones, neurotransmitters or ions by G-protein coupled receptors.[3] These extremely complex attributes are intensively investigated especially regarding fundamental questions of structure and design.[4] 60% of drug targets are found on the cell surface[5] illustrating the significance of these structures. Ion selectivity, ionic rectification and ionic gating are the three outstanding characteristics of ion channels which inspire for imitating these features.[6] Bio-inspired materials, sensor devices and mimicking "smart" gates displays a research area of great interest and challenge the competences and capabilities of today's nanoscience field.[7] Nanochannels can be manufactured from numerous solid-state materials and selectivity towards targets achieved with modification of the surface.[8]

The presented work focuses on both aspects: the chemical synthesis of a pore-forming potassium channel and the design of a smart material combining a chemically synthesized sensing peptide with a solid state material.

Synthesis of ion channels, whether through expression or through chemical synthesis, is not straightforward and trivial.[9] The herein presented synthesis route towards Kcv_{NTS} elucidates the challenges and problems faced during synthetic of extremely hydrophobic structures. Kcv_{NTS} is up-to-date one of the smallest known and full functional viral potassium channels, composed of only 82 amino acids. The integration of structures aiding chemical synthesis, purification and analytics are discussed, utilized and evaluated. Towards Fmoc-based solid phase peptides synthesis (SPPS) of the final product, several steps are taken. The complete sequence is divided into three fragments with fragment 1 (Kcv_{NTS}(41-82), fragment 2 Kcv_{NTS}(41-82) and fragment 3 Kcv_{NTS}(1-15) which are consecutively reunited to yield the native sequence using native chemical ligation (NCL). Pseudoprolines, for backbone stabilization and to decrease aggregation on resin, are integrated into fragment 1, containing the N-terminal Cys moiety. To enable native chemical ligation, fragment 2 is equipped with a C-terminal oxo-ester. NCL of fragment 1 and 2 is successfully carried out in NCL buffer containing the organic solvent hexafluoroisopropanol, HFIP to enable solubilization of the fragments. The product of this NCL is introduced to a further reaction with fragment 3. To prepare for NCL, the N-terminal thioproline, Thz unit is unmasked to yield the needed Cys fragment. Fragment 3 is successfully synthesized incorporating a C-terminal solubilizing tail to the oxo-ester unit. While the solubilizing tail facilitates synthesis and purification, it is readily detached from the sequence during NCL. The second NCL reaction is carried out in ligation buffer containing 2,2,2-Trifluoroethanol, TFE to yield the final product Kcv_{NTS}(1-82) that is analyzed using mass spectrometry (MS), sodium dodecyl sulfate polyacrylamide gel electrophoresis (SDS-PAGE) and circular dichroism (CD) spectroscopy.

For the design of a sensor, composed of a biological component with sensing ability integrated into a stable solid-state material, peptides with heavy metal binding properties were synthesized, purified and analyzed. Representatives of the ATCUN family (amino terminal Cu(II)- and Ni(II)-binding peptides) exhibit the general sequence Xaa-Xbb-His with the mandatory His moiety for the square-planar complex formation with binding of Cu(II) or Ni(II).[10] We designed four peptides, with sequences Ac-DAP-β-Ala-His-$mPEG_4$ (peptide 1),

comprising the original ATCUN motif, Ac-DAP-β-Ala-Ala-mPEG$_4$ (peptide 2) and Ac-DAP-β-Ala-Asp-mPEG$_4$ (peptide 3), representing non-his containing mutants and (5/6)FAM-DAP-β-Ala-His-mPEG$_4$ (peptide 4), a fluorophore containing sequence of peptide 1. The maximum binding constants (at optimal pH) from UV-VIS spectroscopy titration data for peptides 1 and the non-His containing motifs towards Cu(II) are determined to be in a comparable range of $K = 1.2 \times 10^5 - 2.5 \times 10^5\ l \times M^{-1}$. Ni(II) binding is evaluated within a range of $K = 1.3 \times 10^5$ $3.1 \times 10^5\ l \times M^{-1}$ for the mutants (peptides 2 and 3) and $K = 2.5 \times 10^7\ l \times M^{-1}$ for peptide 1. We evaluated the titration data to indicate the formation of the ATCUN like square-planar complex for all peptides, also the non-His containing. This is interesting due to the mandatory His in position 3 missing in the sequences of peptides 2 and 3. The Asp unit in peptide 3 can contribute a carboxyl group to the complex formation whereas peptide 2, with an Ala unit, is dependent on using an additional backbone amide unit to form the 1:1 complex. Peptide 4 is evaluated using fluorescence titration with binding constants determined to be $K = 2.1 \times 10^9\ l \times M^{-1}$ for Cu(II) and $K = 6.1 \times 10^{11}\ l \times M^{-1}$ for Ni(II) binding. Furthermore, a static quenching process is determined with formation of a non-fluorescent complex through Cu(II) and Ni(II) binding. Using peptides 1 and 4, we made use of the pH-dependency of complex formation to shift the selectivity towards Cu(II) binding. The pH 6.5 is evaluated to yield tight Cu(II) binding ($K_{peptide\ 1} = 3.8 \times 10^6\ l \times M^{-1}$, $K_{peptide\ 4} = 6.3 \times 10^6\ l \times M^{-1}$) with negligible Ni(II) binding ($K_{peptide\ 1} = 5.8 \times 10^2\ l \times M^{-1}$, $K_{peptide\ 4} = 4.9 \times 10^3\ l \times M^{-1}$) and a limit of detection for peptide 4-Cu(II) in solution of 13.5 nM. Investigations towards Zn(II) binding shows no indications for the formation of a complex. Immobilization of peptide 4 in the nanopores of a PET foil (12 μm thickness, conically shaped nanopores with tip ~5 nm and base ~300 nm) facilitates current/voltage, *I/V* measurements with femtomolar detection of Cu(II). Making use of the integrated fluorophore and the resulting visualization of the binding event, the designed sensor is investigated using confocal laser scanning microscopy, CLSM. It shows re-usability with regeneration of the Cu(II) binding event after washing with ethylendiaminetetraacetic acid, EDTA. A robust, selective and sensitive sensor system is established, showing re-usability.

Furthermore, scission behavior of the designed peptides towards dsDNA is investigated. Using ascorbate and Cu(II), the DNA strand is cleaved due to the auto-oxidation of ascorbate under Cu(I) and reactive oxygen species (ROS) generation. This cleavage ability is used in the design of anti-cancer metallodrugs, such as cisplatin and therefore interesting in regard to diagnostic applications.[11] Therefore, the scission behavior towards plasmids pUC19, pAKS-IBA3 and paCYTC2 of all four peptides is investigated. The supercoiled dsDNA is transformed to a linearized form through cutting of the DNA strand. All peptides (peptides 1-4) linearize all plasmids using ascorbate and Cu(II). In a next step, the region for scission is investigated by mapping the plasmids and segmenting the DNA sequences. The plasmid pUC19 is cut in a selective region by peptides 1, 2 and 4. Additionally, pASK-IBA3 is cut in a preferred area by peptides 2-4. For pACYCT2 a region can be defined in which the sequence stays intact. The preferred scission area displays an interesting approach in the straight-forward drug design. Furthermore, the ability of peptides 1-4 to linearize DNA can be advanced to the design of device. Using the described sensor from Cu(II) sensing, the immobilized peptide can be used as a scission device allowing only linearized DNA to translocate through the nanopores of the PET foil. In future applications this translocation can additionally be measured, making sequencing of the translocated DNA possible.

2. Abstract (german)

Essentielle und fundamentale biologische Prozesse werden von Ionenkanälen ausgeführt. Unter anderem werden elektrische Signale des ZNS über Kalium-Kanäle abgebildet[1], die Kontraktion von kardialen und glatten Muskelzellen werden durch spannungsabhängige Calciumkanälen verwirklicht[2] und zelluläre Antworten auf Hormone, Neurotransmitter und Ionen durch G-Protein gekoppelte Rezeptoren durchgeführt.[3] Fundamentale Fragen im Bezug auf Struktur und Design dieser hoch komplexen Eigenschaften sind Teil von intensiven Studien und Untersuchungen.[4] Da 60 % der *Drug Targets* die Oberfläche der Zelle, also die Zellmembran adressieren, sind diese Strukturen von großem Interesse.[5] Herausragende Eigenschaften von Ionenkanälen sind die extreme Selektivität und Gating Eigenschaften.[6] Von der Biologie inspirierte Materialien und sensorische Instrumente sind ein dynamischer Bereich der Forschung vor allem im Bezug auf die Ideen und Möglichkeiten, die das Thema „Nanosciences“ betrifft.[7] Stabile und solide Materialien können als Grundlage für Nanoporen genutzt werden und mithilfe von Modifikationen der Porenoberfläche eine bestimmte Selektivität erhalten.[8]

Die hier präsentierten Ergebnisse fokussieren sich auf beide zuvor genannten Aspekte. Zum einen wird die Grundlage der Struktur und des Designs von Ionenkanälen durch Festphasenpeptidsynthese (SPPS) untersucht, zum anderen ein biologisch inspiriertes, smartes Material erstellt, indem solide Nanoporen durch ein sensorisches Peptid modifiziert werden.

Weder die chemische Synthese noch die Expression von Ionenkanälen ist unkompliziert und trivial.[9] Herausforderungen und Probleme, die während der SPPS auftreten, werden in dieser Arbeit im Bezug auf die Synthese des viralen Kaliumkanals Kcv_{NTS} herausgearbeitet. Dieser Kanal ist, zum heutigen Zeitpunkt, einer der kleinsten bekannten Kaliumkanäle. Unterschiedliche Strukturen, welche die Synthese, Aufreinigung und Ligation begünstigen und erleichtern sollen, werden verwendet, diskutiert und in deren Kompetenz bewertet. Zum finalen Produkt sind mehrere Synthese-Schritte nötig. Vorerst wird die komplette Sequenz in drei Fragmente aufgeteilt, Fragment 1 (Kcv_{NTS}(41-82), Fragment 2 Kcv_{NTS}(41-82) und Fragment 3 Kcv_{NTS}(1-15), welche mithilfe der nativen chemischen Ligation (NCL) aufeinanderfolgend zur finalen Sequenz zusammengefügt werden. Pseudoproline werden zur Stabilisierung der Sequenz von Fragment 1 während der Peptidsynthese eingesetzt und verhindern ebenfalls die Aggregation am Harz. Weiterhin zeichnet sich Fragment 1 durch eine N-teminale Cystein Einheit aus, welche zur NCL Voraussetzung ist. Das Fragment 2 trägt den entsprechenden, C-terminalen oxo-ester. Die NCL wird in einem Ligationspuffer, welcher mit dem organischem Lösemittel Hexafluoroisopropanol, HFIP versetzt ist, erfolgreich ausgeführt. Das daraus resultierende Produkt muss für die darauffolgende NCL mit Fragment 3 vorbereitet werden. Die N-terminale Thioprolin-Grupppe (Thz), wird in ein Cystein umgewandelt und das Produkt für die NCL aktiviert. Fragment 3 kann nur mithilfe der Integration eines Löslichkeits-*tags* erfolgreich synthetisiert werden. Dieser *tag* befindet sich am C-Terminus und wird während NCL Konditionen abgespalten, sodass der oxo-ester von Fragment 3 für die NCL zur Verfügung steht. Diese zweite NCL wird in einem Ligationspuffer, welcher 2,2,2-Trifluorethanol (TFE) enthält, durchgeführt, um das finale Produkt, Kcv_{NTS}(1-82) zu generieren. Dieses wird mithilfe von Massenspektrometrie (MS), *sodium dodecyl sulfate polyacrylamide* Gel Elektrophorese (SDS-PAGE) and Circular Dichroismus (CD) analysiert.

Ebenfalls wird in dieser Arbeit die Synthese, Analytik und Charakterisierung von kleinen, Schwermetall-bindenden Peptiden dargestellt, die zur Familie der ATUCN Peptide gehören (Amino terminal Cu(II)- and Ni(II)- binding peptides). Die Integration dieser sensorischen Peptide in solide Nanoporen führt zum Design eines Sensors welcher in Zukunft zu einem diagnostisches Hilfsmittel ausarbeitet werden kann. Die generelle Struktur Xaa-Xbb-His bildet mit Cu(II) und Ni(II) ionen einen quadratisch planaren Komplex und setzt dafür Histidine in der dritten Position voraus. Wir haben vier Peptide synthetisiert, Ac-DAP-β-Ala-His-$mPEG_4$ (Peptid 1), welches das generelle ATCUN motif darstellt, Ac-DAP-β-Ala-Ala-$mPEG_4$ (Peptid 2) and Ac-DAP-β-Ala-Asp-$mPEG_4$ (Peptid 3), zwei ATCUN-Mutanten, die kein Histidine enthalten und (5/6)FAM-DAP-β-Ala-His-$mPEG_4$ (Peptid 4), welches die Sequenz von Peptid 1, kombiniert mit einem Fluorophor, darstellt. Die Daten aus UV-VIS Spektroskopie Titrationen mit Cu(II) und Ni(II) werden genutzt, um Bindungskonstanten zu berechnen. Bindungskonstanten für die Cu(II)-Bindung von Peptiden 1-3 liegen in einem vergleichbaren Rahmen von $K = 1.2 \times 10^5 - 2.5 \times 10^5\ l \times M^{-1}$. Die Bindung von Ni(II) durch die Mutanten bewegt sich im Bereich von $K = 1.3 \times 10^5$ $3.1 \times 10^5\ l \times M^{-1}$ und die von Peptid 1 $K = 2.5 \times 10^7\ l \times M^{-1}$. Wir konnten für alle Peptide, Peptide 1-3, einen quadratisch planaren Komplex evaluieren, auch für die Mutanten, die kein Histidin in ihrer Sequenz beinhalten. Das Komplexierungsverhalten von Peptid 3 kann durch den Einsatz der Carboxy-Gruppe der Asp Einheit beschrieben werden, während Peptid 2 eine Amidgruppe von einer Peptidbindung zur Komplexierung nutzen muss. Durch Integration des Fluorophores in die Sequenz von Peptid 4, wird Fluoreszenztitrationen eingesetzt und Bindungskonstanten von $K = 2.1 \times 10^9\ l \times M^{-1}$ für die Bindung von Cu(II) und $K = 6.1 \times 10^{11}\ l \times M^{-1}$ für Ni(II) berechnet. Weiterhin wird ein statischer Quenchingprozess aus den Berechnungen evaluiert, dieser besagt die Formation eines nicht-fluorezierenden Komplexes durch Bindung der Liganden Cu(II) oder Ni(II). Peptid 1 und Peptid 4 werden zur Generation des Sensors eingesetzt und mithilfe von pH Verschiebungen eine Selektivität für Cu(II) entwickelt. Ein pH Wert von 6.5 wird für dieses Vorhaben ermittelt. Bei diesem pH steht eine Cu(II) Bindung im Vordergrund, mit Bindungskonstanten $K_{peptid\ 1} = 3.8 \times 10^6\ l \times M^{-1}$, $K_{peptid\ 4} = 6.3 \times 10^6\ l \times M^{-1}$, während kaum Ni(II) Komplex gebildet wird ($K_{peptide\ 1} = 5.8 \times 10^2\ l \times M^{-1}$, $K_{peptide\ 4} = 4.9 \times 10^3\ l \times M^{-1}$). Das Detektionslimit von 13.5 nM Cu(II) unterstreicht die Sensitivität. Die Immobilisierung von Peptid 4 auf die Oberfläche der Nanoporen einer Polmerfolie, macht Strom/Spannungs Messungen möglich, sowie das Design eines Sensors (Polyethylenterephthalat, 12 μm Dicke, Poren mit 5 nm *tip* und 300 nm *base* Öffnung). Konzentrationen von Cu(II) ionen im Femtomolaren Bereich konnten mit diesem System gemessen werden. Das integrierte Fluorophor kann weiterhin für visuelle Untersuchungen genutzt werden. Mithilfe eines Fluoreszenzmikroskops, *confocal laser scanning microscopy* (CLSM), wird das Event der Kupferionen-Bindung visualisiert. Die Zugabe von Kupfer führt zum Quenching der Fluoreszenz, welche durch die Zugabe von Ethylendiamintetraessigsäure (EDTA) regeneriert werden kann. Dadurch konnte eine Wiederverwendbarkeit des Sensor-Systems gezeigt werden.

Weiterhin wird die Fähigkeit dieser Peptide untersucht, dsDNA zu schneiden. Werden die Peptide mit Ascorbat und Cu(II) versetzt, so setzt eine Autooxidation von Ascorbat Cu(I) und Reaktive Sauerstoff Spezies (ROS) frei. Diese ist interessant bezüglich des Einsatzes in der Medizin. In der Chemotherapie werden heutzutage vor allem Metallo-verbindungen, wie Cisplatin, als Medikamente eingesetzt.[11] Untersuchungen zur Linearisierung von dsDNA verschiedener Plasmide, pUC19, pASK-IBA3, pACYCT2, werden angestellt und mögliche strukturbedingte Präferenzen für Schnittstellen neben der bekannten Bindung in der kleinen

Furche von DNA[12] erforscht. Alle vier Peptide linearisieren die drei aufgeführten Plasmide in Gegenwart von Cu(II) und Ascorbat. Im nächsten Schritt, werden diese in Bereiche segmentiert und diese auf die Mögliche Schnittstelle untersucht. Folgende Ergebnisse wurden gefunden: das Plasmid pUC19 wird von Peptid 1, 2 und 4 in einer präferierten Region geschnitten, ebenfalls schneiden die Peptide 2 – 4 das Plasmid pAKS-IBA3 in einem bestimmten Sequenzbereich. Für das Plasmid pACYCT2 konnte eine Region definiert werden, indem der DNA Strand nicht geschnitten wird und intakt bleibt. Die präferierten Bereiche könnten weiterhin genutzt werden, um ein *straight-forward drugdesign* zu implementieren. Der zuvor vorgestellte Sensor, bestehend aus dem in Nanoporen immobilisieren Peptid, kann weiterhin genutzt werden, um Plasmid DNA zu schneiden und anschließend eine Translokation ausschließlich der linearisierten DNA durch die Nanoporen durchzuführen. Diese Translokation ruft in den *I/V* Messungen ein Signal hervor, welches zum Sequenzieren von DNA genutzt werden könnte.

3. Introduction

Nanopores are holes exhibiting a diameter in the nanometer range within a membrane or other material and can be classified into two large groups. (**a**) Biological nanopores and (**b**) solid state nanopores with both areas under great scientific development. Interest in these structures arose in the 1990ies because of their extraordinary sensing abilities that go as far as single molecule sensing.[13] The basic principle behind this concept is the translocation of ions, molecules, drugs and other small structures across a membrane and through a pore. Within the cells of organisms, this process is omnipresent and vital.

Biological nanopores are ubiquitous in living systems. From ion channels to other pore-forming structures, the variety is immense. While with the investigation of ion channels medicinal aims regarding e.g. pain treatment[14] and fundamental functional research are focused, other pore-forming structures are used for the determination of DNA[15], hairpin DNA[16] and RNA[17] as sequencing units.

Solid state nanopores were designed after vivid research done with the biological, α-HL, a transmembrane protein from *Staphylococcus aureus*.[18]. With the vision to overcome disadvantages that biological structures usually exhibit, such as instability with regard to pH, buffer or temperature changes and their defined size, research was done on the fabrication of nanopores within solid state material. In the early 21st century the first solid state nanopores were created using a silica membrane (SiN) as the scaffold.[19,20]

Combining a nanopore membrane made from solid-state material and inserting a biological nanopore or naturally occurring peptide/protein with key-lock behavior towards a target one obtains a so called **hybrid nanopore**. These systems are excellent scaffolds from which sensoring devices can be fabricated with stability against thermal, mechanical and electrical stress while exhibiting an ultra-sensitive, selective and reliable sensing unit.

3.1. Membrane proteins

As mentioned before, biological nanopores are ubiquitous and essential for living systems. Cell membranes surround and define their inside, functioning as a semipermeable barrier. One of the important equilibriums that cell membranes control, is the asymmetry of ion concentrations extra- and intercellular. The potassium cation [K^+] is found in concentrations of 5 mM extracellular, 150 mM inside the cell, while [Na^+] is present with 150 mM outside of the cell whereas within the cell it is found in concentrations of 10 mM. Complex protein structures, channel-forming proteins, control passage of cations as well as other organic structures, e.g. sugars while retaining macromolecules.[21] Ion transport is performed in two different manners: through ion channels, ions can diffuse passively by an electrochemical gradient or through an active transport. Ion movement through ion pumps is an active transport that needs energy supplied by hydrolysis of adenosine triphosphate, ATP.[22] For these structures to embed into the lipid bilayer they possess hydrophobic regions that span through or interact with the membrane (Figure 1). The transmembrane proteins (TM proteins) feature a scaffold that is based on α-helices spanning the membrane while single pass α-helical TM proteins are the most abundant, seven-pass α-helical proteins being subsequent.[9] Additional regions around the central channel contribute to a wide variety within this protein family, e.g. controlling access to the pore. Membrane proteins, G-protein-coupled receptors, receptor

tyrosine kinases, ion channels and transporters, such as the sodium/glucose cotransporter, realize vitally important processes.[23]

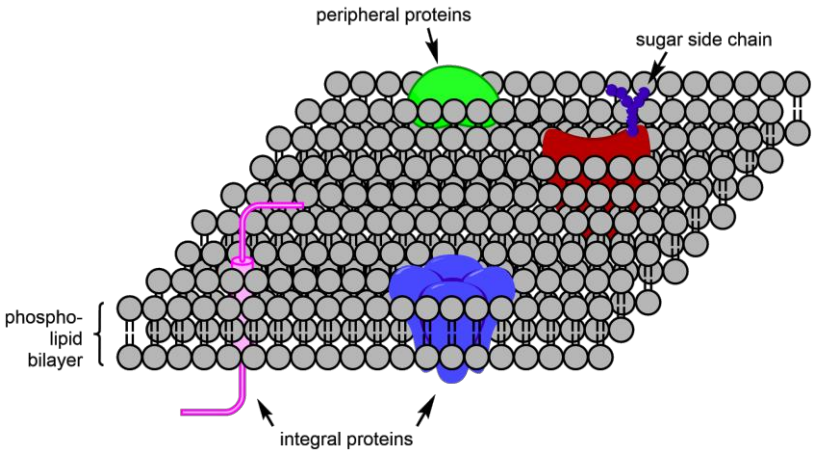

Figure 1. Structure of the cell membrane

The illustration of the cell membrane shows structures embedded (integral membrane proteins) or anchored to the phospholipid bilayer (peripheral membrane proteins). Illustration adapted from Achalkumar *et al.*[24]

Membrane proteins make up 20 – 30% of all proteins within the eukaryotic and prokaryotic proteome[25] and represent around 60% of drug targets. Therefore, FDA-approved drugs are mostly membrane proteins.[26] Examples for approved drugs targeting membrane proteins are the subscribed β_1-adrenceptor blocking agents targeting a G-protein coupled receptor. The serotonin transporter, SERT, displays 12 α-helices and is targeted by serotonin reuptake inhibitors, SRIs, which are frequently prescribed antidepressants. The last example is the blockage of a sodium-dependent glucose transporter (SGLT) by SGLT-2-blockers used by patients with type 2 diabetes.[27,28] But not only the design of new drugs is of great interest, the development of bio-inspired sensors based on TM proteins is demanded because of their unique features involving high ion flux, tremendous selectivity and immense precision. Usually, ion channels are complex, large structures with diameters of 5 – 7 nm at a length of around 10 – 15 nm with a selectivity filter only being 1 – 1.5 nm.[22] The diameter of ions they transport, is around 0.2 – 0.3 nm and they discriminate and transport these structures reliably.[22] Despite their significance, very little is known about their structures, characteristics, biophysical and chemical properties because they are not readily available. Neither expression nor chemical synthesis of these structures is trivial and up until 2003 only around 60 high-resolution structures of membrane proteins were available at databases.[29] Expression using microorganisms is challenging since recombinant expression strategies for hydrophilic proteins are not applicable for hydrophobic structures, over-expression of especially ion-channels often results in cell toxicity and overall handling in regard to extraction and purification is a great issue.[30] Trying to overcome these problems, chemical synthesis using SPPS is the method of choice laying foundations for cross-border cooperation between chemistry and biology.

Unfortunately, SPPS encounters limits as well. Poor handling in regard to aggregation and hydrophobicity of the amino acid sequences of TM proteins are problems that need to be addressed. The challenge lies not only in the synthesis, but in the purification, ligation and refolding of membrane proteins.[23]

3.2. Potassium Channels

Investigation of potassium channels was triggered with the work published by MacKinnon in 1998 that engaged the determination of the x-ray crystalline structure of KcsA (23-119), the integral potassium channel from *Streptomyces lividans*.[1] Even though this ion channel is derived from prokaryotic gram positive bacteria, a prokaryote, it shows structural similarities to eukaryotic potassium channels. The pore region (P-region) of various potassium channels was extensively studied in the 1990ies and led to the conclusion that a certain sequential arrangement is omnipotent and invariant in these types of channels (Figure 2).[31,32] This extremely homologous sequence in the P-region is characterized by eight amino acids TXXTXGYG (X being a variable amino acid).[33] Not only is this selectivity filter extremely small, it is also able to discriminate between the two similar cations Na^+ and K^+ by over a thousand fold even though their atomic radii only differ by 0.38 Å.[34,35] Potassium channels play an inevitable role due to their physiological function: homeostasis and the repolarization the action potential in excitable.[36] Since x-ray data from the first experiments were not sufficient in understanding the exact structure, especially of the pore region, intensive studies were carried out later. Doyle *et al.* investigated the conduction and selectivity of KcsA (25-119).[1] The proposed[37] and further proven tetrameric structure exhibits a symmetry around the central pore, one monomer built from an inward facing transmembrane α-helix connected to a further α-helix that faces the membrane with a selectivity filter only 12 Å long.[1]

Cation	K^+	Rb^+	Cs^+	**Li^+**	**Na^+**
Å	1.33	1.48	1.69	**0.6**	**0.95**

Table 1. Sizes of cations

Cations in bold (Li^+ and Na^+) are not transported across the channel

Table 1 shows sizes of various cations that are interesting in regard to being transported through potassium channels. The cations Li^+ and Na^+ are excluded and thus not transported across potassium channels whereas for Rb^+ and Cs^+ permeation is possible

Additionally, conduction of most potassium channels is exceptionally fast with a flux of 10^8 ions per second.[34] Hodgkin *et al.* investigated the movement of potassium ions across axons in the 1950ies, already observing and proposing that more than one potassium ion has to be present within one channel.[38] The lab around MacKinnon analyzed this hypothesis further, coming to the conclusion that two K^+ ions are usually present within the selectivity filter and are separated by a water molecule (Figure 2). This phenomenon is explained in more detail in chapter 3.2.

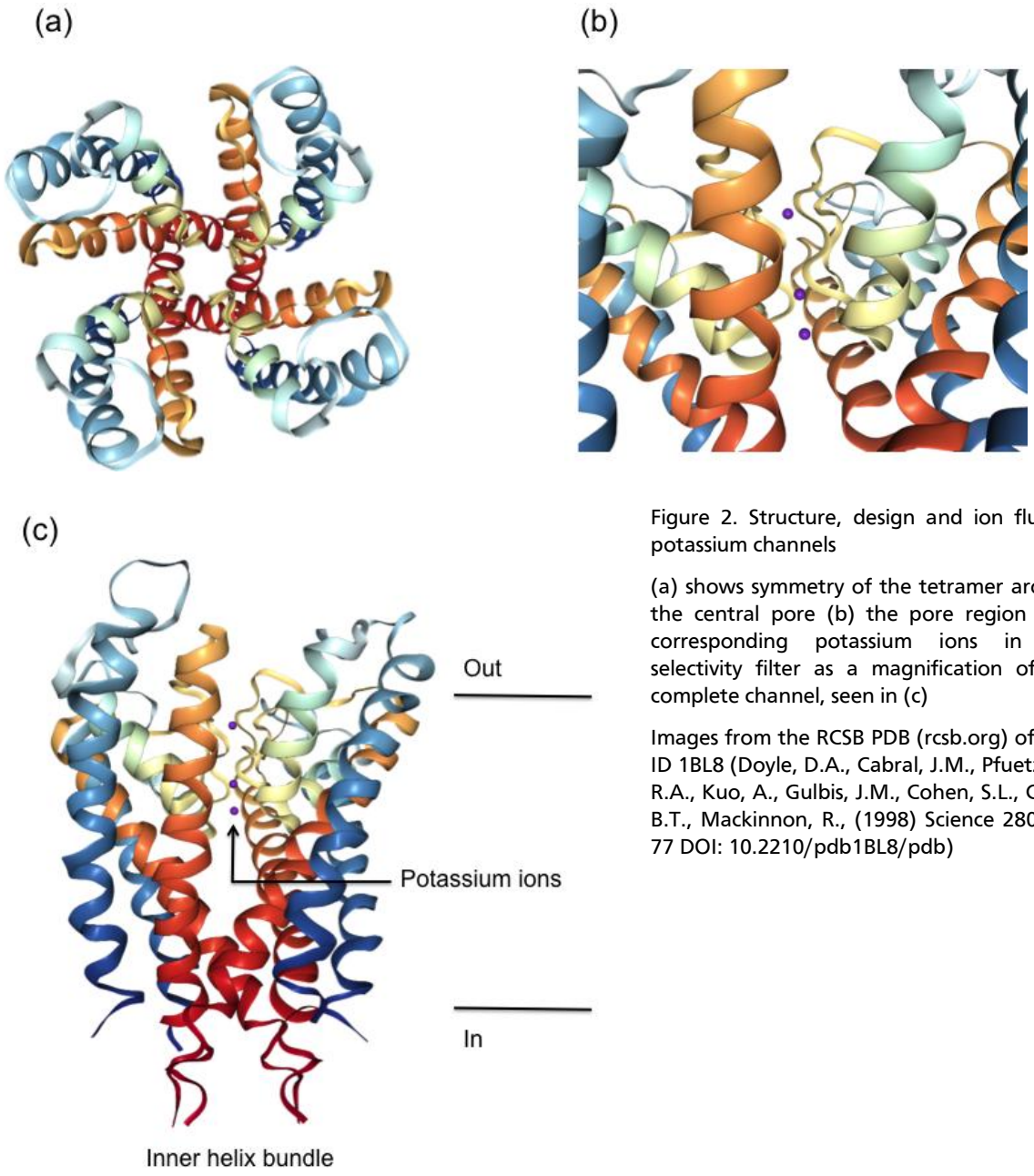

Figure 2. Structure, design and ion flux of potassium channels

(a) shows symmetry of the tetramer around the central pore (b) the pore region with corresponding potassium ions in the selectivity filter as a magnification of the complete channel, seen in (c)

Images from the RCSB PDB (rcsb.org) of PDB ID 1BL8 (Doyle, D.A., Cabral, J.M., Pfuetzner, R.A., Kuo, A., Gulbis, J.M., Cohen, S.L., Chait, B.T., Mackinnon, R., (1998) Science 280: 69-77 DOI: 10.2210/pdb1BL8/pdb)

Regarding the behavior of K^+ ions when entering the pore, four carbonyl oxygen open the selectivity filter towards the extracellular compartment making the hydrated K^+ to shed its hydration shell to enter the pore (Figure 2c). Eight oxygen atoms (shown in red) build a cage-like structure simulating water molecules and thus stabilizing the potassium cation.[39,40] This unique feature of the way K^+ enters the pore is the reason of the distinct discrimination between K^+ and Na^+.

Due to structural accordance of all potassium channels, especially of the conserved sequence of the P-region, the flow of ions is supposed to be universally applicable. Ion flux of all potassium channels is as mentioned above, presumed to be similar due to the conserved P-region. The structure, though, vary greatly. Table 2 coarsely classifies the different structural set-ups of various potassium channels introduced by Kuang et al[41] excluding the class of two pore domains and eight transmembrane helices.[42]

	2TM/P	6TM/P	K2P
Format	- two transmembrane helices - one P-loop	- six transmembrane helices - one P-loop	- four transmembrane helices - two P-loops - dimers (mostly two linked Kir-like sequences)
Examples	Inward-rectifier family -KirBac1.1[43], IRK1[44] Channels of the Kcv family -Kcv_{ATCV-1}[45]	Voltage gated K_V[46] - human *ether-a-go-go*-related gene hERG K^+[47] Ligand gated Kligand - K_{ch}[48]	Four different groups: weak inward rectifiers, acid stimulated, stretch-activated potassium channels, and K^+ channels build with polyunsaturated fatty acids[49]

Table 2. Classification of potassium channels

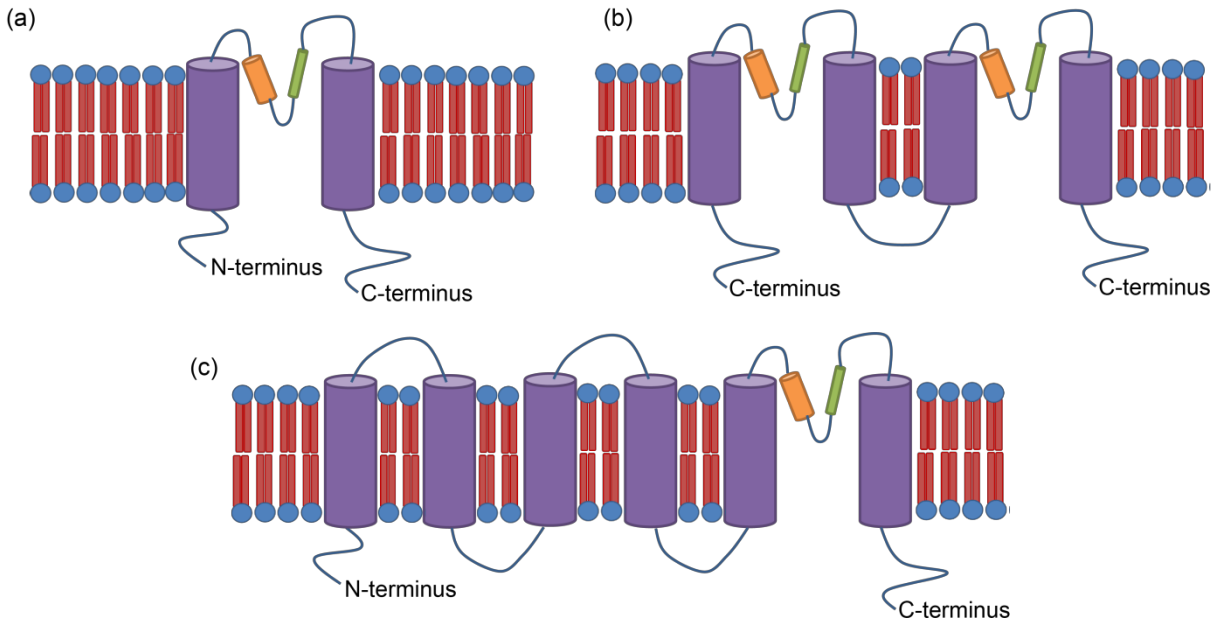

Figure 3. Diverse structures of potassium channels

In (a) the 2TM/P channels are shown, (b) illustrates the K2P channels and (c) the 6TM/P potassium channels. The phospholipid bilayer is shown with blue, hydrophilic heads and two red, hydrophobic tails and the helices of the illustrated potassium channels as purple barrels embedded into the membrane. The orange cylinder represents the pore helix while the green barrel strands for the selectivity filter. The Graphic was adapted from the illustration from Thiel *et al.*[50]

3.3. Kcv – Potassium channels

The family of Kcv channels belongs to the 2TM/P class of potassium channels and are encoded by a Chlorovirus that infects symbiotic chlorella-like green algae. The distinctiveness of these viruses is the presence of an internal lipid membrane which has a crucial role during

the process of early infection.[36] These specific K^+ channels show the signature sequence within the pore-forming helix. They are fully functional and sensitive to K^+ blockers but their size represents to their unique feature.[50] Some of the families' members belong to the smallest known potassium channels. Kcv_{ATCV-1} (**K**$^+$ channel **c**hlorella **v**irus ***A**canthocystis **t**urfacea* **c**hlorella **v**irus-**1**), Kcv_S (**K**$^+$ channel **c**hlorella **v**irus **s**mith) and Kcv_{NTS} (**K**$^+$ channel **c**hlorella **v**irus **n**ext **t**o **s**mith) possess potassium channels containing only 82 amino acids.[51,52] All three display the same, conserved sequence within the filter region, namely: THTTVGYGDL.

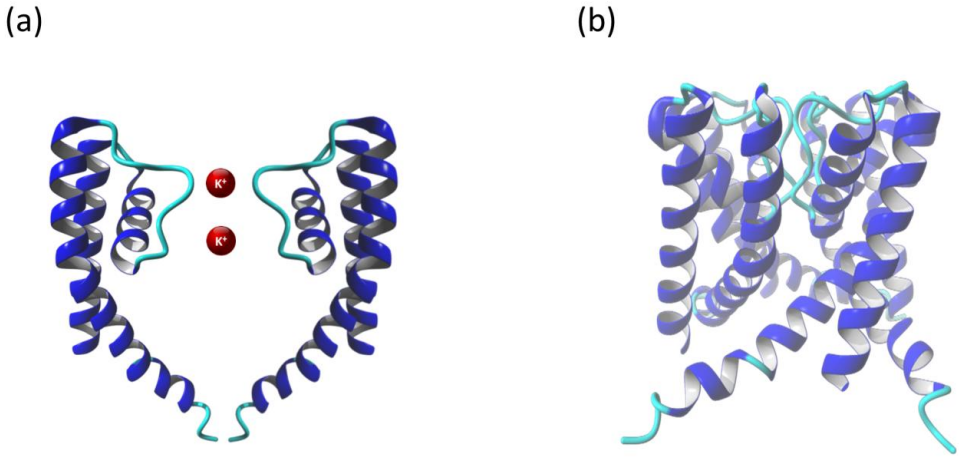

Figure 4. Scheme of Kcv

The figure shows a simulation of a Kcv channel with (a) two opposing monomer units and two potassium ions illustrated in red and the tetrameric form is shown in (b). There are no crystal structures of Kcv channels available, this simulation is only to demonstrate the function and composition

Because of their size, they are almost fully embedded into the cell membrane, thus making them perfect candidates for functional studies with patch-clamp and lipid bilayer methods.[51] Single channel recordings using the patch-clamp method give information on the conductance and kinetics of the investigated ion channel. Therefore, a patch of the membrane of the investigated cell is isolated electrically through light suction into a fire-polished glass pipette.[53] Various difficulties arise when the desired proteins are not sufficiently accessible to patch clamp methods. Proteins from bacterial membranes, for example, display difficulties but are readily measured using the lipid bilayer method.[54,55] Lipid membranes introduced in 1962 by Mueller *et al.*,[56] are still used today to record single-ion channel current measurements at a constant applied voltage.[57] For that, the planar lipid bilayer methods display many advantages. The composition of lipids, the buffers and the protein can be controlled.[54] In Figure 5 a simulation of the tetrameric Kcv_{NTS} is shown as well as a section from planar lipid bilayer experiments by Braun *et al.*[51] The current traces show a high single-channel open-probability which is further calculated to be over 50% and a high conductance of 80 pS. Since function and structure of potassium channels are an exciting research field, the Kcv channels represent attractive models for studies because of their minimal size but functional robustness.

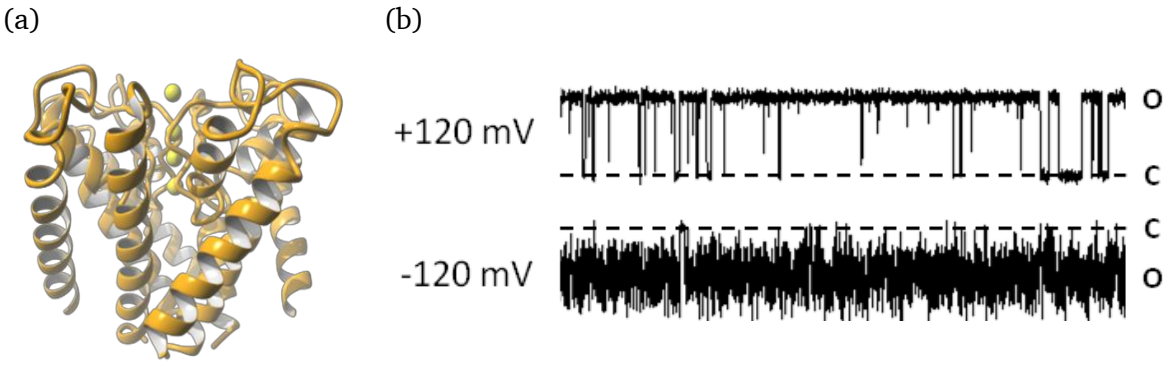

Figure 5. Kcv_{NTS} channel and lipid bilayer recordings

Kcv_{NTS} is shown as a simulation in (a) and current traces from planar lipid bilayer experiments conducted with the native Kcv_{NTS} with O – open and C – closed states of the channel. The current trace was kindly provided by Tobias Winterstein from the Thiel lab (TU Darmstadt). There are no crystal structures of Kcv_{NTS} available, this simulation is only to demonstrate the function and composition

3.4. Peptides/proteins as sensors

Signal transduction of e.g. ion channels within biological cell membranes is one example of the extremely sensitive and selective behavior of proteins. For example, G-protein coupled receptors (GPCR) get triggered by external molecules, ligands and through a conformal change, a signaling cascade is implemented. Hundreds to thousands of second messengers may be activated only by one GPCR.[58] A selected example of a vital sensor system in the human body are the various pH sensors located in the kidney. An adequate pH is essential for normal functioning of cellular enzymes and biochemical reaction. If a pH change is registered, the electrogenic, proton pumping vacuolar-ATPase (V-ATPase) translocates to the surface of the cell for regulation of HCO_3^-.[59] Other pH sensing and modulating biological structures are various GPCR and H^+ ion-sensing channels.[60]

Coming back to the aforementioned potassium channels, ultra-sensitive sensing towards K^+ and the discrimination between Na^+ and K^+ was already introduced. But, not only the conductance is of interest. Blockage of potassium channels, especially those of the Kcv family, is performed e.g. by extermal Ba^{+}[61], by amantadine[62], an anti-viral drug, and TEA (Tetraethylammonium). Just recently, the importance of intrahelical H-bonds was investigated in regard to gating. Rauh *et al.* determined an open probability of 90% for Kcv_{NTS} and 40% for Kcv_S but an amino acid sequence identity of 90% (8 amino acids) coming to the conclusion that a Ser-mediated intrahelical H-bond results in longer closed states.[52] These findings demonstrate the extreme structure-function relationship where only one amino acid within the sequence has a fundamental impact on the open probability of the channel.

The ability to act as sensors is not only restricted to membrane proteins. Numerous protein structures are able to coordinate metals, e.g. the coordination of iron through the porphyrin ring of hemoglobin.[63] A very abundant and essential transition metal in living organisms is zinc. Zinc homeostasis is mediated through monitoring of changes in the free zinc pool by sensing proteins. The MTF1 sensor displays a K_d below 90 μM thus again accentuating the ultra-sensitive sensing behavior of biological structures.[64]

3.4.1. Solid-state nanopores as sensors

Leaving the biological environment, sensing can be performed through channels within solid-state materials. Nanopores in solid state materials are enclosed channels of a certain length, diameter and shape. These attributes can be tuned to the desired shape. The easiest forms of nanopores are of bare structure and can be used for size-selective filtration. By coating the surface with substances of choice, enhanced separation processes are generated that are dependent on the object and substances used.[65]

Different methods for fabrication, tuning and functionalization are summarized in Table 3.

Method	Shape of nanopores	Smallest size of nanopores	Solid-state material	Follow-up protocols	Ref.
Ion-beam sculption	bowel-shaped nanopores	around 2 nm	Si_3N_4, SiO_2, SiN	Atomic layer deposition (ALD) for fine tuning of pore size	20,66,67
Track-etching	various geometries (conical, cylindrical, hourglass, bowel-shaped)	5 nm (after gold plating[68])	Polycarbonate, Polyimide, Poly(ethylene terephthalate), Polycarbonate	Layer-by-layer, ALD	69-71
Transmission electron microscope drilling	cylindrical, hourglass, cylindrical	around 2 nm	SiN, TiN	ALD	72,73
Electrical pulse	*cylindrical	0.5 ± 0.3 nm	Graphene	enlarging of pore in steps of 0.1 ± 0.3 nm/pulse	74,75

Table 3. Different types of nanopore fabrication

*thinnest possible membrane, no variations in shape possible

The multitudinousness of applications emerging from solid state nanopores is distinctively presented by Lee *et al.*[76] The group investigated the selectivity of small molecule transport through gold nanotubules, which can be formed by deposition of gold into polycarbonate track-etched nanopores. By controlling the gold plating time, the diameter of the tubules is tunable, making clean and selective separation of small molecules possible (diameter < 1 nm).[76] Further studies focused on the differentiation between hydrophobic and hydrophilic molecules through chemisorbing either hydrophobic or hydrophilic thiols to the gold nanotubules.[77] Furthermore, charging the membrane with excess positive or negative charge introduces ion selection by rejection of ions of same the charge whereas transport of ions

exposing the opposite charge is possible.[78] Again, Lee *et al.* used the gold nanotubules and introduced a new pH-selective property by chemisorptions of cysteine.[76]

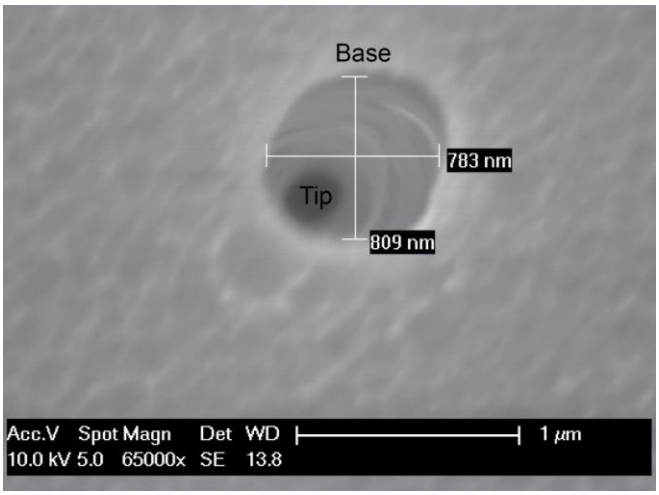

Figure 6. Electron micrograph of a conical nanopore

The image was kindly provided by Mubarak Ali, GSI Darmstadt

Figure 6 shows a conical nanopore within PET foils (12 μm thickness). The advantages of this symmetry of pore is the possibility to mimic biological ion channels through rectification. They display a high selectivity because of the focusing of the electric field at the small tip opening.[79,80] A resistive-pulse technique is used where the single nanopore is installed between two chambers filled with electrolyte solution, usually containing KCl. While potential is applied an ion current is generated. If an analyte is present in the solution and is driven through the nanopore, a block in the ion current is induced, effecting a change in current.

The magnitude or duration of the current block can be attributed to the concentration of the analyte.[81,82] Figure 7 represents the schematic set-up of resistive-pulse measurement set-up with a two-chamber system.

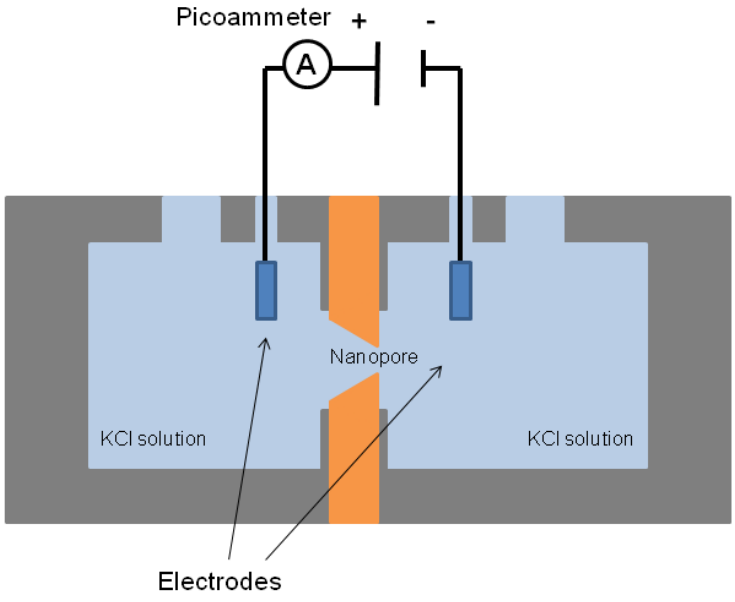

Figure 7. Setting of ion current measurements

The schematic setting was adapted from Zhang *et al.*[83]

With the greater aim of designing sensors that can be used for biomedical or environmental applications, some kind of selective sensing towards a certain analyte is essential. Ligand binding to a receptor is an extremely selective and sensitive procedure and thus presents an optimal scaffold. Two designs of sensor systems are feasible. Using the **first** method, no attachment of the molecular-recognition agent (MRA) is needed. Differences in current when

using only the analyte or the analyte/MRA complex will give information on concentrations of the analyte. This concept is introduced by Sexton *et al.* using BSA and the corresponding binding antibody.[84] **Second**, generation of a hybrid nanopore: with the attachment of a receptor into the solid state nanopores, binding of the ligand can be determined and evaluated through changes in ion current. To generate such a hybrid system out of solid state nanopores the integration of some kind of biologically active substance is mandatory. Siwy et al investigated attachment of MRAs to conically shaped nanopores (gold-coated). With their work they manifested applicability of sensor systems using the biotin/streptavidin, protein-G/immunoglobulin IgG and an antibody to ricin MRA systems. Detection of the analyte (the latter listed structure) was done by the drop in the steady-state ion current when applying a constant transmembrane potential.[85]

Especially the conically shaped nanopores exhibit competences for future applications. Their benefits introduced in 3.4.1 in regard to comparability to membrane proteins and focusing of the current on the tip resulting in high signal output, make them interesting scaffolds for sensor design.[82] Furthermore, high stability of the solid state material (e.g. PET, PC) make them ideal candidates for the design of sensor devices. Possible applications comparable to e.g. glucose sensors are future goals.

3.4.2. The ATCUN motif

Coming back to peptides and proteins that can act as sensors, metal-binding peptides like hemoglobin were introduced earlier in 3.4. Besides iron, there are numerous other trace elements of vital importance for the human body such as copper.[86] There are multitudinous enzymes involved in copper transportation and homeostasis, making copper essential for the normal function of the body, brain development and infant growth.[87,88] Due to its importance, defects in the copper homeostasis can lead to diseases such as Wilson's and Menke's disease with the latter being linked to a lethal Cu^{2+} hyper-accumulation.[87] Copper is calculated to be required in amounts of 1.2 – 2.0 mg/d with a dietary recommendation being 1.5 – 3.0 mg/d.[89] Usually, chronic as well as acute copper toxicity due to excess amounts of copper are relatively rare but when they occur, liver cirrhosis, damage of renal tubes and brain structures is possible.[90] Due to the known risks as well as the need of copper the WHO limited copper concentrations in drinking water to be ≤ 2 mg/l.[91] Through environmental pollution, heavy metals such as Nickel end up accumulating in the human body through inhalation, soil or drinking water leading to problems ranging from skin irritation and allergic reactions to an elevated risk of cancer.[92] In this context, the WHO also included a limit of nickel in drinking-water to be ≤ 0.07 mg/l.[93]

In the human blood plasma, around 10 – 12% of copper ions are bound to albumin, the most abundant protein.[94] In 1960 Peters et al described binding of Cu(II) to bovine serum albumin (BSA) and triggered an avalanche of research concerning this topic.[95,96] Nowadays this structure is known as the **A**mino **t**erminal **Cu**(II)- and **N**i(II)-binding motif (ATCUN motif) occurring not only in BSA but also in human and rat serum albumin (HSA, RSA), neuromedin C and K, human sperm protamine P2a and histatins.[12,97] One of the first experiments to determine the molecular structure of the ATCUN motif was done by Camerman *et al.* in 1975 and is still valid today. They designed the simplest known ATCUN motif Gly-Gly-His and detected a square planar 1:1 binding stoichiometry. The copper is chelated through the

terminal nitrogen of the amino group, the two peptide 1ackbone nitrogens and the nitrogen of the imidazole ring of the histidine moiety.[98]

(a)

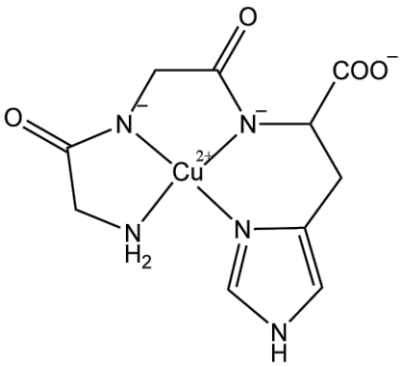

(b)

Structure	Sequence
RSA	Glu-Ala-His
HSA	Asp-Ala-His
BSA (bovine serum albumin)	Asp-Thr-His
P2a	Arg-Thr-His
Histatin 3	Asp-Ser-His
Neuromedin C	Gly-Asn-His
Neuromedin K	Asp-Met-His

Figure 8. Structure and sequence examples

(a) Complex of the simplest ATCUN motif GGH with Cu2+ (b) various ATCUN motifs in natural occurring structures. The lack of the ATCUN motif in e.g. dog and pig serum albumin results in decrease of affinity to Cu(II) and Ni(II)

Making use of the coordination of nickel and copper, theses motifs are interesting sensing units when integrating fluorescent groups that get quenched upon complex formation.[99] The extent of quenching can further be used for the determination of metal-binding efficiency and thus displays characteristics of a fluorescent chemosensor.[100] Making use of the green fluorescent protein (GFP) and attaching an ATCUN motif, Choi *et al*. were able to detect and visualize dynamic copper fluctuations on living cell surfaces.[101] The vision behind this experiment is the Cu^{2+} imaging in neuronal cells, especially the synaptic cleft. ATCUN motifs can also be used as electrocatalysts for water oxidation making detection of DNA possible.[102] Looking further into DNA interactions, cleavage of DNA was investigated and will be introduced in the following section.

3.4.3. DNA scission ability of ATCUN motifs

Besides the intensively studied complexation behavior, these motifs are also interesting in regard to linearization of dsDNA. In nature restriction enzymes fulfill the task. These endonucleases can cleave dsDNA at defined sequences through disruption of the phosphodiester bond of both DNA strands being a protective mechanism towards foreign DNA.[103] Using this defense mechanism in addition with e.g. a specific recognition unit, numerous medicinal applications are possible.

Scission of the ATCUN motif was first described by S. H. Chiou using the tripeptide GGH.[104] He illustrated cleaving activity of a mixture of peptide, Cu(II)-ions and ascorbate on DNA from a bacteriophage and viral DNA. The process of DNA cleavage is provoked by the generation of hydroxyl radicals following this proposed mechanism by Harford *et al.* seen in Equation 1 - Equation 3.[12]

$$ascorbate + 2\,Cu^{2+} \rightarrow dehydroxyascorbate + 2Cu^{+} + 2H^{+} \qquad \text{Equation 1}$$

$$ascorbate + O_2 \xrightarrow{Cu^{2+}} dehydroxyascorbate + H_2O_2 \qquad \text{Equation 2}$$

$$H_2O_2 + Cu^{+} \rightarrow Cu^{2+} + OH^{-} + OH^{\circ}(highly\ reactive) \qquad \text{Equation 3}$$

The released hydroxyl radicals from Equation 3 are further able to cleave the DNA strand. This is initiated by the abstraction of a hydrogen atom from the desoxyribose backbone.[105] While the hydroxyl radical is able to abstract any hydrogen, it was already in the 1980ies that researchers determined the radicals of Cu^{2+} complexes to abstract certain hydrogens.[106]

Studies of peptide-DNA and peptide-drug-DNA interactions led to a rising interest in this research field. Intensive studies came to the conclusion that the stereochemical orientation of the square-planar ATCUN-metal complexes is crucial for DNA cleavage.[107] A preference for A/T-rich regions in dsDNA was evaluated with the binding to the minor groove. Huang *et al.* stated a minor groove binding through the N3 imidazole hydrogen to the N3 of adenine or the O2 of thymine.[108]

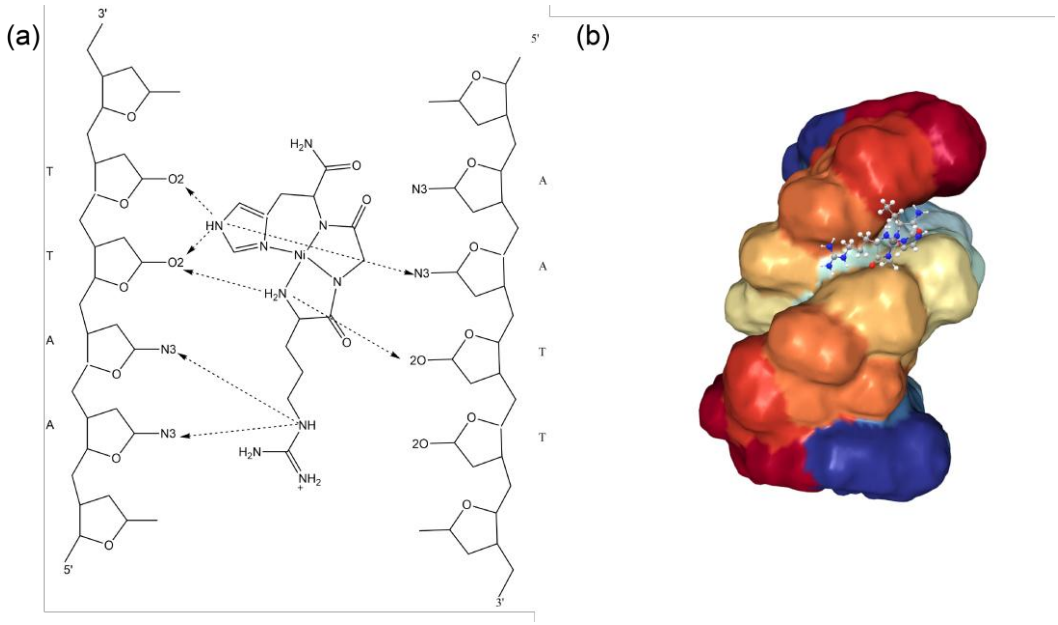

Figure 9. Interactions of the ATCUN motif with dsDNA

Images inspired by simulation studies from Fang *et al.* to illustrate the proposed binding and interactions of the ATCUN motif l-Arg-Gly-His with $d(CGCGAATTCGCG)_2$.[107] (a) shows hydrogen bonding and (b) the relative orientation of the ATCUN motif in the space-filled DNA model (Proteine Data base 1CW9)

Image from the RCSB PDB (rcsb.org) of PDB ID 1CW9 (van Aalten, D.M., Erlanson, D.A., Verdine, G.L., Joshua-Tor,L. (1999) Proc.Natl.Acad.Sci.USA 96: 11809-11814 DOI 10.2210/pdb1CW9/pdb)

In the past, small metallopeptides were used as scaffolds for the development of low molecular drugs. In 1966 Umezawa et al discovered the antibiotic competence of the bleomycin family, a glycoprotein isolated by *Streptomyces verticillus*.[109] Nowadays these structures are commonly used as antitumor agents in the combinational treatment of lymphomas, types of gem-cell cancers and certain head and neck cancers.[110] These glycoproteins bind transition metals, such as Fe(II) and Cu(I) and cleave ssDNA as well as dsDNA through formation of lesions within the strands.[111] Probably one of the most known anticancer drugs is Cisplatin, a metallopeptide that cross-links to DNA.[112] Since this behavior

can also be found in ATCUN motifs, these structures are of great interest in the evolvement of new medications.

In regard to cancer treatment, DNA sequencing of the tumor genome, will enhance treatment and identify mechanisms of drug resistance.[113]

3.4.4. DNA translocation and sequencing through solid-state nanopores

DNA sequencing makes “reading” of a DNA strand possible. Therefore, it is a fundamental for biological research making decoding of genomes possible. Over the last fifty years, sequencing of short oligonucleotides was enhanced to read millions of bases.[114] Nanopores, biological and of solid state material, display interesting candidates in regard to fast and efficient DNA sequencing. With the translocation of a nucleotide unit within the DNA sequence, a current block is generated that is dependent on the base travelling through. The idea of nanopore DNA sequencing was proposed by Deamer and Akeson in 2000[115] based on their findings from 1996, where the biological pore α-Haemolysine, α-HL was successfully used to translocate ssDNA.[15] The α-HL pore displays a pore opening of 2.6 nm with a stem of 2.2 nm and a limiting aperture of 1.5 nm.[116] It passes a steady ionic current of 100 pA with voltages of 100 mV applied through the pore that remains open at neutral pH values.[115]

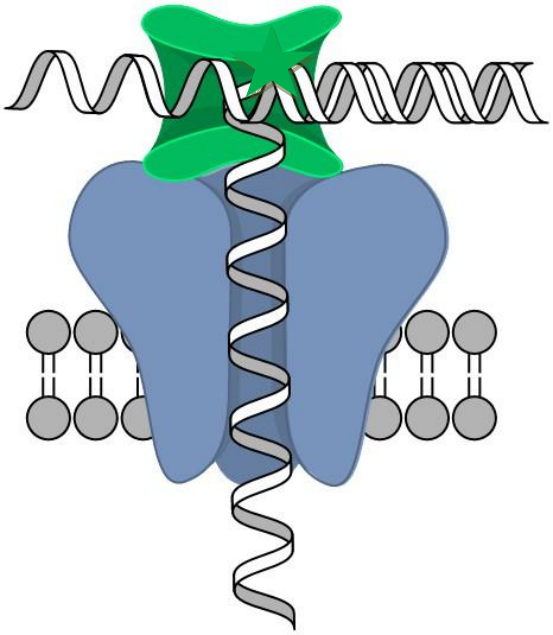

Figure 10. DNA sequencing through a alpha hemolysine nanopore with phi29DNA polymerase attached

Figure showing the translocation of ssDNA through a α-HL nanopore (blue) with phi29 attached (green) inspired from Schneider et al.[117]

Unfortunately, the speed of translocation is extremely high, making signal read-out challenging. Many strategies are proposed slow down the translocation time to make base identification possible and reliable. The Akeson lab designed a blocking oligomer used with phi29 DNAP (bacteriophage phi29 DNA polymerase) atop of a α-HL pore for controlled sequential movement of ssDNA strands.[118] To overcome limitations in translocation of only ssDNA, other pore forming structures were sceened. A pore from *Mycobacterim smegmatis* (MspA)[119] evolved to be an interesting candidate towards DNA sequencing. Combined with the phi29 DNA Polymerase[120] it was investigated towards sequencing of double stranded DNA (dsDNA) adding a Phi29.[121] Still, a high error rate for both systems leaves room for improvement.

Therefore, solid-state nanopores emerged to be possible structures applicable for DNA sequencing. The results from biological nanopores indicated a need for a unit to slow or interfere with the translocation rate. Therefore, functionalization of solid-state nanopores using a DNA-hairpin molecule, also for the transport of the desired sequence, emerged to be a promising approach.[122,123] Solid-state materials from polymers are usually characterized by a great thickness, which is linked to major challenge towards DNA sequencing. A thickness of

only 30 nm corresponds to around 60 bases of an ssDNA molecule, exemplifying these problematics.[117] Recently, graphene-based nanopores were introduced displaying a thickness of a singe carbon atom and could therefore circumvent the introduced difficulties. Successful translocation of dsDNA displays a fundament from which further experiments can be developed.[124]

4. Aim

This thesis focuses on two ways on creating hybrid nanopores. The first approach is based on an example from nature and transport over a membrane in form of ion channels. The idea behind this is the combination of a naturally occurring ion channel and the embedding of this structure into artificial solid/lipid support. A second approach focuses on the usage of solid state/artificial nanopores and the immobilization of functional peptides aiming for a certain selectivity. For that purpose, this thesis addresses both aspects as followed:
(1) The development of a chemical synthesis route for the viral potassium channel Kcv_{NTS} as the first step towards the design of bio-inspired nanopores.
(2) The fabrication of a hybrid material that based on heavy-metal ion coordination through immobilization of the corresponding ion sensitive peptide into track-etched nanopores.

In order to fulfill the first aim, the generation of sufficient quantities of Kcv_{NTS}, to facilitate structural studie, is addressed. Therefore, a robust synthetic route is needed that further allows for future integration of isotopically-labeled amino acids for NMR studies or for straight-forward mutations and additions to the native sequence prior to development of a bio-inspired material. The 82-mer displays a strong hydrophobicity especially within the alpha-helical transmembrane regions. With increasing hydrophobicity the chemical synthesis becomes more challenging. That is why a synthesis of the complete sequence within one step would fail. Therefore, the sequence needs to be divided in a way that ensures the native sequence after ligating the evaluated fragments through native chemical ligation (NCL). In this thesis several approaches are addressed including the correct conditions for the NCL reaction. Additionaly, synthesis of the fragments is challenging as well as purification after solid phase peptide synthesis with the need to address the available possibilities towards fragment generation. Finally, the correct folding and behavior of the product, the synthetic Kcv_{NTS}, needs to be investigated. The difficulties for analytical methods towards such hydrophobic structures are addressed as well.

Approaching the second aim, a small sensing peptide needs to be evaluated that can be integrated into solid-state nanopores for the generation of a sensing device. To exploit the advantages of the hybrid system, the sensor needs to display a robustness, selectivity, sensitivity as well as re-usability. To fulfill the approach, peptides and mutants of the ATCUN family are designed and studied in regard to metal ion selectivity. A selectivity towards only one target is needed to generate a selective sensor. Therefore, binding studies are conducted. Addressing the sensitivity and re-usability several analytical approaches are presented using the selective system. Finally, the applicability of the sensor is discussed. To evaluate the need of the referred mandatory histidine moiety in the ATCUN motif, mutants are investigated towards heavy metal binding. Solid-state nanopores and biological nanopores are interesting regarding DNA sequencing. Aiming towards a sequencing device, first steps are presented making use of the scission ability of the ATCUN peptides. An approach is presented targeting the examination of a scission preference towards several dsDNA plasmids. Furhter studies regarding the scission ability of the designed ATCUN peptides and mutants, when immobilized to the solid-state nanopores, are addressed to use the outcomes for a possible device generation.

5. Methods

5.1. Synthesis and analytics of voltage-gated potassium channels

Synthesis of the 82 amino acid long Kcv protein is performed by division of the sequence into three fragments (Figure 30). All fragments are synthesized on a CEM liberty automated peptide synthesizer using the standard Fmoc-based solid phase peptide synthesis (SPPS) protocol. AmphiSpheres RAM (rink amide resin) (loading 0.38 mmol/g) is used for all synthesis protocols, respectively. Prior to synthesis, the resin is swollen using Dichloromethane (DCM) for 20 minutes under shaking and washed using N,N-Dimethylformamide (DMF). Double coupling is performed for each amino acid at 50 °C and using microwave treatment (35 W). As coupling reagents, 1-[Bis(dimethylamino)methylene]-1*H*-1,2,3-triazolo[4,5-*b*]pyridinium 3-oxid hexafluorophosphate (HATU) (3.9 equ., 0.2 M) in DMF and N-ethyl-N-(propan-2-yl)propan-2-amin (DIEA) (8 equ., 0.4 M) in N-Methyl-2-pyrrolidone (NMP) and are used with the concording amino acid (4 equ., 0.2 M). Deprotection of the 9-fluorenylmethoxycarbonyl (Fmoc)-group is performed in 20% piperidine/DMF (v/v) and controlled through the integrated UV-monitor of the peptide synthesizer for each deprotection step. The final deprotection step is done manually to control the remaining loading of the resin. Final cleavage from the resin is performed using a mixture of trifluoroacetic acid, TFA/triisopropylsilane, TIPS/anisole (90:2.5:2.5% v/v) for 3.5 h at room temperature. The crude peptide is precipitated in ice-cold diethyl ether, centrifuged, and washed with diethyl ether. The obtained crude product is dissolved in acetonitrile, ACN/water mixture and freeze dried (Christ Alpha 1-2 LDplus). All peptides are stored at -30 °C. Complete synthesis of fragment 1 and fragment A is done by automated SPPS according to the described procedure. Synthesis specifications for fragment 2 and 3 are reported in the next paragraph.

Fragment 2 contains the oxo-ester group 2-hydroxy-3-thio-propanic acid (hmp) which is coupled with the two consecutive amino acids manually prior to automated peptide synthesis. For coupling of hmp, hmp(Trt) (4 equ., 0.2 M, 364.06 g/mol) is coupled by double coupling (2 × 1 h) using the standard reaction conditions described above with addition of 1-Hydroxy-7-azabenzotriazole HOAt (4 equ., 0.2 M, 136.11 g/mol). After washing the resin with DCM, dry tetrahydrofurane, THF, is used to prepare the resin for the Mitsunobu reaction. Using this method, the next amino acid, Fmoc-Ser(tBu)-OH (5 equ., 0.2 M, 383.44 g/mol) is coupled using douple coupling (2 × 2 h) with triphenylphosphine, PPh_3 (5 equ., 0.2 M, 262.29 g/mol) and diethylazodicarboxylate, DEAD (5 equ., 40 wt% in toluene, 174.15 g/mol). After Fmoc deprotection, the next amino acid Fmoc-Phe-OH (4 equ., 0.2 M, 387.43 g/mol) is coupled using the standard coupling protocol. No deprotection takes place, the resin is freeze dried for further automated SPPS.

Fragment 3 also contains the oxo-ester group hmp. Manual coupling is analogous to fragment 2 using Fmoc-Thr(tBu)-OH (5 equ. 0.2 M, 397.46 g/mol) for the Mitsunobu reaction. The next amino acid, Fmoc-Phe-OH, is coupled according to fragment 2. Fragment B is synthesized accordingly, with the consecutive amino acids seen in Table 5.

Fragment 3.2 contains a solubility tag attached before hmp coupling. The solubility tag NH_2-Gly-Gly-Gly-Gly-Ser-Lys-Lys-Lys-$CONH_2$ is coupled using the peptide synthesizer following the standard protocol. Coupling of the hmp unit and the following two amino acids is equal to the protocol described for fragment 3.

Sequence	Fragment	Molecular formula	Resin	scale (mmol)
Kcv_{NTS}(36-82)	Fragment A	$C_{239}H_{360}N_{54}O_{63}S_2$	AmphiSpheres RAM	0.1
loading of resin (mmol/g)	**M_{resin} (mg)**	**Calculated peptide mass (mg)**	**M_{resin} end (mg)**	**loading end (mmol/g)**
0.37	270	506	827.7	0.0667

Table 4. Synthesis conditions for fragment A

No. synthesis	1	2	3
AA pos. 36	D36	D36E	D36E
Special features of synthesis	2-methylpiperidine, Pseudoprolines	2-methylpiperidine	2-methylpiperidine, Pseudoprolines
Resin weight (g)	0.556	0.600	0.5802
Resulting resin weight (g)	0.635	0.6336	0.5905
Scale (mmol)	0.1		
Resin	TentaGel® 0.18 mmol/g		
Crude product (mg)	80	25	28
Calculated product (mg)	407	439	426
Synthesis yield (%)	19.7	8.0	6.6

Table 5. Synthesis conditions for fragment B

Sequence	**Fragment**	**Molecular formula**	**Resin**	**scale (mmol)**
Kcv_{NTS}(41-82)	Fragment 1	$C_{209}H_{322}N_{50}O_{55}S_2$	AmphiSpheres RAM	0.25
loading of resin (mmol/g)	**M_{resin} (mg)**	**Calculated peptide mass (mg)**	**M_{resin} end (mg)**	**loading end (mmol/g)**
0.38	1400	1130	669.77	0.22

Table 6. Synthesis conditions for fragment 1

Molecular formula	Calculated $[M+H^+]^+$	Calculated $[M+3H^+]^{3+}$	Measured $[M+3H^+]^{3+}$	Calculated $[M+4H^+]^{4+}$	Measured $[M+4H^+]^{4+}$
$C_{209}H_{322}N_{50}O_{55}S_2$	4480.22	1493.79	1493.80	1120.59	1120.60

Table 7. Measured and calculated masses during LC-MS measurements of fragment 1

Sequence	**Fragment**	**Molecular formula**	**Resin**	**scale (mmol)**
Kcv_{NTS}(16-40)	Fragment 2	$C_{139}H_{199}N_{29}O_{40}S_5$	AmphiSpheres RAM	0.25
loading of resin (mmol/g)	**M_{resin} (mg)**	**Calculated peptide mass (mg)**	**M_{resin} end (mg)**	**loading end (mmol/g)**
0.18	1400	775	225.87	0.08

Table 8. Synthesis conditions for fragment 2

Molecular formula	Calculated $[M+H^+]^+$	Calculated $[M-H_2O+2H^+]^{2+}$	Measured $[M-H_2O+2H^+]^{2+}$
$C_{139}H_{200}N_{30}O_{39}S_5$	3075.57	1529.65	1529.66

Table 9. Measured and calculated masses during LC-MS measurements of fragment 2

Sequence	**Fragment**	**Molecular formula**	**Resin**	**scale (mmol)**
Kcv_{NTS}(1-15)	Fragment 3	$C_{89}H_{152}N_{28}O_{29}S_5$	TentaGel	0.25
loading of resin (mmol/g)	**M_{resin} (mg)**	**Calculated peptide mass (mg)**	**M_{resin} end (mg)**	**loading end (mmol/g)**
0.18	560	226	46.6	0.1

Table 10. Synthesis and conditions for fragment 3

Sequence	**Fragment**	**Molecular formula**	**Resin**	**scale (mmol)**
Kcv_{NTS}(1-15) +solubility	Fragment 3.2	$C_{118}H_{205}N_{29}O_{28}S_2$	AmphiSpheres	0.25
loading of resin (mmol/g)	**M_{resin} (mg)**	**Calculated peptide mass (mg)**	**M_{resin} end (mg)**	**loading end (mmol/g)**
0.38	1354	1353	n.a.*	0.04

Table 11. Synthesis and conditions for fragment 3.2

*Determination of the exact mass of the crude product was not possible due to gel-like structure of the product sticking to the walls of the falcon

Molecular formula	Calculated $[M+H^+]^+$	Calculated $[M+2H^+]^{2+}$	Measured $[M+2H^+]^{2+}$	Calculated $[M+3H^+]^{3+}$	Measured $[M+3H^+]^{3+}$
$C_{118}H_{205}N_{29}O_{28}S_2$	2543.20	1271.76	1271.75	847.17	848.16

Table 12. Measured and calculated masses during LC-MS measurements of fragment 3.2

5.1.1. Terminology of Kcv_{NTS} fragments

Fragment	Sequence
Fragment 1	Kcv_{NTS}(41-82)
Fragment 2	Kcv_{NTS}(16-40)
Fragment 3	Kcv_{NTS}(1-15)
Fragment 3.2	Kcv_{NTS}(1-15)+solubility tag
Ligation product 1	Kcv_{NTS}(16-82)
Ligation product 1.2	Kcv_{NTS}(16-82), after thioproline conversion
Ligation product 2	Kcv_{NTS}(1-82)
Fragment A	Kcv_{NTS}(36-82)
Fragment B	Kcv_{NTS}(1-35)

Table 13. Terminology of fragments

5.1.2. RP-HPLC of Kcv_{NTS} fragments

Dissolution of the fragments for preparative purification is illustrated in Table 14.

Fragment	Protocol
Fragment 1	15 mg of crude product are weighed into a 15 ml falcon. A droplet of concentrated TFA is added to the crude product dissolving around 70% of the crude peptide. 600 μl of ACN are added and vortexed. Around 300 μl of water are added and the falcon centrifuged and the clear solution injected
Fragment 2	25 mg of crude product are dissolved in 1.0 ml of ACN (0.1% TFA)/water (0.1% TFA) solution 1:1 v/v, vortexed and injected
Fragment 3.2	To a falcon of crude product ($\sim$ 10 mg) 500 μl of ACN (0.1% TFA)/water (0.1% TFA) solution 1:1 v/v are added and the solution vortexed. Another 500 μl of water (0.1% TFA) are added and vortexed, respectively. The clear solution is injected into the RP-HPLC

Table 14. Dissolution of the Kcv fragments

RP-HPLC methods are described in Table 15. Eluent and HPLC system:

Eluent A: water (0.1% TFA)
Eluent B: ACN (0.1% TFA)

Analytical RP-HPLC instrument: Waters 2695 alliance equipped with a Waters 2998 photodiode array detector.

Preparative RP-HPLC instrument: Waters 600 equipped with a Waters 2996 photodiode array detector.

Analytical RP-HPLC

Fragment	Method	Column
Fragment 1	Linear gradient of 20% - 95% eluent B over 30 minutes, flow: 1 ml/min, column 30 °C, UV Vis: 214 nm	**MultoKrom High BIO 300-3 C4**;
Fragment 2	Linear gradient from 20% - 65% eluent B over 20 minutes, flow: 1 ml/min, column 30 °C, UV Vis: 214 nm	3 μm particle size, 300 Å pore diameter 125 mm × 4 mm
Fragment 3.2	5 minutes isocratic at 5% eluent B followed by a linear gradient of 5% - 70% eluent B over 20 minutes total, flow: 1 ml/min, column 30 °C, UV Vis: 214 nm	CS Chromatography Service GmbH

Preparative RP-HPLC

Fragment	Method	Column
Fragment 1	Linear gradient from 40% - 95% eluent B over 75 minutes, flow: 10 ml/min, UV Vis: 214 nm	**MultoKrom High BIO 300-5 C4**;
Fragment 2	Linear gradient of 20% - 45% eluent B over 45 minutes, flow: 10 ml/min, UV Vis: 214 nm	5 μm particle size, 300 Å pore diameter, 250 mm × 20 mm
Fragment 3.2	15 minutes isocratic at 5% eluent B followed by a linear gradient of 5% - 70% eluent B within 60 minutes total, flow: 8 ml/min, UV Vis: 214 nm	CS Chromatography Service GmbH

Table 15. RP-HPLC methods for Kcv fragments

5.1.3. Native chemical ligation of Kcv_{NTS} fragments

5.1.3.1. Ligation using ligation buffer A

Native chemical ligation, NCL experiments were performed in ligation buffer A (flushed with argon) containing HFIP as the organic solvent. The following ratio is used 1:1.5 n/n fragment 2 (1.0 mM) : fragment 1 (1.5 mM). Using NaOH (10 M, flushed with argon) the pH is adjusted to ~7.5 and the ligation reaction initiated. Under nitrogen atmosphere, the reaction is carried out for 24 h.

5.1.3.2. Ligation using ligation buffer B

Ligation experiments are conducted according to 5.1.3.1 using ligation buffer B (flushed with argon containing TFE as the organic solvent.

5.1.3.3. Ligation using ligation buffer C

The 1,3-thiazolidine-4-carboxo, thioproline (Thz) conversion experiments are conducted in ligation buffer C. The ligation solution from NCL in buffer A is centrifuged to yield only the protein pellet. The supernatant is disposed and the resulting solid dissolved in the ligation buffer D. With the addition of methoxyamine (200 mM) and lowering the pH to 4.0 ligation buffer C is obtained. The reaction is carried out for 8 h until the loss of -12 Da is detected by MALDI-TOF MS.

The ligation buffer C can further be used to perform the second NCL in a one-pot strategy. In concordance to 5.1.3.1, the ratio of 1:1.5 n/n thioester-forming peptide, fragment 3 (1 mM) to product from the first NCL, ligation product 1 (1.5 mM) is used and the NCL initiated with increasing the pH ~7.5.

5.1.3.4. Ligation using ligation buffer D

Ligation experiments are conducted according to 5.1.3.1 using ligation buffer B (flushed with argon) containing TFE as the organic solvent.

Fragment and molecular formula	**Calculated $[M+H^+]^+$**	**Measured TFE ligation solution $[M+H^+]^+$**	**Measured TFE ligation sediment $[M+H^+]^+$**	**Measured HFIP ligation sediment $[M+H^+]^+$**
Fragment 1 $C_{209}H_{322}N_{50}O_{55}S_2$	4480.22	4480.69	4481.40	4484.82
Fragment 2, hydrolyzed (see 6.6) $C_{136}H_{1950}N_{29}O_{38}S_4$	2973.44	-	-	2971.31
Ligation product 1 **$C_{345}H_{512}N_{78}O_{92}S_6$**	**7417.60**	**7418.28**	**Elevation within the area of product with intensity$_{max}$ at 7426.2**	**7416.62**

Table 16. Molecular masses for MS analysis during ligation 1

5.1.4. Purification using Vivaspin®

The purification protocol using Vivaspin® is conducted after the second ligation and, if no one-pot stategy is pursued, after the first ligation to evaluate its success using MALID TOF MS. Flipping of the Vivaspin® unit is illustrated in Figure 11. It is important to not touch the filter membrane with the pipette tip.

No	Step	× g (fixed bucket)	Time (minutes)
1	Convert into filter of Vivaspin® and fill up to 1.0 ml using 1:3 v/v TFE/water (0.1% TFA)	8000	30
2	Add 500 μl of solvent from step 1	8000	30
3	Add 200 μl of water and vortex throughoutly		
4	Flip Vivaspin®	5000	5
5	Collect remains from the filter washed with water		
6	Add 200 μl of TFE and vortex throughoutly		
7	Flip Vivaspin®	5000	5
8	Collect the remains from the filter washed with TFE		

Table 17. Vivaspin centrifugation

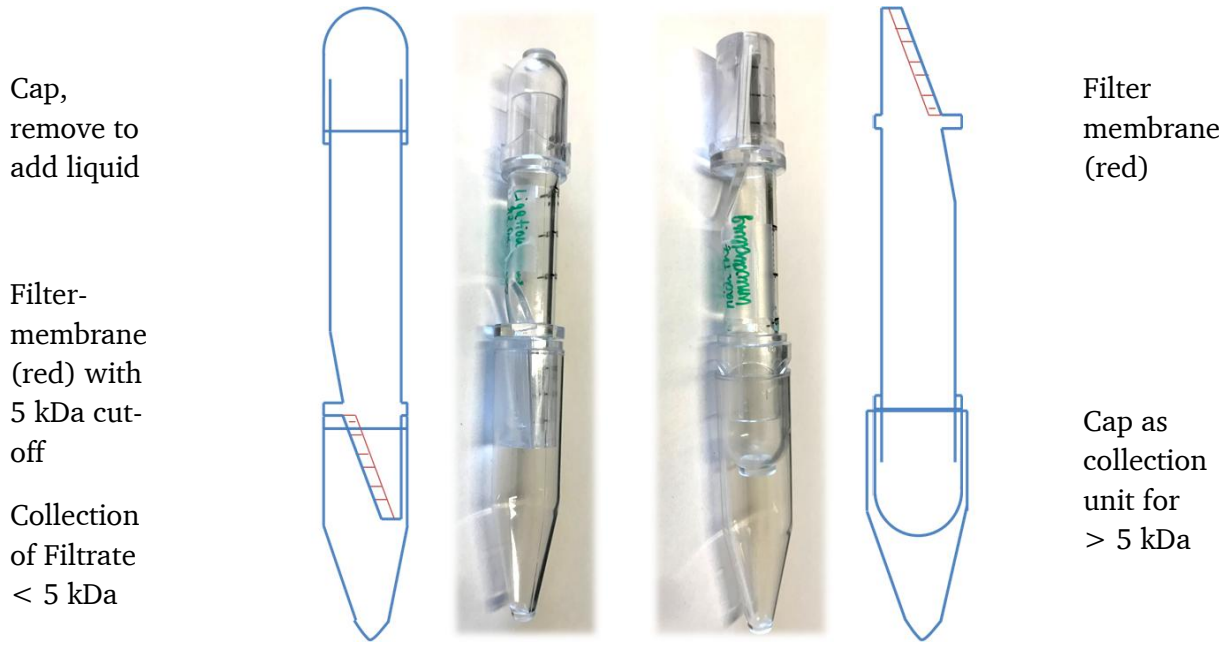

Figure 11. Vivaspin purification

5.1.5. Mass Spectrometry of Kcv_{NTS} fragments

Both LC-MS (liquid chromatography mass spectrometry) using an ESI (electron spray ionization) ion source and MALDI-TOF MS (matrix assisted laser desorption ionization – time of flight mass spectrometry) are applied to characterize and investigate fragments 1 – 4 and ligation products 1 and 2.

LC-MS measurements of fragments 1 – 4 are recorded on Brucker Impact II (Bruker Daltonik GmbH) combined with the RP-HPLC instrument Agilent 1200 using the MultoKrom High BIO 300 C4 column at a flow rate of 0.2 ml/min. The eluent system is composed of eluent A = water (0.1% formic acid, FA) and eluent B = ACN (0.1% FA). The following gradient system is used: equilibration at 25% eluent B for 0.5 minutes followed by a linear gradient 25% - 95% eluent B over 30 minutes. A purging step at 99% eluent B for 10 minutes is added to the method. The applied MS method is the following: MS ESI 800 m/z – 5000 m/z.

LC-MS methods for the Kcv_{NTS}(1-35) and Kcv_{NTS}(36-82) can be found in the following table:

Sample	HPLC Method	Solvents	RP Column	Flow	MS method
Kcv_{NTS} (36-82)	Equilibration at 30% eluent D for 0.5 minutes followed by a linear gradient to 70% eluent D in 20 minutes	Eluent C: H_2O + 0.1% TFA Eluent D: ACN (0.1% TFA)	Vydac219TP diphenyl	0.2 ml/min	MS ESI 800 m/z – 5000 m/z
Kcv_{NTS} (1-35)					

Table 18. LC-MS methods for Kcv_{NTS} fragments

The standard procedure used for MALDI-TOF MS analysis is based on usage of the 2,5-DHAP (2,5-Dihydroxyacetophenone) matrix. For that, to a 2,5-DHAP solution in ethanol (133 mM), diammonium hydrogen citrate (125 μl, 80 mM) are added. The peptide (~0.3 mM, solvent: 1:3 v/v TFE/water (0.1% TFA)) is dissolved 1:1 v/v in water (0.2% TFA). To that mixture, the matrix solution is added 1:1 v/v and pipetted up and down until crystallization takes place. The suspension (0.5 μl) is pipetted on the ground steel target and the MS spectra recorded in linear mode.

For measurement of ligation product 2, the ultrathin layer method, introduced by Cadene *et al.*[125] was used and modified to fit our need.

Sample matrix:

- Saturated α-cyano-4-hydroxycinnamic acid (4-HCCA) in 3:2:1 formic acid/water/isopropanol v/v/v
- Sample (0.3 mM) in octylglucoside, OG (1 mM in water (0.1% TFA)) or in methanol, is dissolved in matrix solution 1:15 or 1:5

Matrix for thin layer

- Saturated 4-HCCA in 1:2 water/acetonitrile v/v
- Dilute 4 times with isopropanol

The matrix for thin layer is spotted on the target (0.8 μl) whereas the sample matrix is spotted onto the ultra-thin yellowish layer (0.5 μl) resulting in a crystalline film.

The third sample preparation technique used is the threelayer method adopted from Keller *et al.*[126] Layer 1 contains 4-HCCA (106 mM) in a methanol/acetone (40:60 v/v) solution. Layer 2 is composed of a saturated 4-HCCA solution in methanol/acetone (40:60 v/v) and layer 3 contains the peptide (~0.3 mM, solvent: 1mM OG in water (0.1% TFA) or methanol) Finally, three layers were plated onto the target as a sandwich from layer 1 to layer 3 in the ratio 3.3:1.3:1.

5.1.6. SDS Page

Sample preparation from ligation buffers B, C and D: 7 μl of the ligation solution are pipetted into 5 μl of TFE/water (0.1% TFA) 30:70 v/v. 10 μl of reducing sample buffer are added if reducing conditions are applied. For native SDS PAGE, 10 μl of non-reducing sample buffer are added. If samples are spiked with K^+, 2.5 μl KCl (1 mM) in water are added to 7.5 μl reducing or non-reducing sample buffer. To ligation product 2 samples 1 μl of OG (1 mM) in water (0.1% TFA) are added. The samples are incubated at 37 °C for 15 minutes and 15 μl of sample added to the wells of the pre-cast gels (Mini-PROTEAN TGX™, 4 – 20% precast gel). The gel is run at 90 V for 45 minutes.

Freeze dried samples are dissolved in 10 μl TFE/water (0.1% TFA) 30:70 v/v. The following staining protocols are adapted from the protocol by Schägger.[127]

5.1.6.1. Coomassie staining

The gel is incubated in the fixing solution for 30 minutes and afterwards stained using the 0.023% Coomassie dye solution for at least 60 minutes. Destaining of the gel is accomplished using 10% acetic acid solution. The gel can further be stored in water or used for additional silver staining.

5.1.6.2. Silver staining

The gel is incubated in the fixing solution for 30 minutes and washed with water twice for at least 60 minutes. The gel is sensitized using the 0.005% sodium thiosulfate solution for 30 minutes and thereafter stained with a 0.1% silver nitrate solution. After washing with water, the silver bands are developed using 2% sodium carbonate and adding 0.036% formaldehyde directly before using the solution. The development can be stopped using a 50 mM EDTA solution

5.1.7. Circular dichroism (CD)

CD measurements are performed on a Jasco J-710 spectropolarimeter under nitrogen atmosphere using the following measurement set-up: UV area from 190 – 260 nm, cuvette path-length of 0.1 cm, data pitch 0.2 mm, scanning speed 100 nm/min and 10 accumulations. All measurements were performed at 21 °C. The peptide (~0.3 Mm) is dissolved in TFE and measured directly.

For CD measurements using the extrusion method with 1-palmitoyl-2-oleoyl-*sn*-glycero-3-phosphocholine (POPC) lipids, 15 equ. of POPC and 1 equ. of peptide 4re dissolved in TFE and freeze dried. The residue is suspended in degassed 10 mM Na_2HPO_4 buffer (pH 7.5) and shaken at room temperature or 2 h. Using freeze/thaw cycles the sample is prepared for extrusion through a 1 μm polycarbonate membrane using a mini-extruder.

5.2. Synthesis and analytics of ATCUN-like peptides

Ac-DAP-β-Ala-His-mPEG$_4$, (Peptide 1) Ac-DAP-β-Ala-Ala-mPEG$_4$ (Peptide 2) Ac-DAP-β-Ala-Asp-mPEG$_4$ (Peptide 3) and (5/6)FAM-DAP-β-Ala-His-mPEG$_4$ (Peptide 4), were synthesized following the standard Fmoc-SPPS using a chlorotrityl chloride resin, Cl-Trt (0.966 mmol/g). The loading of the dried resin with the Fmoc-NH-PEG(4)-COOH residue (2 equ., 0.2 M, 487.54 g/mol) is performed using DIEA (4 equ., 0.4 M, 129.24 g/mol, p = 0.742 g/mol) in DMF. The resin is capped using DCM/methanol/DIEA 16:2:1 v/v and deprotected using 20% piperidine/DMF v/v and coupling efficiency monitored via UV-Vis spectrometry at 301 nm. The following amino acids Fmoc-His(Trt)-OH (4 equ., 0.2 M, 619.71 g/mol), for peptide 1 and 4, Fmoc-Ala-OH (4 equ., 0.2 M, 311.33 g/mol) for peptide 2 and Fmoc-Asp(Ot-Bu) (4 equ., 0.2 M, 411.45 g/mol) for peptide 3 are coupled using the standard Fmoc-based SPPS protocol and with activators HATU (4 equ. 0.2 M, 380.11 g/mol) and 8 equivalents of DIEA (8 equ., 0.4 M, 129.24 g/mol, p = 0.742 g/ml) in DMF. To all peptides, Fmoc-β-Ala-OH (4 equ., 0.2 M, 311.33 g/mol) and Fmoc-Dap(Boc) (4 equ., 0.2 M, 426.46 g/mol) are coupled accordingly. Acetylation of the deprotected peptides 1 – 3 is performed using DMF/Ac_2O/DIEA 5:1:2 v/v/v. To peptide 4 (5/6)-Carboxyfluorescein, 5/6-Fam (4 equ., 0.2 M, 473.39 g/mol) is coupled using an incubated (12 minutes) mixture of Tetramethylfluoroformamidinium hexafluorophosphate, TFFH (4 equ., 0.2 M, 262.29 g/mol) and DIEA (8 equ. 0.4 M, 129.24 g/mol, p = 0.742 g/mol). The in diethyl ether precipitated peptides are washed and the crude product dissolved in ACN (0.1% TFA)/water (0.1% TFA) 1:1 v/v, freeze dried and stored at -30 °C.

Name	Sequence
Peptide 1	Ac-DAP-β-Ala-His-mPEG$_4$
Peptide 2	Ac-DAP-β-Ala-Ala-mPEG$_4$
Peptide 3	Ac-DAP-β-Ala-Asp-mPEG$_4$
Peptide 4	(5/6)FAM-DAP-β-Ala-His-mPEG$_4$

Table 19. Overview of ATCUN-like peptides

Amino Acid	Peptide 1 (mmol/g)	Peptide 2 (mmol/g)	Peptide 3 (mmol/g)	Peptide 4 (mmol/g)
mPEG$_4$	1.25	1.05	1.05	1.310
Fmoc-His(Trt)-OH (1,2)/ Fmoc-Ala-OH (3)/ Fmoc-Asp(Ot-Bu) (4)	0.956	0.877	0.887	1.100
Fmoc-β-Ala-OH	0.717	0.727	0.559	1.200
Fmoc-Dap(Boc)	n.d.	0.587	0.539	1.200

Table 20. Resin loading throughout synthesis

5.2.1. RP-HPLC

Eluent A: water (0.1% TFA)
Eluent B: ACN (0.1% TFA)

Analytical RP-HPLC instrument: Waters 2695 alliance equipped with a Waters 2998 photodiode array detector.

Preparative RP-HPLC instrument: Waters 600 equipped with a Waters 2996 photodiode array detector.

Analytical RP-HPLC

Fragment	Method	Column
Peptides 1 - 3	Isocratic method at 0% eluent B over 4 minutes followed by a linear gradient from 0% - 30% over 20 minutes total, flow: 1 ml/min, UV Vis: 214 nm	**MultoKrom C 18 100-5** 5 μm particle size, 100 Å pore diameter 125 mm × 4 mm CS Chromatography Service GmbH
Peptide 4	Linear gradient of 5% - 40% eluent B over 20 minutes, flow: 1 ml/min, column 30 °C, UV Vis: 214 nm, 494 nm	

Preparative RP-HPLC

Fragment	Method	Column
Peptide 1 -3	Isocratic method at 0% eluent B over 12 minutes followed by a linear gradient from 0% - 30% over 60 minutes total, flow: 8 ml/min, UV Vis: 214 nm	**MultoKrom C18 100-5** 5 μm particle size, 100 Å pore diameter, 250 mm × 20 mm CS Chromatography Service GmbH
Peptide 4	Linear gradient from 5% - 40% eluent B over 60 minutes, flow: 10 ml/min, UV Vis: 214 nm, 494 nm	

Table 21. RP-HPLC methods for ATCUN-like peptides

The purified peptide 4 in Figure 55 is measured on a waters Symmetry^{TM} C_{18} 3.9 × 150 mm columns with a flow of 1 ml/min at 30 °C.

5.2.2. Mass spectrometry of ATCUN-like peptides

To evaluate the complex formation via MS measurements, $CuSO_4$ or $NiSO_4$ (1 equ., in water) is added to the peptide solution (1 mM, phosphate buffer pH 7.4, peptides 1 - 4).

Peptide 4 and 2 are measured using LC-MS on a Brucker Impact II (Bruker Daltonik GmbH) combined with the RP-HPLC instrument Agilent 1200 using the ReproSil gold 120 C18

column (3 μm, 100 mm × 2 mm). The eluent system for peptide-Cu measurements is composed of eluent A – water, eluent B – acetonitrile. with a gradient of 10% - 50% eluent B in 5 minutes. For peptide-Ni measurements, samples are diluted 1:1 v/v with phosphate buffer pH 7.4 and measured using the following gradient: equilibration at 0% eluent B for 5 minutes followed by a linear gradient 0 – 50% eluent B in 10 minutes

For MALDI-TOF MS measurements saturated 4-HCCA is used as the matrix system in water (0.1% TFA)/ACN (0.1% TFA) 1:1 v/v. Sample and matrix are mixed 1:1 v/v and spotted onto the ground steel target. Measurements are operated in reflectron positive (RP) mode.

5.2.3. Amino Acid Analysis

For determination of the content through amino acid analysis (AAA) of each amino acid, the peptide/protein sequence needs to be broken down into the building blocks using hydrolysis. 6 M HCl is sufficient for total hydrolysis when heated to 100 °C for 24 h in a closed system. Pre-column erivatization with aminoquinolyl-N-hydroxysuccinimidyl carbamate, AQC, is performed using AccQ-Flour reagent kit (Waters). Primary and secondary amines react with AQC to form stable urea-derivates that absorb at 254 nm. The reaction is carried out in borate buffer. Using a mixture of amino acids as an external standard (amino acid standard, Thermoscientific) and performing derivatization accordingly, RP-HPLC of the standard and sample can then be compared and the content calculated.

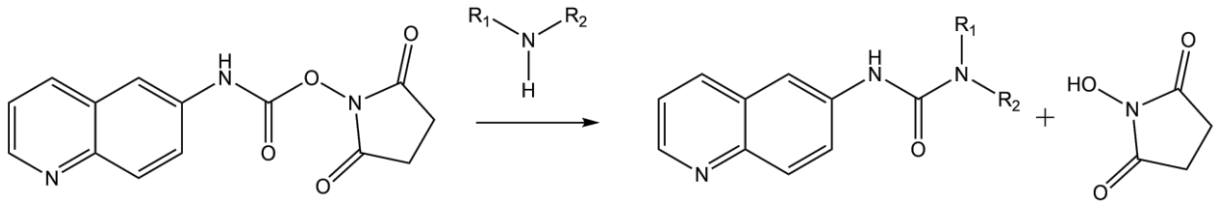

Figure 12. Amino acid analysis

Reaction scheme of primary/secondary amine with ACQ to form UV active urea-derivate

RP-HPLC runs are performed on the Waters 2695 alliance equipped with a Waters 2998 photodiode array detector using the following conditions:

Buffer E	Buffer F	Gradient	flow	Column
50 mM NaAc, pH 5.75	50 mM NaAc, pH 6.00 in 70% acetonitrile	linear gradient of 2% - 20% buffer F over 30 minutes	1 ml/min	MultoKrom C18, 45 °C

Table 22. RP-HPLC conditions for AAA

Within the sequence of peptide 4, only one native amino acid is found: histidine. Thus, amino acid analysis can only be applied by comparing the peak area of histidine within the amino acid standard solution with the peak resulting from the ATCUN sample. To correctly identify the histidine peak, the sample solution is spiked resulting in the double amount of histidine in

the resulting chromatogram compared to the chromatogram of the sample. Furthermore, the amino acid standard and the sample solution are blended, resulting in the spectrum with increased peak areas where amino acids are duplicated.

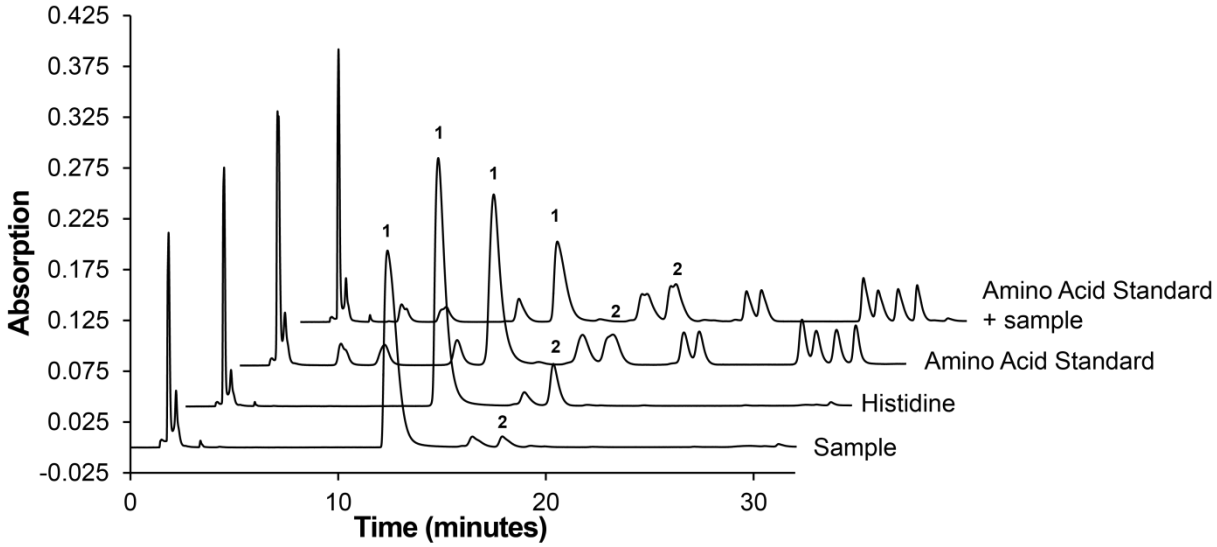

Figure 13. RP-HPLC chromatograms of the amino acid analysis.

Method: linear gradient of 2% to 20% buffer B in 30 minutes using a flow of 1 ml/min and the MultoKrom C18 column at 45 °C.

The stacked chromatogram in Figure 13 shows the different injections. **Peak 1** at 12.2 minutes represents the non-reacted ACQ reagent, showing the highest peak at the histidine injection, being the sample with the least content of amino acid that ACQ can react with. **Peak 2** at 17.8 minutes is generated by histidine and can be found in every injection. When comparing the peak area of **2** in the amino acid standard and the amino acid standard spiked with the sample the peak area almost doubles from an area of 1034759 to 1637255 while the other peak areas stay in the same range.

To evaluate the content, a sample containing only histidine is needed for AAA measurement. Injections of a dilution series result in increasing peak areas that are used for the development of a calibration curve (Figure 14).

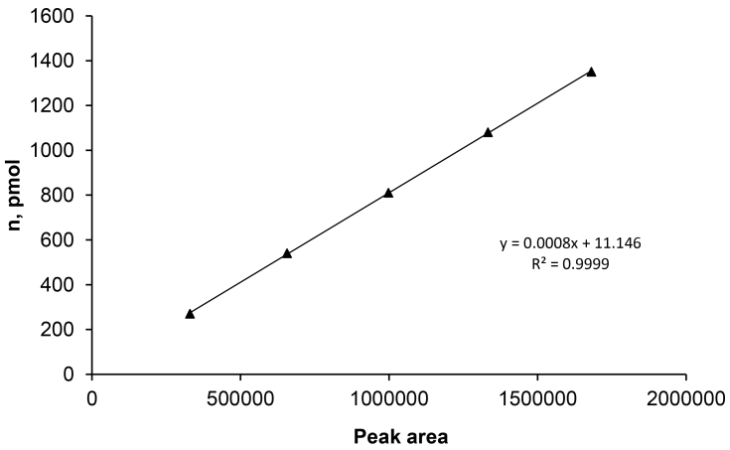

Figure 14. Determination of content using AAA

The following equation is used for the calculation of the content:

$$n_{inject} = {n_{inject} \times V_{vial} \times V_{hydrosylate} \times M_{peptide}} / {4\ \mu l \times V_{inject}}$$

Equation 4. Calculation of content determined through AAA

	(Calculated) value
n_{inject}	0.000269896 μmol
V_{vial}	94 μl
$V_{hydrosylate}$	516 μl
$M_{peptide}$	0.918 mg/μmol
V_{inject}	μl

Table 23. Values to calculate content.

5.2.4. NMR for content determination

NMR spectra were measured on an Avance HD spectrometer at 500 MHz at 298 K by Daniel Tietze. The signal from the protons within the acetyl-group of the external standard N-acetyl alanine were used as our standard signal. For peptides 1 – 3 comparison was done using the acetylated C-terminus. For comparison to peptide 4, protons from the aromatic imidazole moiety of the His-residue were taken. Measurements are done in H_2O/D_2O 9:1 v/v dissolving peptide 1 (2.56 mM), peptide 2 (3.11 mM), peptide 3 (3.03 mM) and peptide 4 (0.55 mM) in 440 μl total volume. The HDO peak was set to a frequency of 4.7 ppm as a reference for the ^{1}H chemical shift. The exact solution from NMR measurements was diluted seven times and injected via RP-HPLC. A calibration curve is obtained from the peak area at different concentrations, making it possible to determine the concentration each time a new batch is purified. RP-HPLC methods used were in accordance to chapter 5.2.1.

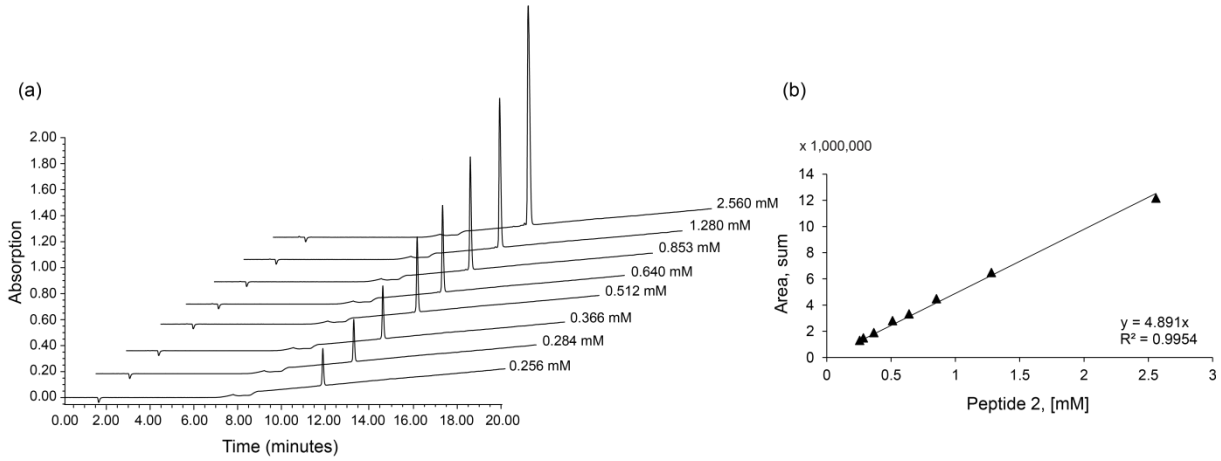

Figure 15. RP-HPLC calibration of peptide 1 after NMR spectroscopy

RP-HPLC conditions isocratic flow of 5% over 5 minutes followed by a linear gradient 5%- 40% eluent B over 20 minutes total with a flow of 1 ml/min, MultoHigh 100 RP 18 column at 30 °C with a retention time of 11.6 minutes.

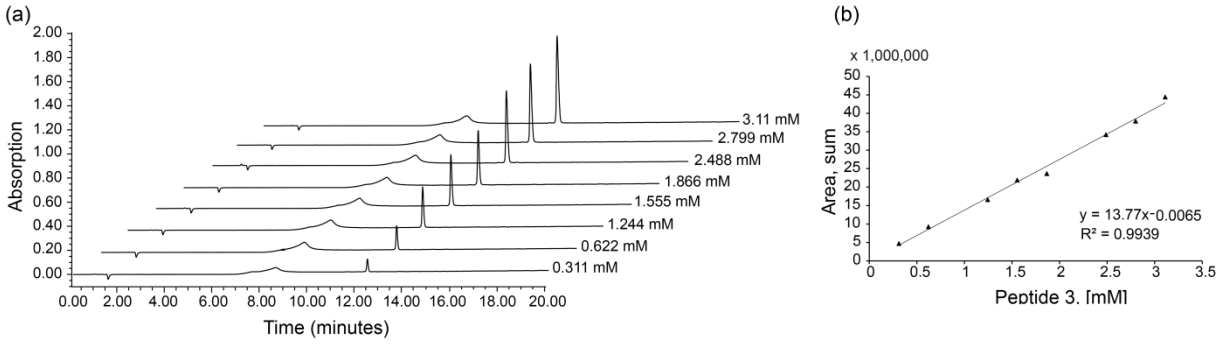

Figure 16. RP-HPLC calibration of peptide 2 after NMR spectroscopy

RP-HPLC conditions isocratic flow of 5% over 5 minutes followed by a linear gradient 5%- 40% eluent B over 20 minutes total with a flow of 1 ml/min, MultoHigh 100 RP 18 column at 30 °C with a retention time of 12.4 minutes.

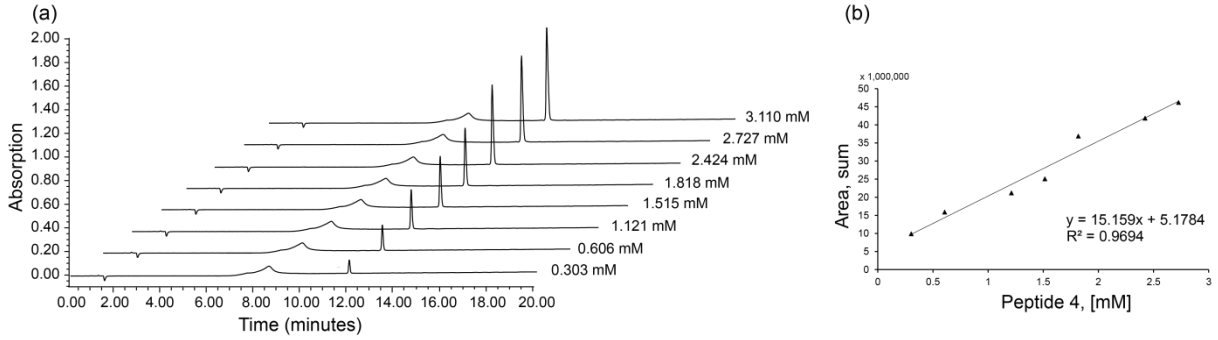

Figure 17. RP-HPLC calibration of peptide 3 after NMR spectroscopy

RP-HPLC conditions isocratic flow of 5% over 5 minutes followed by a linear gradient 5%- 40% eluent B over 20 minutes total with a flow of 1 ml/min, MultoHigh 100 RP 18 column at 30 °C with a retention time of 12.0 minutes.

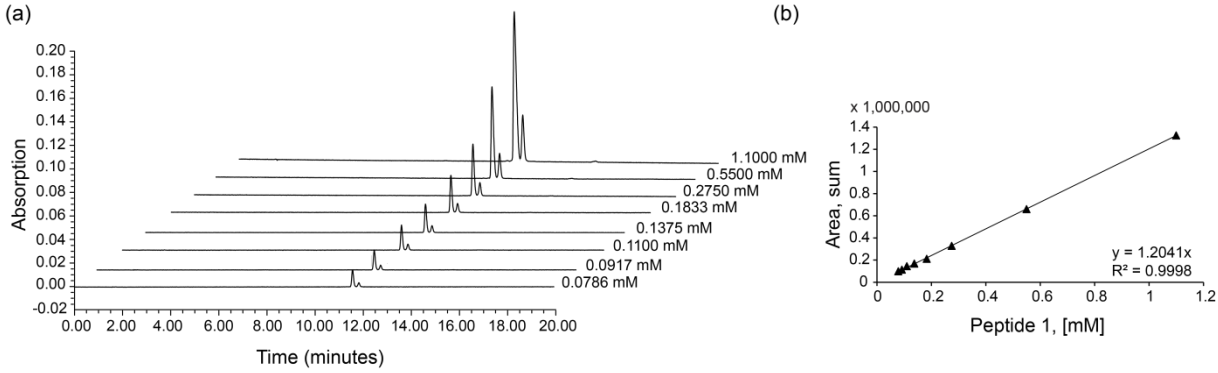

Figure 18. RP-HPLC calibration of peptide 4 after NMR experiments

RP-HPLC conditions: linear gradient of 5% - 40% eluent B over 20 minutes with a flow of 1 ml/min, MultoHigh 100 RP 18 column at 30 °C. Retention times of 11.5 and 11.9 minutes are attributed to the mixed isomers, new retention times to a different column used.

5.2.5. UV VIS titrations

All UV VIS titrations were prepared and executed on Tidas MCS UV/NIR and evaluated using Panorama® program 3.1 (LabCognition).

5.2.5.1. pH titration studies

Evaluation of the optimal pH values for further titration studies is designed as follwod.

To the solution of peptide 1 (1mM, in water) one molar equivalent of $CuSO_4$ (160 mM, in water) or of $NiSO_4$ (160 mM, in water) is added. The pH is lowered with HCl (100 mM, in water) until pH 3. Using NaOH (100 mM, in water) the pH is increased to pH 11 and spectra recorded for each pH step.

To the solution of peptide 2 and 3 (2 mM, in water) one molar equivalent of $CuSO_4$ (320 mM, in water) or of $NiSO_4$ (320 mM, in water) is added. The subsequent steps are according to the experiment set-up of peptide 1.

5.2.5.2. Cu(II) and Ni(II) titration studies

The in Table 24 summarized experiment set-ups are used to evaluate binding constants. To the corresponding peptide solution in the selected buffer system, heavy metal is added in 0.1 molar equivalents to a final of 1.4 equivalents. After each 0.1 equivalent step, a spectrum is recorded.

Peptide	pH	Buffer	Heavy metal
Peptide 1,	6.5	MES, 100 mM	$CuSO_4$ and $NiSO_4$, both 16 mM in water
1 mM in corresponding buffer	6.5	MES, 100 mM	$ZnSO_4$, 16 mM in water
	8.0	TRIS, 100 mM	$CuSO_4$, 16 mM in water
	10.55	TRIS, 100 mM	$NiSO_4$, 16 mM in water
Peptide 2,	10.55	TRIS, 100 mM	$CuSO_4$, 32 mM in water
2 mM in corresponding buffer	10.55	TRIS, 100 mM	$NiSO_4$, 32 mM in water
Peptide 3,	8.0	TRIS, 100 mM	$CuSO_4$, 32 mM in water
2 mM in corresponding buffer	10.55	TRIS, 100 mM	$NiSO_4$, 32 mM in water

Table 24. Buffer systems and set-up for titration studies

5.2.6. Benesi-Hildebrand plot

The Benesi-Hildebrand plot was introduced in 1949[128] and is up to date a widely used method to determine binding constants of complexes displaying a 1:1 and 1:2 stoichiometry. In the following, calculation using this plot will be introduced. For that, our ligand, the heavy metal, will correspond to M while out ATCUN-like peptide represents the molecule, A.

$$M + A \overset{k}{\rightleftharpoons} MA$$

Equation 5. 1:1 complex formation

Furthermore, the Lamber-Beer law is needed, which is expressed in the following equation:

$$A = \varepsilon \times C$$

A – Absorbance
ε - extinction coefficient l × mol^{-1} × cm^{-1}
C – concentration (mol/l)

Equation 6. Lamber Beer law

Inserting the Lamber-Beer law into Equation 5 leads to:

$$\frac{C_A^0}{\Delta A} = 1/[C_M^0 \times K\,(\varepsilon_{MA} - \varepsilon_A)] + 1/(\varepsilon_{MA} - \varepsilon_A)$$

$\boldsymbol{C_A^0}$ & $\boldsymbol{C_M^0}$ - initial concentrations of M and A
ΔA – change of absorbance during complexation
$\boldsymbol{\varepsilon_{MA}}$ **&** $\boldsymbol{\varepsilon_A}$ – absorption coefficients of MA and A

Equation 7. Benesi-Hildebrand Plot

When plotting $\frac{C_A^0}{\Delta A}$ versus $\frac{1}{C_M^0}$ a linear relationship is obtained from where the binding constant K can be calculated from the intercept and the slope.[129]

5.2.7. Fluorescence titration studies

All fluorescence titration studies were executed on a FP-6200 Jasco making use of the quenching of 5/6-FAM upon addition of heavy metals.

To the solution of peptide 4 (1 μM, in 100 mM MES buffer pH 6.5), $CuSO_4$ (1 mM, in water) is added from 0 – 20 molar equivalents. For Ni(II) studies, $NiSO_4$ (100 mM, in water) is added from 0 – 1400 equivalents. For Zn(II) studies, $ZnSO_4$ (100 mM, in water) is added in concentrations of 0.13 – 2.7 mM.

For calculation of binding constants a peptide solution (0.01 μM, in phosphate buffer pH 8.0) is used and $CuSO_4$ (0.32 μM, in water) added in steps of 0.1 molar equivalent until 1.5 equivalents are reached. To investigate Ni(II) binding, $NiSO_4$ (0.32 mM, in water) is added in 0.1 molar equivalent steps until 1.5 equivalents are reached to a peptide solution (0.01 μM, in CAPS buffer pH 10.55)

5.2.8. Stern-Volmer Plot

The Stern-Volmer Plot was introduced in 1919[130] and up until today it is used to describe and calculate various constants involved in a quenching process. In the following the

determination of the Stern-Volmer constant K_{SV}, the Quenching rate constant K_q and the binding constant K are described.

$$\frac{F_0}{F} = 1 + K_{sv}[Q]$$

F_0 – fluorescence intensity with no quencher present
F – fluorescence after quencher added
[Q] – concentration of quencher

Equation 8. Determination of Stern-Volmer constant

To further calculate the biomolecular quenching rate constant K_q this equation is used:

$$K_q = \frac{K_{sv}}{\tau_0}$$

K_q – quenching rate constant ($M^{-1}s^{-1}$)
τ_0 – fluorescence lifetime s^{-1} (approx. 10^{-8} s^{-1} for most protein molecules)[131]

Equation 9. Calculation of the biomolecular quenching rate

This quenching rate can be used to calculate the quenching process. The quenching rate of diffusion collision for diverse quenchers is defined to be $< 2 \times 10^{10}$ $M^{-1}s^{-1}$. Values above this quenching rate indicate a static quenching process.

Furthermore, calculation of the binding constant K is done by plotting $\log([F_0\text{-}F]/F)$ vs $\log(Q)$ following this equation:

$$\log\left(\frac{F_0 - F}{F}\right) = logK + nlog(Q)$$

K – binding constant
n – number of binding sites

Equation 10. Calculation of the binding constant using the Stern-Volmer plot

5.2.9. Determination of the limit of detection (LOD)

For the six-fold blank measurement, 1 μl of blank solution (100 mM MES buffer, pH 6.5) is pipetted to the peptide solution (1 μM in 100 mM MES buffer pH 6.5). From the change of absorbance at λ_{em} 518, the standard deviation, σ is determined.

In a second titration, $CuSO_4$ (1 μM, in water) is added from 0.7 – 60 nM and $NiSO_4$ (10 μM, in water) from 7 – 722 nM to a new peptide 4 solution. To evaluate the LOD, the slope of this titration experiment is needed.

The slope of Δfluorescence intensity vs. concentration Cu(II)/Ni(II) from SI Figure 38 and standard deviation, σ from the blank titration are inserted into Equation 11 and the LOD is calculated as followed using the equation from the International Conference on Harmonization (ICH)[132]:

$$LOD = \frac{3.3 \times \sigma}{S}$$

σ – standard deviation
S – slope

Equation 11. Calculation of the LOD

5.3. Immobilization to solid support

5.3.1. Fabrication of nanopores

PET foils (12 μm thickness) are bombarded with heavy ions (Ag, Pb or U) at the Universal linear accelerator, UNILAC and track-etched using a NaOH solution (9 M). To generate

conically shaped nanopores, etching solution is filled only in one compartment (see Figure 7 for schematic set-up of the two compartments). The resulting free carboxygroups are transformed to primary amines using 1-Ethyl-3-(3-dimethylaminopropyl)carbodiimid, EDC (100 mM in ethanol), pentafluorophenol., PFP (200 mM in ethanol) and diethylamin, EDA (100 mM in ethanol) (Figure 19). Etching and modification of PET foils was done by Ivana Duznovic from RG Prof. Ensinger, Material Science, TU Darmstadt.

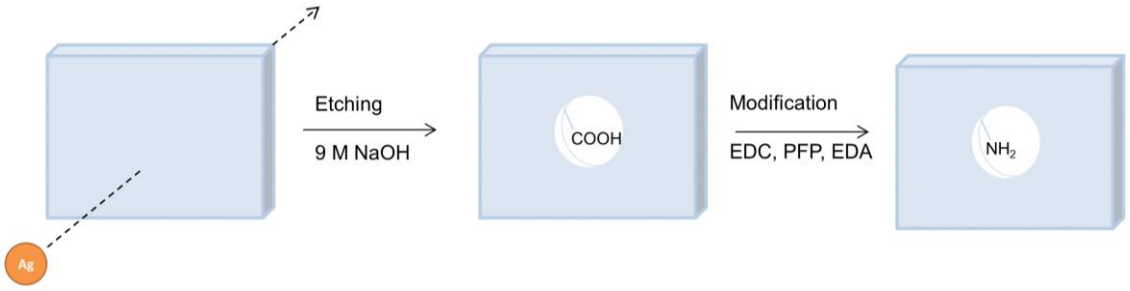

Figure 19. Fabrication of nanopores

Two different geometries were used in the presented studies: conically shaped (**a**) and cylindrical nanopores (**b**) illustrated in Figure 20. For evaluation of the pore geometry, High-Resolution Field-Emission Scanning Electron Microscopy is used cutting a representative piece out of the foil. The piece is plated with a thin gold layer using a sputter coater (Q300TD Sample Preparation System, Wuorum Technologies Ltd) with a gold target (99.9% purity) and argon-plasma (100 s, 3 mA). To obtain a cross section the membrane has to be irradiated by UV-light at 312 nm for 90 hours.

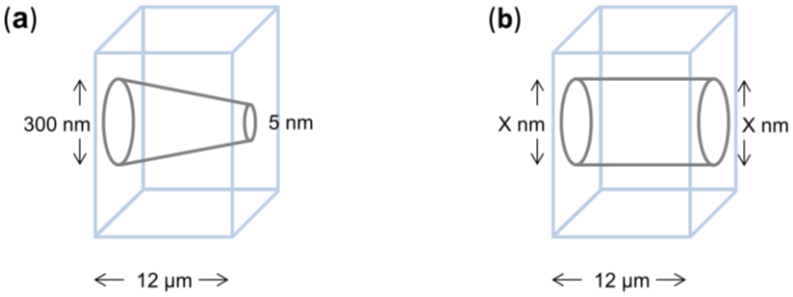

Figure 20. Geometry of nanopores used

Drawings are not to scale.

Nanopores are usually fabricated perpendicular to the plane of the substate while nanochannels are in-plane structures. Nanochannels are frequently fabricated in polymer material.[133] For better reading, nanochannels in PET foils will be referred to as nanopores in the following.

5.3.2. Immobilization of peptides to nanopores

For immobilization of the peptides, two methods were applied. First, coupling using EDC/sulf-NHS and second, using the standard protocol of SPPS amino acid coupling.

To the peptide 4 solution (0.5 mM, in ethanol/water 1:3 v/v), EDC (2 mM final concentration) and sulfo-NHS (5 mM final concentration) are added. The reaction solution is protected from light for 15 – 30 minutes and added to the compartmens surrounding the PET foil. The reaction is carried out overnight.

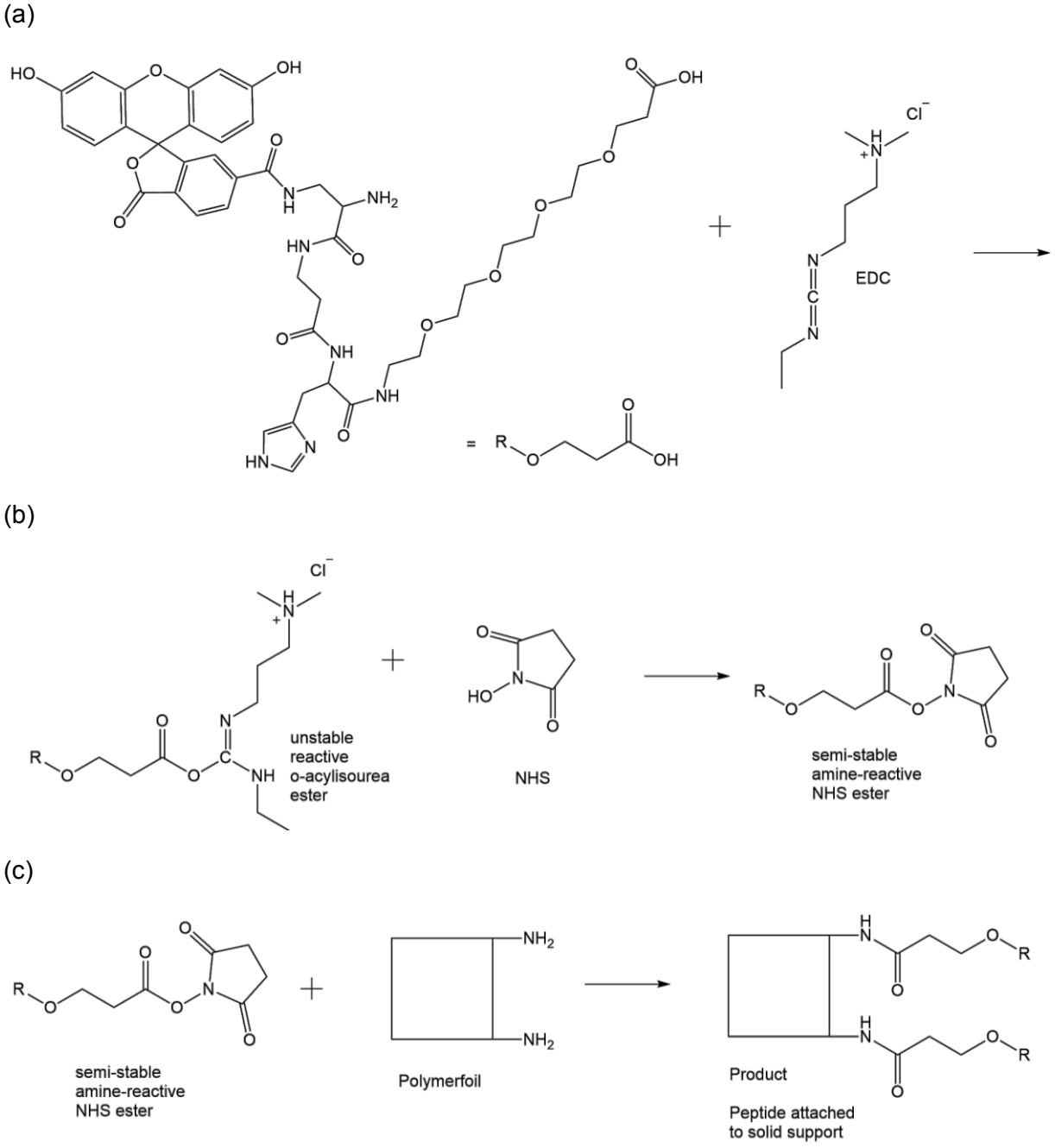

Figure 21. Coupling to solid support using EDC/NHS

Addition of EDC to peptide shown in (**a**) will result in the formation of an unstable intermediate, the O-acylisourea ester that would undergo hydrolyses rapidly. Adding sulfo-NHS to the reaction solution, a semi-stable amine reactive NHS-ester is formed (**b**) that slowly reacts with primary amines under amid bond formation (**c**).[134,135]

For immobilization following the standard Fmoc SPPS protocol, peptide 4 (4 equ., 0.5 mM) is dissolved with HATU (4 equ., 0.5 mM) and DIEA (8 equ., 1 mM) in DMF and the reaction solution filled into the chambers surrounding the PET foil. The reaction carried out overnight and after 16 h, HATU (4 equ., 0.5 mM) and DIEA (8 equ., 1 mM) added again for a reaction time of 2 h.

5.3.3. Characterization of immobilized nanopores

In order to characterize the immobilized nanopores, several methods were applied, namely *I/V* measuremtns and confocal laser scanning microscopy, CLSM.

5.3.3.1. *I/V* measurements

I/V measurements were performed using a picoammeter/voltage source (Keithley 6487, Keithley instruments) by Ivana Duznovic from the research group of Prof. Ensinger (Department of Material Science, TU Darmstadt). The foil containing a single nanopore modified with peptide 4 coupled is fixed between two compartments filled with MES buffer pH 6.5 (100 mM, with 100 mM KCl electrode solution). On the base of the conically shaped nanopores, the ground electrode is placed and on the tip side the working electrode (Ag/AgCl electrodes) (Figure 7). The recording of *I/V* curves is done using a scanning triangle voltage signal from -1 to +1 V.

5.3.3.2. Confocal laser scanning microscopy

CLMS measurements were conducted on the Leica TCS SP8 with using the red laser at 488 nm excitation and 515 – 530 nm emission with Wadim Weber from the research group of Prof. Stein (Protein engineering, TU Darmstadt). The foil is fixated on the object holder using hot agarose solution (1% in TAE buffer). For conically shaped nanopores, the tip opening faces the object holder. The following modified PET foils were used for on/off characteristics and titration experiments: 12 μm thickness, conically shaped, fluence 10^7 pores/cm^2. Foils used to visualize successful coupling using the EDC/NHS method: cylindrical nanopores with 200 nm diameter in the 12 μm thick PET foil with a fluence of 10^7 pores/cm^2.

5.3.3.3. CLSM study of turn on/off characteristics

To investigate re-usability of the hybrid system, $CuSO_4$ (100 μM, in 100 mM MES buffer pH 6.5) solution is pipetted onto the fixated foil and let to diffuse for 5 mintues. An image is taken (sum of 20 stacks travelling vertically through the foil). For reconstitution of the fluorescence, $CuSO_4$ is removed and EDTA solution (1 mM, in water) added and left to coordinate Cu(II) for 5 minutes. The foil is washed and the steps repeated.

5.3.3.4. CLSM study of ion selectivity

To evaluate the sensitivity towards the heavy metals Cu(II), Ni(II) and Zn(II) titration studies were carried out. $CuSO_4$ solution (in 100 mM MES pH 6.5) is added ranging from 10 μM - 100 μM. $NiSO_4$ solution (in 100 mM MES pH 6.5) is added in ranges 10 μM - 1000 μM. For Zn(II) investigations solutions of $ZnSO_4$ (in 100 mM MES pH 6.5) in the range of 1 - 3 mM were used.

5.4. DNA studies of ATCUN-like peptides

In order to perform DNA scission experiments with peptides 1 – 4, DNA plasmids were prepared according to the following procedure. Plasmids pUC19, pASK-IBA3 and pACYCT2 were kindly provided by Wadim Weber from the research group of Prof. Stein and transformed into DH10β competent cells and amplified. The plasmids were isolated and purified using the NucleoSpin® Plasmid DNA purification kit by Macherey-Nagel.[136] The cultivated cells are centrifuged and the cell pellet used for further cell lysis using 250 μl of buffer A1. Additionally, 250 μl of buffer A2 are added to the homogenous suspension and incubated for 5 minutes at room temperature. With the addition of 300 μl of A3 the blue sample turns colorless/white. After centrifugation (11 000 × g, 5 minutes), the supernatant is transferred to NucleoSpin® Plasmid column and centrifuged (11 000 × g, 60 s). The liquid is discarded and the column washed with 500 μl buffer AW (centrifugation at 11 000 × g, 60 s) and 600 μl buffer A4. The silica membrane of the NucleoSpin® Plasmid column is dried (11 000 × g, 2 minutes) and the DNA eluted using 50 μl AE buffer (11 000 × g, 60 s). The concentration of the DNA is determined using a nanodrop ND-1000 Spectrophotometer (pequLab).

5.5. DNA scission experiments

For general DNA scission experiments, the following concentrations are used in volumes of 75 μl total (Table 25). As the solvent, TRIS HCl is used (25 mM, autoclaved)

Solution	**Concentration (μM)**
Peptide 1 – 4	100
$CuCl_2$	90
$NiCl_2$	90
Sodium ascorbate	100
EDTA	Saturated
TRIS HCl buffer pH 7.4	25 mM

Table 25. DNA scission experiments

A solution of peptide (100 μM in 25 mM Tris pH 7.4), heavy metal (90 μM in 25 mM Tris pH 7.4), sodium ascorbate (100 μM in 25 mM Tris) is created and DNA added to yield a final concentration of 0.5 μg. The reaction is carried out for 4 h with sample drawing times of 0 h,

0.5 h, 2 h and 4 h. 25 μl sample are added to 5 μl EDTA and 5 μl purple loading dye. For further DNA extraction from Agarose gels, the reaction conditions are doubled and the DNA concentration increased to 2 μg. For concentration dependent studies (Figure 78), the concentration of peptide is increased to 125 μM or 150 μM with an increase of the concentrations of ascorbate and Cu(II) accordingly.

5.5.1. Agarose gels

After DNA scission experiments, scission activity is visualized and determiend using agarose gels. The samples are loaded to pockets of agarose gels. To cast the gels, hot agarose (1% in TAE buffer), containing 0.02% HD green or Midori green, is added to the casts and let to solidify while cooling down. Samples are loaded to the wells and the gel run at 100 V using a pequlab casting and BIO-RAD system.

To extract DNA from the agarose gel, the band of desired DNA fragment is cut out using a clean scalpel and transferred into an eppendorf tube. Purification is accomplished using the NucleoSpin® PCR clean-up, gel extraction kit from Macherey-Nagel explained in the following.[137]

To 100 mg cut-out gel, 200 μl of the NTI buffer are added and the components heated to 50 °C for 5 – 10 mintues. The clear solution is transferred to the provided clean-up columns and centrifuged (11 000 × g, 60 s). The supernatant is disposed and the column washed with NT3 buffer two times (600 μl, 11 000 × g, 60 s and 300 μl 11 000 × g, 60 s) . The column is dried (11000 × g for 2 minutes) and the DNA eluted using 25 μl of NE buffer (11 000 × g, 60 s). Concentration of the DNA is determined using the nanodrop ND-1000 Spectrophotometer (pequLab).

5.5.2. Polymerase chain reaction

	(a)	**(b)**
Component	**Volume (μl)**	**Volume (μl)**
Sample	1	1
Primer, forward	2.5	2.5
Primer, reverse	2.5	2.5
dNTPs	1	1
Buffer (Phusion® 5 x)	10	10
Water	33	33
Phusion	0.4	0.4
DMSO		1

Table 26. PCR pipetting scheme

The PCR is run using a SensoQuest Labcycler using the following time schedueles

	(a)			(b)		
Step	**Temp (°C)**	**Time**	**Cycles**	**Temp (°C)**	**Time**	**Cycles**
Initial denaturation	98	2 min	1 ×	98	2 min	1 ×
Denaturation of template	98	20 s	35 ×	98	20 s	35 ×
Annealing of primers	54	20 s	35 ×	56	20 s	35 ×
Extension	72	40 s	35 ×	72	90 s	35 ×
Final extension	72	3 min	1 ×	72	3 min	1 ×

Table 27. PCR conditions

The PCR conditions of (a) are applied to pUC19 and pASK-IBA3 primer and (b) for pACYCT2

Amplified DNA samples produced by PCR were purified using the NucleoSpin® PCR clean-up, gel extraction kit from Macherey-Nagel. 5.4 describes the protocol in detail. Instead of cutting out a band from an agarose gel, the NTI buffer is pipetted directly into the PCR solution. To 50 μl of PCR components, 100 μl NTI are intended. From this step on the protocol is analogous to the gel extraction.

6. Results and Discussion: Synthesis and characterization of Kcv_{NTS}

6.1. Kcv_{NTS} Synthesis strategy

As mentioned in the aims, one of the goals is to pave the way for the development of bioinspired nanopores based on biological ion channels. The most intensively studied and best known example in literature is the α-hemolysine (α-HL) pore, a toxin from *Staphylococcus aureus*. It is a mushroom-shaped homo-oligomeric heptamer (of 33.2 kD monomers) with a β-barrel structure transversing the membrane.[116] It is widely used for translocation of various analytes, like metal ions[138] and small organic molecules,[139] through the 1.4 nm pore.[140] Using click chemistry, namely Cu(I)-catalyzed azide-alkyne [3 + 2] cycloadditions (CuAAC) diversification of the pore-structure is shown to be possible.[141] Furthermore, NCL strategies gained attention in semisynthetic modification of α-HL to create so-called nanoreactors.[142] These methods often target orthogonal modifications or modifications at the termini, while the protein's core sequence remains untouched. To fill this gap, we went the first steps towards using membrane proteins as scaffolds for bioinspired nanopores. Our approach focuses on the chemical synthesis of ion channels exploiting the benefit of being able to easily modify the sequence, especially the core sequence. The incorporation of novel functionalities, the possibility to tune selectivity towards ions and the integration of isotopically labeled amino acids for NMR measurements, are some of the advantages of our approach.

For our aim we selected the minimal viral voltage-gated potassium channel Kcv_{NTS} because of its small size (82 amino acids) but full functionality (for detail see 3.3).[51] The first step towards our goal, a successful and robust synthesis strategy has to be developed. As a transmembrane protein that incorporates itself autonomously into the lipid bilayer, Kcv_{NTS} exhibits an extreme hydrophobicity especially within the sequence for the two transmembrane helices. To overcome problems in chemical synthesis, the sequence has to be divided into two or more fragments and fused together to result in the final sequence. Recently, our lab developed a strategy for the synthesis of hydrophobic proteins which uses an oxo-ester, namely the thioester-forming Hmp-group, in combination with a solubilizing tags, aiding NCL reactions.[143] Solubilizing tags are favorable additions of hydrophilic amino acids integrated to hydrophobic sequences. They facilitating SPPS, purification and NCL with especially arginine-based solubilizing units widely used in present and past.[144-147] The following scheme illustrates the NCL reaction using the oxo-ester unit an a solubilizing tag.

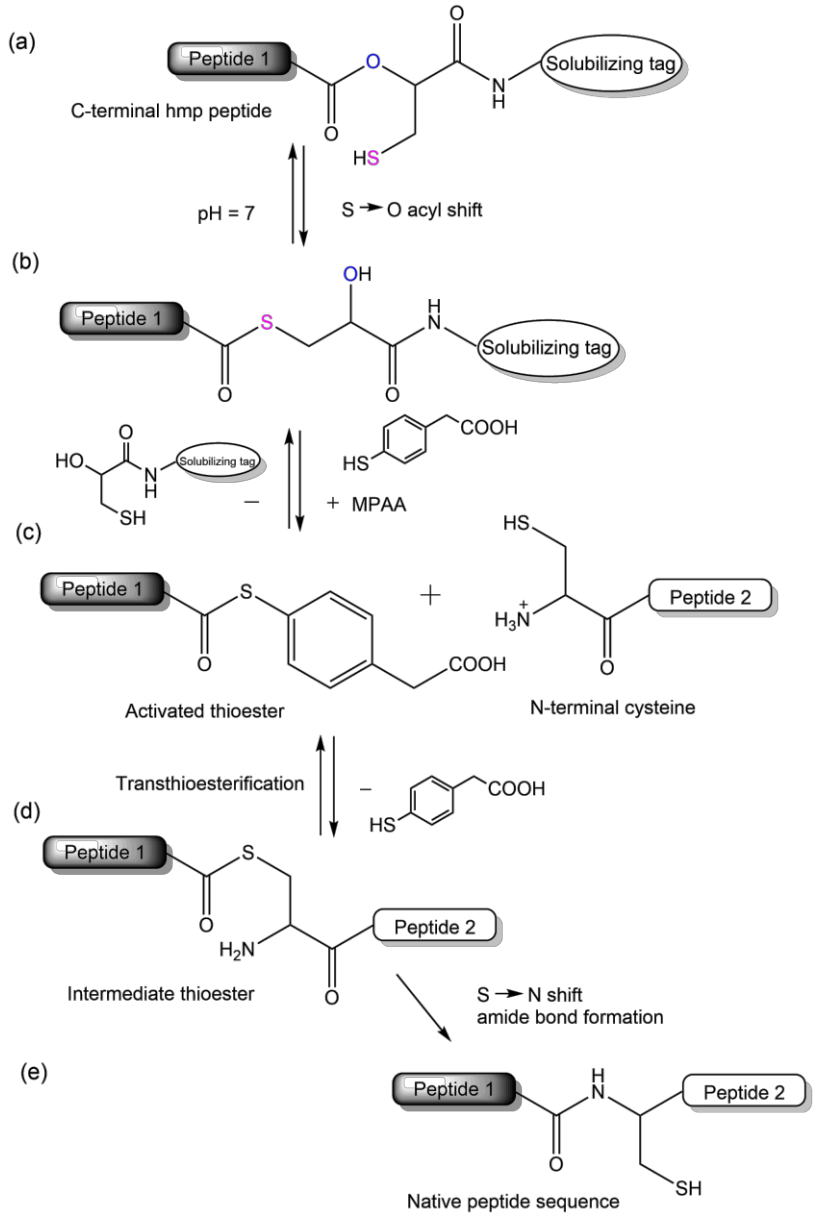

The reaction scheme of the oxo ester based NCL is shown in Figure 22, for which the C-terminal oxo-ester is required at one fragment, while the other fragment exhibits a N-terminal cysteine moiety.

Within the amino acid sequence of Kcv_{NTS}, there is a naturally occurring Cys36 being the perfect starting point for the hmp-based ligation strategy. The first attempt was to synthesize Kcv_{NTS} applying a two-fragment strategy. The following scheme shows the amino acid sequence and segmentation used for the two-fragment approach. Figure 23 also shows structural components (green – selectivity filter region, yellow – pore region, violet – transmembrane helices) and highlights the ligation site at Cys36 in red.

Figure 22. NCL scheme using Hmp

At a pH of > 7 the C-terminal oxo-ester undergoes a S→O acyl shift to generate the thioester from (a) to (b). The generation of the activated thioester from reaction of the MPAA with the N-terminal hmp moiety of the peptide fragment is seen in (c) with the detaching of the solubilizing tag. The thiol-group of the peptide fragment exhibiting the N-terminal cysteine moiety attacks the activated C-terminal thioester (c). An intermediate thioester is formed (d) which readily rearranges through a S → N-acyl shift which leads to an amide bond formation resulting in the native peptide/protein sequence shown in (e).

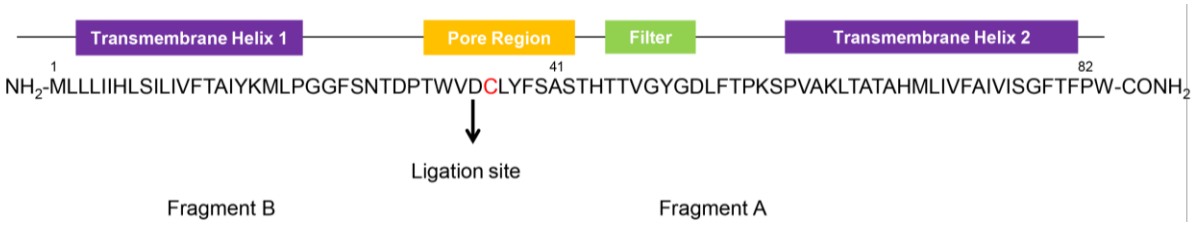

Figure 23. Synthesis strategy using two fragments

Upon the first reaction attempt, pseudoprolines were incorporated into the sequence, for backbone stabilization at positions F39S40 (Fmoc-L-Phe-L-Ser[PSI(Me,Me)Pro]-OH) and at F14T15 (Fmoc-L-Phe-L-Thr[PSI(Me,Me)Pro]-OH). General procedure for the incorporation of psedoprolines into a peptide sequence was first introduced by Mutter's lab and is nowadays one of the most effective methods to increase yields during chemical synthesis of "difficult sequences".[148-150]

Proline-like structures are able to disrupt conformations that leads to aggregation through a so-called "kink" within the backbone of the sequence.[150] Ser, Thr and Cys can be used as scaffolds for mimicking the Pro structure (through oxazolidine for Thr and Ser and thiazolidine for Cys). Cleavage under normal Fmoc-conditions will result in the native peptide sequence (Figure 24).[151]

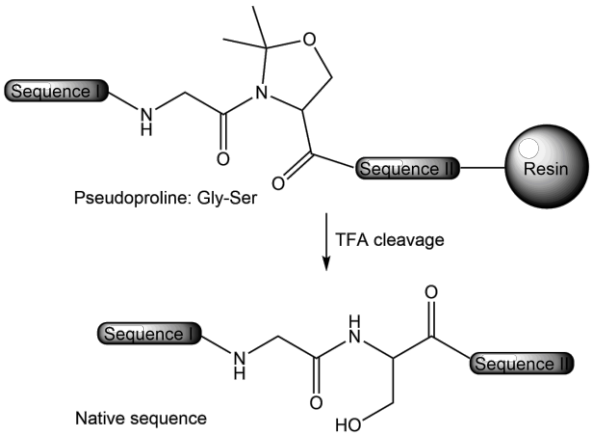

Figure 24. Pseudoprolines

Both fragments, fragment A and B were synthesized according to protocols described in 5.1 with synthesis conditions summarized for fragment A in Table 4 and fragment B in Table 5. A RP-HPLC of the fragment A is represented in Figure 25a. Inspite of usage of pseudoprolines outcome of the synthesis is obviously not as desired. Multiple peaks at the retention time (R_f) range from 3 – 9 minutes indicate terminated shorter sequences of the peptide. However, LC-MS analysis of the peak at R_f 16.2 minutes indicates the right molecular mass of the peptide $[M+4H^+]^{4+}$ with calculated 1274.6611 m/z and found 1274.6623 m/z with a corresponding isotopic pattern (Figure 25b).

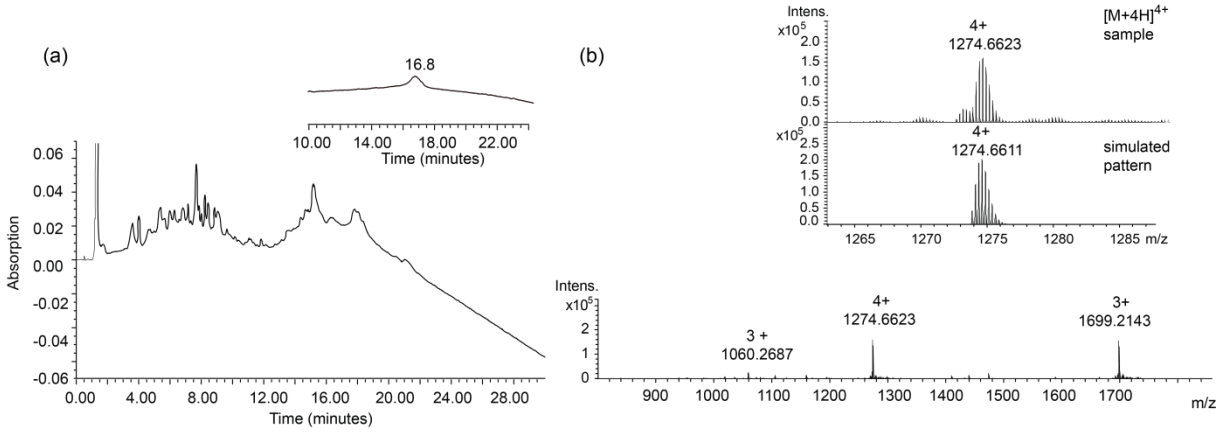

Figure 25. Synthesis out of two fragments. Fragment A

RP-HPLC of the crude product in (a) and insert showing purified fragment, gradient of 25% - 95% eluent B over 30 minutes with a flow of 1 ml/min, column temp 30 °C using the MultoHigh BIO 300 column and (b) ESI-MS chromatogram of the purified fragment A with R_f 16.8 minutes with insert showing $[M+4H^+]^{4+}$ simulation and sample

Several attemps were undertaken to synthesize fragment B successfully indicated in Table 5. According to literature data, the effect of the neighbouring amino acid to Hmp displays a great effect on coupling efficiency. When this amino acid was aspartic acid, researchers obtained a yield < 5% yield compared to e.g. a 69% yield when using valine.[152] That might be the reason, the first attempt to synthesize fragment B was not successful.

As the next step, a mutation was introduced into the sequence. We expected an increased yield with synthesis of Kcv_{NTS} D35E. This mutation does not have an effect on the function of the ion channel (from unpublished results). The synthesis was performed without usage of pseudoprolines. In the final crude product, the desired product could not be found using RP-HPLC and LC-MS analysis.

As the next step, pseudoprolines were incorporated at F14T15 and the mutation D35E was introduced. The RP-HPLC of the crude peptide (Figure 26a) does not show any significant peak. Moreover, LC-MS analysis did not indicate the right molecular mass of the desired product. However, the MS spectra of the desired fragment in the crude product was found within the washing step of the column with $[M+2H^+]^{2+}$ calculated 2034.5727 m/z and measured 2034.5765 m/z (Figure 26b) at 35.9 – 40.0 minutes. It is possible that due to the highly hydrophobic character of fragment B, which is indicated by the Leu, Ile and Val rich sequence at the region 1-12 of the peptide, the product is precipitated during the elution gradient on the RP-HPLC column. For an overview of MS-Spectra at different time points during the run, see SI Figure 1.

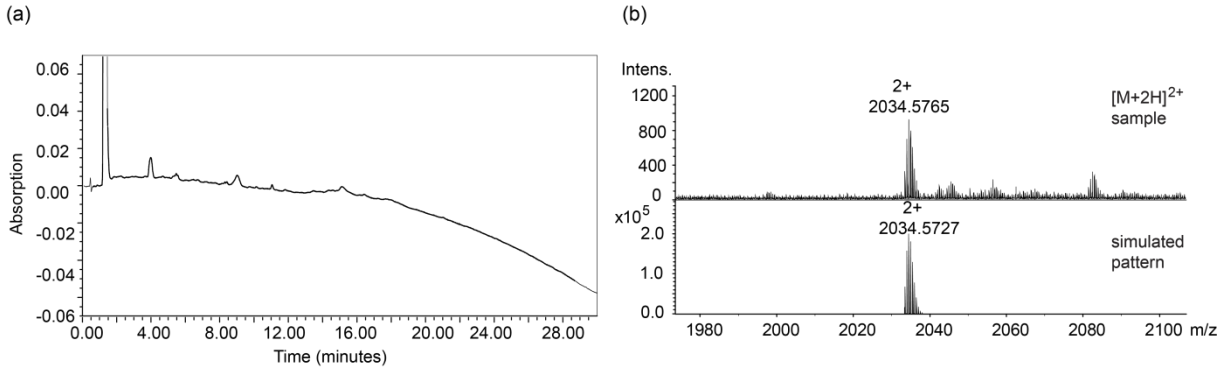

Figure 26. Synthesis out of two fragments. Fragment B

(a) RP-HPLC of the crude product measured with a linear gradient of 25% - 95% eluent B over 30 minutes, at a flow of 1 ml/min, column temp 30 °C using the MultoHigh BIO 300 column (b) ESI-MS of the crude fragment B showing the 3 times charged $[M+3H^+]^{3+}$ simulation and sample measurement 35.9 – 40.0 minutes

Facing the difficulties during the synthesis of the Hmp-peptides, we decided to alter the two-fragment synthesis strategy. The idea was to synthesize shorter fragments and introduce alternative ligation sites since cysteine is not an abundant amino acid with quantities of only 2.25% in protein sequences of mammals.[153] We incorporated the following mutations: A16C and A41C. The newly generated cysteine residues can be readily converted to alanine through the desulfurization process.[154,155]

The following scheme shows the amino acid sequence and segmentation used for this the three-fragment approach. Figure 23 also shows structural components introduced in Figure 3 (green – filter region, yellow – pore region, violet – transmembrane helices) and highlights the ligation site at A16C and A41C in red.

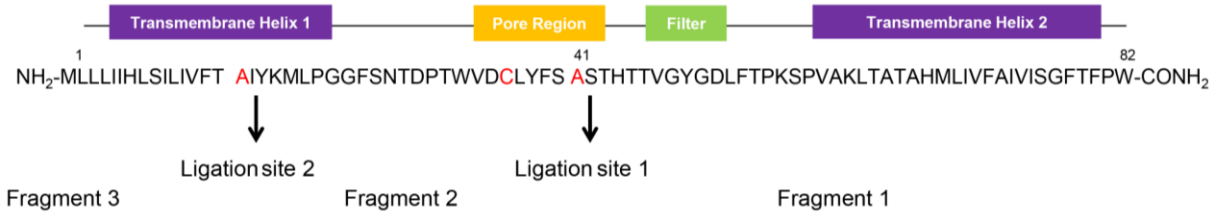

Figure 27. Synthesis strategy using three fragments

Besides the mutations from Ala → Cys, Cys16 hat to be masked in order to selectively connect fragment 1 with fragment 2 and in the next step connect ligation product 1 with fragment 3. One promising residue to mask Cys is the 1,3-thiazolidine-4-carboxo-group, Thz, thioproline group which is commercially avalabile and regularly used for multiple-step and one-pot ligation strategies.[156-158]

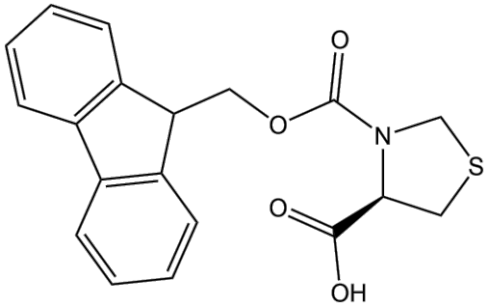

Figure 28. Thioproline moiety

This Thz group is stable throughout the first ligation and can be converted to a cysteine moiety in a simple step which can be performed in the ligation buffer.[159] Moreover, the naturally occuring Cysteine moiety, C36, needs to be protected throughout the synthesis and desulfurizations conditions in order to avoid intermolecular side-reactions and to guarantee for the native sequence.

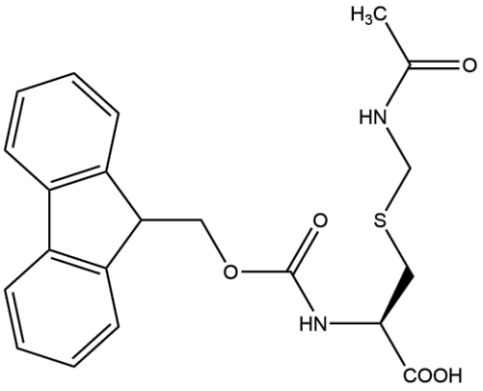

For that, an orthogonally protection via the acetamidomethyl group (Acm) is the method of choice.[160,161] The originally proposed method for Acm removal involved usage of mercury(II)acetate[161], whereas a few years later the practice of using silver salts became more popular.[162] A recent approach focuses on the application of the well-established scavenger, TIPS for both, cleavage to obtain the free thiol as well as the generation of disulfide bridges.[163]

Figure 29. Acm protection group

Both, synthesis and NCL of fragment 1 and fragment 2 were possible with efficient thioproline conversion while fragment 3 could not be purified using the implemented RP-HPLC techniques. From the experience on our lab for the incorporationof solubilzing tags to oxo-ester fragments,[143] we decided to incorporate a spacer containing polyglycine residues due to presumed problems in NCL with the sterical hindrance of the rather big Lys units. Figure 30 shows the third synthesis scheme with the self-removable solubilizing tag in blue.

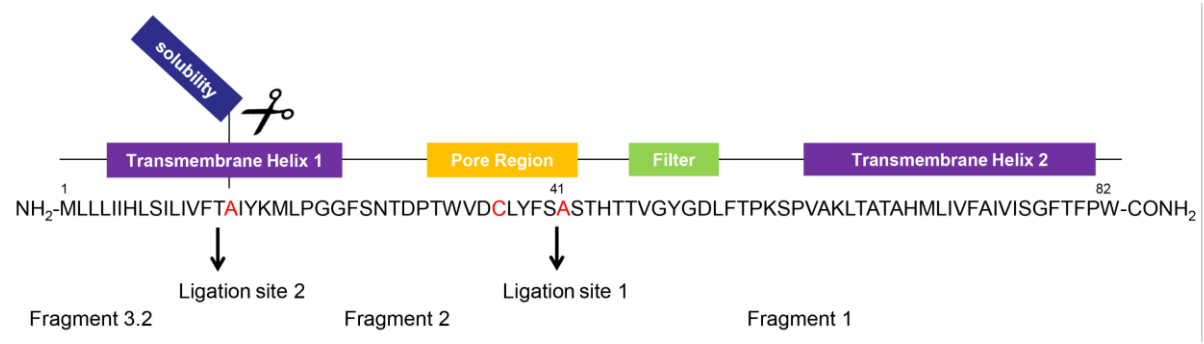

Figure 30. Three fragment synthesis strategy with solubility tag

The pursued synthesis strategy is visualized in Figure 31.

(a)

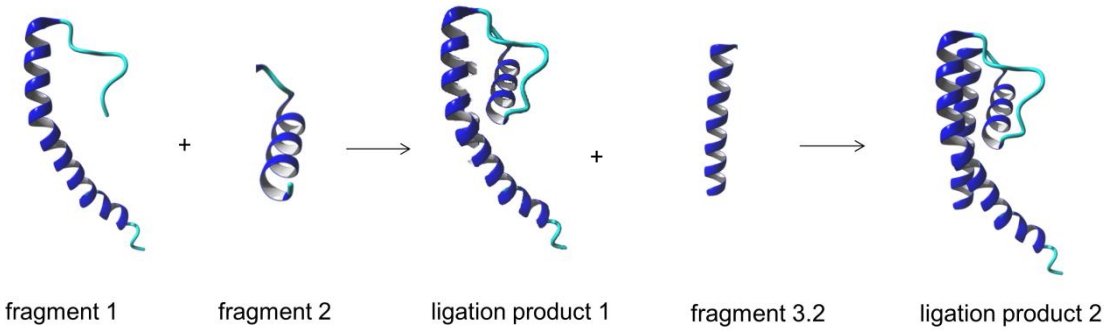

(b)

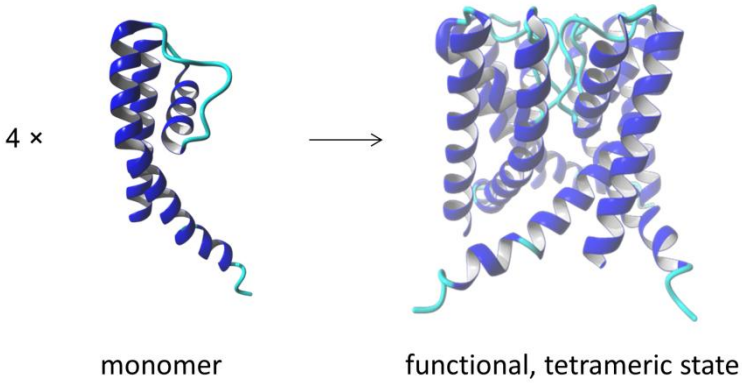

Figure 31. Synthesis strategy for Kcv_{NTS}

During NCL 1, fragment 1 and 2 are ligated to yield ligation product 1 which further reacts, after unmasking of the N-terminal cysteine, with fragment 3.2 to ligation product 2 (a). Four monomers assemble to the functional, tetrameric state of Kcv_{NTS}

6.2. Chemical synthesis of Kcv_{NTS}(1-82)

Synthesis and analytics of fragment 1

Following the standard Fmoc SPPS procedure introduced in 5.1 with synthesis conditions seen in Table 6, fragment 1 is synthesized. The impurities within the crude product, seen in Figure 32a, indicate challenges in purification of the 41 amino acid long sequence. LC-MS analysis of the peak at R_f 17 minutes (Figure 32d) indicate the right expected molecular mass of the fragment at $[M+3H^+]^{3+}$ with calculated 1493.79 m/z and found 1493.80 m/z (Figure 32b,e) and $[M+4H^+]^{4+}$ with calculated 1120.59 m/z and found 1120.60 m/z (Figure 32c,f) and corresponding isotopic patterns. All measured and calculated masses are summarized in Table 7 in the "methods" section. The peak displaying the expected molecular mass, is insignificant in the RP-HPLC chromatogram of the crude product indicating the high amount of impurities. Difficulties in purification are demonstrated by the yield of purified product: from 53.02 mg crude product, only 3.0 mg purified product are obtained (5.7%). Furthermore, dissolution of the sample was only obtained with the addition of neat TFA to the freeze-dried product (Table 14).

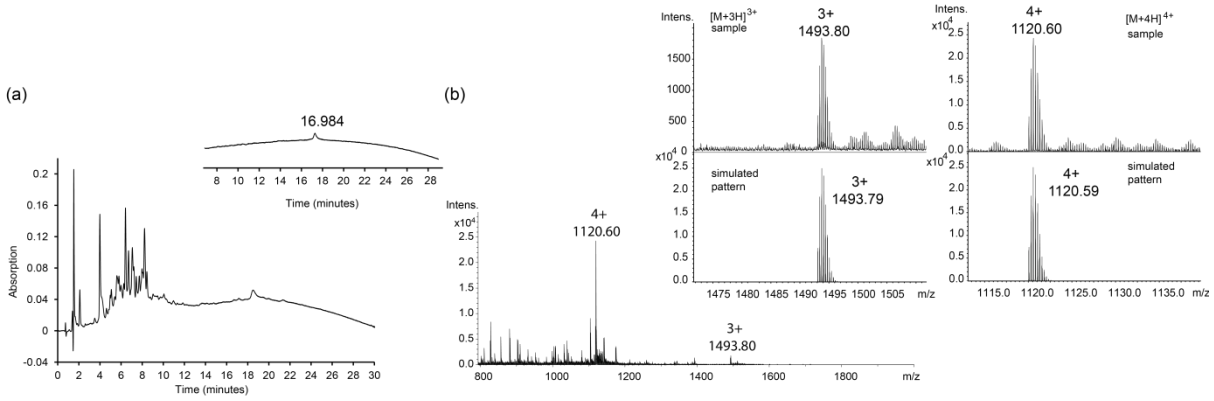

Figure 32. RP-HPLC chromatogram and MS spectra of fragment 1

RP-HPLC chromatogram of the crude product (a) with insert showing purified fragment, gradient: 20% - 95% over 30 minutes eluent B with a flow of 1 ml/min measured on the MultoHigh BIO 300 column at 30 °C. LC-MS showing spectra of the purified product in (b) with the insert showing sample and simulated pattern with $[M+3H^+]^{3+}$ and $[M+4H^+]^{4+}$ from LC-MS with a retention time of LC-MS between 23.1 - 26.5 minutes.

Synthesis and analytics of the fragment 2

Synthesis of the fragment 2 is pursued using manual and automated peptide synthesis according to the fmoc SPPS method introduced in 5.1. with synthesis conditions summarized in Table 8. No decrease in the original loading from 0.18 mmol/g after the Mitsunobu reaction using Phe as the subsequent amino acid was evaluated, illustrating sufficient coupling. The crude product (Figure 33a) indicates a successful synthesis with a low rate of impurities that is confirmed by LC-MS and the expected molecular mass in the peak at R_f 10.6 minutes (Figure 33b). Molecular masses of $[M+2H^+]^{2+}$ with calculated 1529.65 m/z and found 1529.660 m/z were determined within the significant peak (Figure 33c). Table 9 summarizes measured and calculated masses for LC-MS spectra. Purification of 71.26 mg crude product resulted in 17.05 mg pure product, representing an oval yield of 24%. Comparing both fragments 1 and 2, this outcome is expected. Fragment 1 displays the transmembrane helix region and thus is the more challenging fragment for SPPS.

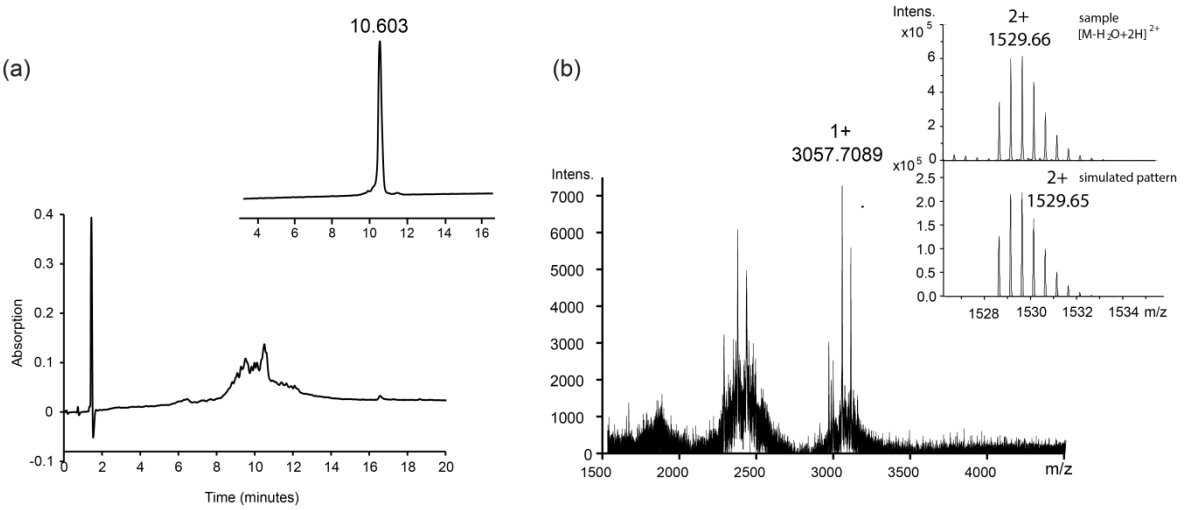

Figure 33. RP-HPLC chromatogram and MS spectra of fragment 2

RP-HPLC of (a) crude product with the insert showin the purified product, gradient: 20 - 65% eluent B over 20 minutes, flow: 1 ml/min on the MultoHigh BIO 300 column at 30 °C. Illustration (b) shows MALDI-TOF MS (HCCA matrix) of the purified fragment with R_f – 10.6 minutes and the LC-MS sample measurement with simulated patterns of $[M+2H^+]^{2+}$ with a retention time of LC-MS between 16.5 – 18.7 minutes.

Synthesis and analytics of the fragment 3

This section highlights synthesis and analytics of fragment 3 that is further modified to exhibit a solubilizing tag (fragment 3.2). Fmoc-SPPS is performed similar to fragment 2 using manual and automated synthesis (5.1). The RP-HPLC chromatogram seen in Figure 34a illustrates elution of this fragment, prior dissolved in a mixture of 0.3 mM N-dodecyl-beta-maltoside, DDM, in ACN (0.1% TFA), water (0.1% TFA) (17:3 v/v) as a solvent due to being insoluble in 100% ACN (0.1% TFA). Non-ionic detergents, such as OG and DDM, can be used to aid solubilization of membrane proteins because they are considered to be non-denaturing.[164]. Above their critical micelle concentration, CMC, they self-assemble to micelles which embed the ion channel. The literature value for the CMC of OG is 20 – 25 mM[165] and for DDM 0.17 mM.[166] Another RP-HPLC chromatogram, with addition of 30 mM octylglucoside, OG can be seen in SI Figure 2. However, even optimization of dissolution led to a chromatogram not displaying any significant peaks. The molecular mass of the peptide was found within the purging step of the LC-MS method and cannot be appointed to any peak within the gradient. That means that even here, as already described for fragment B, the stationary phase of the MultoHigh BIO 300 C4 column, strongly interacts with the peptide which does not elute sufficiently. Molecular masses of $[M+H^+]^+$ with calculated 1843.1025 m/z and found 1843.1012 m/z and $[M+2H^+]^{2+}$ with calculated 922.0549 m/z and found 922.0530 m/z were detectable within the purging step (Figure 34b,c). Purification using RP-HPLC was not possible and thus, does not seems to be an appropriate method.

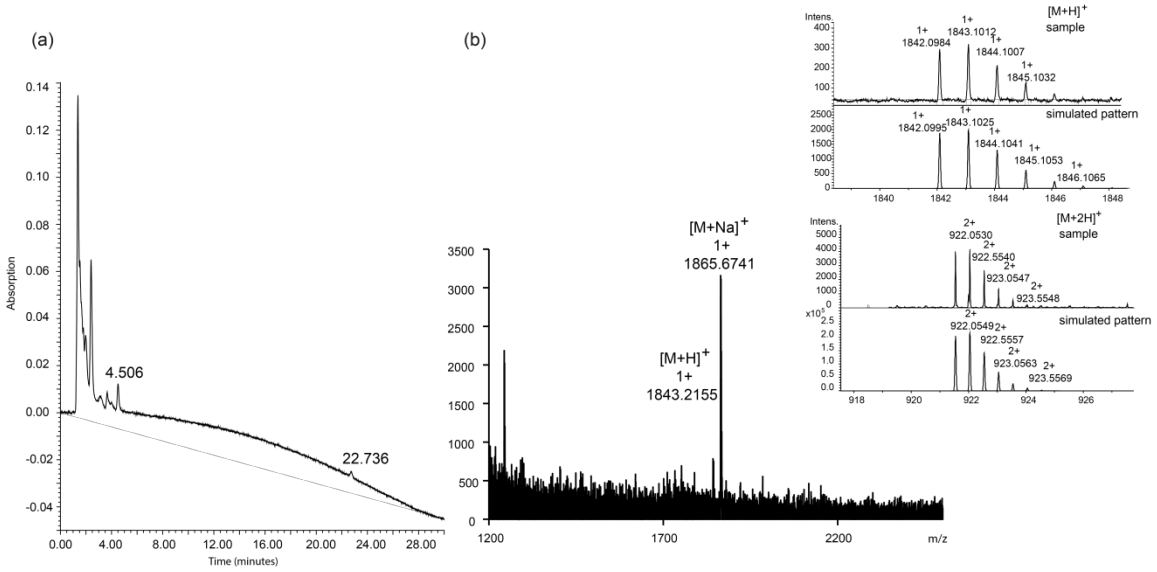

Figure 34. RP-HPLC and ESI MS of fragment 3

RP-HPLC of (a) crude product gradient: 60% - 99% eluent B over 30 minutes with a flow of 1 ml/min on the MultoHigh BIO 300 column at 30 °C. Illustration of (b) shows the MALDI-TOF MS (HCCA matrix) of the crude product with the insert showing LC-MS sample measurement of sample and simulated pattern of the fragment as $[M+H^+]^+$ and $[M+2H^+]^{2+}$ form a retention time of LC-MS between 26.5 – 28.8 minutes

Synthesis and analytics of fragment 3.2

Following a three-step synthesis protocol, the solubilizing tag is synthesized automatically, followed by manual coupling of the oxo-ester unit and finished with automated peptide synthesis introduced in 5.1 Due to failed attempts, usage of TentaGel® resin was re-evaluated and compared to AmphiSpheres RAM. Table 28 summarizes outcomes of trial synthesis protocols (0.1 mmol scale) with AmphiSpheres being superior to TentaGel.

Resin	**AmphiSpheres RAM**	**TentaGel**
Initial loading	0.380 mmol/g	0.18 mmol/g
Loading after solubilizing tag	0.095 mmol/g*	0.095 mmol/g
Loading after Mitsunobu	0.075 mmol/g	0.021 mmol/g
Loading at end	0.031 mmol/g	Aborted after Mitsunobu due to low loading

Table 28. Comparison of two resin types for synthesis of fragment 3.2

*loading after the solubility tag corresponds to TentaGel loading. This led to the conclusion that the loading on the label of the AmphiSpheres RAM® does not correspond to the true loading.

Synthesis conditions are summarized in Table 11 and illustrate a decrease in loading of 0.38 mmol/g to only 0.04 mmol/g (89.5% initial loading) while using AmphiSpheres RAM resin. This emphesizes the challenges still connected to the synthesis of the last fragment albeit optimization of resin choice and the integration of a solubilizing tag took place. Many impurities emboss the appearance of the chromatogram of the crude product, again

illustrating the great challenge the synthesis exhibits (Figure 35a). The corresponding mass of the product was found within the peak at 5.9 minutes of the LC-MS method (5.1.5) with $[M+2H^+]^{2+}$, calculated 1271.76 m/z and found 1271.75 m/z and $[M+3H^+]^{3+}$, calculated 847.17 m/z and found 848.16 m/ (Figure 35b-f). The product peak in the corresponding RP-HPLC chromatogram at 16 minutes cannot be assigned to an explicit peak in the chromatogram of the crude product. Table 12 summarizes measured and calculated masses for LC-MS measurements.

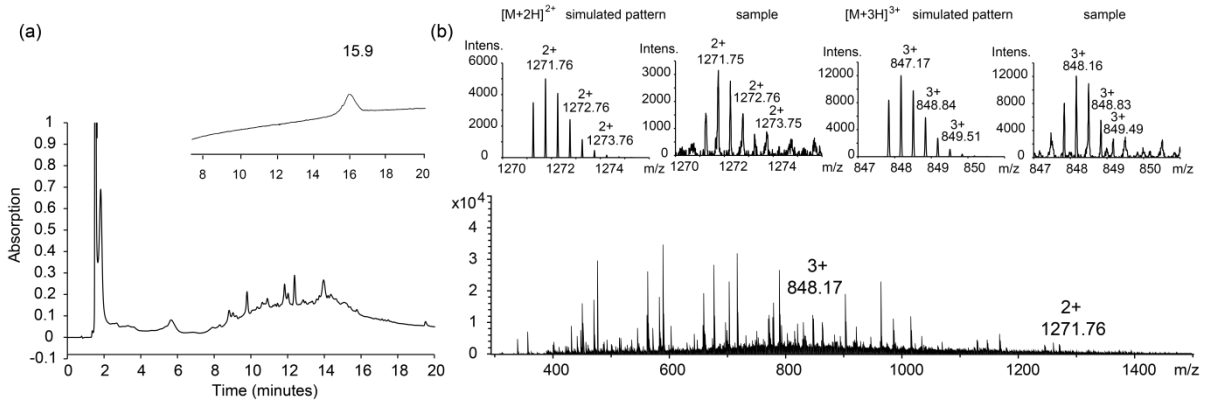

Figure 35. RP-HPLC and MS spectra of fragment 3.2

RP-HPLC chromatograms of the crude product (a) and the purified fragment (d), gradient: 5% eluent B for 5 minutes followed by a linear gradient 5% - 70% eluent B over 20 minutes with a flow of 1 ml/min on the MultoHigh BIO 300 column at 30 °C. LC-MS of peak at R_f 15.9 minutes with insert showing $[M+2H^2]^{2+}$ and $[M+3H^2]^{3+}$ sample and the corresponding simulated patterns with a retention time during LC-MS of 17.2 minutes

6.3. Native chemical ligation 1

The solution, in which the ligation is carried out, is an aqueous buffer solution containing either guanidinium hydrochloride, Gdn·HCl or urea and Na_2HPO_4. Albeit solubility tags are used for better solubilization, it is rather uncommon that the fragments will dissolve totally. To enhance solubility, the addition of organic solvents is crucial. In literature the partial adding of TFE,[143,167] HFIP[143] and DMF[168,169] is described. Urea or Gdn·HCl are added for denaturation, meaning the unfolding of the amino acid sequence to bypass non-wanted aggregation.[170] Other detergents, such as sodium dodecyl sulfate, SDS were also investigated to enhance solubility in the ligation solution.[171] When looking at the natural environment of membrane proteins, it makes sense to investigate the addition of lipids to the solution. Hunter *et al.* investigated a lipid bilayer system, a cubic lipidic phase matrix, to perform NCL of a hydrophobic polypeptide[172] whereas Clayton *et al.* utilized dodecylphosphocholine (DPC) as well as TFE.[173]

To optimize ligation conditions, HFIP (ligation buffer A, 5.1.3.1) and TFE (ligation buffer B, 5.1.3.2) are investigated as organic solvents for ligation using organic solvent/water 1:3 v/v. Ligation conditions are according to 5.1.3.1 for HFIP and 5.1.3.2 for TFE. During both conditions, a sediment is formed after 4 h of reaction time. Figure 36b shows sediment formation after 24 h of ligation 1 using ligation buffer A with (Figure 36a) showing clear solution at the starting point. Evaluation of the results form ligation experiments is done applying MALDI-TOF MS measurements according to 5.1.5.

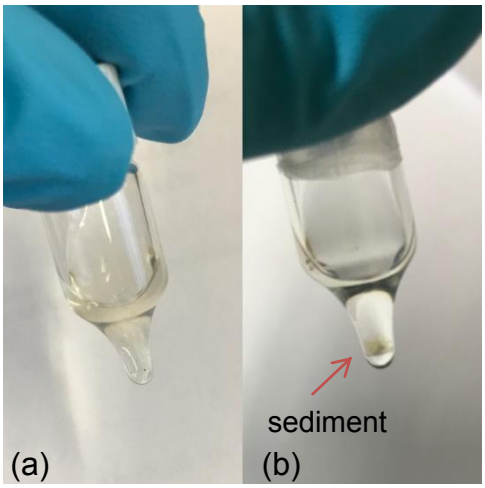

Figure 36. Sediment formation during HFIP ligation

For evaluation of the ligation outcome, crucial masses of educts and the product are summarized in Table 16. Using MALDI-TOF MS, the sediment as well as ligation solutions of both NCL preparations (ligation 1 using buffer A or buffer B) are investigated in regard to product formation. Figure 37a shows MALDI-TOF MS spectra from the solution using buffer B, (b) sediment from buffer B and (c) sediment from buffer A.

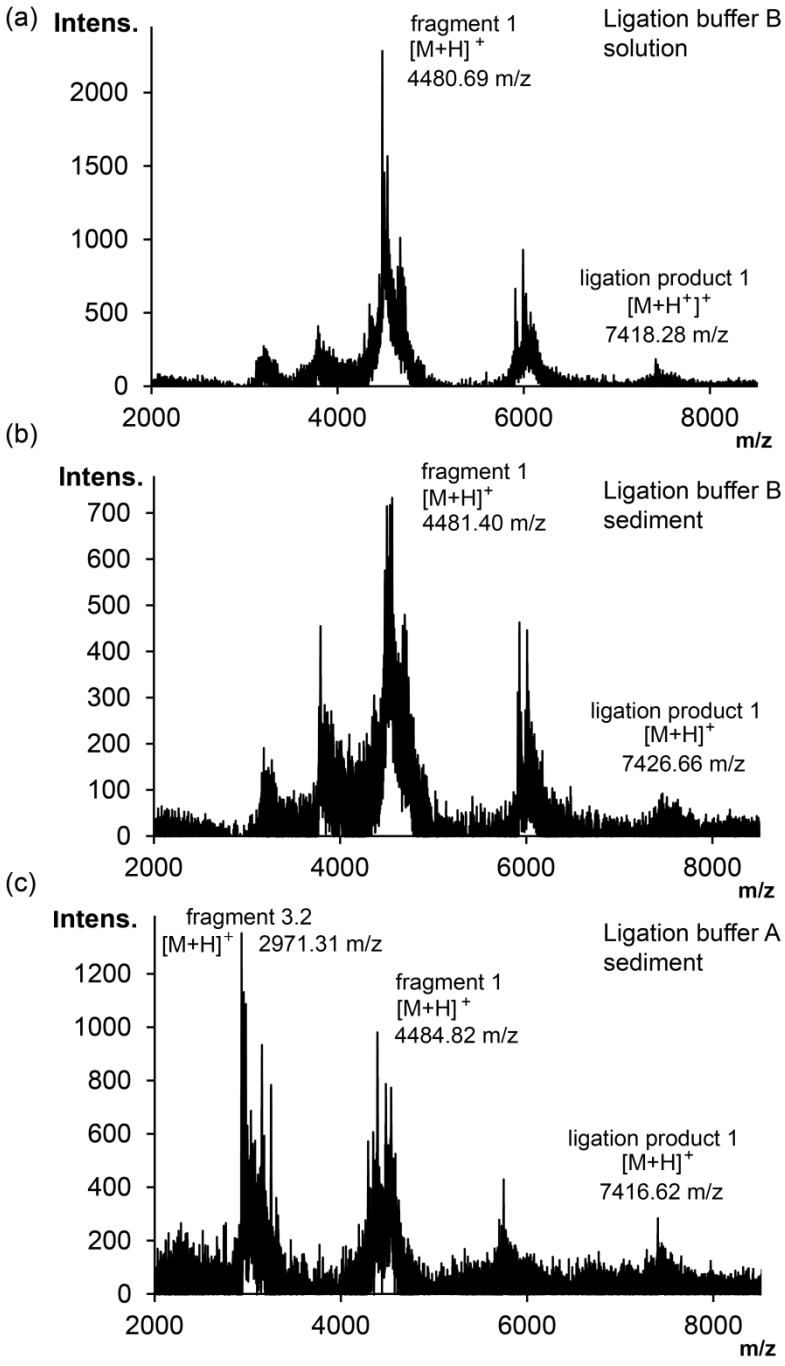

Figure 37. Comparison of ligation using buffer A and buffer B

All MALDI-TOF MS spectra are recorded using the LP mode and DHAP as the matrix system. Samples from sediment are dissolved in TFE/water (0.1% TFA) 1:3 v/v

Both NCL methods using ligation buffer A with HFIP and ligation buffer B with TFE are applicable due to product formation using both. However, using the strategy with buffer B, the product can be found in both, the solution and the sediment making this method inferior to usage of buffer A. This is because a further needed step in merging both product fractions for unmasking of the thioproline group would be needed. The sediment from the ligation in buffer A can easily be separated from the remaining solution by centrifugation and used for further thioproline conversion in buffer C.

Additionally, we can extract further information from this experiment. HFIP will not be a suitable solvent for further experiments due to precipitation of the product while TFE seems to be employable. Using 1:2 v/v of TFE leads to partial precipitation but is also able to dissolve the product. We hypothesized that increasing the portion of TFE could lead to complete dissolving of the product and prosperous thioproline conversion.

6.4. Unmasking of the N-terminal thioproline group

The product within the sediment of the HFIP ligation in buffer A is re-dissolved in the ligation buffer C (Table 45) yielding a clear solution. Addition of methoxyamine·HCl and a lowering of the pH to 4 results in the ring-opening of the Thz moiety and conversion to the cysteine fragment indicated by a loss of 12 Da (see Figure 38).

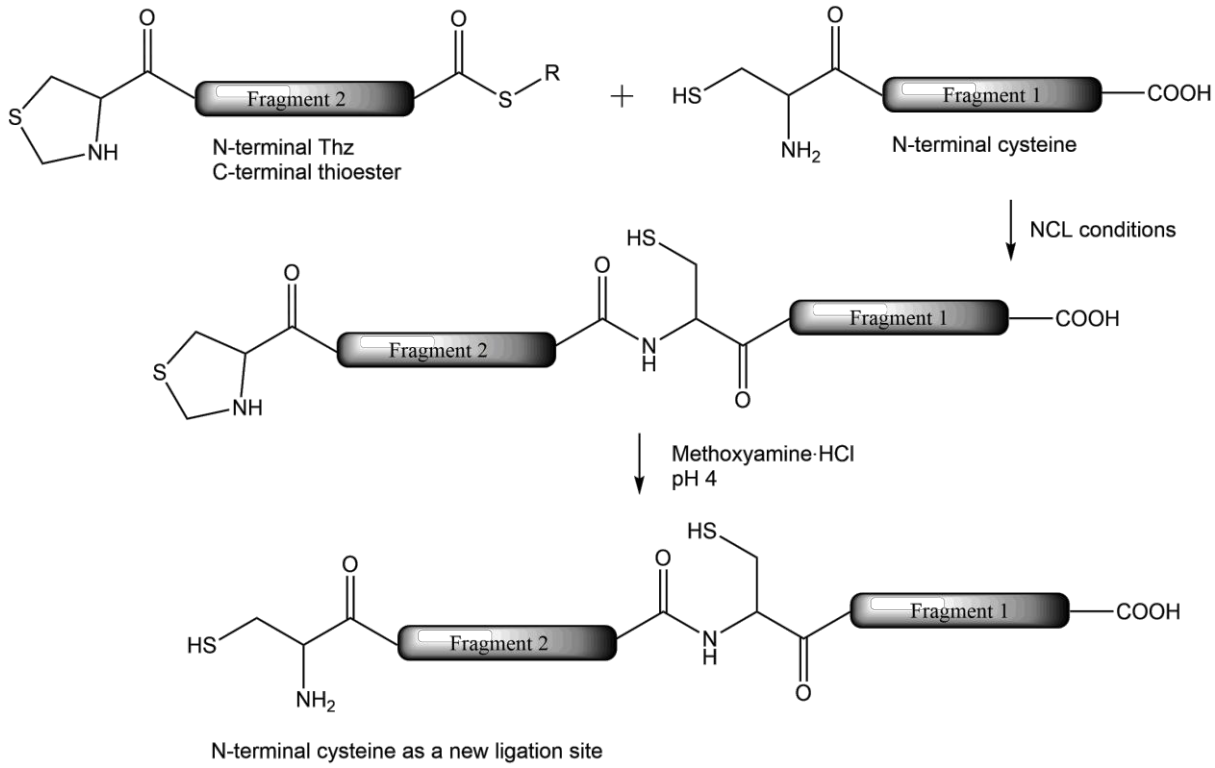

Figure 38. Conversion of the N-terminal thioproline moiety from ligation 1 to N-terminal cysteine

The first step shows the NCL using a thioester and a cysteine (**a**). A amide bond is generated between both fragments, the sequence now exhibits the N-terminal thioproline moiety (**b**). Using methoxyamine·HCl and lowering the pH to 4 the thioproline is unmasked and converted to a N-terminal cysteine (**c**).

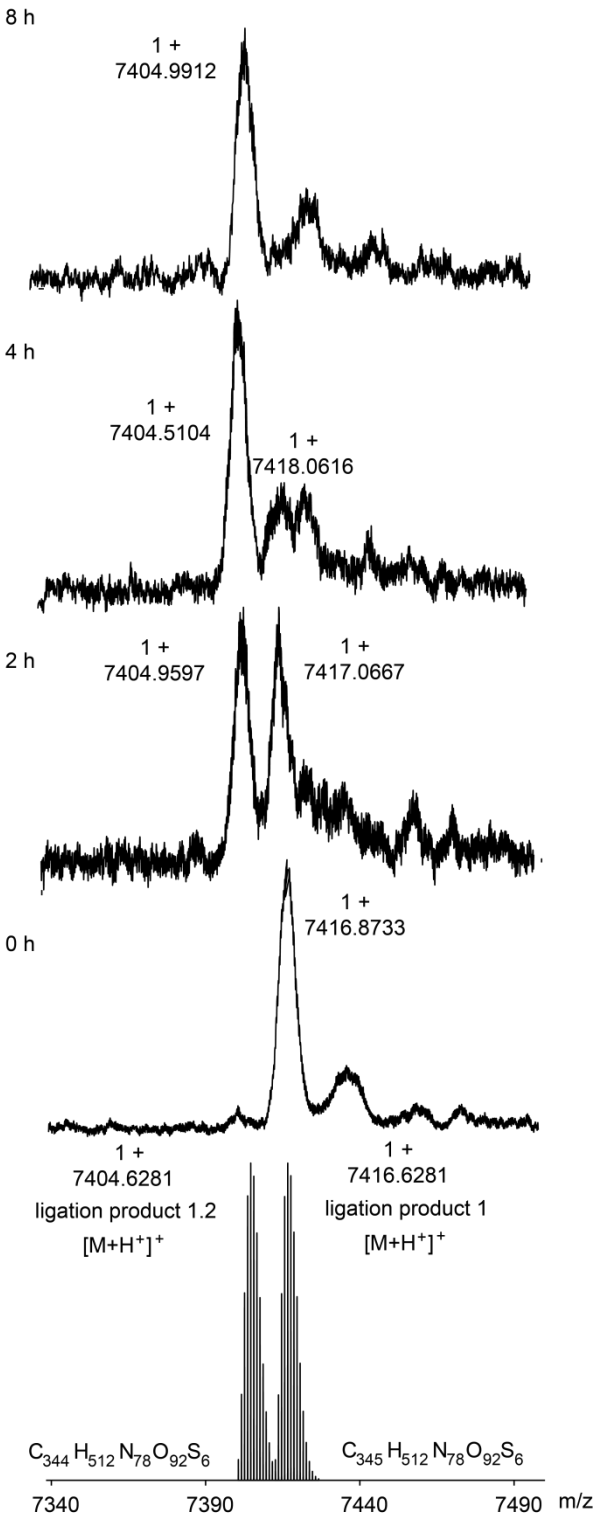

Figure 39. Unmasking of the thioproline unit after ligation 1

MALDI-TOF MS showing the simulated pattern of the educt, ligation product 1 and product, ligation product 1.2 indicated by a loss of 12 Da over the time course of 8 h. All spectra are recorded in an linear positive (LP) mode with DHAP as the matrix

To monitor the loss of 12 Da, MALDI-TOF MS is performed (for the used DHAP protocol see 5.1.5.). The drawn samples are directly put on dry-ice to stop further conversion and further measured. Figure 39 shows the conversion of the thioproline moiety over the time course of 8 hours. The simulated patterns of the ligation product 1 $[M+H^+]^+$ as well as the ligation product 1.2 are shown with a loss of a C atom (-12 Da) in the molecular formula from $C_{345}H_{512}N_{78}O_{92}S_6$ to $C_{344}H_{512}N_{78}O_{92}S_6$.

At the time point 0 h, only presence of ligation product 1 (Figure 39) can be evaluated whereas over 2 h two peaks are visible which can be appointed to ligation prouct 1 and ligation product 1.2.

After a time course of 2 – 4 h, and increase in the peak intensity of ligation product 1 can be investigated with increasing intensities of the peak representing ligation product 1.2. At 2 h conversion time, around half of the educt (ligation product 1) is converted to the N-terminal cysteine fragment (ligation fragment 1.2) while after 4 h this proportion of ligation product 1.2 : ligation product 1 is 3:1 respectively. The full conversion of the thiopoline moiety to the N-terminal cysteine can be observed after 8 h.

6.5. Vivaspin® purification

For purification of the hydrophobic ligation product 1.2 from fragment 1 and fragment 2, Vivaspin® concentrators (polysulfone, PES membrane, cut-off 5 kDa) were used as a mass-filtration unit. The cut-off of 5 kDa may not be enough to separate the ligation product 1.2 (9.1 kDa) from fragment 1 (4.5 kDa) but should be sufficient to separate the hydrolyzed fragment 2 (3.0 kDa). The protocol used is described in 5.1.4. The success of the filtration is evaluated by MALDI-TOF MS using the DHAP matrix (5.1.5). The MS-spectrum of the filtrate (solution filtrated through the membrane) does not reveal any of the above mentioned fragments, only a peak of m/z 2941 which cannot be assigned to any fragment (Figure 40a). Additionaly, the remaining solution above the filter membrane is analyzed. Since no fragment is found in the filtrate, all other components, fragment 1, fragment 2 and ligation product 1 should be determined in this fraction. As seen in the insert of Figure 40a, none of the fragments are found within that fraction leading to the conclusion that the fragments, due to the great hydrophobicity, remain and interact with the PES membrane. After washing the membrane with water, an aliquot is taken, diluted using 1:3 TFE/water (0.1% TFA) v/v and MALDI-TOF MS applied. With a mass peak of $[M+H^+]^+$ at m/z 4478.94 fragment 1 is identified supporting the hypothesis of interaction with the membrane (Figure 40b). However, a washing step using water can be used to separate parts of fragment 1 from the ligation solution. Employing a second washing step using 1:3 TFE/water (0.1% TFA) v/v the ligation product 1.2 with $[M+H^+]^+$ at 7404.33 m/z is found aside from hydrolyzed fragment 2 with $[M+H^+]^+$ at 2978.28 m/z and fragment 1 with $[M+H^+]^+$ at 4478.94 m/z (Figure 40c). Flipping the filter and applying centifugational forces lead to an increased elution of of the ligation product 1.2, $Kcv_{NTS}(16\text{-}81)$ (Figure 40d) as well as an increased intensity of fragment 1. These results lead to the conclusion that due to hydrophobicity of all fragments, fragment 1, fragment 2 and ligation product 1.2, stick to the filter membrane and are only realeased after several washing steps and the addition of organic solvent. Vivaspin® filtration can thus be used to reduce the amounts of fragment 1 because is released also by washing with water, and to concentrate the ligation product 1.2 as well as separating the added salts within the ligation buffer system.

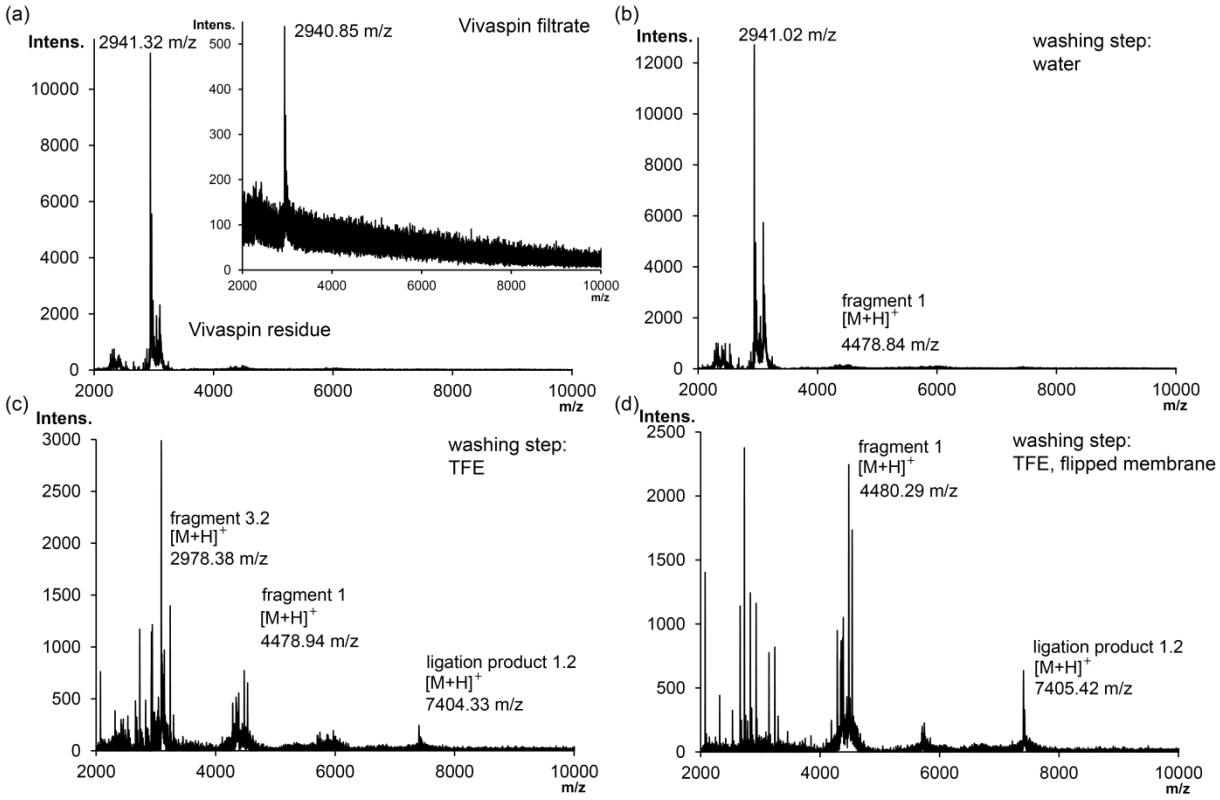

Figure 40. Vivaspin® filtration/purification

Different stages of the Vivaspin® filtration are shown. (a) shows MS spectra of the residual solution while the insert shows spectra of the filtrate at the bottom. (b) Illustrates the spectra after the washing step using water, (c) using TFE in water. Lastly, (d) shows spectrum of the flipped membrane that was washed with TFE. All spectra were recorded using DHAP as the matrix in the LP mode.

6.6. Hydrolysis of the fragment 2

The ligation reaction can only take place as long as both fragments, the C-terminal thioester and the N-terminal cysteine, are present in the solution. While fragment 1 is added in excess, fragment 2 represents the crucial factor. Not only is it deficient in concentration, it can also be inactivated through hydrolysis of the oxo-ester unit which leads to inactivation of this fragment.

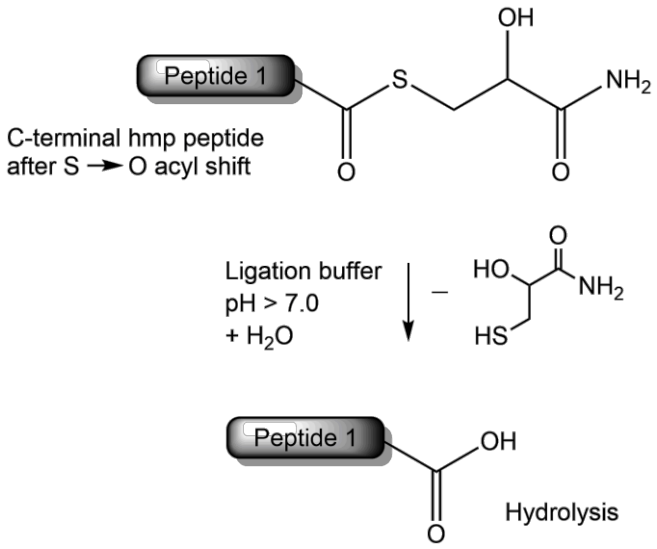

Figure 41. Hydrolysis of oxo-ester

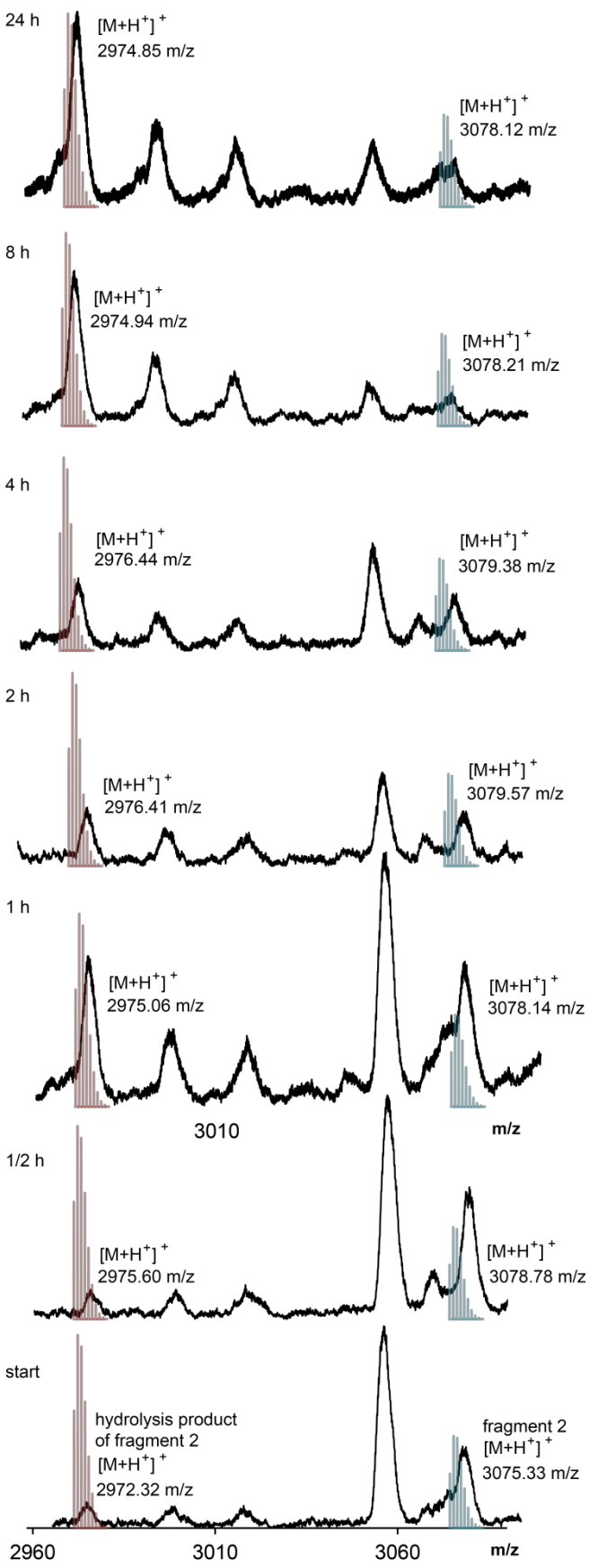

Figure 42. Hydrolysis of fragment 2

To monitor the hydrolysis process, at different time points of the ligation reaction samples are drawn and investigated using MALDI-TOF MS.

A scheme of the hydrolysis is illustrated in Figure 41 with Figure 42 showing hydrolysis (simulated patterns in red) of fragment 2 (intact fragment with simulated patterns in blue) over a time course of 24 h.

With the start of the ligation 1 using ligation buffer B, illustrated in Figure 42 bottom, fragment 2 is still intact with no change in peak intensities seen until 30 minutes. After 1 h, the peak appointed to the hydrolysis product, increases and reaches intensities comparable to the intact product. Until 4 hours of reaction the portion between inact and hydrolyzed fragment 2 does not change. From 8 h on until 24 h no intact fragment 2 can be visualized using MALDI-TOF MS which leads to the conclusion that a further addition of fragment 2 after 8 h of reaction time is beneficial to keep the ligation reaction going. After 8 h the NCL is aborted since no oxo ester of fragment 2 is available for reaction with the N-terminal cysteine moiety of fragment 1.

Hydrolysis of the C-terminal hmp-oxo ester of fragment 2 over the course of 24 h. All spectra were recorded using DHAP as the matrix and the LP mode.

6.7. Native chemical ligation 2

The successional ligation, NCL 2 of ligation product 1.2 with fragment 3.2, is performed in ligation buffer D (5.1.3.4). Figure 43 illustrates the change in the MS spectra from the first (a) to the second ligation (b) and (c). Again, a sediment is formed within the 24 h of ligation reaction (Figure 44). Both fractions, the solution and the sediment were used for further MALDI-TOF analysis.

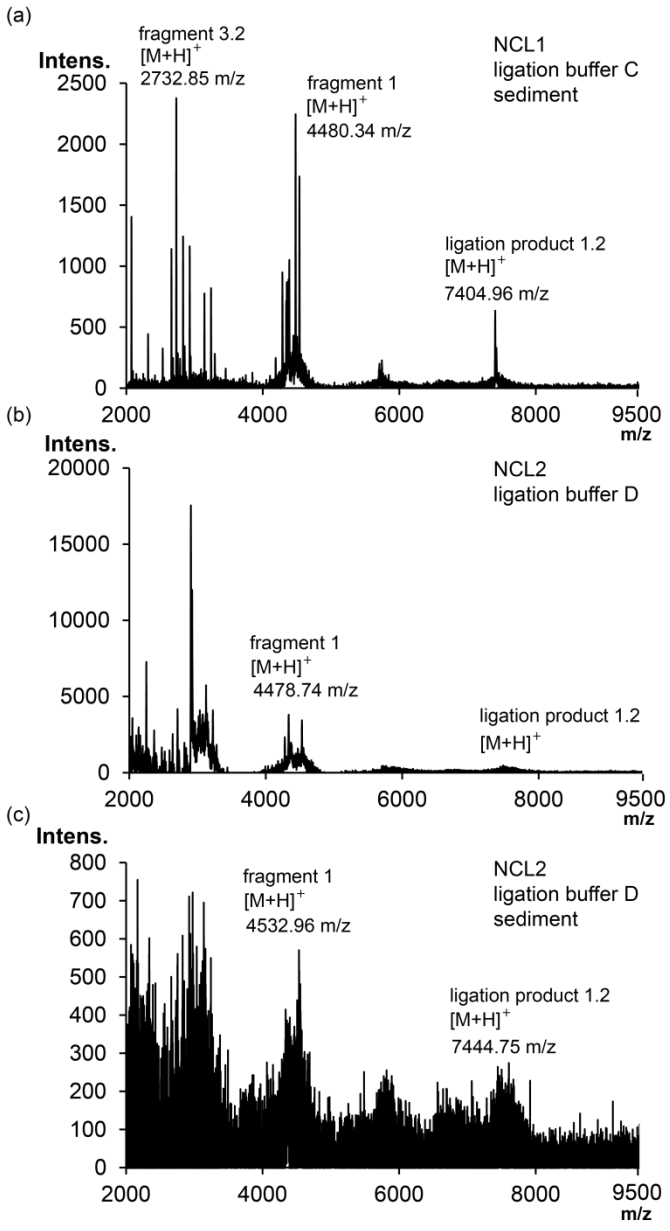

Figure 43. MALDI TOF results of the second ligation

Illustration of MALDI-TOF MS spectra from the first ligation after Thz conversion (a) and the second ligation solution (b). Measured using DHAP matrix and LP mode. (c) showing a spectra of the sediment measured using the Thinlayer method with MeOH as the solvent

The ligation solution is acidified using 1:3 TFA/water (0.1% TFA) v/v and the spot on the MALDI target washed with water (0.1% TFA) to suppress interfering salts from the ligation buffer D.

Figure 43a shows a spectra of the first ligation reaction in ligation buffer C after unmasking of the thioproline unit and serves for comparison to Figure 43b. A significant decrease of the peak representing the ligation product 1.2 with $[M+H^+]^+$ at 7404.96 m/z gets visible. Furthermore, fragment 2 is still visible because it could not be separated using the VivaSpin® centrifugation methods (6.5). Since it displays a N-terminal Cys moiety, there is a possibility of fragment 1 to react with fragment 3.2. This would result in a peak of $[M+H^+]^+$ ($C_{295}H_{469}N_{67}O_{73}S_3$) with a mass of 6218.44 m/z. This peak cannot be found within the spectra of the solution (Figure 43b) nor the sediment of the second ligation (Figure 43c). Neither is the ligation product 2 found within those two fractions. The product would be represented by a peak with $[M+H^+]^+$ at 9144.84 m/z. To investigate the sediment, it is dissolved in 1:3 TFA/water (0.1 % TFA) v/v.

For investigation of the sediment, the DHAP method did not show a sufficient spectra. Therefore, additional methods for MALDI-TOF MS of hydrophobic membrane proteins were applied and tested (5.1.5). First, Sinapinic acis, which is often used as a matrix for high molecular weight samples for measurements in LP positive mode[174], (SI Figure 3) did not show any superiority. Second, the comparison of sandwhich methods led to the conclusion that the thinlayer method using methanol as a solvent is the method of choice, generating the most intensive peaks (SI Figure 4). To illustrate this superiosity, the DHAP spectra is compared to the thinlayer method in SI Figure 5. Unfortunaltely, even though optimization of the matrix system and sample preparation led to a better MS spectra, the product cannot be determined.

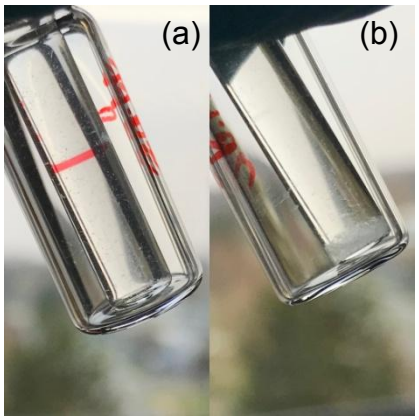

Figure 44. Sediment generation during the second ligation

(a) start of ligation reaction (b) after 24 h

As seen in 6.5, applying a purification step using the Vivaspin® ultracentrifugation units, does not efficiently remove fragments such as fragment 1 with a molecular weight of around 4.5 kDa. These findings suggested a one-pot ligation strategy using the ligation buffer C. However, Vivaspin® purification if beneficial to prepare the samples for MALDI-TOF MS due to separation of salts from the buffer system. Figure 45 shows MALDI-TOF MS of the acidified ligation solution form ligation 2 in 1:3 TFE/water (0.1% TFA) v/v using the DHAP matrix and LP mode. Both, Figure 45a and b represent the exact same spot on the target plate while (b) has been washed twice using 1 μl of water (0.1% TFA). The results are discussed in 6.7, this illustration shows that washing the spot, to avoid interferences of salt such as urea on the ionization, on the target is crucial for the generation of significant spectra.

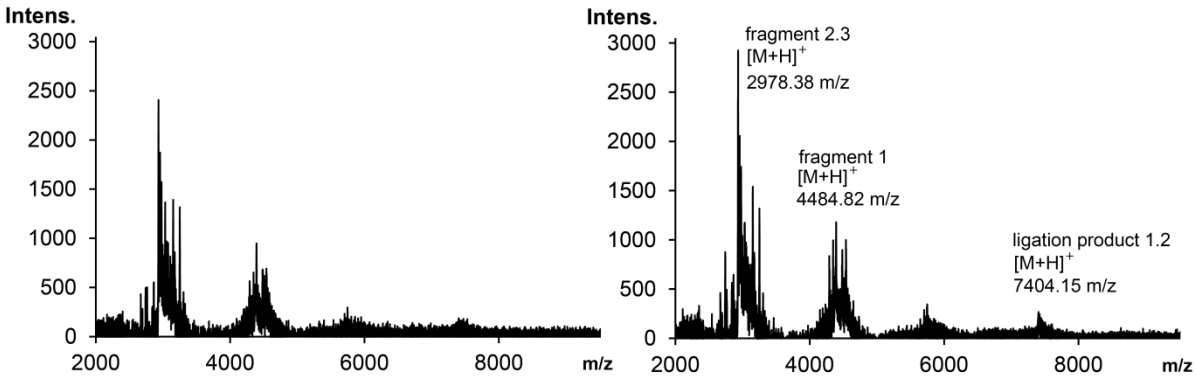

Figure 45. One-pot ligations strategy

(a) One-pot ligation solution in DHAP matrix (b) same spot from (a) washed 2 x with water (0.1% TFA)

6.8. Characterization of the final product Kcv_{NTS}(1-82)

Detection of the correct size of Kcv_{NTS} using SDS PAGE

Looking at the MS results it can be seen that ionization is strongly dependent on the matrix used as well as the sample preparation. It is possible that the product is present but not ionized and thus not detectable in the methods applied. Only the appliance of different analytical methods will give information on product formation. A further method used to identify product formation is SDS PAGE, sodium dodecyl sulfate polyacrylamide gel electrophoresis. With the addition of SDS to the sample buffer, proteins denaturate and bind SDS non-covalently resulting in a negative charge that is constant due to micellar effects with an overall similar charge-to-mass ratio. The sample then migrates through the gel from the cathode (-) to the anode (+) according to its size when applying an electric field.[175,176] Two types of staining procedures were performed, Coomassie stain and silver stain. While Coomassie binds to basic and hydrophobic proteins, making them visible through a blue color, the sensitivity is rather low with a value of around 25 ng/band. Thus, a further staining is used to visualize also difficult and small amounts of protein. Silver staining can be sensitive towards 0.5 ng protein/band.[177] Usually, samples are boiled at 95 °C with the SDS-containing sample buffer, following Schägger's recommendation, incubation at 37 °C for 15 minutes is sufficient for membrane proteins.[127]

First, Coomassie stain is applied resulting in the gel found in the supporting information (SI Figure 6). Silver staining is performed to make further bands visible or to intensify already visible bands (Figure 46). For the used protocol, see 5.1.6.

(a) (b)

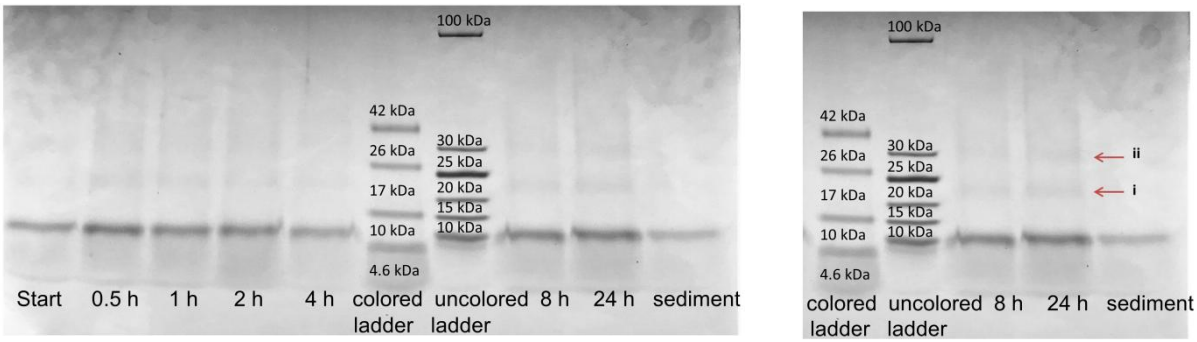

Figure 46. SDS PAGE of second ligation

(a) and (b) showing silver stain of the same gel with (b) an extract

Besides the significant band at 10 kDa, which coincides with the mass of the product (9.1 kDa), two more bands are visible. In the extract (b) two red arrows indicate the other visible bands, *i* at around 20 kDa and *ii* at 30 kDa. Since they represent the mass of the product multiplied by 2 × for *i* and 3 × for *ii,* those bands match the masses for oligomeric formations, the dimer and trimer of the product. This behavior of forming oligomeric structures with denaturing SDS PAGE conditions is very common. While e.g. Kcv showed formation of the monomeric and tetrameric structure with the addition of K^+ ions to the sample solution[178] investigated by Pagliuca *et al.,* SDS PAGE of BM2 (1-51) showed formation of all oligomeric states, the monomer, di-, tri- and tetramer.[179] Looking at the starting point of

the NCL 2, the significant band at around 10 kDa is visible and comparable to the bands of the NCL 0.5 h – 24 h while no oligomeric forms at 20 kDa and 30 kDa are detected. This sample though, represents the starting point of the NCL 2 which, at 0 h, should not contain the product. Since membrane proteins usually do not run strictly according to their size due to aggregation and their hydrophobic nature it could be possible to not see a significant difference in height of the band of the ligation product 1.2 at 7.5 kDa and the product of NCL 2 at 9.1 kDa. Further information from this SDS PAGE is the non-existence of additional bands within the sediment sample which leads to the conclusion that the product of the second ligation can only be found within the ligation solution, not the sediment.

With the addition of DTT to the loading buffer, formation of disulfide bridges is disrupted. A further SDS PAGE Gel is run using the 24 h samples of NCL 2 and denaturing, reducing (red.) and native conditions.

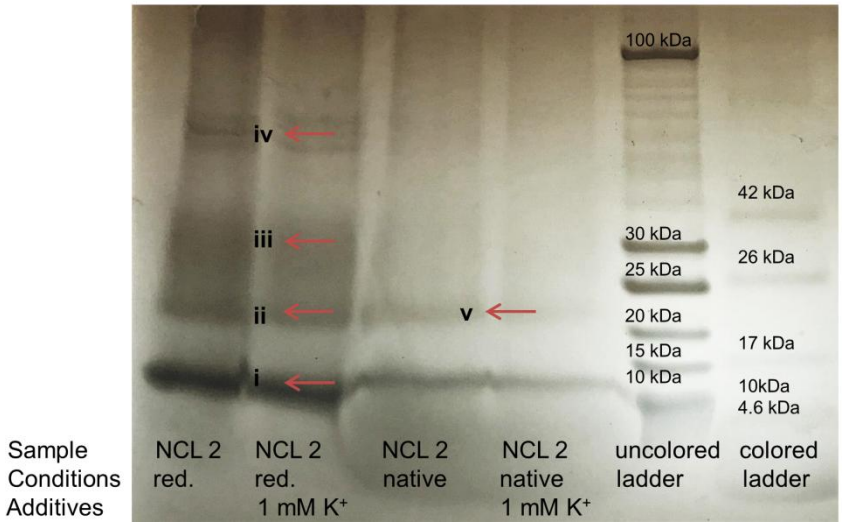

Figure 47. SDS PAGE using denaturing and native conditions

Looking at the second gel (Figure 47), a forth band indicated by the red arrow *iv* is visible in the samples dissolved in the reducing sample buffer. This forth band can be arranged between 42 kDa and 100 kDa and represents the tetrameric form of the product, Kcv_{NTS}. It becomes visible, that the addition of K^+ does not influence formation of potential oligomeric forms when taking the samples directly from the ligation solution containing salts and buffers. Looking at the native conditions from the same initial solution, formation of only a second band in the range of 20 kDa can be found, visualized with a red arrow *v*. Dismissing DTT from the sample buffer, disulfide bridges can be formed. The synthesized sequence exhibits two potential cysteine residues for disulfide bridge formation which would result in around 20 kDa. Also, these conditions will not lead to oligomeric behavior which is represented in this gel.

To evaluate bands *i, ii, iii* and *vi* to really be oligomeric forms of our product, a positive sample is needed. Native Kcv_{NTS} samples were gratefully provided by Tobias Winterstein from the Thiel lab. Both samples represent Kcv_{NTS} in different lipid environment.[180] Coomassie stain of the gel can be found in the supporting information (SI Figure 7).

Looking at the sample **ligation product 2 solution** in the agarose gel (Figure 48) we can see a similar image compared to Figure 46. Only three oligomeric forms are visible indicated by the red arrow pointing at *i* (monomer), *ii* (dimer) and *iii* (trimer). A possible tetrameric form as seen in Figure 47 is not visible, again emphasizing the difficulties attached to analytics of membrane proteins. Furthermore, **ligation product 2 Vivaspin** represents the same solution discussed afore but purified using the Vivaspin® protocol after TFE washing and flipping of the membrane. Since no further bands are visible but the significant band at 10 kDa, using Vivaspin® for purification of the NCL 2 is not recommended. Also, **ligation product 2, 4 weeks** does not show any significant peaks indicating that the product may not be stable stored in the ligation solution at -30 °C for more that 4 weeks. In accordance to Figure 46, the sediment (**ligation product 2 sediment**) does not show oligomeric behavior. **Ligation product 1.2** represents the ligation solution of the first ligation showing two bands. Since the first product displays one transmembrane region, formation of oligomeric states could be possible. Furthermore, the obtained bands from ligation 1 and ligation 2 are not similar indicating a product formation after NCL 2. Coming to the positive samples, native Kcv_{NTS} we can see that there are multiple bands visible. The channel is synthesized using expression and further integrated into nanodiscs or lipids, no further purification step is applied. Thus, multiple bands are visible which do not match completely. Bands *iv, v and vi* can be attributed to *iii, ii* and *i* while band *vi* runs similar to *i* in Figure 47. These results indicate a successful synthesis and the presence of the synthesized Kcv_{NTS}.

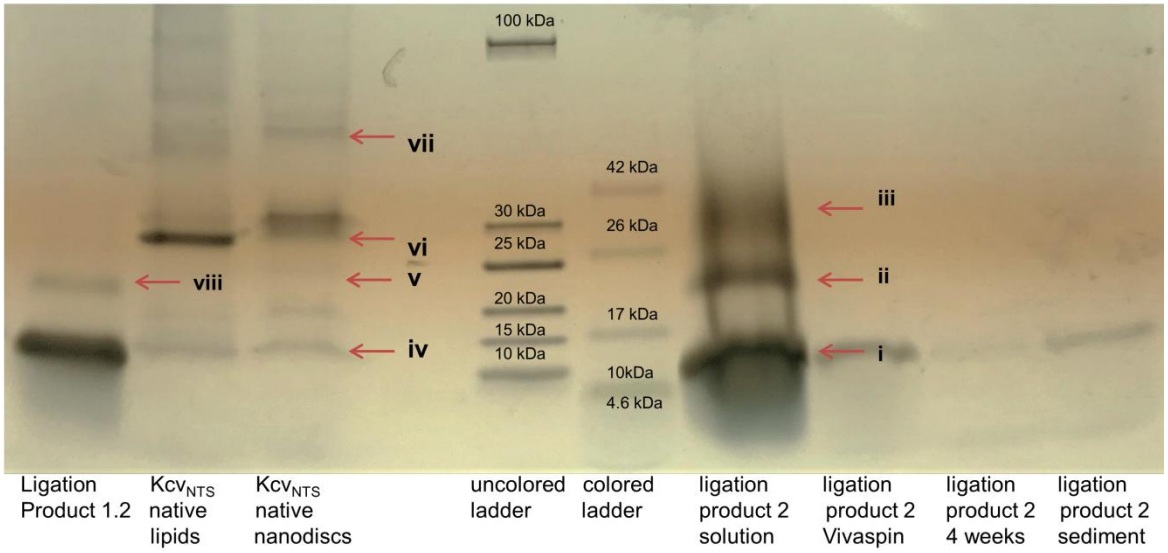

Figure 48. SDS PAGE with Kcv positive samples

Determination of the predominant overall fold of Kcv_{NTS}(1-82) with circular dichroism spectroscopy

Circular dichroism is a powerful and useful tool to investigate not only the folding properties of proteins but it can also be applied in investigating conformational changes over time or in dependency on temperature to obtain data on kinetics.[181,182] Three decisive bands characterize the existence of α-helical structures: two negative bands at 222 nm and 208 nm as well as a positive band at 193 nm.[183] In Figure 49 the CD spectra of ligation preparations are shown as well as the positive Kcv_{NTS} sample from Figure 48 (**Kcv_{NTS} native nanodiscs**). Also, a blank measurement in shown in (a) indicated by a blue color. Unfortunately do all samples show

very little absorption. Additionally, the positive sample does not show a clearly defined α-helical structure which could be appointed to the nanodiscs within the solution having an interfering absorption behavior. Only the ligation in orange shows a spectra that can be evaluated and meets the requirements of α-helical proteins. The spectra displays a minimum around 208 nm and a further on at 222 nm. Looking at the wavelengths range of 190 – 200 nm we can see a "zick-zack" behavior which can be translated to insufficient concentration but a tendency for a positive CD value can be carefully evaluated. Since dissolving of the product is needed to obtain evaluable spectra, another method is used that has been successfully applied in literature.[184] To generate an environment similar to a cell membrane, lipids can be used, e.g. POPC to preserve the native state of the membrane protein.[185] To generate a narrow size distribution of POPC vesicles, they are extruded through a 1 μm polycarbonate membrane and measured directly. Unfortunately, no usable spectra could be recorded (see SI Figure 8). Again, this investigation suggests successful synthesis and existence of Kcv_{NTS} but again shows the difficulties in analyzing membrane proteins.

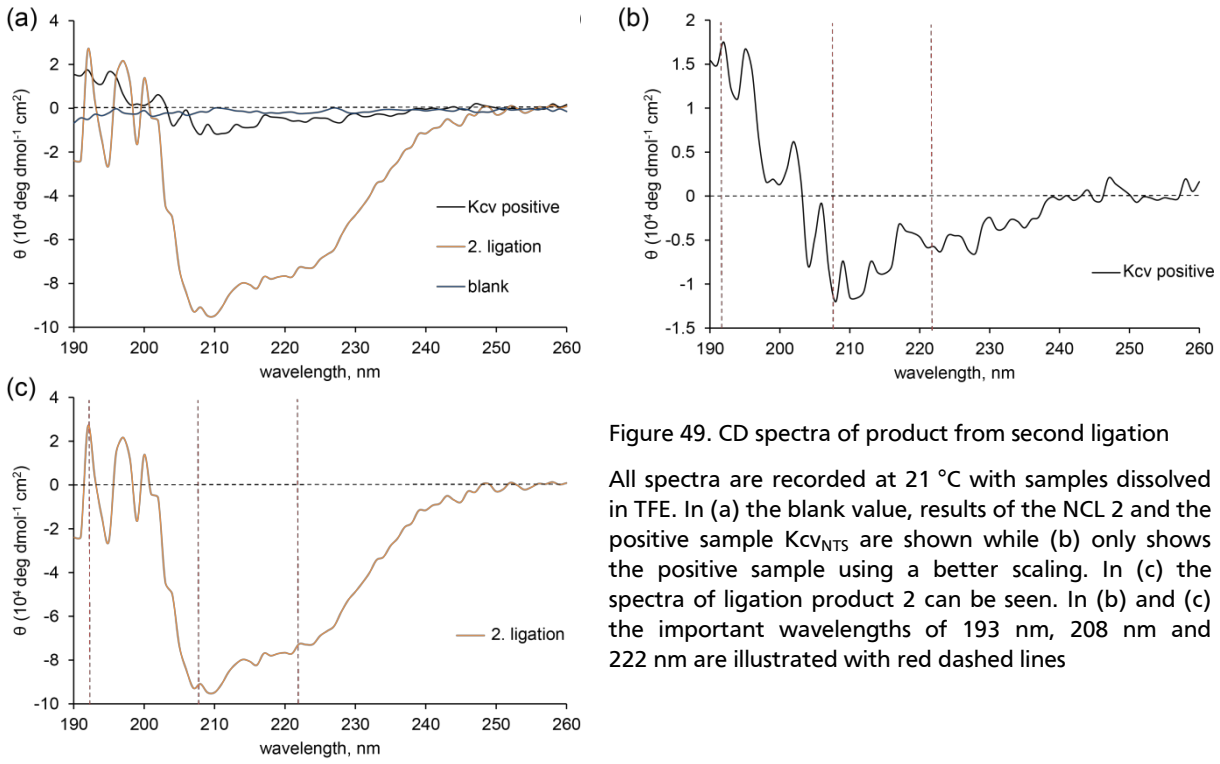

Figure 49. CD spectra of product from second ligation

All spectra are recorded at 21 °C with samples dissolved in TFE. In (a) the blank value, results of the NCL 2 and the positive sample Kcv_{NTS} are shown while (b) only shows the positive sample using a better scaling. In (c) the spectra of ligation product 2 can be seen. In (b) and (c) the important wavelengths of 193 nm, 208 nm and 222 nm are illustrated with red dashed lines

7. Conclusion and outlook: Kcv_{NTS}

Successful synthesis, purification and characterization of membrane proteins face numerous challenges. A major component contributing to the difficulties is the sequence itself, usually exhibiting hydrophobic amino acids especially in the transmembrane regions, predominantly build up from α-helices penetrating the membrane. Two of the major problems related to these hydrophobic amino acids during SPPS are (1) incomplete amino acid coupling reactions and the tendency to (2) aggregate on-resin. According to the results presented in section 6 the synthese of Kcv_{NTS} faced challenges in regard to synthesis, purification and analytics.

Synthesis. Incomplete coupling can be targeted by the careful evaluation of coupling reactants and conditions. HATU was chosen as the coupling reagent because of its superiority and high coupling efficiency with quick coupling times leading to high yields during SPPS.[186,187] HATU displays an excellent stability in DMF (>99% in closed vial over 48 h) and can thus be applied for automated peptide synthesis.[188] Furhtermore, inter- and intramolecular aggregation can be reduced with elevated temperatures.[189] Microwave irradiation during automated SPPS is employed during synthesis of the Kcv_{NTS} fragments leading to precise and controlled elevation of the temperature (see 5.1). The problem of aggregation on resin can be approached by the incorporation of structures stabilizing the backbone, namely pseudoprolines. According to our results (Table 5) and evaluating the yield of the product outcome (fragment B) from 8.0% to 6.6% while using pseudopolines for fragment B, we do not see a positive development in synthesis yield with the addition of pseudoprolines. For difficult sequences, resins with proper swelling characteristics, little cross-linking and low-loadings are recommended.[190,191] For fragment 3.2, we evaluated AmphiSpheres 40 RAM resin to be superior to TentaGel R RAM resin (see Table 28). Albeit the AmphiSpheres 40 RAM resin holds a higher loading capacity then the TentaGel R RAM resin (0.38 mmol/g compared to 0.18 mmol/g), this resin shows a high content of long PEG units which enhance synthesis if difficults peptide sequences.[192]

Other employable alternatives for minimization of aggregation are usage of Hmb-amino acids[193] and depsidipeptide units (O-acyl isopeptides) for backbone modification and stabilization through disruption of amide bond patterns.[194,195] Additionally, the choice of the SPPS protocol could target these difficulties and be applied in further synthesis optimization steps.[30,196,197]

Purification. The purification step is essential for sufficient analytics and efficient native chemical ligation reactions. For extremely hydrophobic fragments, such as fragment B, fragment 3 and fragment 3.2, RP-HPLC reaches its limits, although optimization of the stationary phase of the column took place. We used a wide pore silica of 300 Å, which allows for larger peptides and proteins to better interact with the surface and a butyl phase (C4) that is suitable for proteins and larger, hydrophobic peptides.[198] For efficient purification, complete dissolution is required. To guarantee this state, fragment 2 was dissolved adding droplets of concentrated TFA first (Table 14) and fragment 3 was only soluble with addition of detergents such as OG and DDM. Ultimately, usage of detergents did not lead to sufficient purification of fragment 3 which resulted in the incorporation of a solubilizing unit. While we integrated a hydrophilic tail at the C-terminal hmp oxo-ester unit, there are various alternatives possible from side-chain solubilizing units to N-terminal tags[199]. For our need, the C-terminal solubilizing tag displays the best method since it is readily detached during the NCL reaction with no additional cleavage step needed.

Additionaly, larger fragments from the herein presented ligation experiments, ligation product 1, 1.2 and 2, could not be purified using optimized RP-HPLC or dissolution protocols. Therefore, the purification using Vivaspin® concentrators was established. As presented in 6.5, fragment 1 was partially separated from the ligation solution with ligation product 1.2 being concentrated due to release of the fragments during different washing steps.

This purification method holds great potential with optimization needed. As presented, washing and flipping of the membrane is needed and only with the addition of TFE (1:3 TFE/water (0.1% TFA) v/v), ligation product 1.2 is released. Applying a gradient of the TFE/water mixture will lead to more sufficient separation and better concentration of the product. The increasing amounts of TFE are to be evaluated carefully in regard to the stability of the membrane.

Analytics. An optimized purification method facilitates analytics such as MALDI-TOP MS, LC-MS and SDS. Using the Vivaspin® filtration units prior to MALDI-TOF MS measurements, samples from ligation solutions, that contain high amounts of interfering salts, are ionized more efficiently.[200] Also, washing of spots on the MALDI target, using water (0.1% TFA), that are taken directly form reaction solutions, e.g. during Thz conversion, will lead to optimized and better sprectra (Figure 45). There are various protocols published targeting membrane proteins. Presented in this work is the thinlayer and threelayer methods (5.1.5) that led to more precise spectra compared to the mainly used 2,5-DHAP method (Figure 43 and SI Figure 5). Still, ionization of the ligation product 2 was not possible leaving room for optimization of MALDI-TOF MS methods.

Ionization of membrane proteins displays an enormous challenge. To circumvent ionization of these large structures, a digestion, generating multiple fragments with lower masses, is a method that is applicable. Therefore, the method of peptide mass fingerprinting (PMF) is an interesting and important analytical tool.[201]

Native Chemical ligation, NCL. The hmp peptides were successfully synthesized presented in 6.2. Therefore, NCL using this mehod is very reliable for the Kcv_{NTS} sequence and has been successfully used at our lab. The choice of solubilizing tag, though, is of great interest since the herein used consists of eight amino acids possibly leading to sterical hinderance during NCL 2. Baumruck *et al.* from our lab investigated efficiency of different solubility tags on model peptides and a sequence of BM2 when using the hmp building block for NCL. Improvement of solubility was achieved with the addition of one ADO unit (8-amino) and a Lys_5 tag.[143] The inserted solubility tag used for the synthesis of Kcv_{NTS} consists of the soluble amino acids, Lys and a spacer consisting of Gly units and is self-cleavable during NCL. Consisting of eight amino acids this tag is rather big and could be decreased in size to prevent sterical hindrance during NCL. There are numerous examples for alternative solubility tags in literature. To point out one of a very recent idea to incorporate a solubility tag is the method introduced by Brailsford *et al.* making use of the orthogonal Acm protection group. With the addition of several arginine groups to its acetyl group, they generated a novel solubility tag, Acm^R, that is only cleaved off, when mild reducing conditions are used in an additional step.[202] This would make the solubility tag stable throughout NCL.

Focusing on improving NCL conditions, we evaluated addition of two organic solvents, HFIP and TFE with the latter in two concentrations (1/3 TFE and 2/3 TFE). Recently, the replacement of solvents by ionic liquids has been studied by Baumruck *et al*. in our lab and

may represent an interesting new approach and alternative to the aforementioned organic solvents.[203,204] Another interesting proposal to facilitate NCL emerged in recent years with the ever-growing corporation between chemistry and biology. Amide bond formation is performed by ligases in living systems, leading to the idea to make use of these enzymes to fuse several protein fragments to their native sequence. A recent summary by Schmidt *et al.* highlight the possibilities.[205]

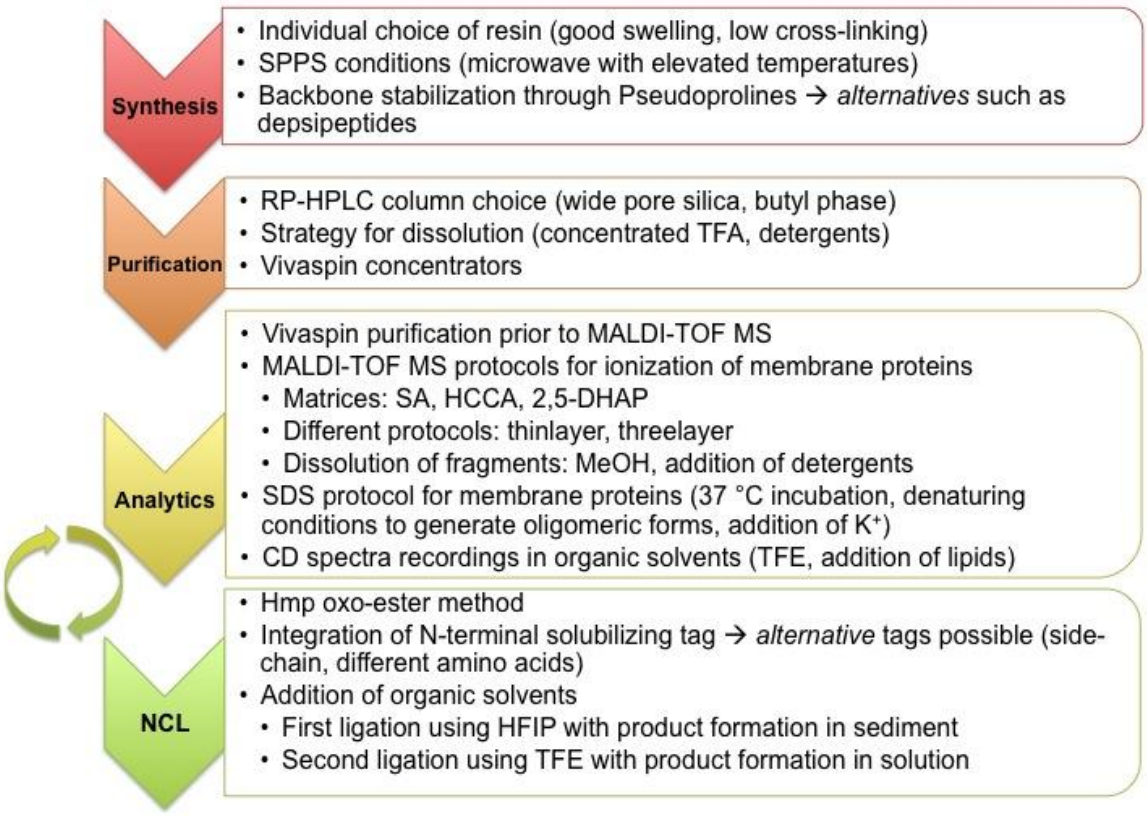

Figure 50. Optimized synthesis strategy

Summary. Various optimization protocols were used during the challenging synthesis of the membrane channel Kcv_{NTS}. The first attempt in the fully chemical synthesis of the 82-mer transmembrane potassium channel protein Kcv_{NTS} followed a two-fragment strategy that, unfortunately, did not lead to the desired product. Through the high hydrophobicity of the peptide fragments, optimization various steps, from synthesis conditions to purification, analytics and NCL were needed. The final ligation, following a three-fragment approach, resulted in positive results with SDS Page gels showing oligomeric bands at the desired masses (see Figure 47 with bands at 10 kDa, 20 kDa, 30 kDa, 40 kDa) and CD spectroscopy shows the predminant formation of the alpha-helical structure. Figure 50 summarizes the herein presented optimizations of various steps towards successful synthesis of Kcv_{NTS}.

Outlook. Due to the lack of final product material, electrophysiological studies were not possible. These will make comparison to behavior of the native Kcv_{NTS} possible. Up-scaling of the synthesis is needed to generate sufficient amounts of product. Furthermore, when a robust synthesis route is evaluated, the integration of isotopically labeled amino acids can make NMR experiments possible which will bring structural insights. Additionaly, further mutations can then be integrated for functional studies.

8. Results and Discussion: Development of a hybrid nanosensor

8.1. Strategy towards the design of a hybrid nanosensor

This section focuses on the incorporation of biologically relevant peptides into nanopores of solid state material for the generation of hybrid nanopores. These hybrid systems are favorable over just biological nanopores or only solid state nanopores because they combine the advantages of both systems into one. Biological nanopores show extreme sensitive and selective behavior towards targets with atomically precise structures and the possibility to synthetically modify the sequences while advantages of solid state nanopores are the robustness of the materials towards pH changes, thermal and mechanical stress as well as the control of size and shape.[206] Combining both structures, unveils endless possibilities for extreme sensitive and selective sensing in a robust system that can futher be used for the generation of a sensor device.

As a first example in these studies, a modified Amino-terminal Cu(II) and Ni(II) binding motif, ATCUN motif, was chosen as the basic biological structure for this hybrid system. The relevance of an applicability of the ATCUN motif as a sensor is presented in 3.4.2. The proposed Cu(II) and Ni(II) binding is interesting in regard to using this characteristic for development of a sensing hybrid material.

For this development, the following steps have to be carefully taking into consideration:

1. Screening for the available ATCUN motifs in literature
2. Design of a peptide structure that can be covalently coupled to the solid-state material
3. Synthesis and characterization of the ATCUN peptides
4. Investigation of binding properties towards Cu(II), Ni(II) and Zn(II)
5. Immobilization of the peptide to the solid support
6. Characterization of the hybrid material

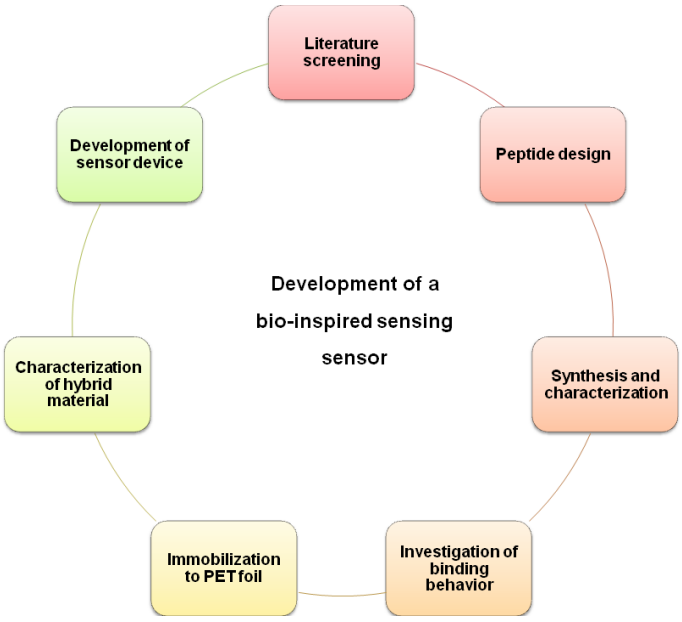

Figure 51. Design towards the bio-inspired sensing peptide sensor

(1) The ATCUN motif consists of a minimum of three amino acids with histidine being mandatory in the third position while the first and second amino can be any arbitrary moiety. The simpliest structure generated from the general sequence Xaa-Yaa-His is Gly-Gly-His.[207] Numerous examples for variations of this ATCUN-motif sequences are described in literature. The integration of unnatural amino acids through SPPS makes various applications possible. Inserting isotopically labeled, ^{15}N amino acids enable structural investigations in regard to complex formation.[208] Moieties, such as β-amino acids facilitate the addition of e.g. fluorophores for visualization of a binding event. The 2,3-diaminopropionic acid, Dap, is widely used for addition of fluorophores.[99,209,210] We evaluated 5/6-Carboxyfluoresceine, 5/6-FAM, to be an interesting moiety to be integrated due to the straight-forward insertion into the sequence through SPPS.

(2) For the generation of a hybrid device, both systems, the biological sensing peptide 4 and the solid state nanopores, need to be compatible in regard to the covalent coupling. The peptide has to be attached from either N-terminus, C-terminus or from integrated side-chains to the solid state material while the sensing ability has to be guaranteed after immobilization. Attachment from the C-terminus was evaluated to be optimal for our system due to primary amines from side chains that could interfere with coupling from the N-terminus. To guarantee full functionality of the sensing characteristics of the peptide, a spacer is needed to generate distance from the nanopore surface to the sensing unit of the peptide. Ganesh *et al.* investigated several spacer lengths (from $O(CH_2)_4$ to $O(CH_2)_8$) on a glycosly acceptor coming to the conclusion that a longer spacer will increase reactivity and mimic solution-phase environments.[211] While iterative amino acids, e.g several Gly-units, are possible spacers compatible with SPPS, we aimed for using the spacer to also enhance the characteristics of our peptide sequence. Torrado *et al.* used two serine units within their peptide sequence as a spacer and to improve water solubility. We evaluated a PEG unit (miniPEG4) to fulfill our requirements since it improves the overall hydrophilic nature.[212]

(3) Having determined the sequence and important features of the sensing peptide, synthesis, purification and analytics are needed. Peptide synthesis following the fmoc-based SPPS protocol is employed. Therefore, the linker and fluorophore need to be evaluated to be compatible with fmoc-SPPS.

(4) The binding characteristics towards Cu(II), Ni(II) and Zn(II) have to be determined and compared. Especially in regard to selectivity, it has to be carfully investigated and determined at which conditions Cu(II) or Ni(II) are favored over one another. Our sensor design is based on the work of Imperiali work and stated to be selective towards Cu(II) due to the integration of the β-amino acid, Dap.[99] This statement has to be reviewed in experiments and proven as correct or incorrect. Furthermore, quenching of fluorescence with addition of Cu(II), Ni(II) and Zn(II) needs to be evaluated and characterized.

(5) For the immobilization, various protocols are available. Cu-free click-chemsitry,[213] cysteine to gold coupling[214] and EDC/NHS immobilization[215] are methods frequently used, just to name a few. With expertise in SPPS, we decided to try using HATU/DIEA for immobilization and to compare success over the EDC/NHS method, which was also applicable to our need. Therefore, a blank foil needs to be investigated in regard to stability towards DMF for HAUT/DIEA immobilization.

(6) The characterization of the hybrid material comprises several analytical methods that are needed. First, the requirements of the system need to be defined. For us, the selectivity and

sensitivity towards Cu(II), the robustness of the system in regard to overall stability and storage time, as well as the re-usability of the system are of great importance. *I-V* measurements are a method applicable to investigate all of these requirements. To underline and verify results from *I-V* investigations, further analytical methods need to be performed. Due to the integration of a fluorescent moiety, fluorescence microscopy can be applied, especially in regard to show the re-usability and feasability of the system.

A scheme of the immobilization of the sensing peptide and the function of the sensor is illustrated in Figure 52.

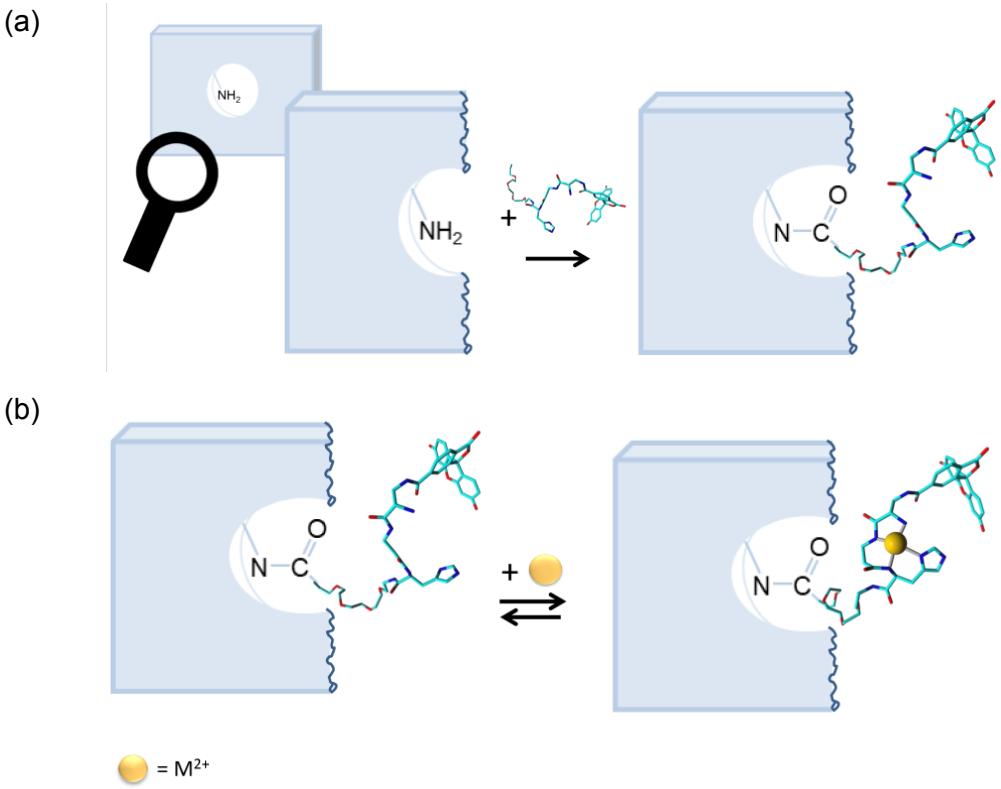

Figure 52. Scheme and sensor idea

The magnifying glass in (a) shows the cut-out of one nanopore within the PET foil that has already been prepared to exhibit a $-NH_2$ group for coupling of the peptide. In (b) a heavy metal is added and the peptide 1 coordinates the heavy metal ion M^{2+}

We synthesized four peptides, all exhibiting the miniPEG linker for immobilization. **Peptide 4** carries the fluorophore, 5/6-FAM for visualization of the binding event. The sequence of **peptide 1** is similar to peptide 4 but lacks the fluorescent moiety.. To gain further insight into the coordination behavior emanating from the amine groups within our motif, we designed two mutants. Instead of the crucial histidine moiety in the third position, we inserted alanine, **peptide 2** and aspartic acid, **peptide 3**, and evaluated the binding behavior in solution.

8.2. Synthesis of ATCUN-like peptides

The ATCUN-like peptides (1 – 4) were synthesized as described in 5.2. The general structure is shown in Figure 53 and varies in positions R and R_2. Based on the described motif by Torrado *et al.* X_n-(Dns)-βAla-His-Ser-Ser-NH_2 (with X_1 = L-β-aminoalanine (Baa), X_2 = L-(α,ɣ-

diaminobutyric acid (Amb) or X_3 = L-ornithine (Orn)[99] we designed our peptide 4 incorporation a linker and fluorescent moiety. We determined this motif to be ideal for our experiment since they were able to shift the binding behavior towards Cu(II) binding. Table 29 gives an overview of the sequences and molecular formulas as well as molecular weights.

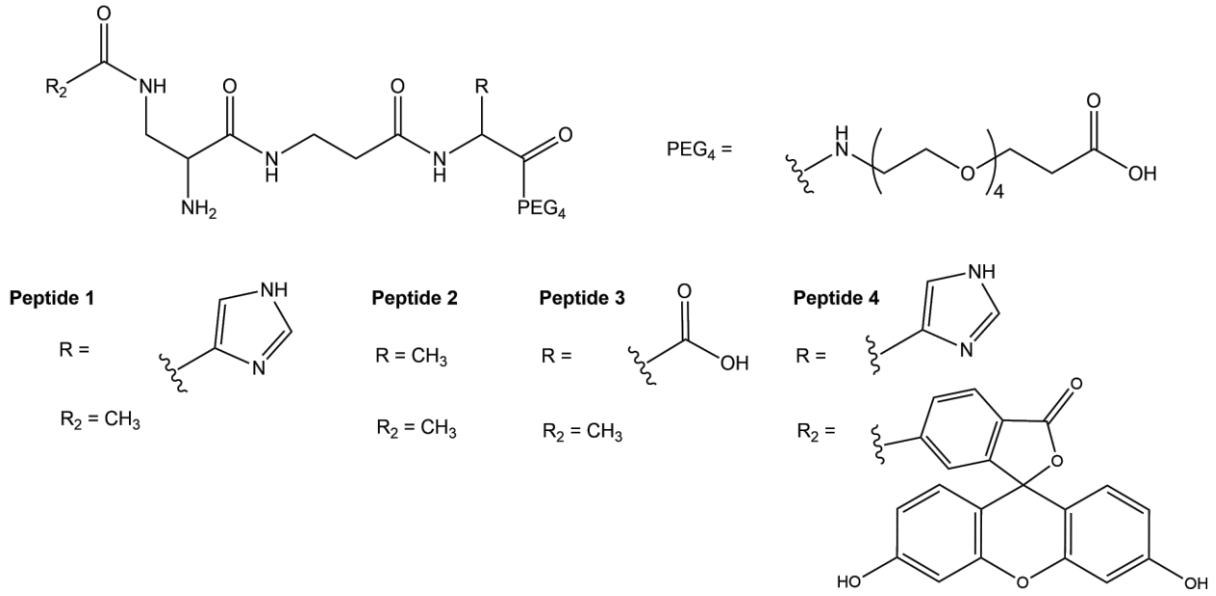

Figure 53. Structures of peptides 1 - 4

Name within text	Rest	Molecular formula	Calculated $[M+H^+]^+$	Measured $[M+H^+]^+$
Peptide 1	R = His R_2 = CH_3	$C_{25}H_{43}N_7O_{10}$	602.31	602.31
Peptide 2	R = Ala R_2 = CH_3	$C_{22}H_{41}N_5O_{10}$	536.29	536.29
Peptide 3	R = Asp R_2 = CH_3	$C_{23}H_{41}N_5O_{12}$	580.28	580.28
Peptide 4	R = His R_2 = 5/6-FAM	$C_{44}H_{51}N_7O_{15}$	918.35	918.34

Table 29. Overview of peptides 1 - 4

During synthesis the efficiency of coupling is monitored with UV-Vis control of the deprotected Fmoc values (Table 20). While loading reaches 92% of the initial value for peptide 4 prior to coupling of the fluorophore, final loading of peptides 2-4 are within 50 - 60% of the initial loading. The decrease of the coupling efficiency from peptide 4 to peptide 3 illustrates the loss in loading throughout storage of the Cl-Trt resin.

After successful synthesis, the crude product is analyzed using RP-HPLC. The resulting peaks can be collected from the analytical RP-HPLC method, freeze dried and evaluated using ESI-MS.

Confirmation of the molecular masses of peptide 1 - 4 were given measuring the samples from RP-HPLC using ESI-MS (for detail see Table 29).

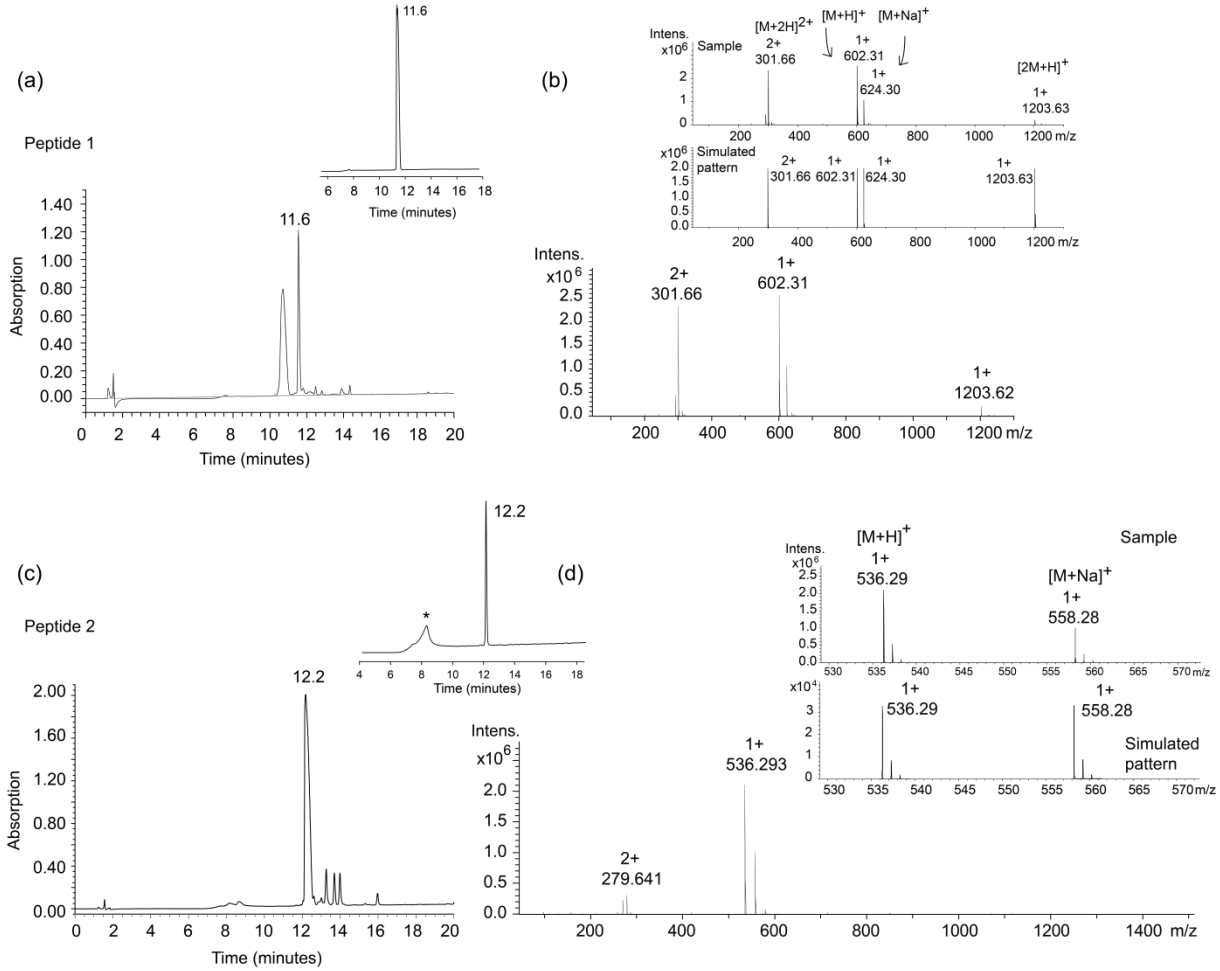

Figure 54. RP-HPLC and ESI MS of peptide 1 and peptide 2

(a) RP-HPLC of the crude product with insert showing purified peptide 1 at a retention time of 11.6 minutes and the respective ESI MS spectra (b) with isotopic pattern of sample and simulated pattern. RP-HPLC conditions: isocratic flow of 5% over 5 minutes followed by a linear gradient 5%- 40% eluent B over 20 minutes total with a flow of 1 ml/min, MultoHigh 100 RP 18 column at 30 °C. (c) RP-HPLC of the crude product with insert showing purified peptide 2 at a retention time of 12.2 minutes and the respective ESI MS spectra (d) with isotopic pattern of sample and simulated pattern. RP-HPLC conditions: isocratic flow of 5% over 5 minutes followed by a linear gradient 5%- 40% eluent B over 20 minutes total with a flow of 1 ml/min, MultoHigh 100 RP 18 column at 30 °C. *the peak at 8 minutes is generated through a change in pressure changing from the isocratic method to a linear gradient

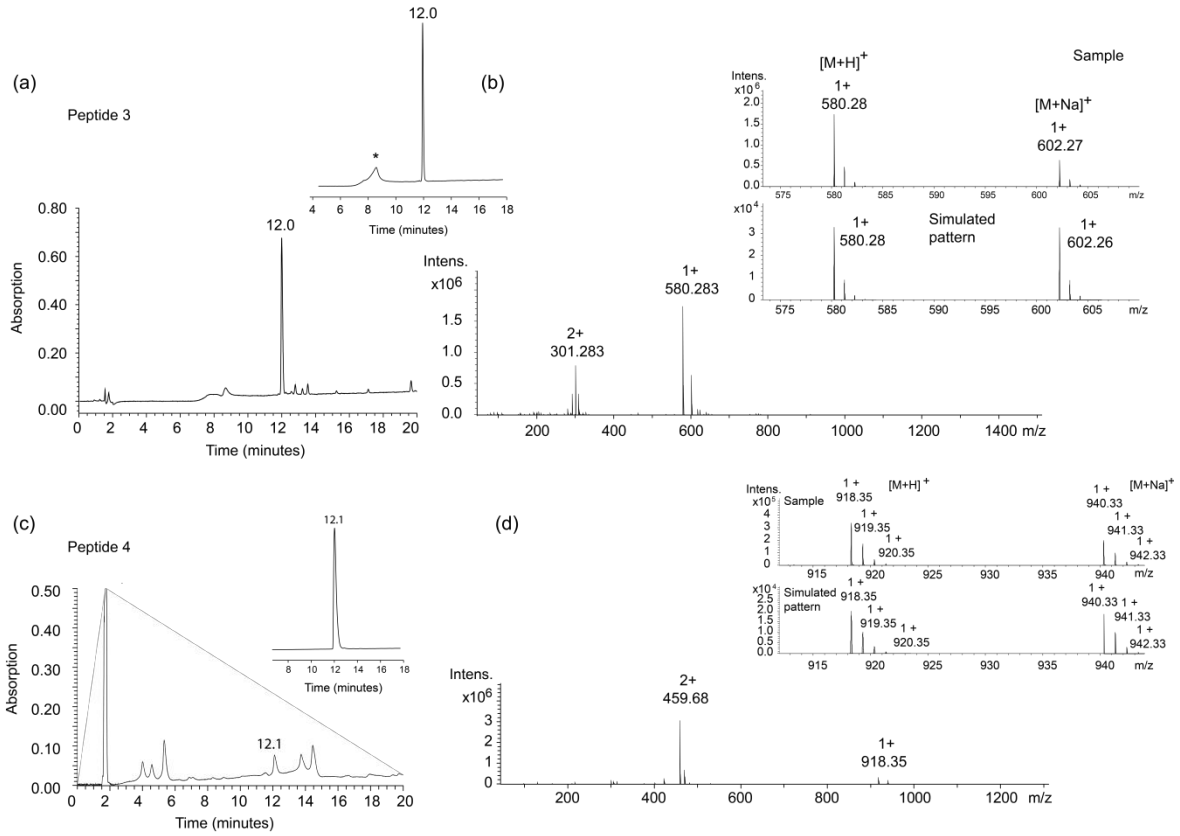

Figure 55. RP-HPLC and ESI MS of peptide 3 and peptide 4

(a) RP-HPLC of the crude product with insert showing purified peptide 3 at a retention time of 12.0 minutes and the respective ESI MS spectra (b) with isotopic pattern of sample and simulated pattern. RP-HPLC conditions: isocratic flow of 5% over 5 minutes followed by a linear gradient 5%- 40% eluent B over 20 minutes total with a flow of 1 ml/min, MultoHigh 100 RP 18 column at 30 °C. *the peak at 8 minutes is generated through a change in pressure changing from the isocratic method to a linear gradient. (c) RP-HPLC of the crude product with insert showing purified peptide 4 at a retention time of 12.1 minutes and the respective ESI MS spectra (d) with isotopic pattern of sample and simulated pattern. RP-HPLC conditions: linear gradient of 5% - 40% eluent B over 20 minutes with a flow of 1 ml/min, Waters® symmetry^{TM} C18

Through the integrated photo-diode array detector, PDA, the correct peak of peptide 4, exhibiting the fluorescent moiety, was readily identified using 214 nm for amide bond absorbance and 494 nm for 5/6-FAM absorbance. The correct mass was confirmed by ESI-MS.

RP-HPLC and ESI MS are implemented and widely used analytical methods but give little information of the actual pureness of the compound. Impurities, especially salts, are usually not visible in both methods but are a major pollutant. It is relevant to determine the actual mass of the peptide for further characterization of the complexation towards heavy metal ions. NMR spectroscopy (see 5.2.4) and amino acid analysis (AAA, see 5.2.3), both coupled to RP-HPLC, were applied.

To determine the content of the ATCUN-like peptides *via* NMR spectroscopy, a concentration-dependent calibration of N-acetyl alanine was used as an external standard. Afterwards, concentration-dependent RP-HPLC chromatograms were recorded using the stock solution of each peptide. The content of peptide 1 was calculated to be 67.7%, peptide 2 to be 73.4% and peptide 3 to be 77.3%. Correct weighing of peptide 4 was not possible due to little product formation. Therefore, NMR spectroscopy measurements were performed without a calculated

concentration. The concentration determined from NMR spectrosocopy and calibration using RP-HPLC for peptide 4 was 0.55 mM for the established stock solution. For RP-HPLC chromatograms and calibrations see Figure 18 - Figure 17.

	Concentration calculated (mM)	Concentration determined via NMR (mM)	Content determined via NMR (%)
Peptide 1	3.78	2.56	67.7
Peptide 2	4.24	3.11	73.4
Peptide 3	3.92	3.03	77.3

Table 30. NMR spectroscopy for content determination

The content of peptide 4 was evaluated using a further method, amino acid analysis with a known concentration of the peptide. The protocol described in 5.2.3 is applied resulting in a final content value of 67%. Interestingly, the evaluated content range between 67% and 77%, meaning that around 30% of the measured weight using an analytical scale, correspond to impurities, especially salts.

8.3. Determination of binding affinity by UV-Vis and fluorescence spectroscopy

8.3.1. pH-dependent binding of metal ions to peptide 1

To determine the optimal pH value for the coordination of copper ions, peptide 1 was used in the following pH titration experiment, which lacks the fluorophore 5/6-FAM, due to the fluorophore absoption interfering with the absorption of the peptide-metal complex (see SI Figure 27). Formation of the complex with a dilavent metal ion, M^{2+}, is illustrated in Figure 56.

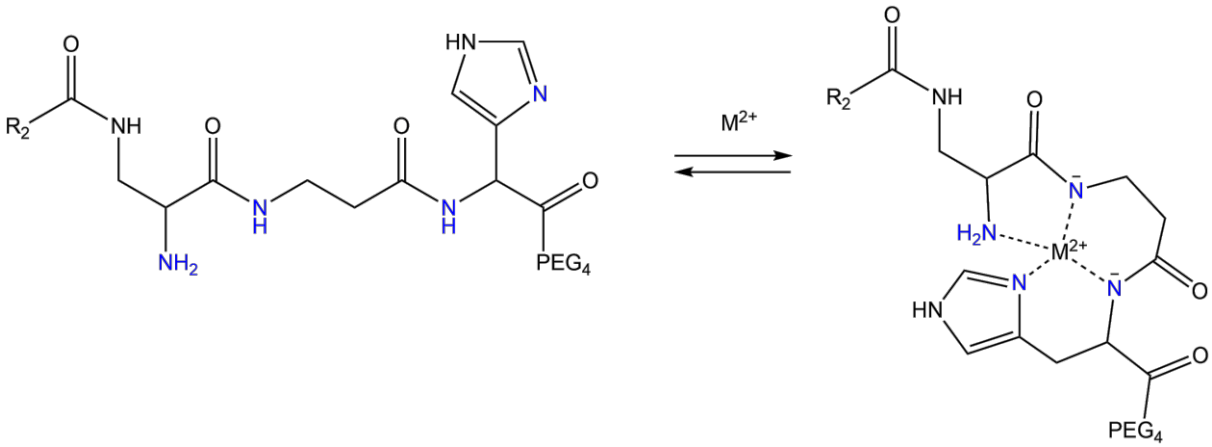

Figure 56. Complex formation

The addition of 1 equivalent of Cu(II) ions and Ni(II) ions to peptide 1 results in an absorption maximum at 550 nm for Cu(II) and 450 nm for Ni(II) seen in Figure 57a.

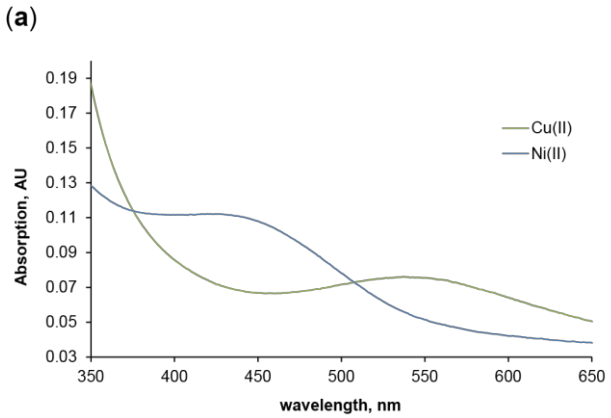

Figure 57. UV VIS spectra of peptide 1 with copper and nickel

(a) shows absorption spectra at optimal pH values and with addition of 1 equivalent heavy metal, Cu(II) and Ni(II); green: addition of 1 equ. Cu(II) to 1 mM peptide 1 in water at pH 8; blue: addition of 1 equ. Ni(II) to 1 mM peptide 1 in water at pH 10.55.

Throughout the titration the pH is steadily increased with the solution containing peptide-Cu(II) and peptide-Ni(II) in one molar equivalent, respectively. Efficient Cu^{2+} binding to peptide 1 occurrs at pH values greater pH 5 rising to a maximum of complex formation at pH 9 indicatd by a plateau (Figure 58a). Looking at the absorption maximum of the spectra at each pH value, we see a shift from λ 800 nm at low pH values, where no adequate coordination can be found, to a stable maximum around λ 550 nm from pH 5.5 on to pH 11 (Figure 58b). A maximum at λ 800 nm and low pH values indicates the existence of an aqua complex.[216] With raising the pH, peptide 1-Cu(II) complex formation enhances thus making a *d-d* transition band at λ 550 nm visible. This is expected giving that ATCUN peptides form a 1:1 square-planar complex with the N_4 donor atom set.[216,217]

Next, pH-dependent Ni(II) binding to peptide 1 is investigated. Form the presented results (Figure 58a) the peptide 1-Ni(II) complex requires pH values to be above pH 7 to see absorption of the complex. Rising steadily, a pH value of > pH 10 is needed to give complete complexation. With an increasing pH the absorption maximum shifts to longer wavelengths (Figure 58b) with a presice turning point at pH 7 from λ 400 to λ 460. This shift is generated from the *d-d* transition band of the square planar peptide-nickel complex.[216]

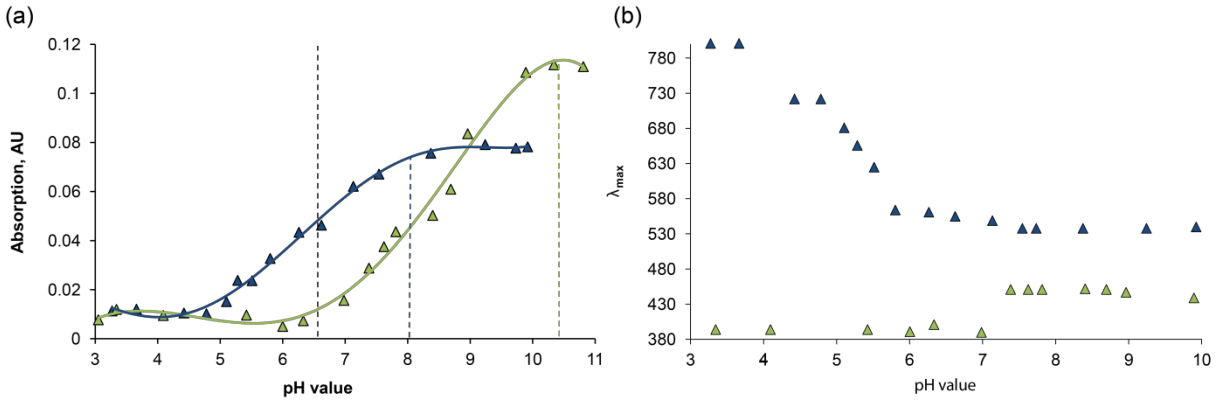

Figure 58. pH dependent Cu(II) and Ni(II) coordination to peptide 1

SI Figure 28 shows the complete spectra of the extracted points presented in SI Figure 28.

Determination of peptide 1-Cu(II) and –Ni(II) binding behavior at 100% complex formation

To further characterize the behavior of peptide 1 towards Cu(II) and Ni(II) ions, the binding constants towards these ions are determined from titration experiments at pH values where the complex is completely formed. They can be evaluated from Figure 58b for the λ_{max} of around 550 nm for peptid 1-Cu(II) and 450 nm peptide 1-Ni(II) according to Neupane *et al.*[216] In Figure 58a these values for 100% complex formation are indicated with dashed lines (blue for Cu^{2+} and green for Ni^{2+}). Due to the MES buffer system not being suitable for the basic conditions, Tris buffer was chosen. It is frequently used for UV-Vis titration experiments in biological sytems and displays a buffer capacity of pH 7.5 – 9.0.[218]

The peptide 1-Cu(II) complex is completly formed at pH values > 8. Therefore, titration experiments were conducted according to 5.2.5.2. With the addition of Cu(II) ions, the absorption at λ_{max} 561 nm rises (SI Figure 11a) and reaches molar extinction coefficients of around 80 $mol^{-1} \times cm^{-1}$. These findings are in good correlation to literature where Neupane *et al.* investigated the 1:1 stoichiometry of linear ATCUN motifs in the range of 530 – 545 nm[216] while Gajda *et al.* determined the square planar complex to be generated at λ 525 nm in the pH range of pH 5-10 for the peptide GGHA.[217]

In Figure 58b, the dominant peptide 1-Ni(II) complex is appointed to wavelengths of around λ 440 nm – 460 nm starting from pH > 7 with complete complex formation at pH values > 10. Therefore, titration experiments were conducted according to 5.2.5.2. With this addition of Ni(II) ions, the absorption at λ_{max} 458 nm rises (SI Figure 12a). Adding more than 1 molar equivalent of Ni(II) ions to the peptide solution results in no further increase in the absoption an the molar extinction coefficient (SI Figure 12b). This behavior can be seen in complexes that are formed in a 1:1 fashion, like the ATCUN complexes are described in literature.[216]

With UV-Vis titration experiments indicating the 1:1 binding behavior, we investigated solutions of peptide1-Cu(II) and –Ni(II) (in PBS buffer pH 7.4) in LC-MS experiments. SI Figure 20 shows peptide 1-Cu(II) binding and SI Figure 24 peptide 1-Ni(II) binding and therefore confirm results from UV-Vis experiments.

Binding behavior of peptide 1 towards Cu(II)/Ni(II) and Zn(II) at pH 6.5

Having in mind the design of a selective copper sensor within a complex system, the pH value can be adjusted to a selective predominant complexation of Cu(II) ions at pH 6.5. This pH is indicated with a black dashed line in Figure 58 and correlates to the pH_{50} value for peptide 1-Cu(II) whereas binding to Ni(II) is insignificant. Therefore, a buffer within that range was selected. MES buffer is listed as a Good's buffer thus displays advantageous characteristics for metal titration experiments. Given its structure, the tertiary amine is sterically hindered and thereby not able to coordinate metal ions (SI Figure 29).[219] With a pKa of 6.15[220] the buffer capacity at pH 6.5 is within a good range.

With a λ_{max} of 551 nm the peptide 1-Cu(II) complex is formed reaching a plateau at an extinction coefficient of 60 $mol^{-1} \times cm^{-1}$. The dominant species at 551 nm is present from pH 5.5 on (see Figure 58b) and can be attributed to the 1:1 square planar complex. Figure 59b shows an approximation to the plateau area at a little over 0.6 equivalents of Cu(II)

added to the peptide 1 solution. With pH 6.5 being slightly over the pH_{50} range, >50 % of possible complexes are formed, verified by these findings.

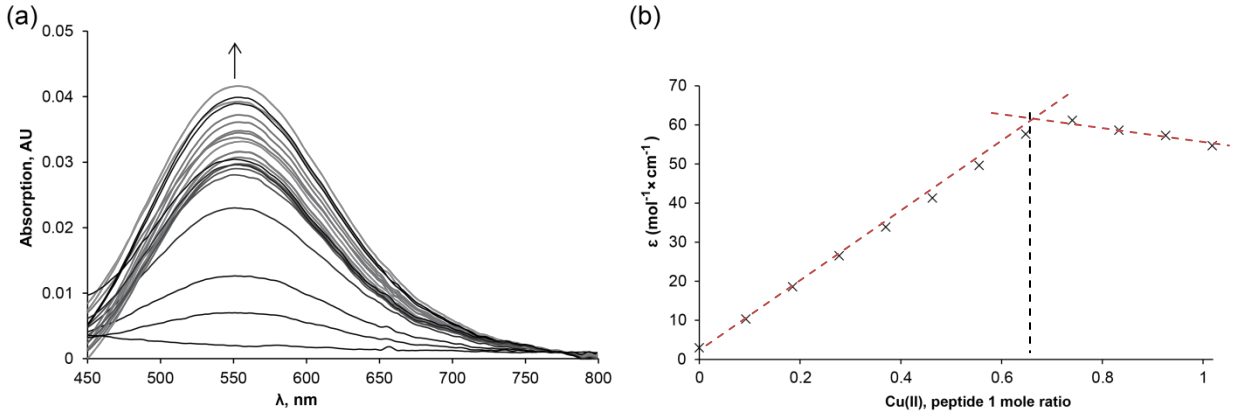

Figure 59. UV VIS titration of Cu(II) to peptide 1 in MES buffer at pH 6.5

UV-VIS titration experiments of peptide 1 (1 mM peptide, in MES buffer pH 6.5). (a) Increase in absorption upon addition of 0.1 equivalents Cu(II) ($CuSO_4$, in water), wavelengths of 450 - 800 nm. (b) Extinction coefficient of the peptide 1-Cu(II) complex vs. equivalents of Cu(II) added.

According to Figure 58 insignificant binding of Ni(II) ions is observed at pH 6.5. Therefore, no saturation in Ni(II) binding can be reached conducting the titration experiment at pH 6.5 with λ_{max} of only 393 nm (SI Figure 13). Adding 20 equivalents of Ni(II) ions to the peptide solution does not result in the ATCUN-like absorption maximum of λ 425 nm – 450 nm determined in literature.[216,217]

Certifying selective Cu(II) binding to peptide 1 at pH 6.5, the binding towards Zn(II) ions was investigated using UV-Vis titration experiments. Figure 60 shows that there is no significant rising of the A_{max} upon addition of increasing Zn(II) concentrations. Figure 60b shows the negligible increase at λ 584. Comparing the rise in absorption values at the λ of complex coordination of peptide 1-Cu(II)/-Ni(II) and -Zn(II), it becomes visible that at pH 6.5 is extremely selective towards Cu(II) in comparison to Ni(II) and that there is no binding of Zn(II) (see Figure 60).

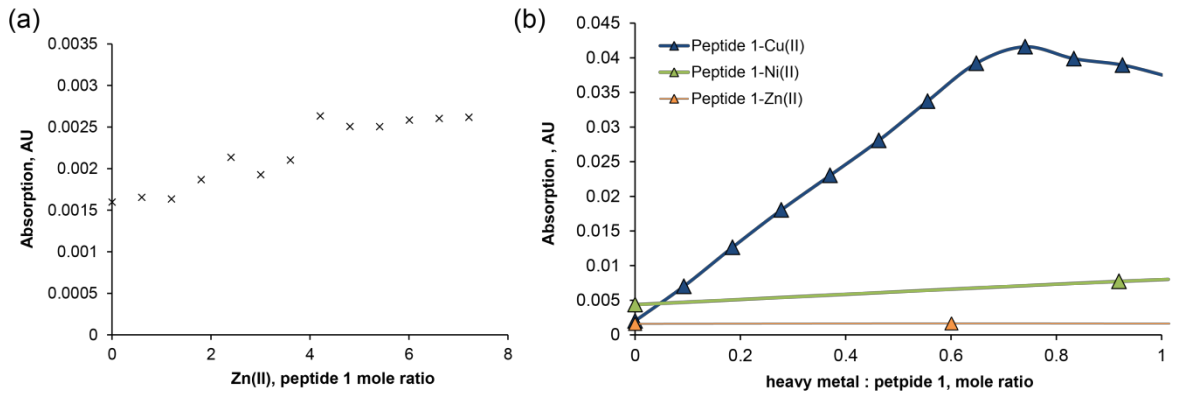

Figure 60. UV-Vis titration of Zn(II) to peptide 1

(a) Change in absorption at λ 584 of peptide 1 solution (1 mM, MES buffer pH 6.5) upon addition of Zn(II) (0.1 M $ZnSO_4$, in water) with (b) comparison of the addition of 1 equivalent Cu(II), Ni(II) and Zn(II) to peptide 1 at pH 6.5

To determine the binding behavior from UV-Vis experiments, binding constants are calculated using the Benesi Hildebrand plot according to Tietze *et al.*[221]

First, binding constants at pH 6.5 illustrate the insufficient binding towards Ni(II) with a logK(Ni) of 2.76. With the logK(Cu) being at 6.57, selective binding towards Cu(II) is verified and comparable to other ATCUN based Cu(II)-sensor systems.[222] Kulprachakarn et al. investigated Cu(II) binding to Hepcidin (Asp-Thr-His) to be logK = 7.7 showing a similar result.

Comparing the findings to the titration data at pH 6.5, we see a significant rise in binding constants for the peptide 1-Ni(II) complex from K = 5.8×10^2 l × mol^{-1} to 2.5×10^7 l × mol^{-1} at pH 8. Furthermore, the λ_{max} 458 at pH 10.55 indicates the ATCUN-like complex formation. For peptide 1-Cu(II) binding, no improvement in binding was evaluated with binding constants being within the same range of 3.8×10^6 l × mol^{-1} at pH 6.5 and 9.8×10^5 l × mol^{-1} at pH 8. These findings indicate that the buffer system affects binding constants.[223] Therfore, UV-Vis titration experiments for calculation of the binding constants for and characterization of peptide 2 and 3-Cu(II)/-Ni(II) complexes were conducted in Tris buffer.

Species	Heavy metal	pH	K (l × M^{-1})	logK	$\Lambda_{max,\ buffer}$
Peptide 1	Cu(II)	6.5	3.8×10^6	6.57	551
	Ni(II)	6.5	5.8×10^2	2.76	393
Peptide 1	Cu(II)	8.0	9.8×10^5	5.99	561
	Ni(II)	10.55	2.5×10^7	7.39	458
Peptide 2	Cu(II)	10.55	1.7×10^5	5.23	501
	Ni(II)	10.55	3.1×10^5	5.50	436
Peptide 3	Cu(II)	8.0	1.2×10^5	5.08	584
	Ni(II)	10.55	1.3×10^5	5.12	441

Table 31. Binding constants for peptide 1 – 4-Cu(II) and –Ni(II) complexes

8.3.2. pH-dependent binding of metal ions to non-His containing peptides 2 and 3

The presented binding constants of the non-His containing peptides 2 and 3, show that there is a efficient Cu(II) and Ni(II) binding that is comparable to the His-containing ATCUN motif peptide 1. The ATCUN motif is composed of the Xaa-Xbb-His sequence (Xaa and Xbb = variable amino acid) and, as stated in literature, His in the third position, is mandatory for the motif and the resulting 1:1 square planar complex formed with Cu(II) and Ni(II) ions.[12] Neupane *et al.* investigated the behavior of ATCUN mutants lacking this motif coming to the conclusion, that when converting His to Asp or when stabilizing the peptide structure through macrocyclizaiton, ATCUN-like complexes are formed even with His being absent.[224]

pH-dependent binding of metal ions to peptide 2 and 4

Figure 61 shows all obtained pH dependent titration experiment data, including peptide 1 for comparison of determined values. The addition of Cu(II) ions to peptide 2 and peptide 3

results in the generation of a λ_{max} of 504 for peptide 2-Cu(II) with a pH value of pH > 10 for optimal complex formation and λ_{max} of 563 for peptide 3-Cu(II) with a pH value of 8 for optimal complex formation. Comparing the values to peptide 1, the 1:1 square planar ATCUN-like complex of peptide 1-Cu(II) is formed exhibiting a λ_{max} of 537 with optimal complex formation at pH 8. Comparing titration curve progressions, peptide 3 and peptide 1 show comparable behavior towards complex formation at the corresponing pH values while peptide 2 shows different behavior displaying a very gradual formation of the complex (Figure 61a).

All three peptides display a shift from the Cu(II) aqua complex at 800 nm to the peptide-Cu(II) complex through a *d-d* transition. Peptide 2, again, shows a different behavior, exhibiting two absorption maxima at λ_{max} of 625 from pH 5 – 7.5 and a shift to a λ_{max} of 492 with further increasing of the pH. While peptide 1, the original ATCUN motif, uses the imidazole moiety of the histidine as the side chain ligand, peptide 3 uses the carboxyl group, both resulting in the formation of the ATCUN-like complex.[216] Peptide 2, exhibiting only an Alanine, must use an additional backbone amide to form the 1:1 square planar complex. The absorption maximum at λ_{max} of 625, which represents a second absorption maximum of peptide 2 can, most likely, be appionted to a different protonation state (Figure 61b).

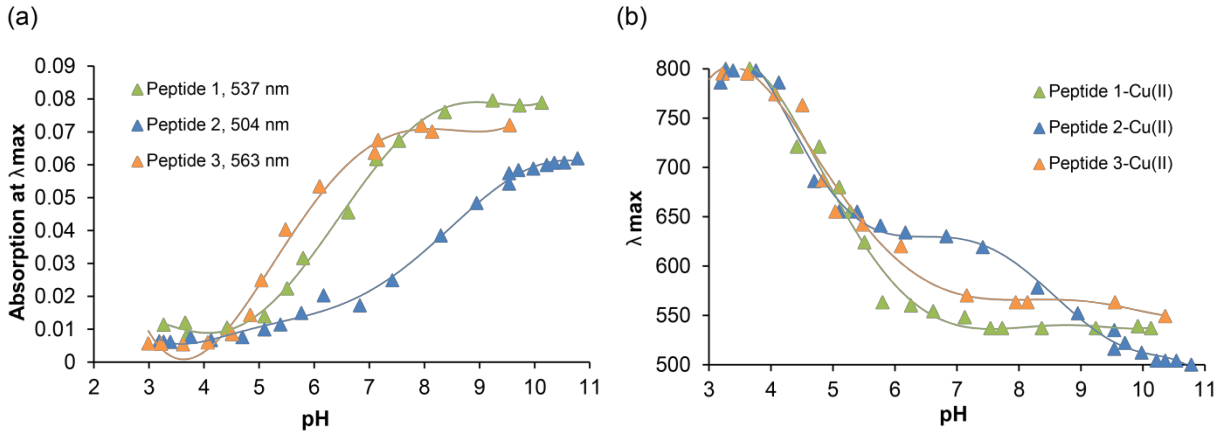

Figure 61. UV-Vis pH studies of peptide 1 – 3-Cu(II) complexes

Behavior of peptides 1 – 3 (1 mM peptide 1, 2 mM peptides 2 and 3) using 1 equ. of Cu(II) ($CuSO_4$, in water) towards different pH values in regard to complex formation

Towards Ni(II), all peptides show similar behavior with peptide –Ni(II) complex formation at pH values > 10 (Figure 62a). In regard to complex formation, similar λ_{max} are determined from pH titration experiments. Peptide 1-Ni(II) shows λ_{max} at 438 nm, peptide 2-Ni(II) an λ_{max} at 455 nm and peptide 3-Ni(II) at λ_{max} at 440. As stated in 8.3, a λ between 425 nm – 450 nm is determined for ATCUN-Ni(II) complexes in literature.[216,217] Therefore, Ni(II)-coordination is most likely formed on basis of ATCUN-like complex formation for all three peptides, peptide 1-3. Identical binding behavior was found by Neupane *et al.* describing a discrete, two-state transition form a Ni(II)-aqua complex to a species exhibiting *d-d* transition bands at 440 nm. Additionaly, they evaluated no evidence for multiple species at any investigated pH value for the ATCUN mutants GGCL and GGML.[224]

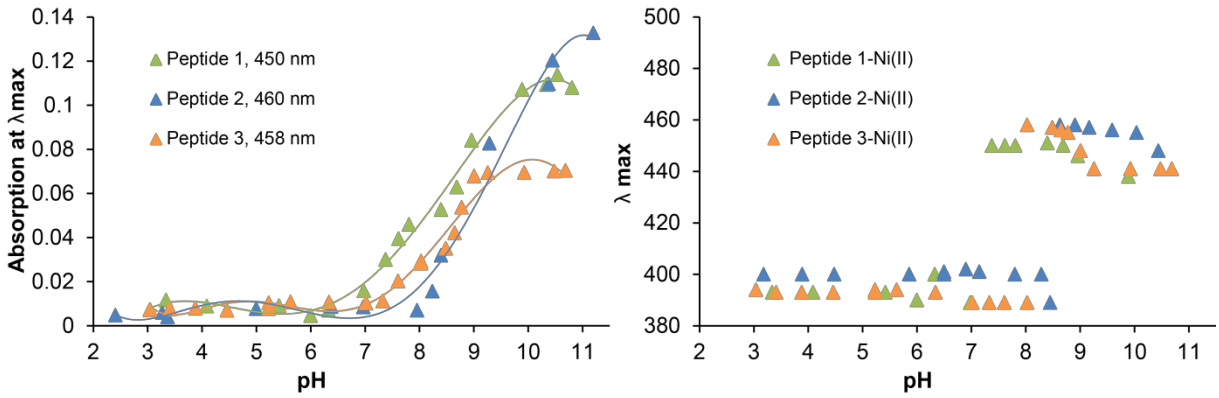

Figure 62 UV-Vis pH studies of peptides 1 – 3-Ni(II) complexes

Behavior of peptides 1 – 3 (1 mM peptide 1, 2 mM peptides 2 and 3) using 1 equ. of Ni(II) ($NiSO_4$, in water) towards different pH values in regard to complex formation

In a comparative study, Appleton *et al.* investigated binding of Cu(II) to HSA and dog serum albumin, DSA. DSA does not exhibit the ATCUN motif with a N-terminal sequence of Glu-Ala-Tyr and thus binds Cu(II) in a different manner. They evaluated the Cu(II) binding to the ATCUN motif in a 1:1 square planar fashion to be at around 525 nm from pH values of 6.5 on.[225] Looking at Figure 61b we can see that peptide 1 and peptide 3 fulfills these requirements showing a rapid blue shift from the aqua complex at λ 800 nm to λ 525 nm at pH values of around pH 6. Peptide 2 shows the blue shift at higher pH values around pH 9 and thus can be compared to the finding of Appleton *et al.* with DSA, where a shift to around 515 nm is only reached at pH values of pH 10 while below this pH the λ_{max} oscillated around 640 nm.[225]

Determination of peptide 2 and 3-Cu(II) and –Ni(II) binding behavior at 100% complex formation

To evaluate binding constants, UV-Vis titration experiments are performed according to peptide 1 using pH values which show efficient complex coordination identified from Figure 61b for Cu(II) binding and Figure 62b for Ni(II) binding.

The addition of Cu(II) to peptide 2 leads to an increase in the absorption at a λ_{max} of 501 nm at pH 10.55 (SI Figure 16) and Ni(II) to an increase in the absorption at a λ_{max} of 436 nm at pH 10.55 (SI Figure 18).

Peptide 3-Cu(II) complex formation is indicated by the increase of the absorption at a λ_{max} of 584 nm (SI Figure 17) and binding towards Ni(II) is seen with an increase of the absorption at λ_{max} of 441 nm (SI Figure 19).

In addition, MALDI-TOF MS of the peptide 2 and 3-Cu(II) and –Ni(II) complexes was performed, to emphasize the findings from UV-Vis titration experiments. The 1:1 binding of peptide 2-Cu(II) and peptide 3-Cu(II) can be found in SI Figure 21, SI Figure 22. Ionization of the peptide 3-Ni(II) displayed a challenge. While Peptide 2-Ni(II) was found (SI Figure 25) with extreme low intensities, ionization of peptide 3-Ni(II) complex was challenging not resulting in a significant spectra.

Binding constants were calculated using the Benesi-Hildebrand method and are summarized in Table 31. All non-His containing complexes, peptide 2-Cu(II) and –Ni(II) as well as peptide 3-Cu(II) and Ni(II) show similar binding constants within the range of $K = 1.2 \times 10^5 – 3.1 \times 10^5$ l × M^{-1}. Comparing all binding constants of peptides 1-3 at the pH values for complete

complex formation, we can identify a preference towards Ni(II)-binding, especially pronounced for peptide 1-Ni(II) binding with a logK(Ni) of 7.39 compared to logK(Cu) 5.99.

8.3.3. pH-dependent binding of metal ions to peptide 4

To visualize the binding event, we integrated a fluorescent moiety into the structure of peptide 1. 5/6-FAM is coupled at the N-terminus, R_2 (Figure 53) leading to synthesis of peptide 4. Torrado *et al.* were one of the first to integrate a fluorescent moiety, 5-(dimethylamino)naphthalene-1-sulfonamide (Dns) into an ATCUN motif and determined fluorescence quenching of 93% for Cu(II) and 65% for Ni(II) ions.[99] Fluoresence quenching is a process that decreases the fluorescence intensity of a fluorophore with addition of a quencher due to molecular interactions.[226] Two types of quenching are possible: dynamic and static quenching. While dynamic quenching is caused by a molecular collision, static quenching results from the forming of a non-fluorescent complex with addition of the quencer.[227] To observe formation of peptide 4-Cu(II) and peptide 4-Ni(II) complex, quenching of fluorescence of the 5/6-FAM unit through heavy-metal ion addition is monitored (see Figure 63).

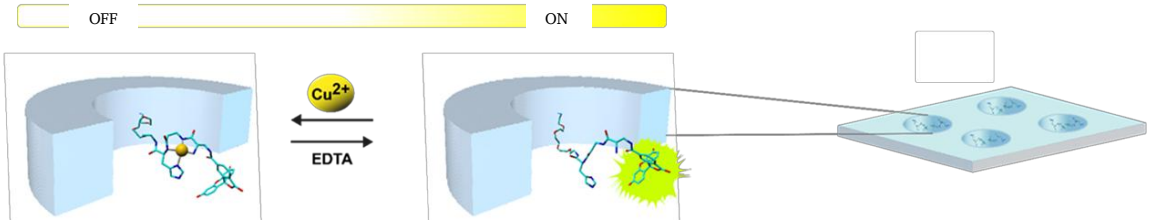

Figure 63.Quenching of fluorescence of peptide 4

Literature data describes excitation of 5/6-FAM to be at λ 494 nm and emission at 519 nm.[228] We evaluated the optimal emission and excitation to be λ_{ex} 494 and emission λ_{em} 518 nm (Figure 64) with no interference of the MES buffer system (SI Figure 30).

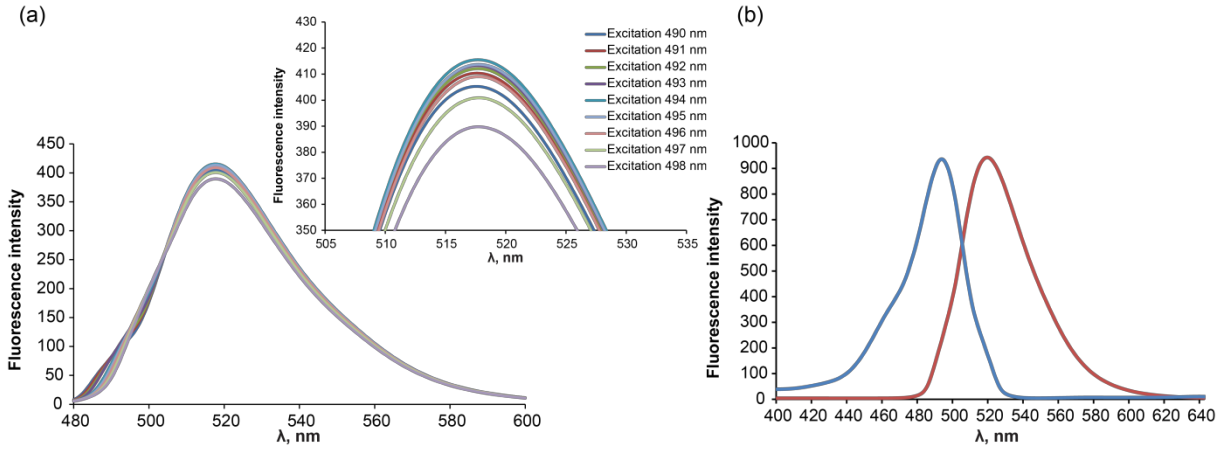

Figure 64. Determination of excitation and emission wavelength

(**a**) Peptide 4 (1 µM in MES buffer pH 6.5) fluorescence spectra showing emission resulting from different excitation wavelengths (490 – 498 nm) with insert showing magnification. (**b**) Emission and excitation at λ_{Em} 518 and λ_{Ex} 494 nm.

Additionaly, to ensure the non-binding behavior of the fluoresceine unit itself, it was subjected to titration experiments with Cu(II). As seen in SI Figure 31, even after addition of 40 equivalents of Cu(II) ions to the 5/6-FAM solution, no difference in the spectrum can be determined. This titration confirmes no binding of Cu^{2+} to the fluorophore. After determination of the experiment set-up, fluorescence quenching of peptide 4-Cu(II) and peptide 4-Ni(II) complexes was investigated with fluorescence titration.

Determination of binding behavior of peptide 4-Cu(II) and -Ni(II) at 100% complex formation

Analogous to the UV-VIS studies, investigation of the optimal pH was conducted. Peptide 4-Cu(II) binding is investigated at pH 8 in PBS buffer. Tris buffer was not feasible due to high absorption of the buffer itself during fluorescence titration experiments. The formation of the peptide 4-Cu(II) complex is indicated by decrease of fluorescence intensity of λ_{max} 518 nm from 963 to 95 using 1.5 equivalents of Cu(II) ions (SI Figure 32). This represents a final quenching of 90%. Compared to findings from pH 6.5 (88% quenching with addition of 20 equivalents Cu^{2+}), pH 8 is superior due to less molar equivalents of Cu(II) needed to quench around 90% of fluorescence.

The Good's buffer CAPS was chosen for pH 10.55 measurements, displaying the least interference with the absorption spectra of buffers tested. Peptide 4-Ni(II) complex formation is indicated by the decrease of fluorescence intensity at λ_{max} 518 nm from 997 to 261 with a final quenching of 76% (SI Figure 33). After addition of 0.9 equivalent of Ni(II) ions, a plateau is reached. This behavior was also evaluated during UV-Vis titration experiments at pH 10.55 with peptide 1-Ni(II) and described with the formation of the 1:1 peptide-Ni(II) complex.

Determination of binding behavior of peptide 4- Cu(II), -Zn(II) and Ni(II) at pH 6.5

In correspondence to the investigation of peptide 1-Cu(II) and Ni(II) binding at pH 6.5 experiments towards peptide 4 were undertaken at this pH regarding the sensor application. Upon addition of Cu(II) ions, quenching of fluorescence from fluorescence intensities of 920 at λ_{max} 518 nm to intensities of 114 after addition of 20 equivalents of Cu(II) is investigated. This represents a quenching of 88% in total. The change influorescence intensity ΔF (F_0-F) comes to a plateau beginning at >10 equivalents Cu(II) added(Figure 65a-b). Furthermore, addition of more than 20 equivalents of Cu^{2+} does not result in a significant change of the fluorescence intensity. These findings can be compared to literature where Pearce *et al.* determined a 40% quenching caused by ten equivalents of Cu(II) to an ATCUN motif, Dap(LR)-Asp-His-Dap(DE)-Ser-Ser-$CONH_2$ containing a rhodamine (LR) and coumarin (DE) fluorophores (in 50 mM HEPES buffer pH 7.0).[209]

The behavior towards Ni(II) ions was investigated accordingly. The formation of the peptide 4-Ni(II) complex results in quenching with an decrease of fluorescence intensities at λ_{max} 518 nm from 894 to 509 after addition of 1360 equivalents of Ni(II) ions representing a total quenching of 43%. Futher addition of Ni^{2+} does not result in a significant decrease of fluorescence intensities (Figure 65c-d).

Comparing these values to Cu(II) binding and the generation of peptide 4-Cu(II) complex, 43% quenching is reached with addition of only 6 equivalents of Cu^{2+}. These findings affirm

findings from titration studies. The pH value of 6.5 is not suited for Ni(II) coordination while Cu(II)-binding is selective and sensitive.

Additionally, binding of another bivalent heavy metal was investigated. The addition of 73 equivalents of Zn(II) to peptide 4 results in a decrease of fluorescence intensity of 4% and can therefore be neglected (Figure 65e-f).

The negligible binding of Zn(II) to peptide 4 can be compared to peptide 1-Zn(II) binding (5.2.5.2).

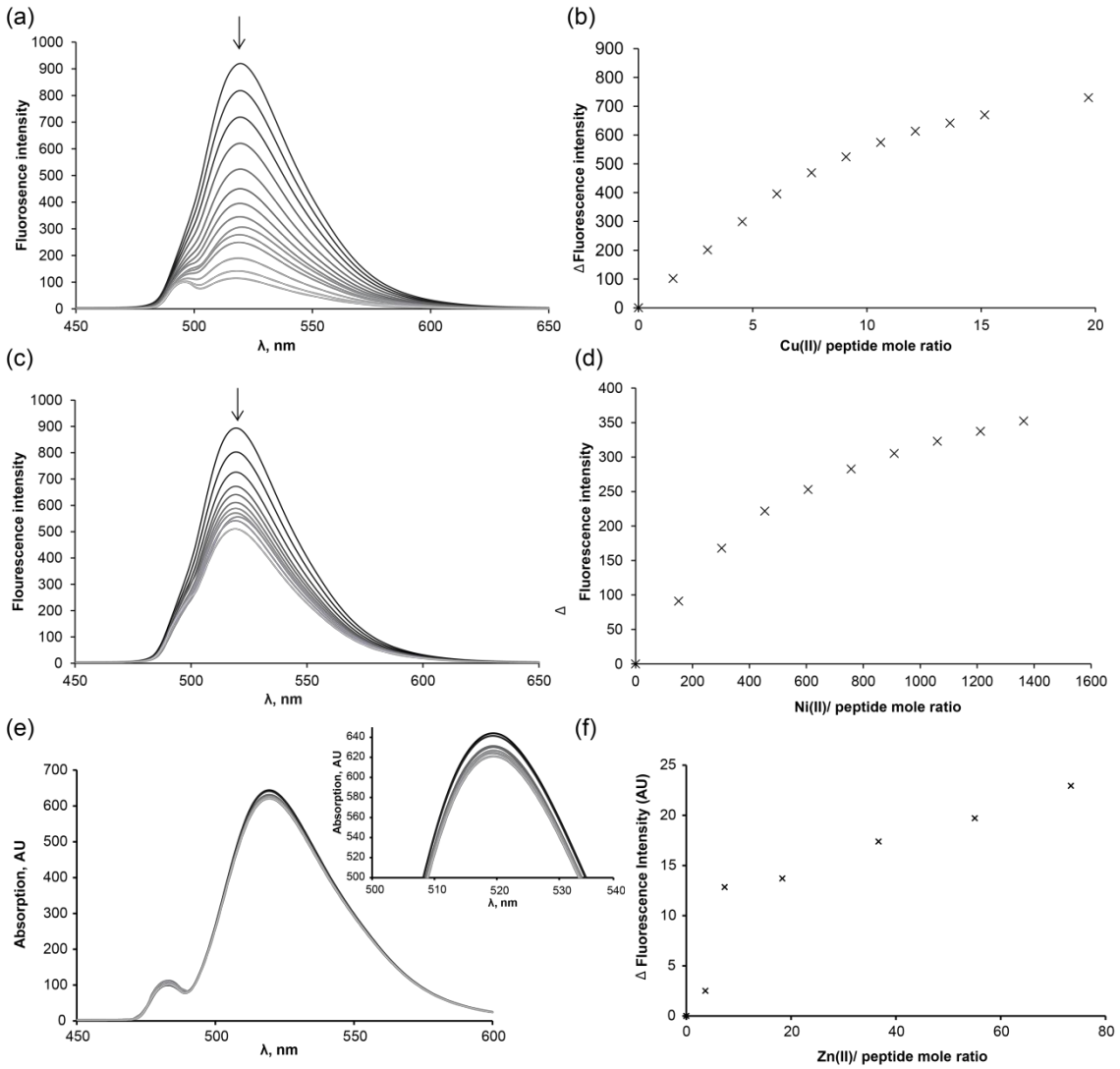

Figure 65. Fluorescence titration of Cu(II) to peptide 4 in MES buffer pH 6.5

Fluorescence titration experiment of peptide 4 (1 µM, in MES buffer pH 6.5). (a) decrease of fluorescence intensity upon the addition of Cu(II) to the peptide solution (b) change in fluorescence intensity vs. Cu(II) equivalents added to the peptide solution (c) decrease in fluorescence intensity upon the addition of Ni(II) to the peptide solution (d) change in fluorescence intensity vs. Ni(II) equivalents added to the peptide solution. (e) insignificant decrease in fluorescence intensity upon addition of Zn(II) to the peptide solution (f) change in fluorescence intensity vs. Zn(II) equivalents added to the peptide solution.

From obtained fluorescence quenching data the binding constants and quenching behavior are determined using the Stern-Volmer plot (see 5.2.8) according to to Li *et al.*[229]. In literature, the property of Cu(II) or Ni(II) ions to quench the fluorescence signal upon binding can be

described as a static quenching process due to formation of a non-fluorescent complex.[226] SI Figure 34 shows plotting of peptide 4-Cu(II) and SI Figure 35 the Ni(II) data.

To evaluate a 1:1 binding, LC-MS experiments were conducted, verifying this binding behavior (SI Figure 23 and SI Figure 26).

Due to the demonstrated applicability of pH 6.5 to selectively bind Cu(II), the limit of detection (LOD) towards Cu(II) and Ni(II) was determined using fluorescence titration experiments. The limit of detection, LOD, is a value that gives information on the lowest point at which the used analytical approach is feasible while the limit of quantitation, LOQ describes a value at which the measurement works with high confidence.[230] For our sensor system, both values, the LOD and LOQ, are determined to characterize the sensibility and selectivity. Therefore, mearusements are conducted in MES buffer pH 6.5 following the protocol described in 5.2.9. The LOD for peptide 4-Cu(II) is calculated to be 13.5 nM and for peptide 4-Ni(II) 0.23 μM. Changing the value 3.3 in Equation 11 to the value 10 will result in the calculation of the LOQ which is 40.91 nM for peptide 4-Cu(II) and 0.71 μM for peptide 4-Ni(II). These values show extreme sensitivity towards Cu(II) with less sensitivity towards Ni(II).

The Stern-Volmer plots were applied for determination of quenching rates and binding constants of peptide 4-Cu(II) and peptide 4-Ni(II) and can be found in the supporting information (SI Figure 36 and SI Figure 37). Table 32 displays the calculated values.

Comparing values of peptide 4-Cu(II) and peptide 4-Cu(II) fluorescence titration experiments at pH 6.5 and pH 8.0 has to be done carefully due to different buffer systems used. It can be determined that there is a significant increase in the logK values towards Cu(II) as well as Ni(II) for peptide 4-Cu(II) at pH 6.5 from logK 6.8 to 9.3 and for peptide 4-Ni(II) from logK 3.26 to 11.79. Haas *et al.* investigated copper transport proteins (Ctr, ATCUN sequence Met-Asp-His) and mutants to exhibit binding constants towards Cu(II) of logK 11.0 +/- 0.3.[231] Studies of Neupane *et al.* reassure the determined binding constans. They evaluated binding constants to exhibit values of at least 10^8 $M^{-1.224}$

The calculated binding constant and logK for the coordination of peptide 4-Ni(II) at pH 6.5 are in concordance to UV-Vis titration data of peptide 1-Ni(II). The pH is not suited for formation of the Ni-complex, therefore binding constants are extremely low with peptide 4-Ni(II) logK 3.26 and peptide 1-Ni(II) logK 2.76. Looking at peptide 4-Cu(II) binding, a binding constant with the value of 6.27×10^6 $l \times M^{-1}$ is comparable to chemosensor presented by Zheng *et al.* They introduced a dansylated Gly-Gly-His-Gly ATCUN motif with a binding constant towards Cu(II) of $K = 3.8 \times 10^6$ $l \times M^{-1}$ in phosphate buffer at pH 6.8.[232] Due to the pH dependency of heavy metal coordination, a pH of 6.5 can be used to guarantee only efficient Cu(II) binding with negligible Ni(II) binding which shows a successful implementation of the idea to generate a selective Cu(II) sensor. Furhtermore, the quenching constant of K_q of 10^{13} $M^{-1}s^{-1}$ indicates a static quenching process, as assumed (5.2.8). The quenching constants for static quenching are comparable to those reported by Crouse *et al.* with K_q for BSA-Ni(II) and BSA-Cu(II) complexes to be within the range of 10^{12} and 10^{13} M^{-1} s^{-1}.[233] The maximum possible quenching behavior is investigated analogous to UV-Vis titration experiments increasing the pH to optimal complex formation.

	Cu(II)				Ni(II)			
	K_q ($M^{-1}s^{-1}$)	K ($l \times M^{-1}$)	logK	pH	K_q ($M^{-1}s^{-1}$)	K ($l \times M^{-1}$)	logK	pH
Peptide 4	2.75×10^{13}	6.27×10^{6}	6.80	6.5	4.9×10^{10}	1.8×10^{3}	3.26	6.5
	5.28×10^{16}	2.06×10^{9}	9.3	8.0	1.19×10^{20}	6.1×10^{11}	11.79	10.55

Table 32. Binding constants of peptide 4 towards Cu(II) and Ni(II)

In general, Ni(II)-binding is determined to be more favorable when investigating optimal pH values for complex formation with logK(Ni) 7.40 > logK(Cu) 5.99 for peptide 1 and logK(Ni) 11.79 > logK(Cu) 9.3 for peptide 4 as well as for the non-His containing mutants.

Torrado *et al.* explain preferred Cu(II) binding through modification of the peptide backbone with changing the sequence from Baa(Dns)-Gly-His-Ser-Ser to Baa(Dns)-β-Ala-His-Ser-Ser (Baa – L-β-aminoalanine)[99] and describe this replacement to generate a highly selective chemosensor for Cu(II).[209] Our sequence, (5/6)FAM-DAP-β-Ala-His-$mPEG_4$ (peptide 4) and (5/6)FAM-DAP-β-Ala-His-$mPEG_4$ (peptide 1) was inspired by their work due to the aim of the generation of a Cu(II) selective sensor. Looking at our results, the preference for Cu(II) can only be obtained from tuning the pH not from the sequence itself. All structures, peptides 1-4 show preference for Ni(II) ions, not for Cu(II).

8.4. Generation of hybrid nanopores

After complete characterization of the fluorescently labelled peptide 4 towards Cu(II), Ni(II) and Zn(II) at different pH values and in regard to detection limits, immobilization of the peptide to the nanopore containing polymer foil are performed. Therefore, polyethylene terephthalate, PET, foils were track-etched to reveal conically shaped nanopores according to 5.3.1. To control successful track-etching, high-resolution field-emission scanning electron Microscopy, HR-FT-SEM, is performed. Figure 66 shows images of a track-etched PET foil with a pore density of 10^7 pores / cm^2 and a pore diameter of around 200 nm at the base from two different angles. While in Figure 66a and b, a top view shows different magnifications of the same pores, Figure 66c shows a cross section of the pore geometry. The protocol for generation of a cross section is described in 5.3.1.

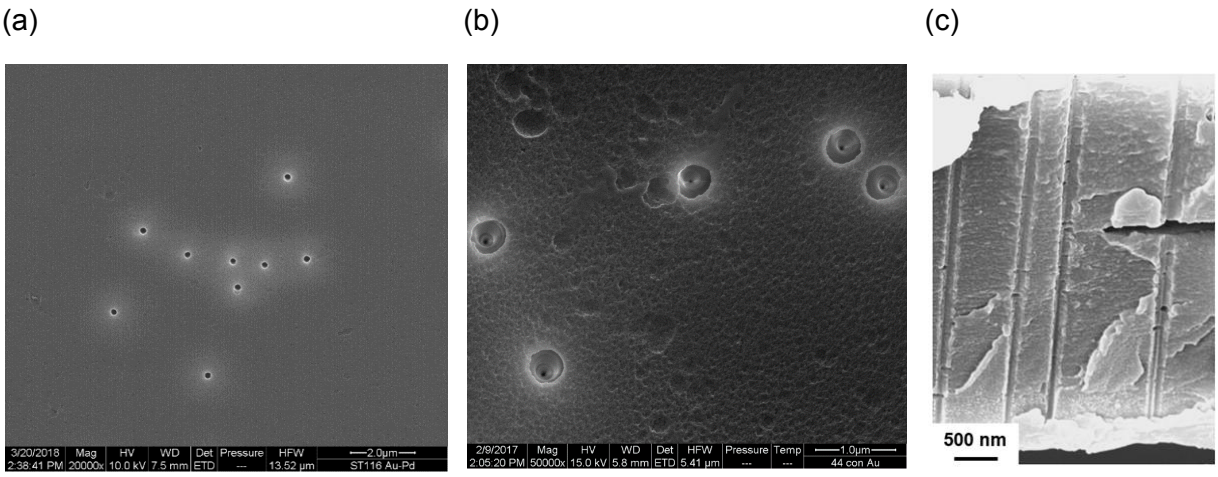

Figure 66. HR-FT-SEM images of conically shaped track-etched nanopores in PET foils

(a) Top view of nanopores with a magnification of 20000 × (b) of 50000 × (c) shows a cross section of conically shaped nanopores. Fluence 10^7 pores per cm^2. Images were kindly provided by Ivana Duznovic.

In order to immobilize peptide 4, two methods of immobilization were tested. A widely used method, intensively described in literature, is the coupling using EDC/NHS herein performed according to 5.3.2. Additionaly, we tested an immobilization method using HATU and DIEA. For both methods the existence of a primary amine and a carboxylic group containing part is essential. The designed peptides, peptide 1 – 4, all exhibit a linker, the PEG-unit, that is integrated into the peptide sequence for the immobilization at the C-terminus of the peptide. The solid state material, in our case the PET foil, needs to display primary amines (see Figure 21). No difference between the performance of hybrid foils generated by either method emerged. Therefore, the HATU/DIEA is chosen as the standard protocol since it does not require pre-activation that is needed for the EDC/NHS preparation. SI Figure 39 shows a PET foil with immobilized peptide 4 from the EDC/NHS protocol.

Characterization of hybrid nanopores through Atomic Force Microscopy

Atomic force microscopy can be applied for high resolution imaging within fractions of nanometers and was therefore chosen to investigate the hybrid nanopores. Amplitude modulation atomic force microscopy (AM-AFM) is also known as tapping-mode AFM. A stiff microlever is excited to (or near) the free resonance frequency and the oscillation amplitude used for measurement of topography or phase differences in the sample surface.[234] Figure 67 shows results from AFM measurements of a pore with immobilized peptide 4 (Figure 67c and d) and a track-etched blank pore (Figure 67a and b). Images of the topography (Figure 67a and c) of the hybrid and blank foil are comparable while images of phase difference (Figure 67 b and d) show differing behavior. While the phase difference of the pore from the blank foil does not show a change of material, in Figure 67d a significant white circular structure characterizes the image. This circular region represents the pore opening as seen in the topography image (Figure 67c). The white color in the phase difference image illustrates areas of soft material and therefore represent the peptide that is bound to the nanopore.

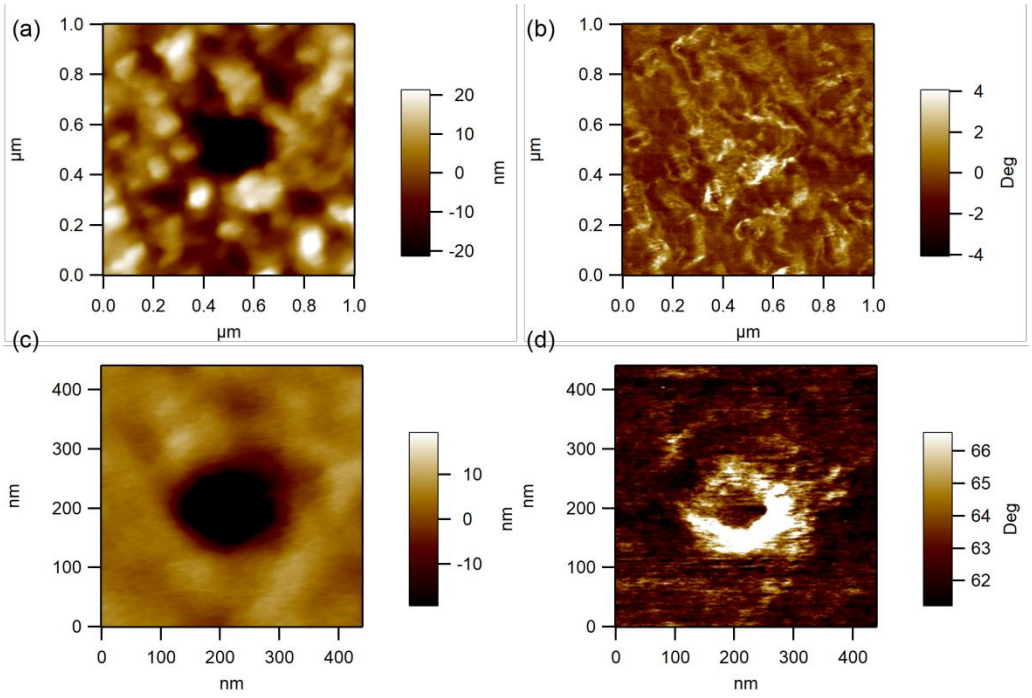

Figure 67. AFM of peptide 4 immobilized to conically shaped nanopores

The top pictures (a) and (b) represent a blank nanopore, no peptide 2oupled to the surface whereas (c) and (d) show a pore with peptide 4 coupled. (a) and (c) show the topography of the foils surface and (b) and (d) show the change in phase differences. Images generated by Dr. Christian Dietz (TU Darmstadt)

8.4.1. Confocal laser scanning microscopy (CLSM)

The integration of the fluorescent moiety enables visualization of the hybrid nanopores and the investigation of the behavior towards heavy metal ions. First, the success of covalent binding to the peptide to the nanopores was investigated using CLSM with Wadim Weber (RG Prof. Stein, TU Darmstadt)

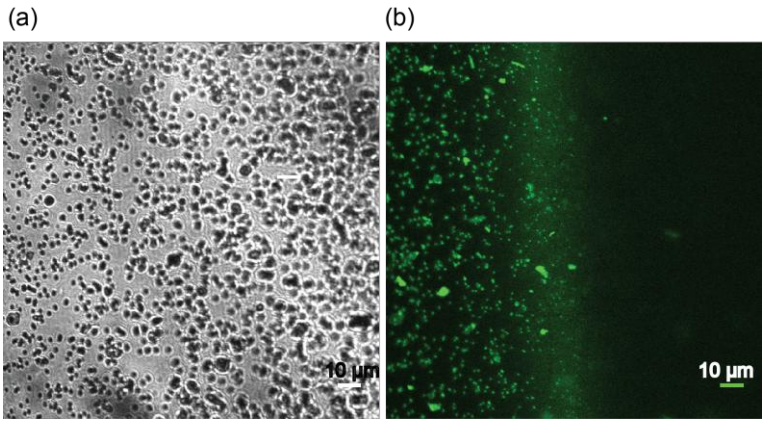

Figure 68. CLSM of etched area

Figure 68 shows the brightlight and fluorescence image of the functionalized PET foil. Here, the functionalized part is indiacted by green fluorescent spots generated from peptide 4 coupled to the nanopores, whereas the unfunctionalized zone does not show any fluorescence (Figure 68b) but pores (Figure 68a).

This appearance is influenced by the so-called “etching zone”. Only within this area, etching with NaOH is conducted (5.3.1) thus only this area exhibits primary amine groups which are needed for immobilization of peptide 4. After multiple washing steps with water, no leaking of the material was detected, again, indicating covalent binding.

Overlaying the brightlight image (Figure 69a) with the fluorescence image (Figure 69b) and visualizing the fluorescent areas with green results in Figure 69c. This image shows the successful immobilization with the green spots indicating peptide 4 coupled to pores of the PET foil.

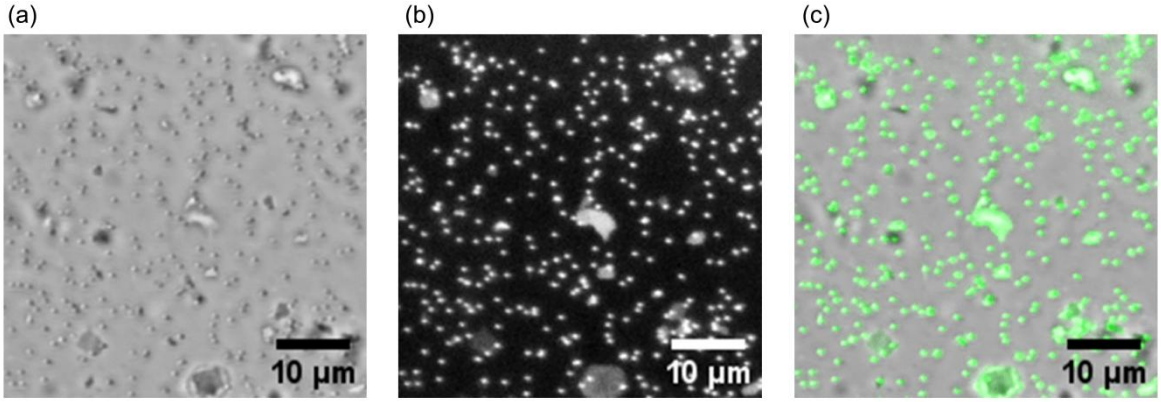

Figure 69. Brightlight, fluorescence and overlay

PET foil with conically shaped nanopores with an opening of 300 nm and a tip size of 5 nm under CLSM with an emission at 488 nm and excitation between 515 – 530 nm

The quenching of the fluorescence from immobilized peptide 4 with the addition of Cu(II) is investigated. Therefore, a $CuSO_4$ solution is added to the fixated hybrid foil leading to a visible decrease in fluorescence intensity. With the addition of EDTA, the fluorescence is restored. After washing, the cycle can be repeated. Seven on/off circles are presented in Figure 70. Fluorescence intensities are displayed in the bar chart showing the decrease and increase of signal from the pore according to Cu(II) or EDTA addition in comparison to a reference point that is not influenced by quenching.

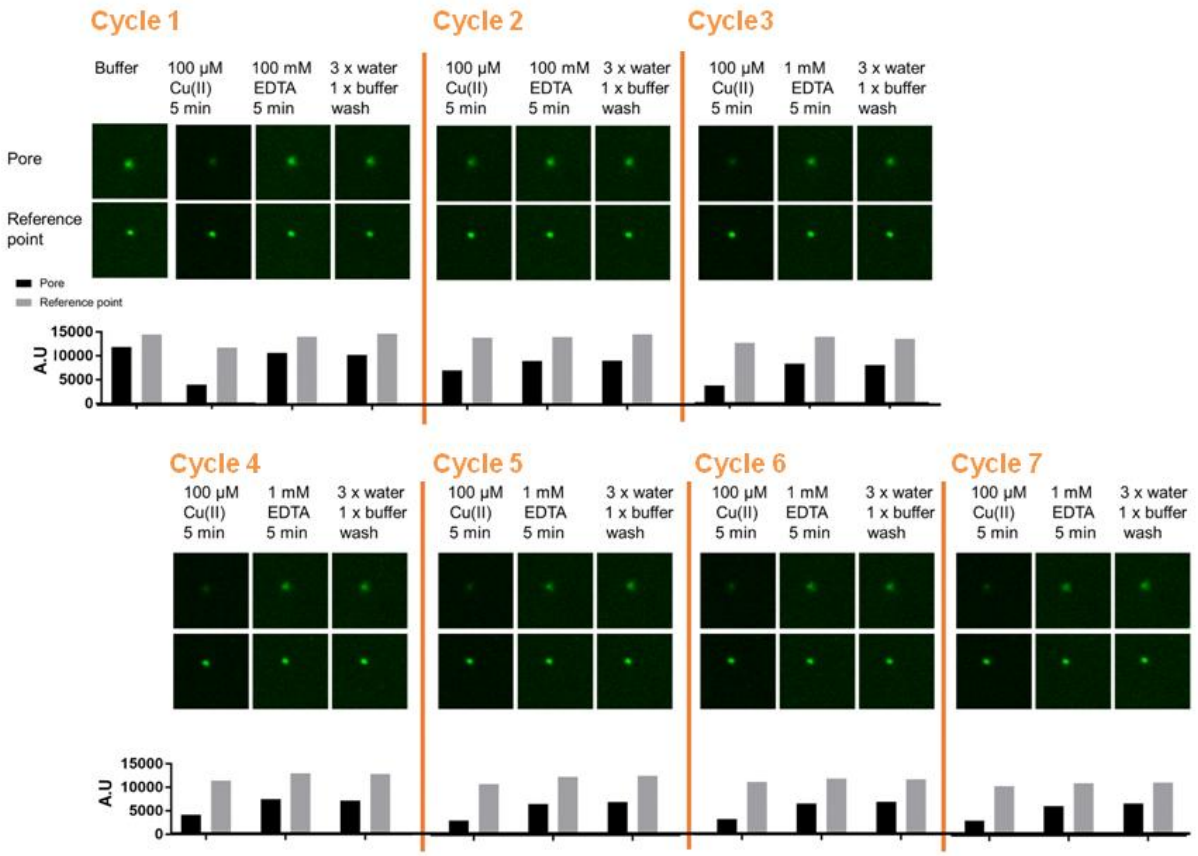

Figure 70. On-Off behavior of hybrid pore with Cu(II)

Plotted by Wadim Weber (RG Prof. Stein, TU Darmstadt)

Next, a titration experiment is implemented to evaluate the sensitivity of immobilized peptide 4 towards Cu(II), Ni(II) and Zn(II). With the addition of increasing concentrations of Cu(II), a decrease of fluorescence intensity within the pore is investigated (Figure 71a). Using according concentrations of Ni(II) towards immobilized peptide 4, no decrease in fluorescence intensity is determined. Only an 10 fold increase in Ni(II) concentration results in a detectable decrease in fluorescence intensity (Figure 71b). Towards Zn(II), no decrease of fluorescence intensity can be detected (Figure 71c). These findings are supported by results from UV-Vis and fluorescence titration experiments. At pH 6.5 peptide 4, in solution and immobilized to PET foils, displays selectivity towards Cu(II) ions while Ni(II) binding is weak and Zn(II) binding not present. A detectable decrease in CLSM measurements of fluorescence intensity with addition of Cu(II) requires mikromolar concentrations which indicates a low sensitivity of CLSM measurements.

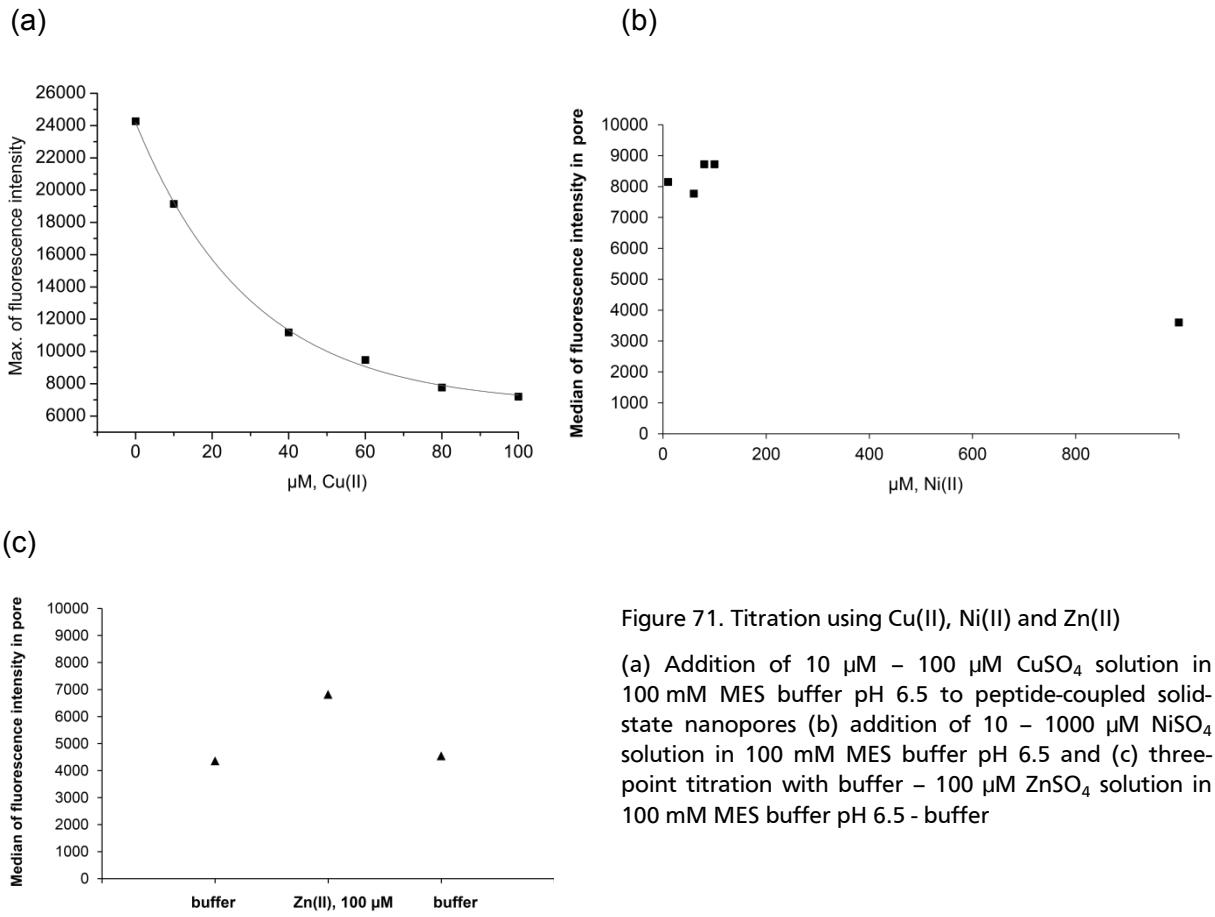

Figure 71. Titration using Cu(II), Ni(II) and Zn(II)

(a) Addition of 10 µM – 100 µM $CuSO_4$ solution in 100 mM MES buffer pH 6.5 to peptide-coupled solid-state nanopores (b) addition of 10 – 1000 µM $NiSO_4$ solution in 100 mM MES buffer pH 6.5 and (c) three-point titration with buffer – 100 µM $ZnSO_4$ solution in 100 mM MES buffer pH 6.5 - buffer

8.4.2. *I-V-* measurements

Using current/voltage, *I/V* measurements (5.3.3.1), the hybrid system of immobilized peptide 4 to conically shaped nanopores, is investigated in regard to sensor sensitivity towards Cu(II), Ni(II) and Zn(II) ions. The set-up is illustrated in Figure 72.

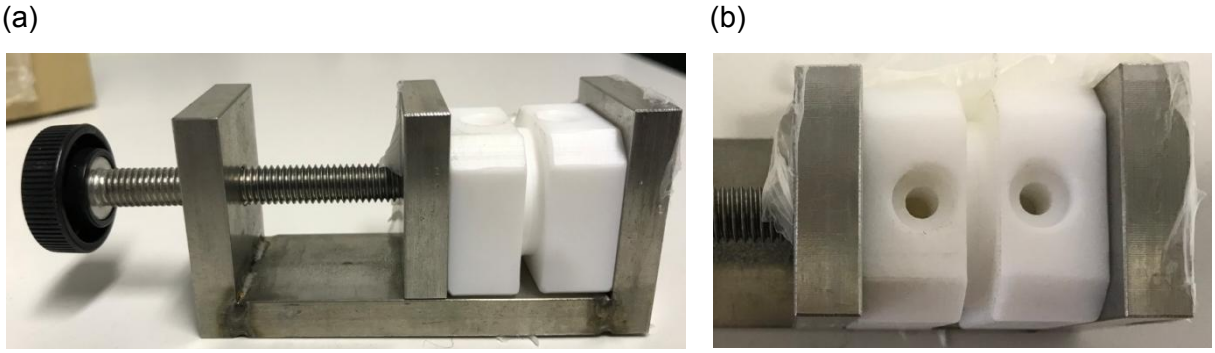

Figure 72. Measurement set-up, *I/V*

Before the addition of Cu^{2+} to the electrolyte solution, a rectifying behavior of the pore is determined (Figure 73a). For positive voltage polarity, as increase in ion condution is present with a decrease for negative voltage polarity leading to an asymmetric I-V curve.[235] With the addition of Cu(II) a increase of positive current is visible. With formation of the peptide 4-Cu(II) complex a positive charge on the pore surface is generated changing the ion

transport. While the rectifying condition represents an “off state”, the transport characteristics of the pore are switched on with Cu(II) addition. Adding Ni(II) and Zn(II) does not result in a change of the rectifying, “off-state” condition (Figure 73a). The successive increase of positive current starts with Cu(II) ion concentrations in the femtomolar range (Figure 73b) illustrating an extreme sensitivity of *I-V* measurements. Applying the on-off conditions from microscopy experiments, the behavior seen in 8.4.1 is confirmed. The addition of Cu(II) leads to an increase in current while addition of EDTA decreases the current to the ground state indicating a full reversibility of Cu(II) binding to the immobilized peptide.

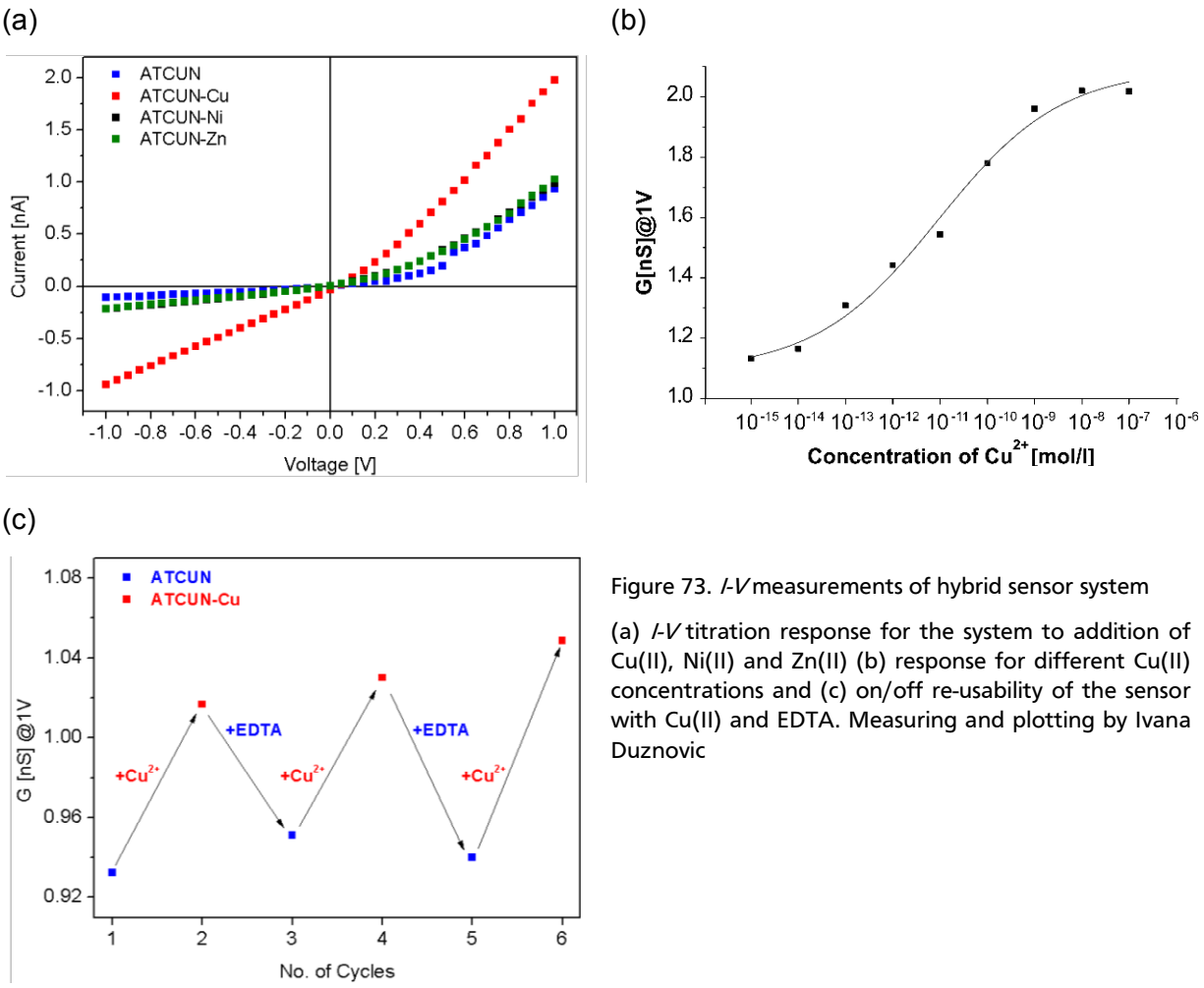

Figure 73. *I-V* measurements of hybrid sensor system

(a) *I-V* titration response for the system to addition of Cu(II), Ni(II) and Zn(II) (b) response for different Cu(II) concentrations and (c) on/off re-usability of the sensor with Cu(II) and EDTA. Measuring and plotting by Ivana Duznovic

9. Conclusion and Outlook: Development of a hybrid nanosensor

At the introduction, six bullet points, that need to be considered for the synthesis and establishment of a sensor from scratch, were imposed:

1. Screening for the available ATCUN motifs in literature
2. Design of a peptide structure that can be covalently coupled to the solid-state material
3. Synthesis and characterization of the ATCUN peptides
4. Investigation of binding properties towards Cu(II), Ni(II) and Zn(II)
5. Immobilization of the peptide to the solid support
6. Characterization of the hybrid material

Screening literature, we came across the motif X_n-(Dns)-β-Ala-His-Ser-Ser-NH_2 from the lab of Imperiali[99] **(1)** and designed a scructure which offered structural components for the immobilization to nanopores of PET membranes, 5/6-FAM-DAP-c-His-$mPEG_4$ and variants (peptides 1-4) **(2)**. Successful synthesis is done implementing the standard fmoc-SPPS protocol, purification using the RP-HPLC technique and characterization of the purified product using ESI.MS **(3)**.

(4) First, binding properties of the peptides in solution are characterized. pH titration studies revealed optimal Cu(II) and Ni(II) binding to be strongly dependent on the pH value. For peptides 1, 2 and 4 a pH of ≥ 8, is sufficient for complete Cu(II) binding with formation of 1:1 square-planar ATCUN-like complexes. For the binding and coordination of Ni(II), a pH of ≥ 10.55 is sufficient for all peptides 1-4. For the non-His containing Peptide 2, the Ala mutant, Cu(II) binding is sufficient only at pH values above 10.55. For design of a Cu(II)-selective sensor, tuning of the pH is evaluated to be an excellent tool. Therefore, pH titration experiments were reconsidered in regard to heavy-metal selectivity. The pH value of 6.5 was evaluated to be optmimal for this aim. While Ni(II) binding of all peptides is minimal, Cu(II) binding is efficient, displaying the pH_{50} value for peptides 1 and 2, which are used for immobilization to the nanopores. We were able to determine a limit of detection, LOD, towards Cu(II) binding at pH 6.5 in solution to be 13.5 nM, emphasizing a high sensitivity. Imperiali's lab identified the integration of β-amino acids to shift the binding preferences towards Cu(II) but they do not take into account that the ATCUN motifs are strongly pH dependent.[99] We integrated the β-Ala moiety but did not see a preference for Cu(II). In the overall study, applying the optimal pH values for Cu(II)- and Ni(II) binding, there is a preference towards Ni(II) binding seen for all peptides 1-4. Several research groups investigated the influence of the amino acids in position 1 and 2 coming to the conclusion that the pk_a of these residues impact preferences towards Cu(II) and Ni(II) with low pK_a values enhancing Cu(II) affinities.[236,237] In regard to the selectivity of the sensor application, no binding towards Zn(II) is evaluated from titration experiments.
Furthermore, the design of ATCUN mutants was accomplished by synthesis of Asp and Ala mutants. ATCUN peptides are characterized by a His moiety at the third position[238] and we investigated Cu(II) and Ni(II) behavior mutating this crucial amino acid. MS and titration experiments show, that there is a 1:1 Cu(II) and Ni(II) binding. Neupane *et al.* investigated linear and cyclic ATCUN motifs without the imidazole unit, coming to a similar conclusion. All cyclic and linear peptides show 1:1 binding towards Cu(II) and Ni(II) in a square-planar fashion.[216]

(5) The immobilization is successfully implemented using HATU/DIEA which was not described in literature before. Also, EDC/sulfo-NHS proved itself to be a successful immobilization method but due to pre-activation of the reaction solution is evaluated to be inferior to HATU/DIEA coupling.

(6) AFM and CLSM were also used for proving the success of immobilization and to characterize the hybrid system as described in **(5)**. Using AFM, the phase difference images prove presence of the peptide within the nanopores of the PET foil with comparison to a blank foil. Using the fluorophore, attached to peptide 4, CLSM studies were carried out, underlining the ability of the peptide to bind Cu(II) when immobilized on the surface of the nanopores. With that result, miniPEG4 is affirmed to be an adequate linker usefull for immobilization while preserving an intact sensing unit. Furthermore, CLSM studies show the selectivity towards Cu(II) binding in comparison to binding Ni(II) and Zn(II). Additionaly, the sensor is exposed to an on/off study aiming to show re-usability. We confirmed a regeneration using EDTA of the sensor system for at least 7 iterations. *I-V* measurements are performed to underline and verify results from microscopy studies. Adding Cu(II) to the electrolyte solution, the hybrid system switches from an "off" state showing rectification, to an increased current. This increase is detectable form Cu(II) concentrations as low as within the femtomolar range underlining an extreme sensitivity. The selectivity is proven with addition of Ni(II) and Zn(II) to the hybrid system, not resulting in an increased current. Furhtermore, on/off studies in from *I/V* measurements reassure finding from CLSM experiments. The robustness is confirmed with CLSM showing fluorescence signal of the immobilized peptide in the nanopores of the PET foil over several months with storage of the foils at 8 °C in water.

Looking at Cu(II) sensors from literature, we were able to optimize the present systems. One example for a fluorescent copper sensor grafted to a surface is stated by Zheng *et al.*[239] They made use of the ATCUN motif with the design of Dns-Gly-His-Lys(NC) (NC – nitrocinnamate for interaction with the PEG gel) and inserted the motif into a cross-linked polyethylene glycol hydrogel (PEG). While the Cu(II) efficiently and selectively quenched the fluorophore restoring for re-usability of the sensor takes 18 hours. Another recent example is the design of a ATCUN Cu(II) sensor Cys-Gly-Gly-Gly-His immobilized to nanoporous membrane to construct a ion-selective electrodes (ISE). This hybrid system by Papp *et al.* shows a good linearity within the range of 10^3 M^{-1} – 10^6 M^{-1} M^{-1}.[240] Furthermore, α-HL was intensively studied towards Cu(II) sensing. With a detection limit of 12 nM presented by Guo *et al.* designed a sensitive and selective nanopore sensor.[241] For the integration into a sensoring device, nanopores within a solid-state material display numerous advantages especially in regard to stability which is not given using biological nanopores.

As for future prospects of our sensor, there are various possibilities. Studies with complex and/or real samples would be the next step. Starting off, complex systems, e.g. buffer solutions spiked with different heavy metals or serum samples could be used to define selectivity and sensitivity of the hybrid pore system. Next off, environmental probes from lakes, soil or from humans such as blood and urine samples could be investigated. Integration into a real device would be the final step in the development of a senor.

10. Results and Discussion: DNA scission and sequencing of ATCUN-like peptides

Literature reports show that the ATCUN motif based on the general structure Xaa-Xbb-His linearizes supercoiled DNA[10] which enables further possible applications for our hybrid nanosensor. The advantageous use of our proposed nanopore system would result in a one-step method to linearize supercoiled DNA and within this step, filter out the linearized DNA with the translocation through the pore (Figure 74). The system will be designed to hold back nicked and supercoiled DNA. Therefore, restriction enzymes as well as extensive purification of the linearized form can be bypassed. Furhtermore, using *I/V* measurements, the system could be used as a sequencing device. The translocation of the linearized DNA will generate a current signal. This signal is dependent on the base translocating through the pore making sequencing a possible target. The importance of new sequencing devices is introduced in 3.4.4.

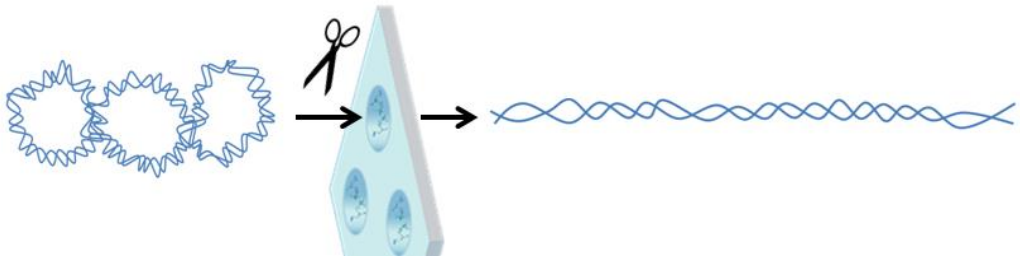

Figure 74. Proposed sensor design for DNA scission

The ability to promote linearization is based on the generation of reactive oxidative species which cleaves the DNA, introduced in 3.4.3. The following scheme illustrates the proposed mechanism from chapter chapter 3.4.3. Zimmerman *et al.* investigated the auto-oxidation of ascorbate in the presence of Cu(II) and O_2 having toxic affects on the bacteria *Serratia marcescens.* The proposed redox scheme can be adapted to the cleavage activity of the ATCUN like peptides.[242]

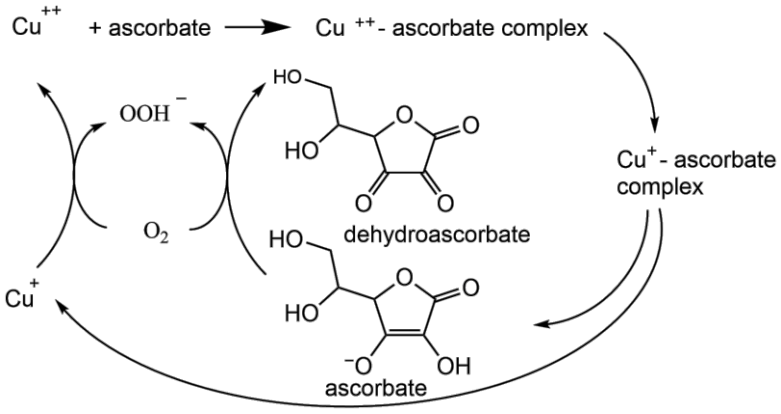

Figure 75. Mechanism towards DNA scission

Redox scheme adapted from Zimmerman *et al.*[242]

The process of DNA linearization consists of three subsequent steps in which both DNA strands from a dsDNA plasmid (closed circular form) need to be broken. Breaking of the first strand will lead to a nicked form whereas breaking of the second strand in proximity (around 10 bp) to the first cut will result in linearized dsDNA.[243]

All three forms can be visualized on an agarose gel. Since the supercoiled form III is extremely packed and shows a small volume, the movement across the agarose gel when current is applied, is extremely fast. The linear form I moves according to its size and can be evaluated by adding a protein ladder with defined masses (in kilobases, kb). The nicked form II is the relaxed state from breaking one strand of supercoiled dsDNA. It is the largest in size and thus moves the slowest.

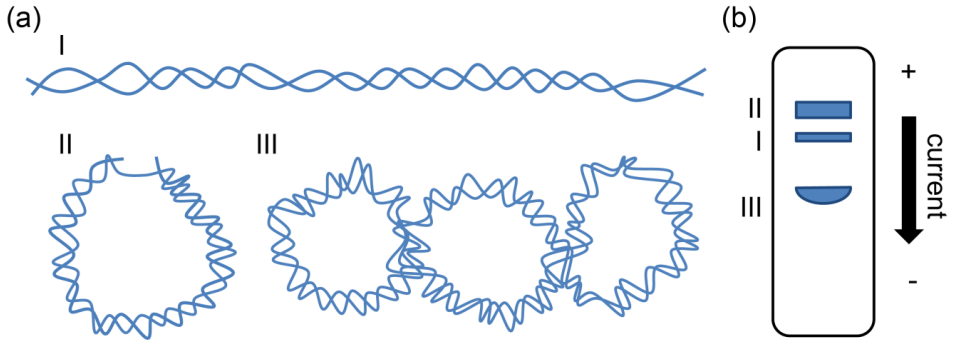

Figure 76. Linear, nicked and supercoiled dsDNA

(a) shows the three conformations of DNA, I – linear, II – nicked and III – supercoiled form and their movement across an agaorse gel (b)

The set-up of DNA scission experiments is based on a protocol introduced by Jin *et al.* altering the conditions to our need.[207]

10.1. Scission of plasmid pUC19

Based on published results which describe the use of GGH and KGGH towards linearization of pUC19,[207] we were aiming to prove scission behavior of our designed peptides 1-4 since to our knowledge, no reports on their behavior is known. The used plasmid pUC19 contains 2686 base pairs (bp). As shown in Figure 75, Cu^{2+} and Ascorbate, Asc, contribute to the generation of ROS but linearization of plasmids require the Cu(II) to be coordinated through the ATCUN motif[207] and are therefore investigated to the contribution to the linearization effect. Therefore, these components are applied as samples towards a negative control to exclude scission of pUC19 using only Cu(II) or Asc or Cu(II) and Asc. Furthermore, samples of only Cu(II) or Asc combined with peptide 4 are investigated to show that adding only one component is not efficient. BamHI-HF, Bam, is used as the restriction enzyme to guarantee linearization for further comparison on the gel. The result of our negative control seen in Figure 77 using peptide 4 and peptides 1 – 3 (SI Figure 40) display no scission towards pUC19. Only the system containing Cu^{2+} and Asc (Figure 77) show a result, found also in literature. Adding both components to a plasmid sequence will lead to so-called “smearing” of the DNA described in literature.[104] Using Asc only, nicked pUC19 is seen after 6 h incubation time, however no linearized DNA is determined.

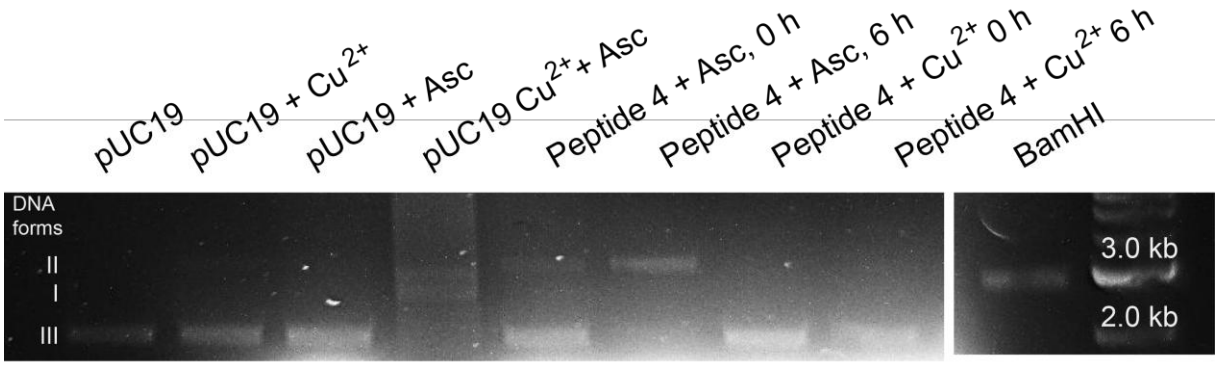

Figure 77. Negative samples of pUC19, Cu^{2+} and ascorbate

Next, we evaluated if scission is accomplished adding the peptide to the mixture. Peptide 1-Cu(II) + Asc shows sufficient linearization of pUC19 within 4 h (SI Figure 42). Furthermore, both non-His containing peptides, peptide 2 and peptide 3, show efficient linearization of pUC19 in addition to Asc and Cu(II) within 4 h (SI Figure 43). Additionaly, peptide 4-Cu(II) + Asc shows scission of pUC19 and was further used to evaluate a sufficient concentration of the components.

Figure 78 shows that using 100 μM peptide 4 (the according concentrations for Cu(II) and Asc are presented in 5.5) leads to sufficient scission becoming visible within 30 minutes. At this time point, no supercoiled DNA is visible anymore. Looking into 2 h and 4 h reaction time, a decrease of the intensity of nicked DNA is evaluated with an intensifying band for linearized DNA. The obtained results of scission efficiency using 125 μM peptide 4 do not differ from the 100 μM experiments. Using 150 μM the nicked band seems to disappears after 4 hours which would lead to the conclusion that only linearized pUC19 is obtained. Since the DNA bands show extreme low intensities, and therefore cannot be evaluated correctly, 150 μM is not chosen for further experiments but 100 μM peptide and the according Asc and Cu(II) concentrations.

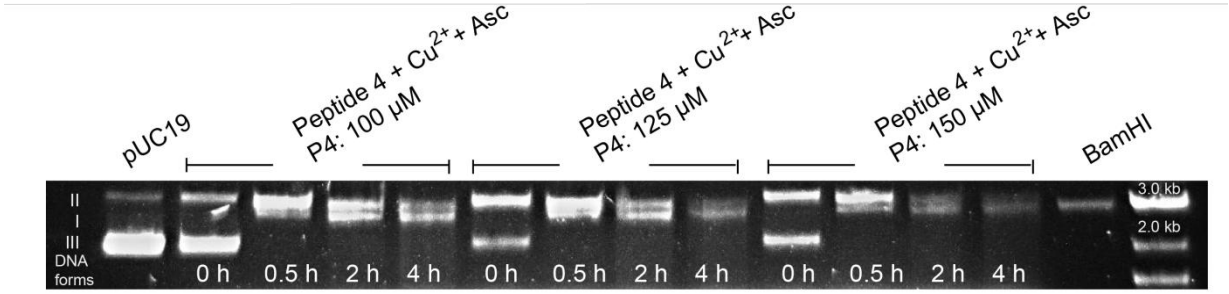

Figure 78. Scission of pUC19 using different concentrations

In the next step we investigated the 30 minute range in which the supercoiled DNA is completely converted to nicked and linearized DNA. Figure 79 shows the steady disappearance of supercoiled DNA (III) within 20 minutes with a corresponding increase in the nicked DNA form (II). The linearized DNA (I) becomes visible after 10 minutes reaction time. All following experiments are conducted for 4 hours to ensure sufficient linearization.

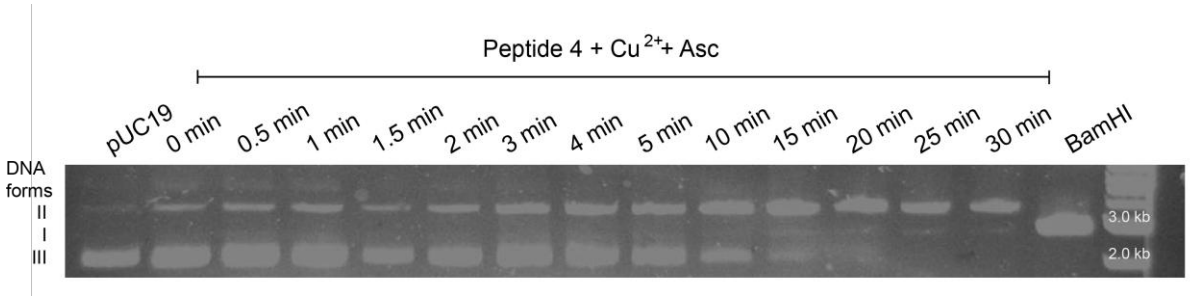

Figure 79. Scission of pUC19 with peptide 4 - copper complex at different time points

While using Ni(II) at the same conditions as Cu(II) to linearize pUC19, no scission can be observed for all peptides, peptide 1-4 (see peptide 1-Ni(II) and peptide 4-Ni(II) in SI Figure 41 SI Figure 42 and peptide 2-Ni(II) and peptide 3-Ni(II) inSI Figure 43) as well as for our negative controls (SI Figure 41). All four designed peptides 1-4 cut dsDNA of the supercoiled plasmid pUC19 adding Cu(II) and Asc while Ni(II) and Asc does not lead to linearization.

Ni(II) disability to cut DNA is ascribable to the differing redox properties nickel exhibits in biological systems, proteins and peptides.[12] Nickel needs to be in a trivalent oxidation state and reduced to Ni^{2+} to fulfill the requirements for the reaction using ascorbate.[244]

Determination of the preferred region of scission, pUC19

According to literature data (mentioned in 3.4.3), where the scission behavior of the general motif Gly-Gly-His and mutants was studied towards a small oligonucleotide, the preferable region for linearization of dsDNA by ATCUN complexes is described to be at A/T rich regions.[108] Since the peptide structures of our designed motifs differ from those presented in literature, we were interested in this preference. Furthermore, we set up an experiment to evaluate a distinct region of scission towards a whole plasmid. Thus, the pUC19 plasmid was segmented into three areas (Figure 81). Area **A**, contains 800 bp, **B** 930 bp and **C**, comprises 1070 bp. The three areas are defined by using reverse, rv and forward, fw primers and analyzed by polymerase chain reaction, PCR. Fragments which are not affected by scission of peptides 1-4 will be amplified by PCR and thus visible within the agarose gel. The plasmid, pUC19 is incubated with the reaction solution, containing peptides 1 – 4, Cu(II) and Asc for 4 h and the linearized band cut from the gel. The DNA is extracted and exposed to PCR using the primer pairs for each region. The results can be seen in Figure 81.

The positive samples which contain intact, supercoild dsDNA of pUC19 show applicability of the designed experiment. Applying PCR for region A with pUC A fw and PUC A rv a band at around 800 bp is visible within the agarose gel. For region B, pUC B fw and pUC B rv lead to a band at the height of almos 1 kb and applying pUC C fw and pUC C rv for area C, a band at a little over 1 kb is obtained. All three with bands for each region in the corresponding height of the ladder (Figure 81c).

Peptides 1 and 4 are displayed in Figure 81a and b. For both peptides, sufficient amplification of region A and B can be evaluated while no amplification of C becomes visible with a missing band in the agarose gels. Additionaly, the experiment was conducted using the non-His containing peptides, peptide 2 and peptide 3. The results towards segementation of pUC19 are seen in SI Figure 44, indication the same behavior for peptide 3 with region C not visible

in the agarose gel. For peptide 2, the Ala mutant, all fragments, A, B and C are seen in the gel with the band for region C showing significantly less intensity compared to A and B. Table 33 summarizes the appearance of bands for regions A, B and C using all peptides.

Usage of fw and rv primers induce amplification of a defined DNA segment only when the sequence is intact. A non-appearance of a band after PCR results from an incontinuous DNA sequence. Therefore, we can come to the conclusion that within the C region, there is a break of the DNA sequence which thus leads to insufficient amplification.

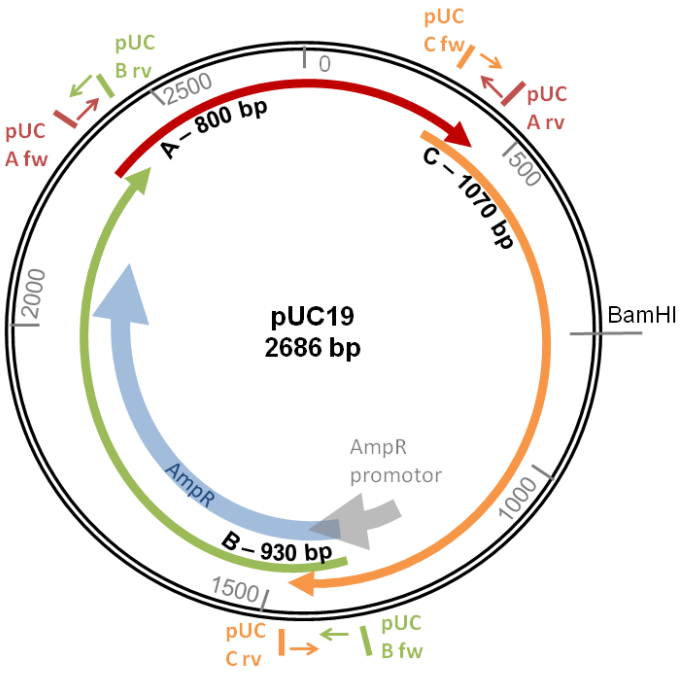

	A	B	C
P 1	✓	✓	✗
P 2	✓	✓	✗
P 3	✓	✓	✓
P 4	✓	✓	✗

Table 33. Evaluation of areas A, B and C of pUC19 amplyfied by PCR regarding peptide scission

Figure 80. Map of pUC19 with areas A, B and C

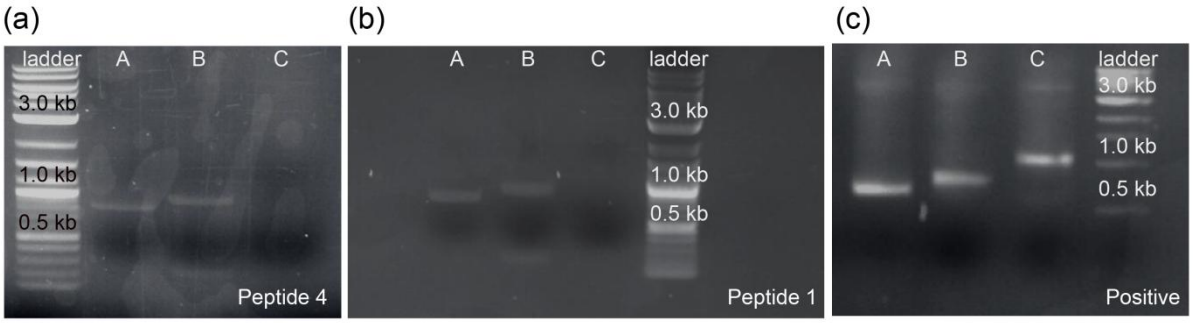

Figure 81. pUC19 segmentation in three areas

The linearized pUC19 is amplified using PCR into three segments. Linearization by (a) peptide 4 (b) peptide 1 and positive sample (c)

Segment	A	B	C
Primer reverse	pUC A rv	pUC B rv	pUC C rv
Primer forward	pUC A fw	pUC B fw	pUC C fw

Table 34. pUC19 segmentation, three fragments

Using a nanodrop, concentrations of DNA can be evaluated using UV-Vis absorption spectra. Concentrations of the three fragments, A, B and C from the positive experiment reveal similar concentrations of the amplified regions within 41.2 – 47.3 ng/μl while for peptides 1, 3 and 4 a significant lower values for region C (15 – 20 ng/μl) are apparent. This supports findings from the agarose gels. Region C is not amplified sufficiently, again confirming that within this region, the scission takes place.

Area	A (ng/μl)	B (ng/μl)	C (ng/μl)
P1	50.2	47.2	21.4
P3	37.5	37.2	15.1
P4	72. 5	83.3	17.7
pos.	41.2	47.3	45.0

Table 35. Nanodrop results of pUC19 regions A, B and C

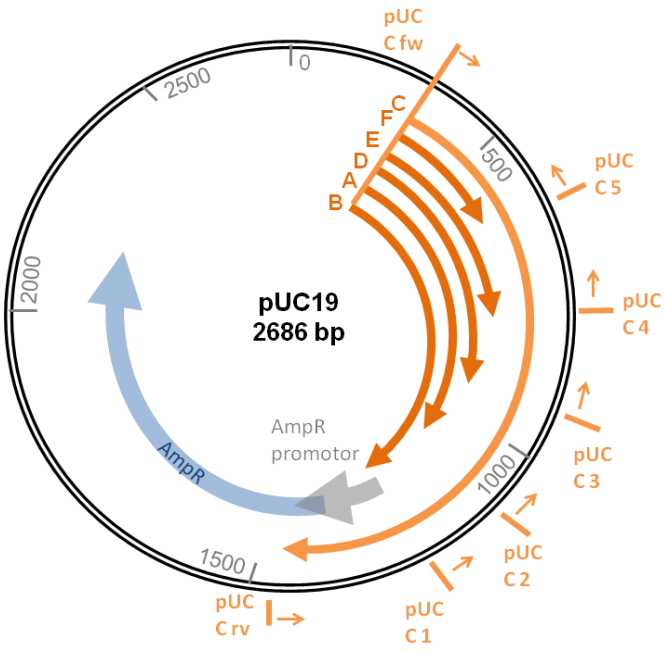

Figure 82. Segmentation of region C

As we got an indication that peptides 1, 2 and 4 specifically cut the dsDNA at region C, the next step was to narrow down the region of the cutting position within the fragment C. For this purpose, region C was divided into five smaller segments (Figure 82).

The results from the segmentation (Figure 83) indicate that there is no defined point of scission because all fragments are visible in the agarose gel. We can therefore conclude that scission is most likely performed in area C of pUC19 while within that region there is not a defined sequence succession where the plasmid DNA is cut.

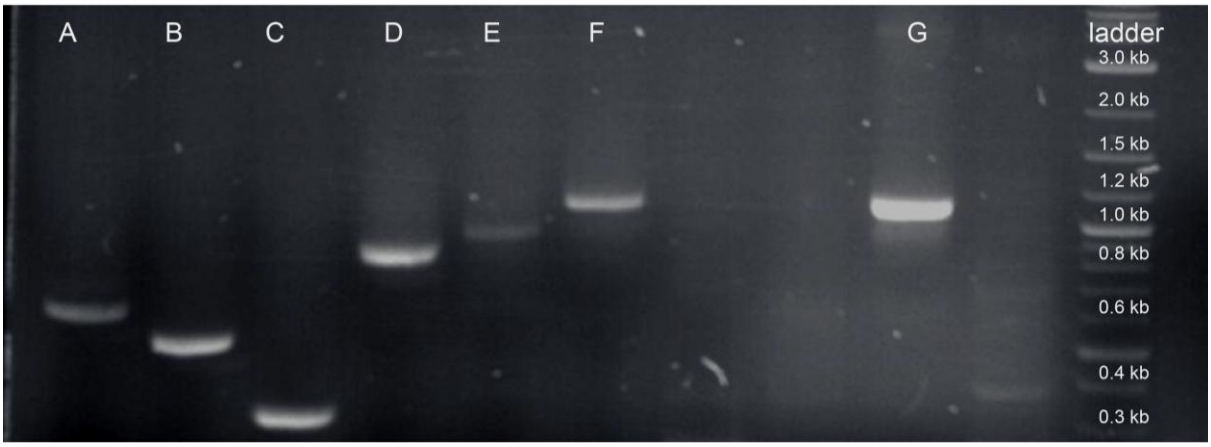

Figure 83. Agarose gel showing PCR of segmentated region C

	A	B	C	D	E	F	G
Segment size (kb)	650	540	330	870	760	1070	1070
Primer reverse	pUC C3	pUC C4	pUC C5	pUC C1	pUC C2	pUC C rv	pUC C rv, positive sample
Primer forward	pUC C fw						

Table 36. Segmentation of area C of pUC19

10.2. Scission of pASK and pACY

To clarify if this approach is applicable to other dsDNA plasmids, we selected pASK (pASK-IBA3) and pACY (pACY-CT2). As pUC19, pASK shows an ampicillin resistance (AmpR) while pACY is resistant against chloramphenicol (CmR). The scission ability of peptides 1 – 4 towards these plasmids was proven. In Figure 84 results of the time-resolved scission behavior of the peptide 1-Cu(II) and peptide 4-Cu(II) complex towards pASK and pACY are shown. For peptide 4-Cu(II) scission experiments, an equal intensity of nicked and linearized DNA becomes visible with the linearized band intensifying for pASK within 4 hours. Peptide 1-Cu(II) complexes exhibit equal concentrations of nicked and linearized DNA for both plasmids, pASK and pACY remaining equal over the time course of 4 hours.

Furthermore, scission of pAKS and pACY using peptide 2-Cu(II) and peptide 3-Cu(II) can be seen in SI Figure 45. Results from peptide 3, the Asp-mutant, are in accordance to findings from peptides 1 and 2 with scission ability visible showing equal concentrations of nicked and linearized DNA over a scission time of 4 hours.

Peptide 2 shows little scission ability. Bands with equal intensities indicating linearized and nicked DNA can be observed after 30 minutes. However, unexpectedly no bands can be observed at a later time point indicating a denaturing process of the DNA. Therefore, all other

scission experiments for peptide 2-Cu(II) towards pASK and pACY are evaluated at only 30 minutes of reaction time.

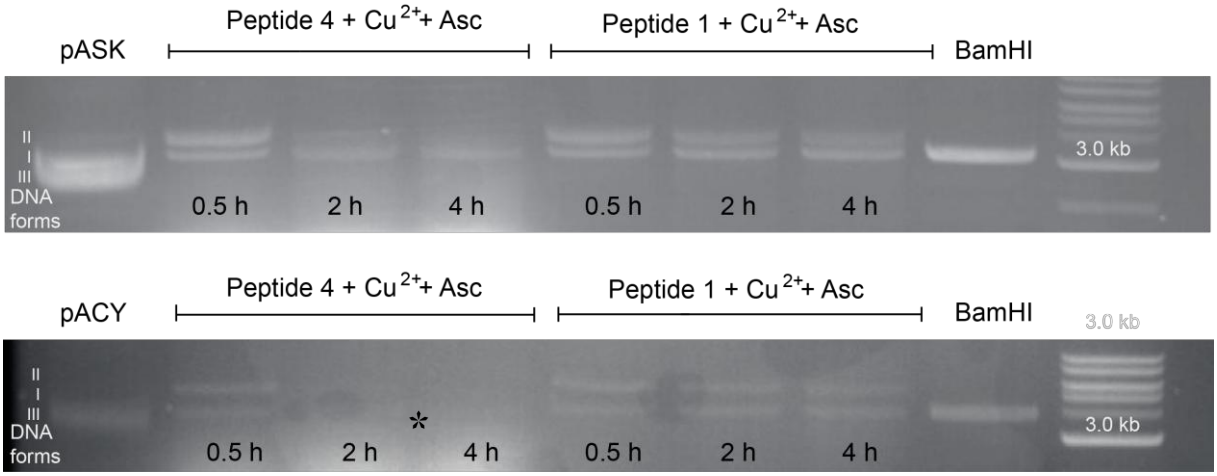

Figure 84. Scission of pASK and pACY using peptide 4 and peptide 1 + Cu^{2+} and Asc

*linearized and nicked bands are covered by fluorescence of 5/6-FAM from peptide 4

With positive scission results of both dsDNA plasmids, pASK and pACY were segmented according to pUC19 to evaluate possible sites for scission.

Determination of the preferred region of scission, pASK

In order to identify the scission segment of pASK, the plasmid was divided into four parts: A (710 bp), B (1120 bp), C (790 bp) and D (1400 bp) (Figure 85). Mapping pASK, four corresponding primer pairs, rv and fw, were used (pASK A fw and rv, pASK B fw and rv, pASK C fw and rv and pASK D fw and rv). For peptide 4, regions A, B and C are sufficiently amplified and visible in the agarose gel whereas region C is not visible (Figure 86). Similar data is obtained for peptide 2-Cu(II) and peptide 3-Cu(II) (SI Figure 46). Again, regions A, B and C are visible in the agarose gel with region D not amplified and thus not visible. Only peptide 1 shows a different behavior with all bands corresponding to the regions A, B, C and D (SI Figure 46).

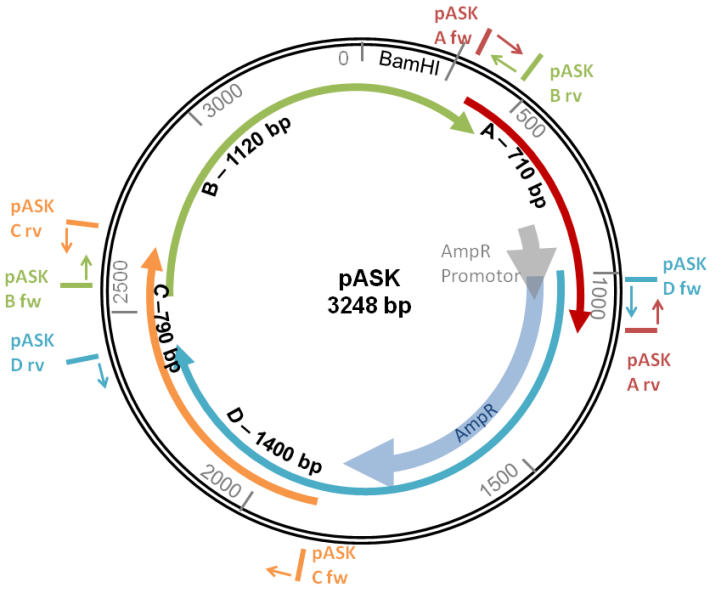

Figure 85. Map of pASK plasmid with segments A, B, C and D

AmpR refers to ampicillin resistance

	A	B	C	D
P 1	✓	✓	✓	✓
P 2	✓	✓	✓	✗
P 3	✓	✓	✓	✗
P 4	✓	✓	✓	✗

Table 37. Evaluation of areas A, B, C and D of pASK amplyfied by PCR regarding peptide scission

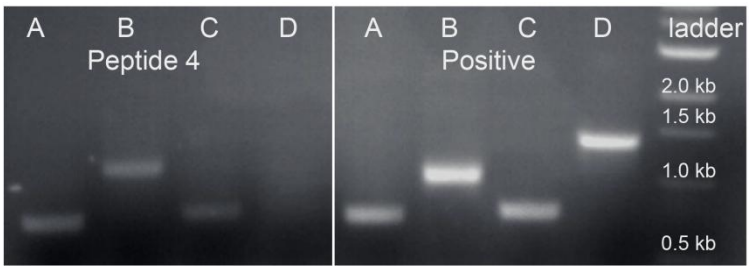

Figure 86. Segmentation of pAKS using peptide 4 + Cu^{2+} and Asc

	A (PA)	B (PB)	C (PC)	D (PD)
Primer reverse	pASK A rv	pASK B rv	pASK C rv	pASK D rv
Primer forward	pASK A fw	pASK B fw	pASK C fw	pASK D fw

Table 38. Forward and reverse primers for segmentation of pASK

Determination of the preferred region of scission, pACY

Similar to pUC19 and pASK, the plasmid pACY was defined into three regions, A (540 bp), B (2240 bp) and C (2070 bp). Results of the amplification for the corresponding regions after scission using peptides 1-4-Cu(II) + Asc show amplification only of region A, whereas region B and C are not visible in the agarose gel (Figure 88).

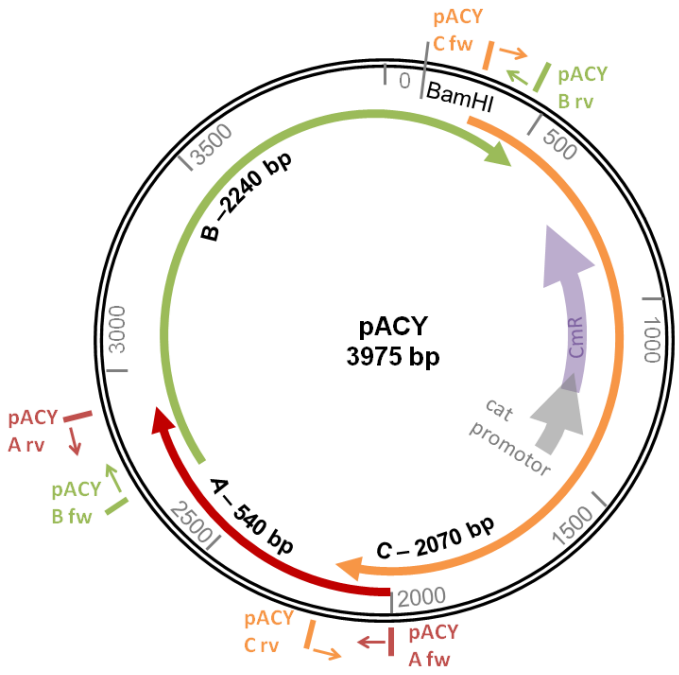

Figure 87. Map of pACY showing three segments A, B and C

	A	B	C
P 1	✓	✗	✗
P 2	✓	✗	✗
P 3	✓	✗	✗
P 4	✓	✗	✗

Table 39. Evaluation of areas A, B, and C of pACY amplyfied by PCR regarding peptide scission

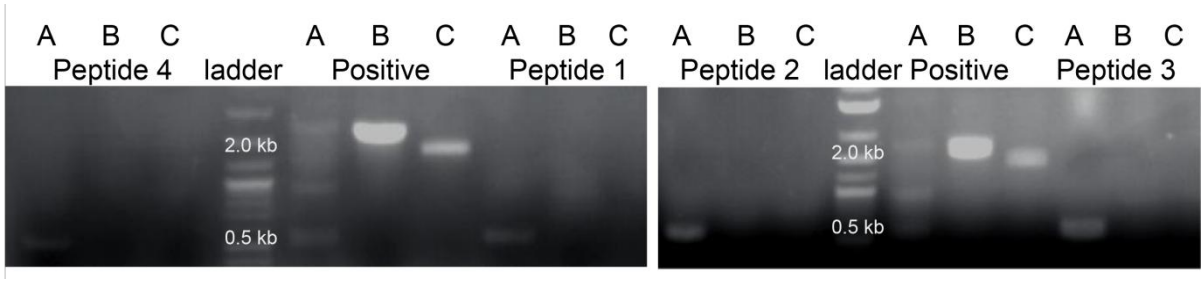

Figure 88. Scission of pACY using peptides 1 - 4 with Cu^{2+} and Asc

Segment	A	B	C
Primer reverse	pACY A rv	pACY B rv	pACY C rv
Primer forward	pACY A fw	pACY B fw	pACY C fw

Table 40. Forward and reverse primers for segmentation of pACY

Looking into the occurrence of AATT and TTAA within the segmented regions and the plasmid sequences itself, the following values are determined:

Plasmid	Sequence	Region A	Region B	Region C	Region D	Total repetitions found
pUC19	AATT	0 × 0%	3 × 43%	**4 ×** **57%**	-	7
	TTAA	1 × 3%	8 × 62%	**5 ×** **38%**	-	13
	TT	64 × 31%	68 × 33%	**91 ×** **44%**	-	208
pASK	AATT	3 × 23%	4 × 31%	4 × 31%	**6 ×** **46%**	13
	TTAA	7 × 33%	5 × 24%	9 × 43%	**8 ×** **38%**	21
	TT	97 × 33%	93 × 31%	80 × 27%	**105 ×** **35%**	296
pACY	AATT	3 × 13%	**7 ×** **30%**	**16 ×** **70%**	-	23
	TTAA	2 × 9%	**9 ×** **39%**	**13 ×** **57%**	-	23
	TT	41 × 14%	**148 ×** **49%**	**199 ×** **39%**	-	302

Table 41. AATT, TTAA and TT sequence regions in pUC19, pASK and pACY

Please note that the regions are overlapping an the addition of the number of repetition does not equal the value from the last column

The nucleotide sequence of region C of pUC19 displays AATT 57% and TTAA 38%, region D of pASK AATT 46% and TTAA 38%. For pACY region A is amplified and thus visible in the agarose gel, this region exhibits AATT 13% and TTAA 9%. Looking at these figures, a certain preference for the A/T rich regions can be evaluated. Coming back to Figure 9 the AATT/TTAA preference is discussed with a sequence of an ATCUN motif carrying a lysine unit. Since the design peptides 1-4 do not exhibit this group, regions including only the TT sequence are also evaluated. The results are comparable to AATT and TTAA regions with the sequence TT displaying the highest occurrence within the cut areas. For further evaluation, structural studies have to be designed.

10.3. Towards the design of a sensor system for sequencing of DNA

After determining a specific region in which pUC19 is cut using peptides 1, 2 and 4, we were aiming to develop a solid-state hybrid system in order to be able to filtrate the supercoiled DNA from the linearized form without the need for restriction enzymes. The experiment set-up is illustrated in Figure 89.

First, we designed an experiment using passive diffusion using the gradient from the left chamber to the right chamber. While on the left side, all reaction components, pUC19, Cu(II) and Asc are added in buffer solution, the right chamber only contains only the buffer.

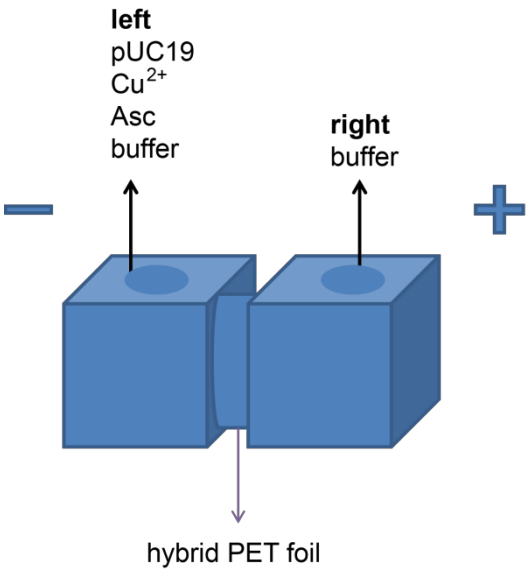

Figure 89. DNA sequenching experiment set-up

The presented results in Figure 90 show efficient scission of pUC19 using immobilized peptide 4 to conically shaped nanopores. Therefore, the scission ability of the designed peptide remains intact. However, no DNA, neither linear nor nicked DNA was found in the right chamber of the set-up, indicating that there is no translocation of DNA material through the pores.

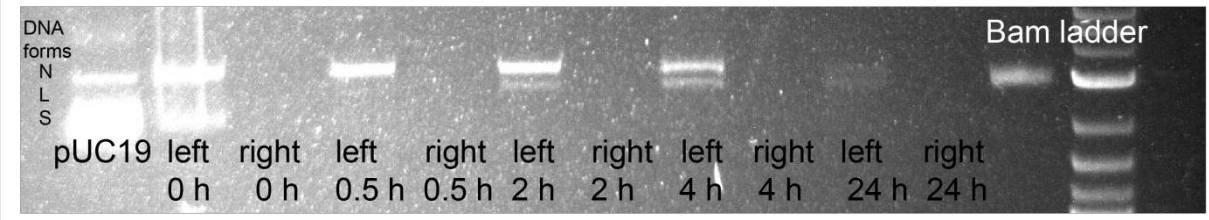

Figure 90. DNA scission through nanopores using passive diffusion

In the next step, we decided to apply a voltage to the system. Using -50 mV we wanted to translocate the negatively charged DNA to the cathode, from left to right chamber. Unfortunately, the application of a external force did not result in the translocation of DNA but again showed efficient scission of pUC19 (Figure 91).

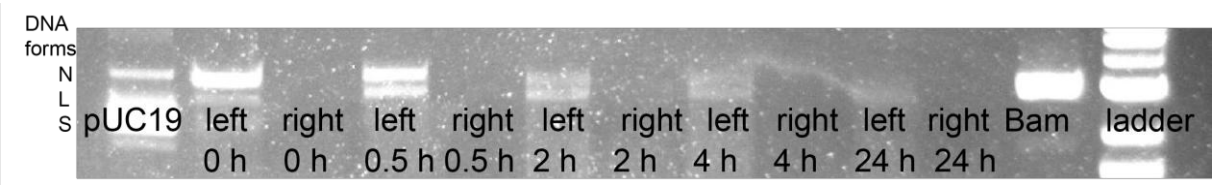

Figure 91. DNA scission through nanopores using -50 mV, peptide 1 immobilized

Having used only conically shapes nanopores, we decided to alter the pore geometry. Additionaly, we increase the voltage applied to our system. The results of an experiment set-up using -1 V, cylindrically shaped nanopores with diameters of 100 nm, 200 nm and 300 nm are summarized in Figure 92. Again, results are comparable to the conically shaped nanopores. No DNA is found to travel to the right chamber.

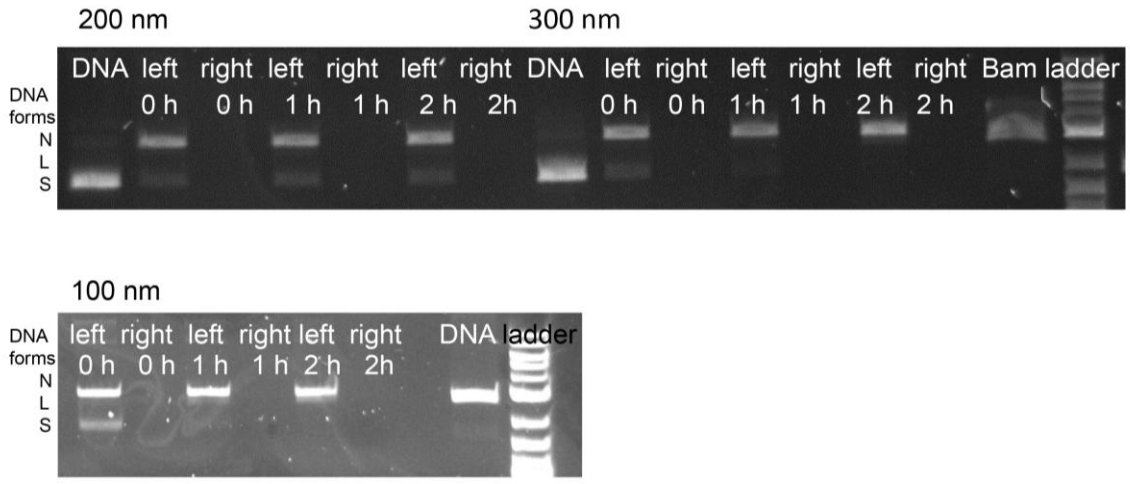

Figure 92. DNA scission through nanopores using cylindrical nanopores with -1 V, peptide 1 immobilized

In the next step, we added mechanical force. Therefore, we investigated two syringe types and pressed the reaction solution through the pores of the PET nanopores. Results from both experiments show translocation of the DNA through the pores, but only generation of nicked DNA. While the main weakness of syringe 1 is the short contact time of the reaction solution with the immobilized peptide in the pores of the PET foil, syringe 2 was evaluated to circumvent this disadvantage. Also, pores displaying a smaller diameter were chosen for the syringe 2 trying to hold back nicked DNA. Unfortunately, the altering of the syringe system did not result in linearized DNA.

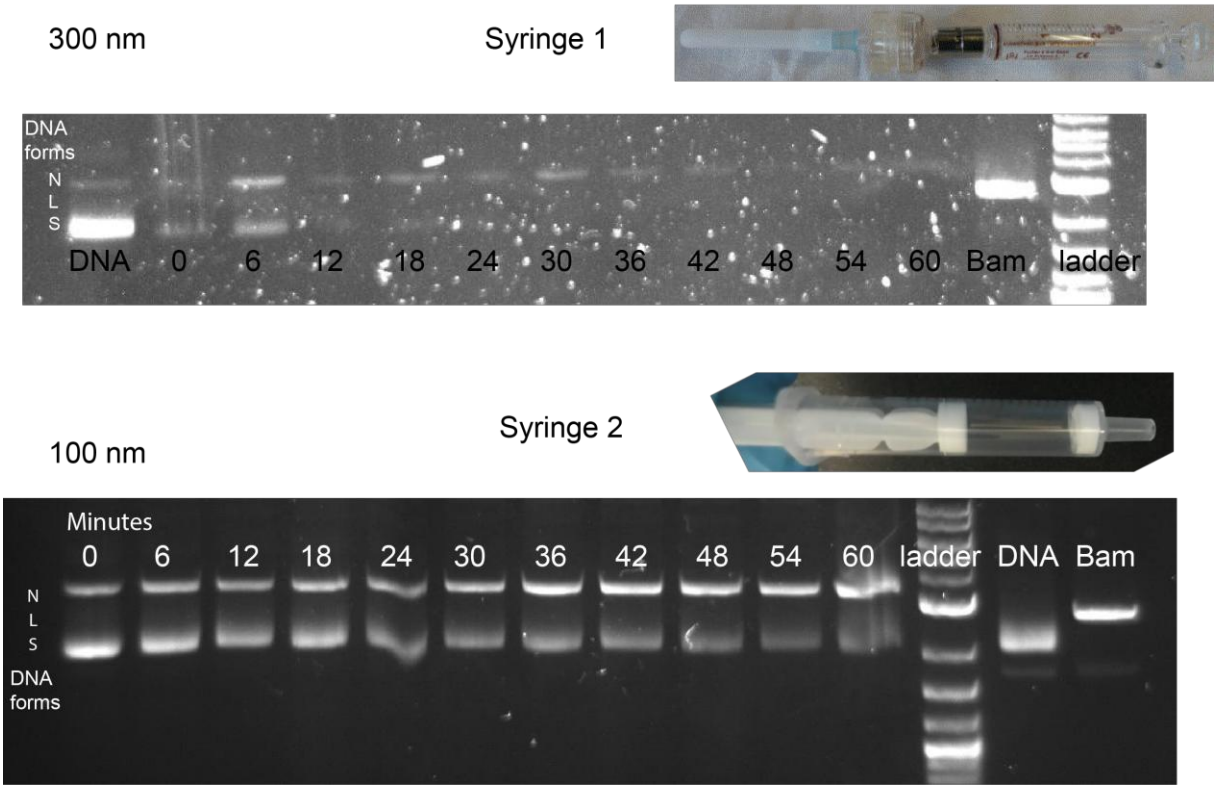

Figure 93. DNA scission through nanopores using syringes, peptide 1 immobilized

11. Conclusion and Outlook: DNA scission and sequencing of ATCUN-like peptides

Summarizing the presented outcomes a preference in scission of plasmids carried out by copper-complexes of ATCUN-like peptides was determined. This preference was found for pUC19, which was segmented into areas A, B and C to be within region C. For pASK, a preference was determined for region D, with the plasmid segmented into four areas A, B, C and D. The last plasmid from the scission experiments, pACY, was segmented into three areas A, B and C with scission taking place in regions B and C. While literature refers to preference of A/T rich sequences determined by scission of short DNA strands, these findings indicate an even more distinct binding and scission mechanism. Additionaly, looking into the sequences and the occurrence of AATT/TTAA and TT regions, findings emphasize the scission preference for these base-pair appearances.

The ability of explicit and selective binding is of immense interest in regard to diagnostic applications. Consequently, ATCUN-like peptides fulfill several important factors for development of metallonucleases. They also show a constraining molecular shape to fit the minor groove of DNA. This ability is of great interest for desired targeting specific domains of DNA.[245] Dr. Uerpmann *et al.* designed a cylinder binding to DNA in specific orientations opening up new target routes for DNA cleavage.[246]

The search for new anti-cancer drugs is a great field of interest. The most widely used anticancer chemotherapeutics are platinum-metallodrugs.[247] These structures exhibit cytotoxicity and dose-limiting toxic side effects making them flawed. The exploration of other transitions metals for anticancer applications is ongoing. Especially copper, Cu^{2+} represents an interesting candidate. Since it is an endogenous metal, it may be less toxic compared to Pt and may lead to less side effects.[248] The aforementioned advantages of ATCUN-like peptides and our findings on selective DNA cleavage make them interesting candidates in search for new anticancer drugs.

In regard to the generation of a device for DNA scission and translocation, we were able to perform several experiments that indicate a way to pursue. We were able to show successful scission of supercoiled plasmid DNA through immobilized peptide 4 and peptide 1. In the future, altering the pore geometry or using other solid-state nanopore systems, the translocation may be successful. Traversi *et al.* were able to translocate circular plasmid DNA, pNEB (2713 bp) through graphene based nanopores. They emphasize the applicability of graphene nanoribbons towards DNA sequencing due to the thickness of only 0.335 nm.[249] While this thickness corresponds to only two base pairs of a DNA strand, our PET foil exhibits a thickness of 12 μm making translocation extremely difficult. It was Kaya *et al.* that successfully translocated a 50 bp DNA sequence through PET foils that were 12 μm thick. The fabricated conically shaped nanopores with a tip opening of 20 nm and a base of 800 – 900 nm making use of different concentrations of methanol added to etching solution to obtain this exact pore size.[250] These examples show that there are numerous parameters that affect DNA translocation but also yield hope that we can be succesfull in our aim of generating a sequencing device in the nearest future.

12. Materials

12.1. Chemicals

IUPAC	Abbreviation/name used
($^2H_2$)Water, deuterium oxide	D_2O
(2*S*,3*S*)-1,4-Bis(sulfanyl)butane-2,3-diol	DTT
(4-Sulfanylphenyl)acetic acid	MPAA
1,1,1,2,2,2-Hexafluoro-2-propanol	HFIP
1-[Bis(dimethylamino)methylene]-1*H*-1,2,3-triazolo[4,5-*b*]pyridinium 3-oxid hexafluorophosphate	HATU
1-Ethyl-3-(3-dimethylaminopropyl)carbodiimide	EDC
1-Hydroxy-7-azabenzotriazole	HOAt
1-palmitoyl-2-oleoyl-sn-glycero-3-phophocholine	POPC
2-(N-Morpholino)ethanesulfonic acid	MES
2,2,2-Trifluoroacetic acid	TFA
2,2,2-Trifluoroethanol	TFE
2,5-Dihydroxyacetophenone	2,5-DHAP / DHAP
2-[2-[bis(carboxymethyl)amino]ethyl-(carboxymethyl)amino]acetic acid; sodium	(Disodium) EDTA
2-Amino-2-(hydroxymethyl)-1,3-propandiolactate	Tris acetate
2-Amino-2-(hydroxymethyl)propane-1,3-diol	Tris
2-hydroxy-3-mercapto-propionic acid	hmp
2-Methylpiperidine	2-Methylpiperidine
3-(4—hydroxy-3,5-dimethoxyphenyl)prop-2-enoic acid	Sinapinic acid
3-(Cyclohexylamino)-1-propanesulfonic acid	CAPS
3‘,6‘-dihydroxy-1-oxospiro[2-benzofuran-3,9‘-xanthene]-5-carboxylic acid	5/6 FAM
Acetic acid	AcOH
Acetonitrile	ACN
Alternating D-galactose and 3,6-anhydro-alpha-L-galactopyranose	Agarose
Bovine Serum Albumin	BSA

Carbonic diamide	Urea
Coomassie brilliant blue R-250	Coomassie blue
Copper(II) sulfate	$CuSO_4$
Diaminomethanal	Urea
Dichloromethane	DCM
Diethyl azodicarboxylate	DEAD
Dimethyl sulfoxide	DMSO
Ethoxyethane	Diethyl ether
Fluoro-N,N,N',N'-tetramethylformamidinium hexafluorophosphate	TFFH
Formic acid	FA
Hydrochloric acid	HCl
Isopropyl alcohol	Isopropanol
Magnesium acetate	MgOAc
Methanal	Formaledhyd
Methanol	Methanol
N,N-Dimethylformamide	DMF
N-[Tris(hydroxymethyl)methyl]glycine	Tricine
N-cyclohexyl-3-aminopropanesulfonic acid	CAPS
n-Dodecyl β-D-maltoside	DDM
N-ethyl-N-(propan-2-yl)propan-2-amin	DIEA
N-hydroxysuccinimide	NHS
Nickel(II) sulfate	$NiSO_4$
N-Methyl-2-pyrrolidone	NMP
Octylglycoside	OG
Piperidine	Piperidine
Potassium acetate	KOAc
Potassium dihydrogen phosphate	K_2HPO_4
Propane-1,2,3-triol	Glycerol
Sodium acetate	NaOAc

Sodium carbonate	Sodium carbonate
Sodium dihydrogen phosphate	Na_2HPO_4
Sodium dodecyl sulfate	SDS
Sodium hydroxide	NaOH
sodium; (2*R*)-2-[(1*S*)-1,2-dihydroxyethyl]-4-hydroxy-5-oxo-2*H*-furan-3-olate	Sodium ascorbate, Asc
Sodiumhydroxide	NaOH
Tetrahydrofuran	THF
Trifluoroacetic acid	TFA
Triphenylphosphine	PPh_3
Tris(2-carboxyethyl)phosphine hydrochloride	TCEP
Zinc(II) sulfate	$ZnSO_4$
α-Cyano-4-hydroxycinnamic	4-HCCA

Table 42. Chemicals.

12.1.1.Amino Acids

Fmoc protected amino acids	Chemical name	Single/Three letter code
Fmoc-Ala-OH×H_2O	N-α -(9-Flouenylmethyloxycarbonyl)-L-**alanine**, monohydrate	A / Ala
Fmoc-Arg(Pbf)-OH	N-α -(9-Flouenylmethyloxycarbonyl)-N'-2,2,4,6,7-pentamethyldihydrobenzofuran-5-sulfonyl-L-**arginine**	R / Arg
Fmoc-Asn(Trt)-OH	N-α -(9-Flouenylmethyloxycarbonyl)-N-beta-trityl-L-**asparagine**	N / Asn
Fmoc-Asp(OtBu)-OH	N-α -(9-Flouenylmethyloxycarbonyl)-L-**aspartic acid** β-t-butyl ester	D / Asp
Fmoc-Cys(Trt)-OH	N-α -(9-Flouenylmethyloxycarbonyl)-S-trityl-L-**cysteine**	C / Cys
Fmoc-Cys(Acm)-OH	N-α -(9-Flouenylmethyloxycarbonyl)-S-(acetyl-aminomethyl)-L-**cysteine**	C / Cys
Fmoc-Gln(Trt)-OH	N-α -(9-Flouenylmethyloxycarbonyl)-N-ɣ-trityl-L-**glutamine**	Q / Gln
Fmoc-Glu(OtBu)-OH×H_2O	N-α -(9-Flouenylmethyloxycarbonyl)-L-**glutamic-acid**-ɣ-t-butyl ester monohydrate	E / Glu
Fmoc-Gly-OH	N-α -(9-Flouenylmethyloxycarbonyl)-**glycine**	G / Gly
Fmoc-His(Boc)-OH	N-α-(9-Fluorenylmethyloxycarbonyl)-N-im-(t-butyloxycarbonyl)-L-**histidine**	H / His
Fmoc-Ile-OH	N-α -(9-Flouenylmethyloxycarbonyl)-L-**isoleucine**	I / Ile
Fmoc-Leu-OH	N-α -(9-Flouenylmethyloxycarbonyl)-L-**leucine**	L / Leu
Fmoc-Lys(Boc)-OH	N-α-(9-Fluorenylmethyloxycarbonyl)-N-ε-t-butyloxycarbonyl-L-**lysine**	K / Lys
Fmoc-Met-OH	N-α -(9-Flouenylmethyloxycarbonyl)-L-**methionine**	M / Met
Fmoc-Phe-OH	N-α -(9-Flouenylmethyloxycarbonyl)-L-**phenylalanine**	F / Phe
Fmoc-Pro-OH×H_2O	N-α -(9-Flouenylmethyloxycarbonyl)-L-**proline**, monohydrate	P / Pro
Fmoc-Ser(tBu)-OH	N-α -(9-Flouenylmethyloxycarbonyl)-O-t-butyl-L-**serine**	S / Ser

Fmoc-Thr(tBu)-OH	N-α -(9-Flouenylmethyloxycarbonyl)-O-t-butyl-L-threonine	T / Thr
Fmoc-Trp(Boc)-OH	N-α -(9-Flouenylmethyloxycarbonyl)-N-in-t-butyloxycarbonly-L-tryptophan	W / Trp
Fmoc-Tyr(tBu)-OH	N-α -(9-Flouenylmethyloxycarbonyl)-O-t-butyl-L-tyrosine	Y / Tyr
Fmoc-Val-OH	N-α -(9-Flouenylmethyloxycarbonyl)-L-valine	V / Val
Fmoc-Thz-OH	(S)- N-α -(9-Flouenylmethyloxycarbonyl)-thiazolidine-4-carboxylic acid	
Fmoc-L-Phe-L-Ser[PSI(Me, Me)Pro]-OH	(S)-3-(N-(9-Flouenylmethyloxycarbonyl)-L-phenylalaninyl)-2,2-dimethyloxazolidine-4-carboxylic acid	
N-Acetyl-L-alanine	(2S)-2-acetamidopropanoic acid	

Table 43. Amino acids

12.1.2.Resins

Resin	Loading (mmol/g)	Supplier
AmphiSpheres 40 RAM	0.38	Agilent Technologies
TentaGel R RAM	0.18	Rapp polymere GmbH
2-Chlorotritylchlorid	0.966	Carbolutions

Table 44. Resins used for SPPS

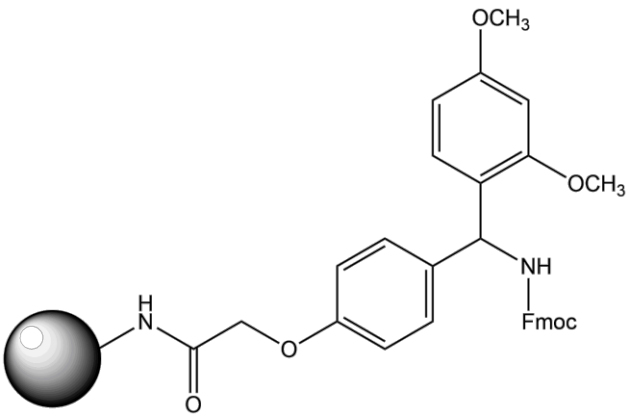

Figure 94. Rink amide linker (RAM)

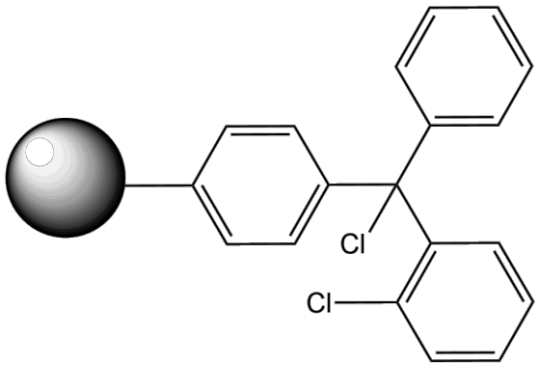

Figure 95. 2-Chlorotritylresin

12.2. Buffers and Standard Solutions

12.2.1. Kcv_{NTS}

12.2.1.1. Native chemical ligation

pH	Name	Ingredients	Organic solvent
7.0 – 7.5	**Buffer A**: HFIP ligation buffer	4 M Urea 0.1 M Na_2HPO_4 150 mM TCEP 100 mM MPAA	1/3 HFIP
7.0 – 7.5	**Buffer B**: TFE ligation buffer (**1**)	8 M Urea 0.2 M Na_2HPO_4 150 mM TCEP 100 mM MPAA	1/3 TFE
4.0	**Buffer C**: Thz conversion	8 M Urea 0.2 MNa_2HPO_4 150 mM TCEP 100 mM MPAA 200 mM Methoxyamine 30 mM TCEP (additionally)	2/3 TFE
7.0 – 7.5	**Buffer D**: TFE ligation buffer (**2**)	8 M Urea 0.2 M Na_2HPO_4 150 mM TCEP 100 mM MPAA	2/3 TFE

Table 45. Buffers for native chemical ligation

12.2.1.2. SDS PAGE

pH	Name	Ingredients
7.00	Reducing sample buffer	12% SDS 6% mercaptoethanol 30% glycerol 0.05% Coomassie blue G-250 150 mM Tris/HCl
7. 00	Nonreducing sample buffer	12% SDS 30% glycerol 0.05% Coomassie blue G-250 150 mM Tris/HCl
8.25	Cathode buffer (10x)	1 M Tris 1 M Tricine 1% SDS
8.9	Anode buffer	1 M Tris 0.225 M HCl

Table 46. Buffers for SDS Page

Name	Ingredients
Coomassie stain	0.025% Coomassie blue G-250 10% acetic acid 90% water
Fixing solution	50% methanol 10% acetic acid 100 mM ammonium acetate
Sensitizing solution	0.005% Sodium thiosulfate In water
Incubation solution	0.1% silver nitrate In water
Development solution	0.036% formaldehyde 2% sodium carbonate In water
Stopping solution	50 mM EDTA In water

Table 47. Solutions for SDS Page. Coomassie and silver stain

12.2.2.ATCUN-like peptides

12.2.2.1. Amino Acid Analysis

pH	Name	Ingredients
5.75	**Buffer E**	50 mM NaAc In water
6.00	**Buffer F**	50 mM NaAc in 300 ml H_2O ad 1000 ml acetonitrile

Table 48. Buffers for AAA

12.2.2.2. Titration and structural studies

pH	Name	Ingredients
6.50	**MES buffer, 100 mM**	1.952 g MES, free acid Ad 100 ml H_2O Adjust pH using NaOH solution
8.00	**Phosphate buffer 100 mM**	50.00 ml 0.4 M K_2HPO_4 46.8 ml 0.4 M NaOH Ad 200 ml H_2O
8.00	**TRIS buffer, 100 mM**	0.6052 g TRIS base Ad 50 ml H_2O Adjust pH using NaOH
10.55	**TRIS buffer, 100 mM**	0.6052 g TRIS base Ad 50 ml H_2O Adjust pH using NaOH
10.55	**CAPS buffer, 100 mM**	1.1066 g CAPS Ad 50 ml H_2O

Table 49. Buffers for titration experiments

For I/V measurements, the MES buffer (100 mM) is spiked with 100 mM KCl.

12.2.2.3. DNA studies

pH	Name	Ingredients	Supplier
7.4	**TRIS HCl buffer (Stock solution, 1 M)**	60.57 g Tris base 32.5 ml HCl (12 M) Ad 500 ml water	/
7.9	**CutSmart buffer**	50 mM Potassium acetate 20 mM TRIS-acetate 10 mM Magnesium acetate 100 μg/ml BSA	New England Biolabs
n/a	**Phusion® HF buffer**	n/a	New England Biolabs
8.5	**TAE buffer (50 x)**	40 mM Tris free base 2 mM Disodium EDTA 20 mM glacial acetic acid	/

Table 50. Buffers for DNA studies

pH	Name	Ingredients	Supplier
8.8	Elution buffer **NE**	5 mM Tris/HCl	Macherey-Nagel
5.0 – 6.0	Binding buffer **NTI**	Guanidinium thiocyanate 30 – 45%	Macherey-Nagel
n.A.	Wash buffer **NT3**	Ethanol	Macherey-Nagel
n.A.	Resuspension buffer **A1**		Macherey-Nagel
n.A.	Lysis buffer **A2**	Sodium hydroxide solution	Macherey-Nagel
n.A.	Neutralization buffer **A3**	Guanidine hydrochloride	Macherey-Nagel
n.A.	Wash buffer **AW**	Guanidine hydrochloride 2-propanol	Macherey-Nagel
8.5	Elution buffer **AE**	5 mM Tris/HCl	Macherey-Nagel

Table 51. Buffers and solutions for DNA purification

12.3. Plasmids

pUC19 – supplier: ThermoFisher Scientific

pASK-IBA3plus (pASK) – supplier: IBA, BioTAGnology Cat. No.: 2-1402-000

pACYCT2 (pACY) – was gifted from Luc Ponchon Addgene plasmid #45799

12.4. Purification Kits

Application	Name of kit	Supplier
Gel extraction	NucleoSpin® Gel and PCR Clean-up	Macherey-Nagel
PCR purification	NucleoSpin® Gel and PCR Clean-up	Macherey-Nagel
DNA purification	NucleoSpin® Plasmid DNA purification	Macherey-Nagel

Table 52. DNA purification kits

12.5. Primer

12.5.1.For pUC19

Name	Sequence	Binding site
pUC A fw	TCTCATGACCAAAATCCCTTAACGTGAG	2237 .. 2264
pUC A rv	GAGCGGTATCAGCTCACTCAAGG	324 .. 347
pUC B fw	CTTTCCTGCGTTATCCCCTGATTCTG	280 .. 305
pUC B rv	GGTCTGACGCTCAGTGGAACG	2269 .. 2289
pUC C fw	TATCCCCTGATTCTGTGGATAACCG	291 .. 315
PUC C rv	CCACTCGTGCACCCAAVTGATC	1389 .. 1410
pUC C1	GTGCCACCTGACGTCTAAGAAAC	1140 .. 1162
pUC C2	CCTCTGACACATGCAGCTCCCGG	1033 .. 1055
pUC C3	TGGCTTAACTATGCGGCATCAG	925 .. 946
pUC C4	ATTCAGGCTGCGCAACTGTTG	816 .. 836
pUC C5	TGGCGTAATCATGGTCATAGCTG	610 .. 632

Table 53. Primer for pUC19

12.5.2.For pASK-IBA3 (pASK)

Name	Sequence	Binding site
pASK A fw	TTTGTCTGCCGTTTACCGCTAC	321 .. 342
pASK A rv	CCACTCGTGCACCCAACTGATC	1051 .. 1072
pASK B fw	TCTCATGACCAAAATCCCTTAACGTGAG	2514 .. 2541
pASK B rv	GCTTAATGCGCCGCTACAGG	365 .. 384
pASK C fw	GGTGCCTCACTGATTAAGCATTGG	1780 .. 1803
pASK C rv	GGTCTGACGCTCAGTGGAACG	2546 .. 2566
pASK D fw	AACGCTGGTGAAAGTAAAAGATGCTG	1023 .. 1048
pASK D rv	CACATTTAAGTTGTTTTTCTAATCCGCAGATGATCAATTCAAGGC	2380 .. 2425

Table 54. Primer for pASK-IBA3

12.5.3.For pACYCT2 (pACY)

Name	Sequence	Binding site
pACY A fw	TGTCTCATTCCACGCCTGACACTC	2185 .. 2209
pACY A rv	CCGGAAGCTTCTCATTAGGCACCGGGATCTCGA	2702 .. 2724
pACY B fw	GGGCTTGTTAGCAGCCGGATCTCACAGCGGTTTCTTTACCAGACTCGAG	322 .. 346
pACY B rv	TCAAATGTAGCACCTGAAGTCAGCC	2587 .. 2611
pACY C fw	AGATCTCAATGGATATCGGCCGG	273 .. 296
pACY C rv	GTGTCAGGCGTGGAATGAGACAAAC	2157 .. 2181

Table 55. Primer for pACYCT2

The primers were kindly designed by Alexander Gräwe (RG Stein, TU Darmstadt)

13. Appendix

13.1. Supporting Information

Supporting Information: Synthesis and characterization Kcv_{NTS}

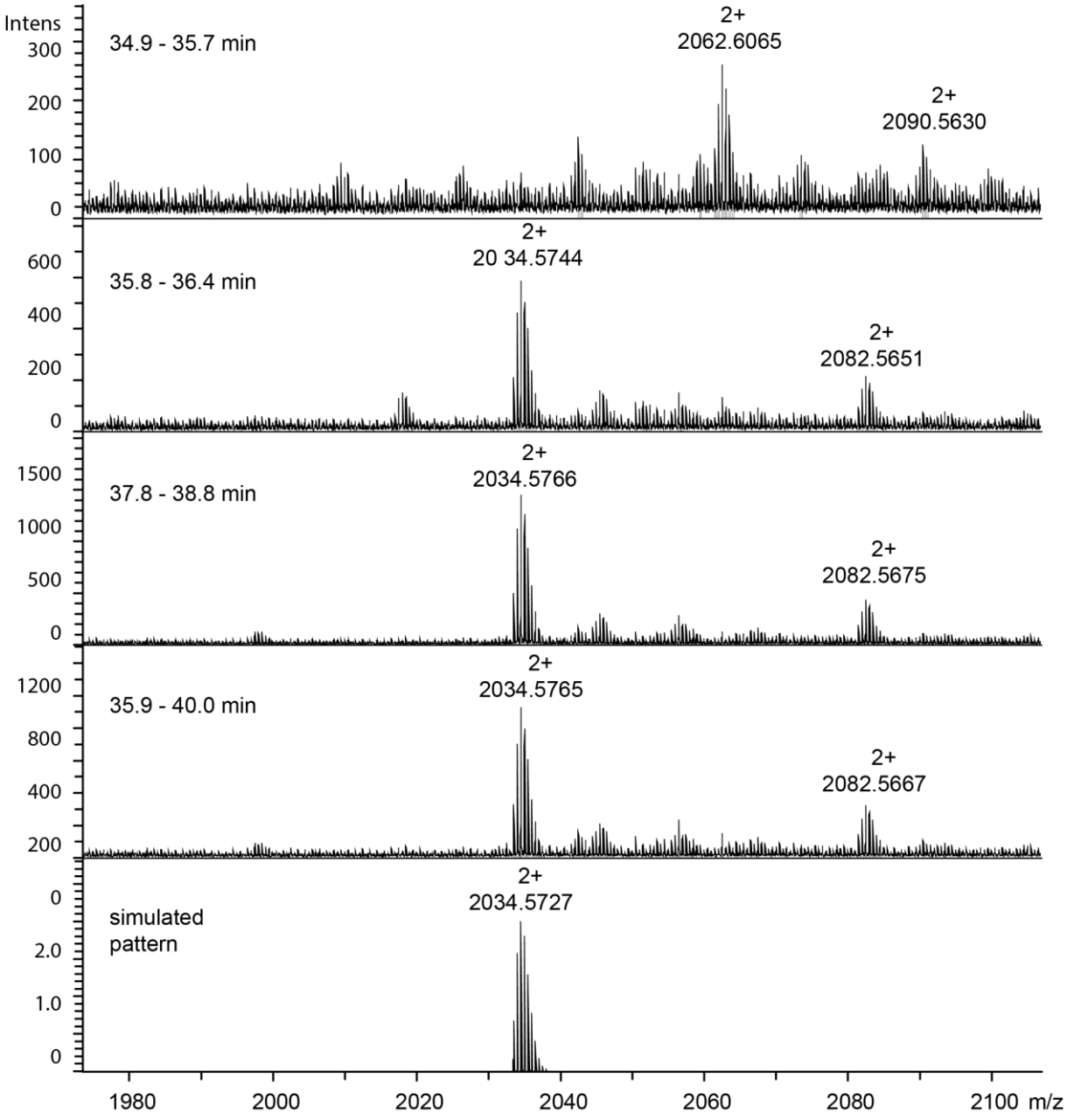

SI Figure 1. LC-MS overview of fragment B

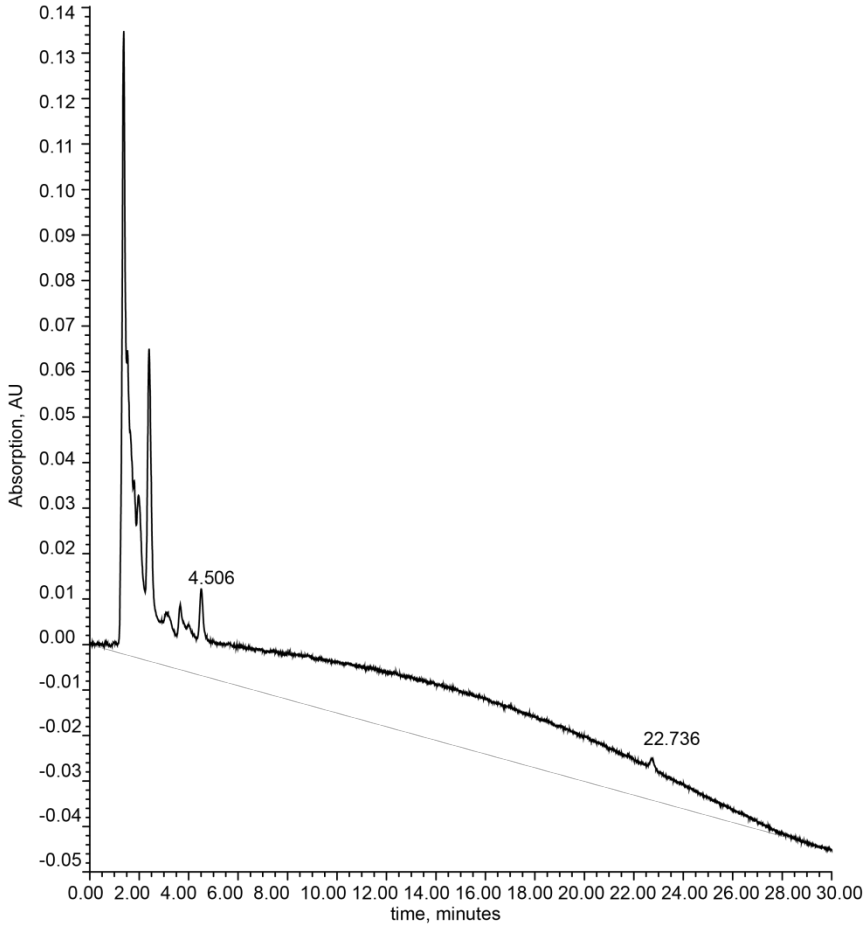

SI Figure 2. RP-HPLC of Hmp fragment in OG, crude product

RP-HPLC of crude product gradient: 60% eluent B to 99% in 30 minutes with a flow of 1 ml/min on the MultoHigh BIO 300 column at 30 °C

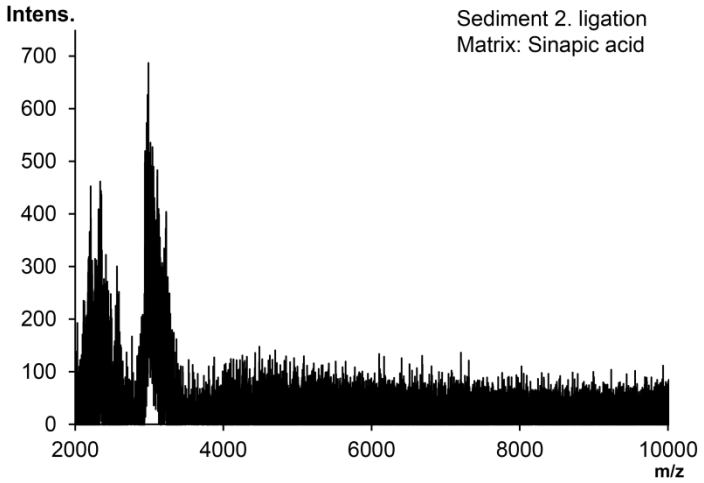

SI Figure 3. Second ligation using SA as MALDI-TOF MS matrix

The spectra is recorded in the LP mode

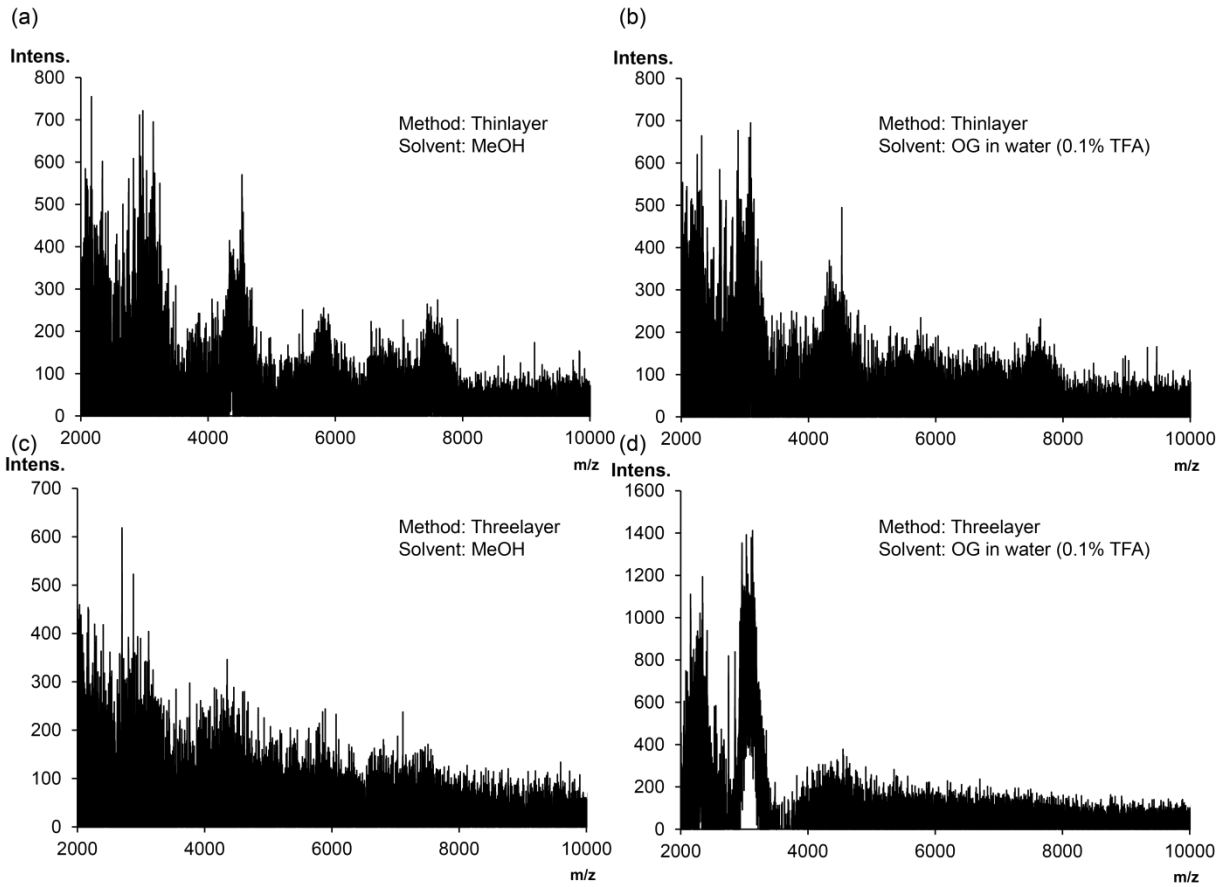

SI Figure 4. Second ligation using different methods for MALDI-TOF MS

(a) Displays the Thinlayer method using MeOH as the solvent for the sediment of the second ligation and (b) using 1 mM OG in H_2O + 0.1% TFA. (c) shows the Threelayer method with MeOH as the solvent and (d) 1 mM OG in H_2O + 0.1% TFA for dissolving the sediment. All spectra are recorded in the LP mode

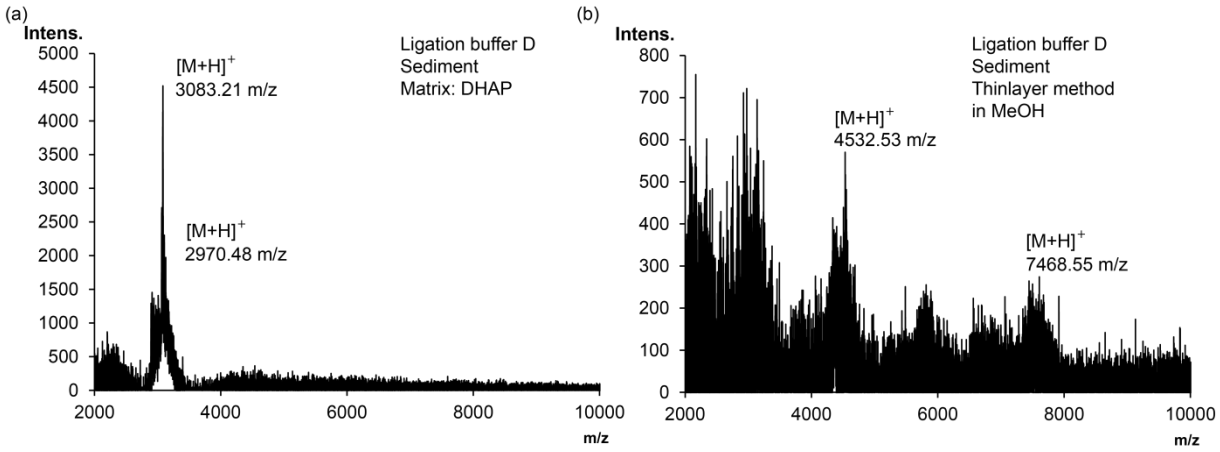

SI Figure 5. Comparison of DHAP and Thinlayer method for investigation of sediment from second ligation

Using DHAP as the matrix for MALDI-TOF MS of the sediment from the second ligation results in a spectra displaying little peaks (a) with (b) the Thinlayer method with MeOH as a solvent showing numerous peaks in areas > 4000 m/z

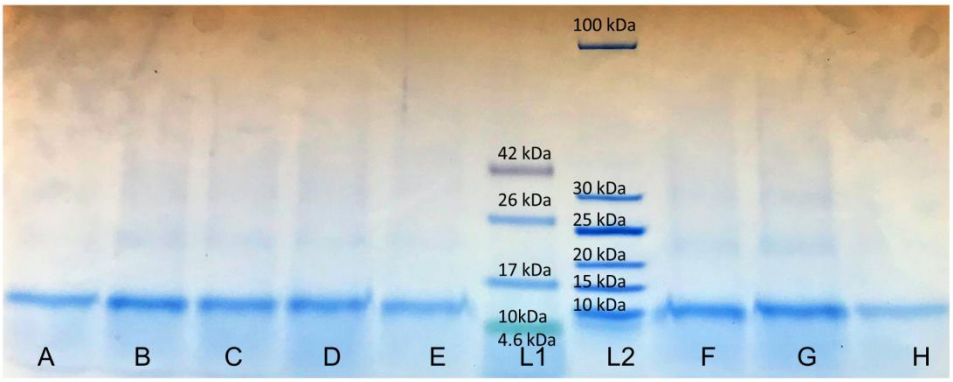

SI Figure 6. SDS PAGE Coomassie stain of second ligation

A	**B**	**C**	**D**	**E**	**F**	**G**	**G**	**L1**	**L2**
Start	30 min	1 h	2 h	4 h	8 h	24 h	Sediment	Colored protein ladder	Uncolored protein ladder

SI Table 1. Samples for SDS PAGE of the final product Kcv_{NTS} 1

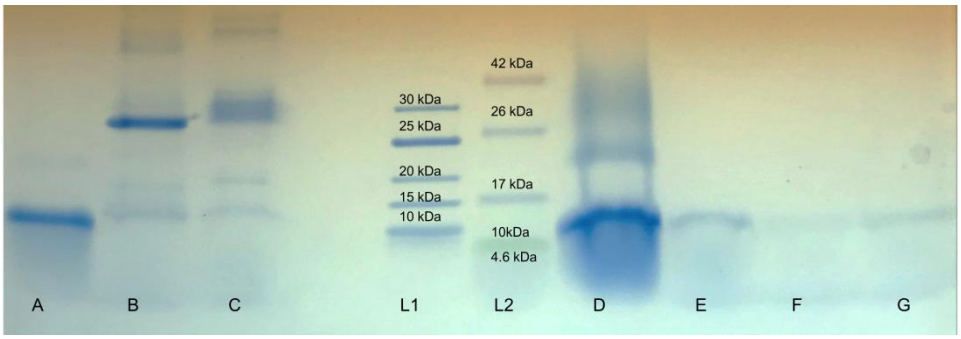

SI Figure 7. SDS PAGE Coomassie stain of ligation solution and positive samples

A	**B**	**C**	**D**	**E**	**F**	**G**
ligation product 1.2	Kcv_{NTS} in lipids	Kcv_{NTS} in nanodiscs	**ligation product 2** (solution)	**ligation product 2**, Vivaspin centri-fugation	**ligation product 2** (solution other batch)	**ligation product 2** (sediment)

SI Table 2. Samples for SDS PAGE of the final product Kcv_{NTS} 2

L1 – uncolored protein ladder

L2 – colored protein ladder

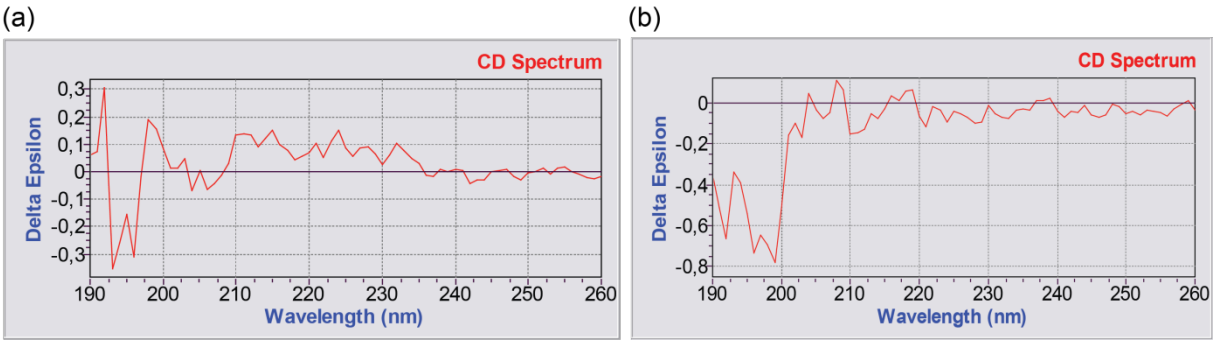

SI Figure 8. CD spectra using POPC lipids

(a) blank sample POPC (b) ligation TFE sample using POPC and the extrusion method

To further evaluate the applicability of the AAA method, a validation was conducted.

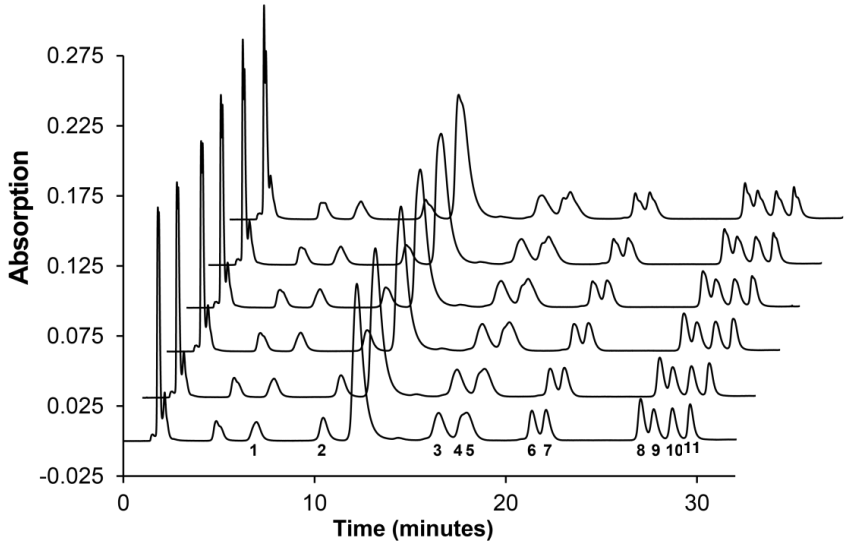

SI Figure 9.Amino Acid Standard

Method: linear gradient of 2% to 20% buffer B in 30 minutes using a flow of 1 ml/min and the MultoKrom C18 column at 45 °C.

Number	1	2	3	4	5	6	7	8	9	10	11
Retention time (min)	6.7	10.4	16.5	17.9	17.9	21.3	22.1	27.0	27.7	28.7	29.6

SI Table 3. Retention times of amino acids during AAA

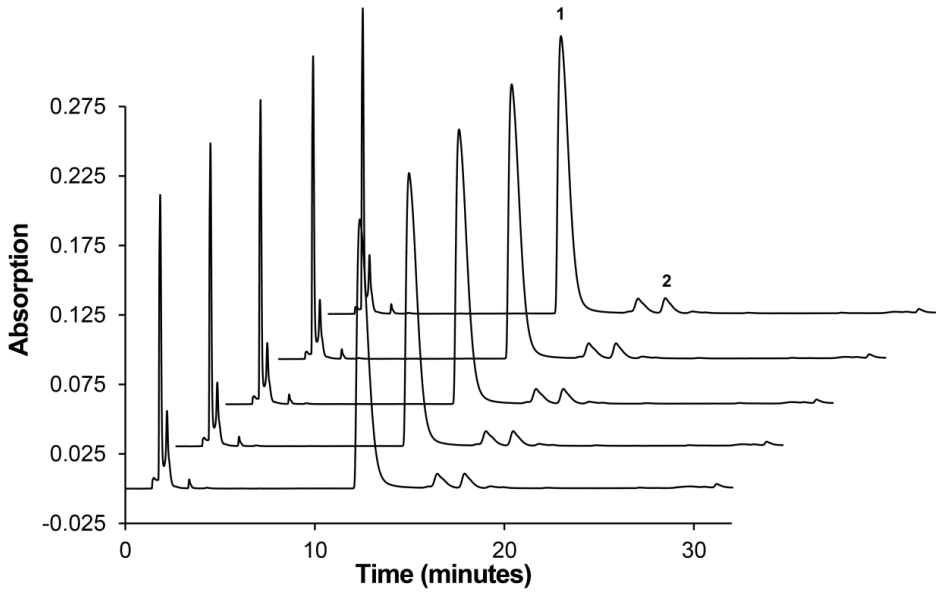

SI Figure 10. Injections of sample

Method: linear gradient of 2% to 20% buffer B in 30 minutes using a flow of 1 ml/min and the MultoKrom C18 column at 45 °C. 1 in the chromatogram, the His moiety of the sample, shows a retention time of 17.0 minutes.

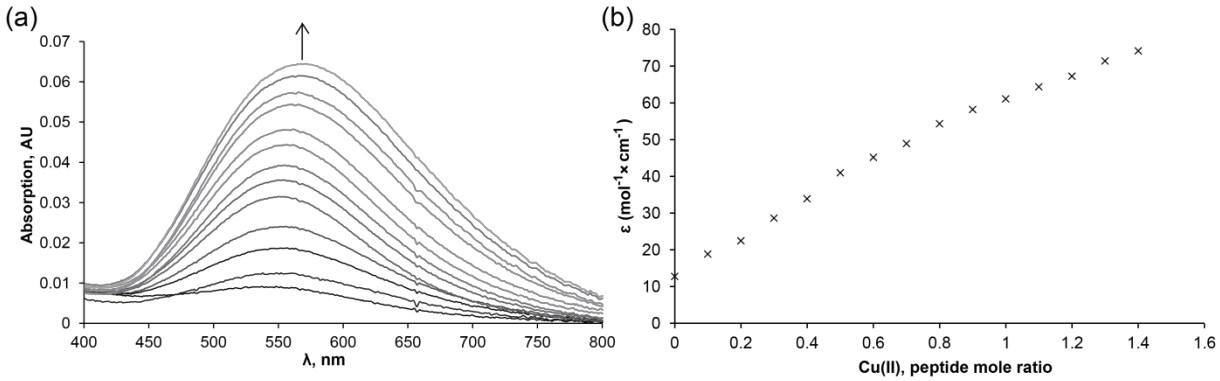

SI Figure 11. UV VIS titration of Cu(II) to peptide 1 in TRIS buffer pH 8.00

UV-VIS titration experiments of peptide 1 (1 mM peptide, in Tris buffer pH 8). (a) increase in absorption upon addition of 0.1 equivalents Cu(II) ($CuSO_4$, in water), wavelengths of 400 - 800 nm. (b) extinction coefficient of the peptide 1-Cu(II) complex vs. equivalents of Cu(II) added.

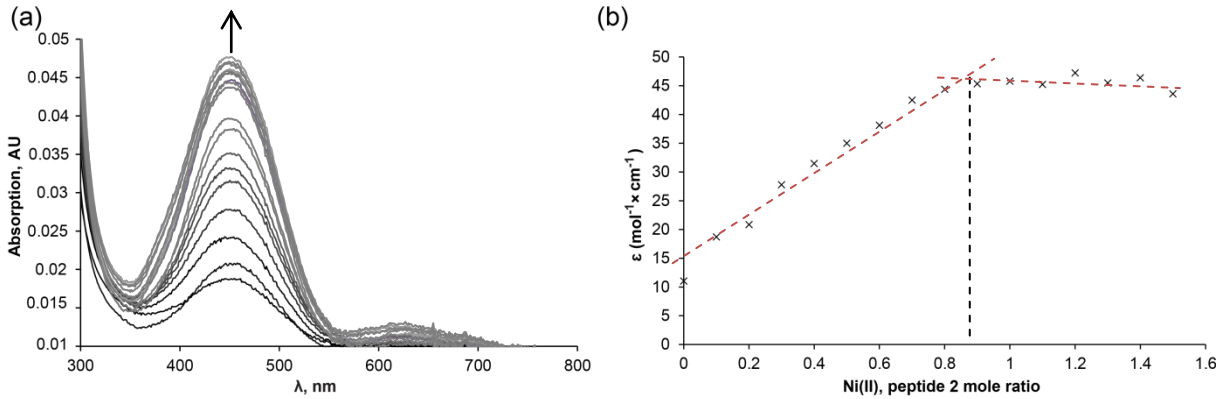

SI Figure 12. UV VIS titration of Ni(II) to peptide 1 in TRIS buffer pH 10.55

UV-VIS titration experiments of peptide 1 (1 mM peptide, in Tris buffer pH 10.55). (a) increase in absorption upon addition of 0.1 equivalents Ni(II) ($NiSO_4$, in water), wavelengths of 300 - 800 nm. (b) extinction coefficient of the peptide 1-Ni(II) complex vs. equivalents of Ni(II) added.

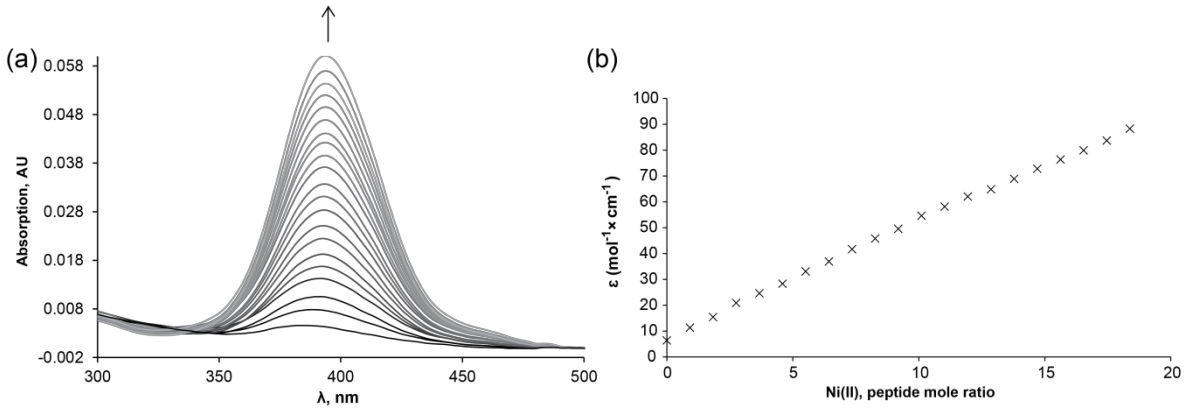

SI Figure 13. UV-Vis Titration of Ni(II) to peptide 1 in MES buffer pH 6.5

UV-VIS titration experiments of peptide 1 (1 mM peptide, in MES buffer pH 6.5). (a) increase in absorption upon addition of 0.1 equivalents Ni(II) ($NiSO_4$, in water), wavelengths of 300 - 500 nm. (b) extinction coefficient of the peptide 1-Ni(II) complex vs. equivalents of Ni(II) added.

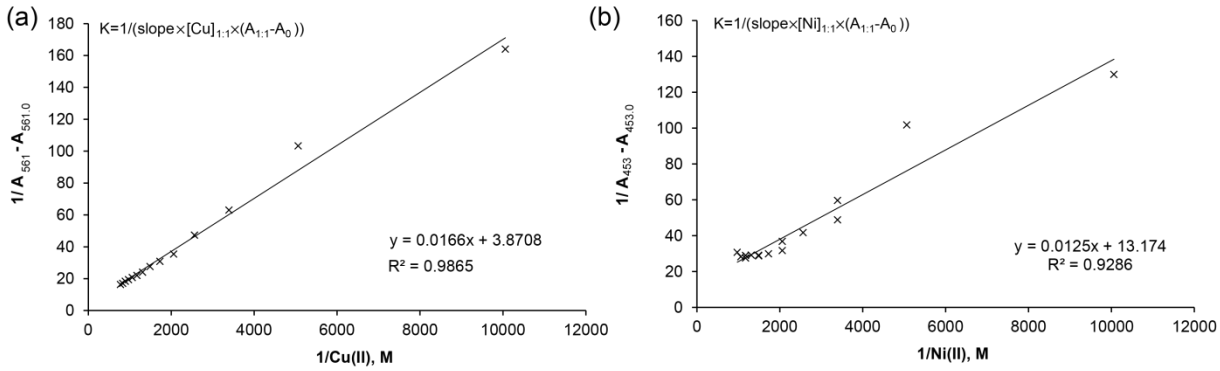

SI Figure 14. Benesi Hildebrand plot of Cu(II) and Ni(II) titrations to peptide 1 at optimal pH values

UV VIS titration experiments of 1 mM peptide 1 in (a) Tris buffer pH 8.0 and addition of Cu(II) and (b) Tris buffer pH 10.55 and addition of Ni(II).

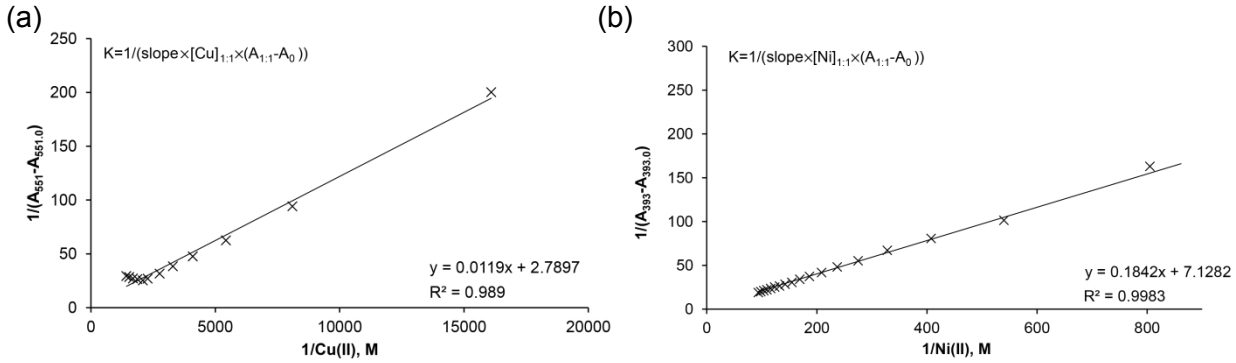

SI Figure 15. Benesi Hildebrand plot for peptide 1-Cu(II) and peptide 1-Ni(II) binding at pH 6.5

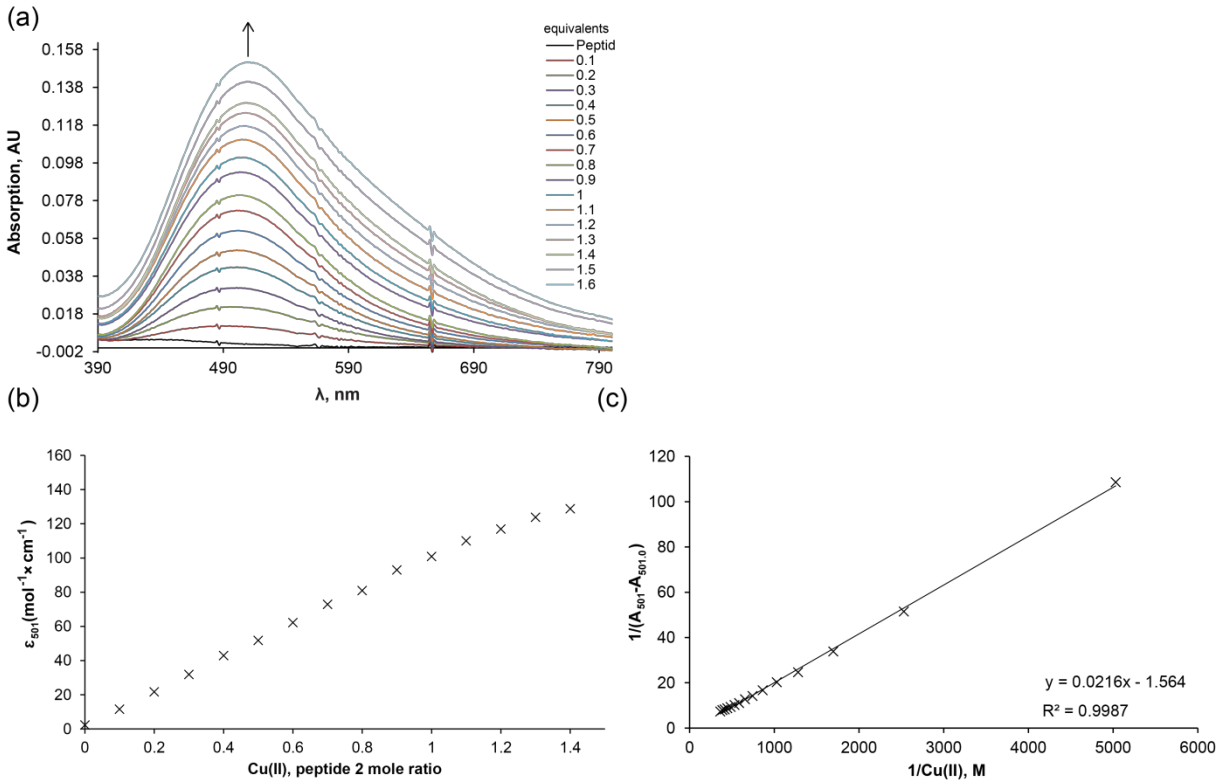

SI Figure 16. Cu(II) titration to peptide 2 at pH 8 in 100 mM Tris buffer

(a) Increased absorption of peptide 2 solution upon addition of Cu(II) between 390 – 800 nm to visualize absorption of the peptide 2-Cu(II) complex. (b) describes increase of the extinction coefficient in regard to equivalents of copper added to the peptide solution. (c) shows the Benesi Hildebrand plot with a correlation coefficient of $R^2 = 0.9987$. Λ_{max} for the peptide 2opper complex is 501 nm.

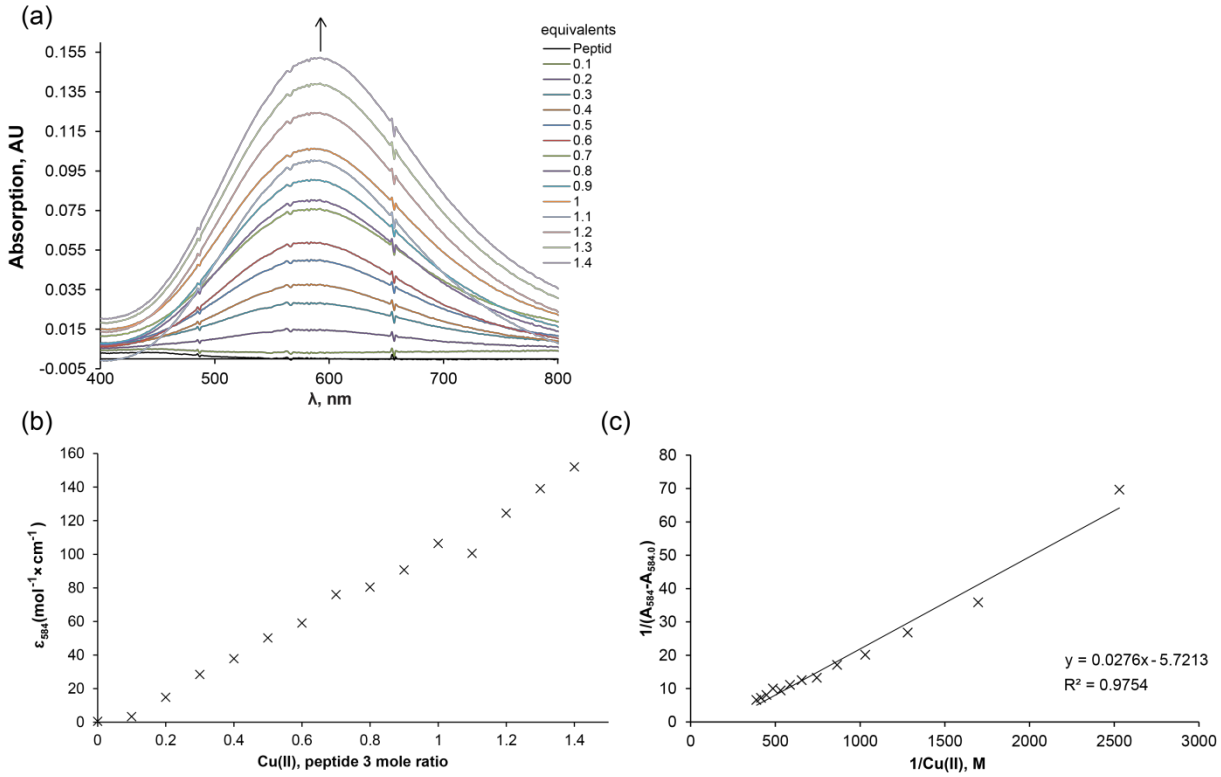

SI Figure 17. UV VIS titration of Cu(II) to peptide 3 at optimal pH

(a) Increased absorption of peptide 3 solution upon addition of Cu(II) between 400 – 800 nm to visualize absorption of the peptide 3-Cu(II) complex. (b) describes increase of the extinction coefficient in regard to equivalents of copper added to the peptide solution. (c) shows the Benesi Hildebrand plot with a correlation coefficient of $R^2 = 0.9754$. Λ_{max} for the peptide 2opper complex is 584 nm.

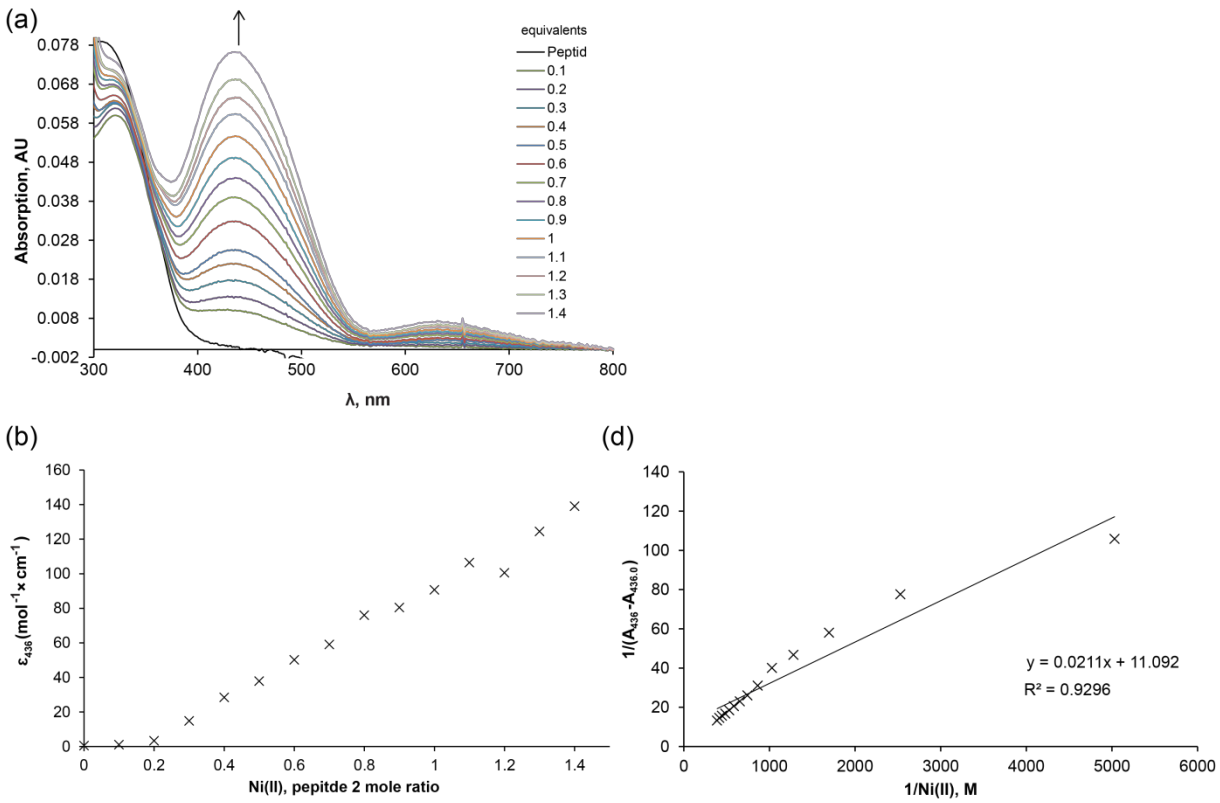

SI Figure 18. UV VIS titration of Ni(II) to peptide 2 at optimal pH

(a) Increased absorption of peptide 2 solution upon addition of Ni(II) between 300 – 800 nm to visualize absorption of the peptide 2-Ni(II) complex. (b) describes increase of the extinction coefficient in regard to equivalents of nickel added to the peptide solution. (c) shows the Benesi Hildebrand plot with a correlation coefficient of $R^2 = 0.9296$. λ_{max} for the peptide nickel complex is 436 nm.

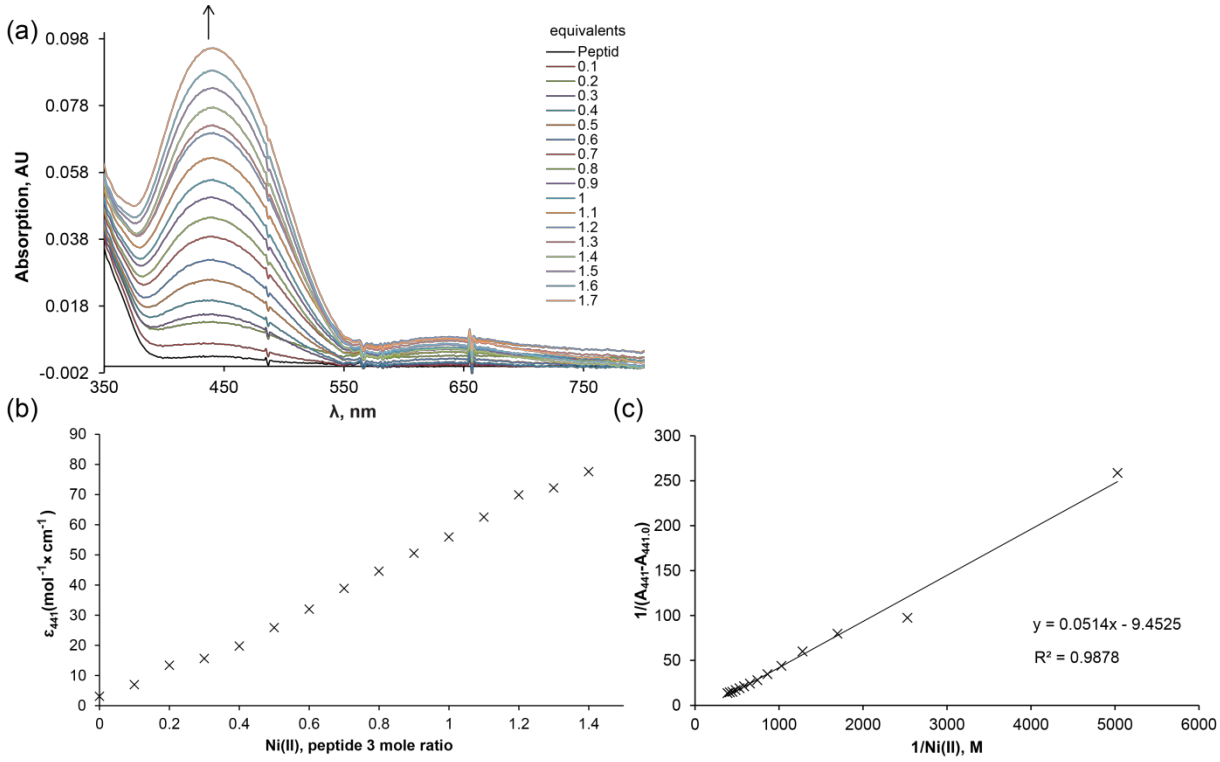

SI Figure 19. UV VIS titration of Ni(II) to peptide 3 at optimal pH

(a) Increased absorption of peptide 3 solution upon addition of Ni(II) between 350 – 800 nm to visualize absorption of the peptide 3-Ni(II) complex. (b) describes increase of the extinction coefficient in regard to equivalents of nickel added to the peptide solution. (c) shows the Benesi Hildebrand plot with a correlation coefficient of $R^2 = 0.9878$. λ_{max} for the peptide nickel complex is 441 nm.

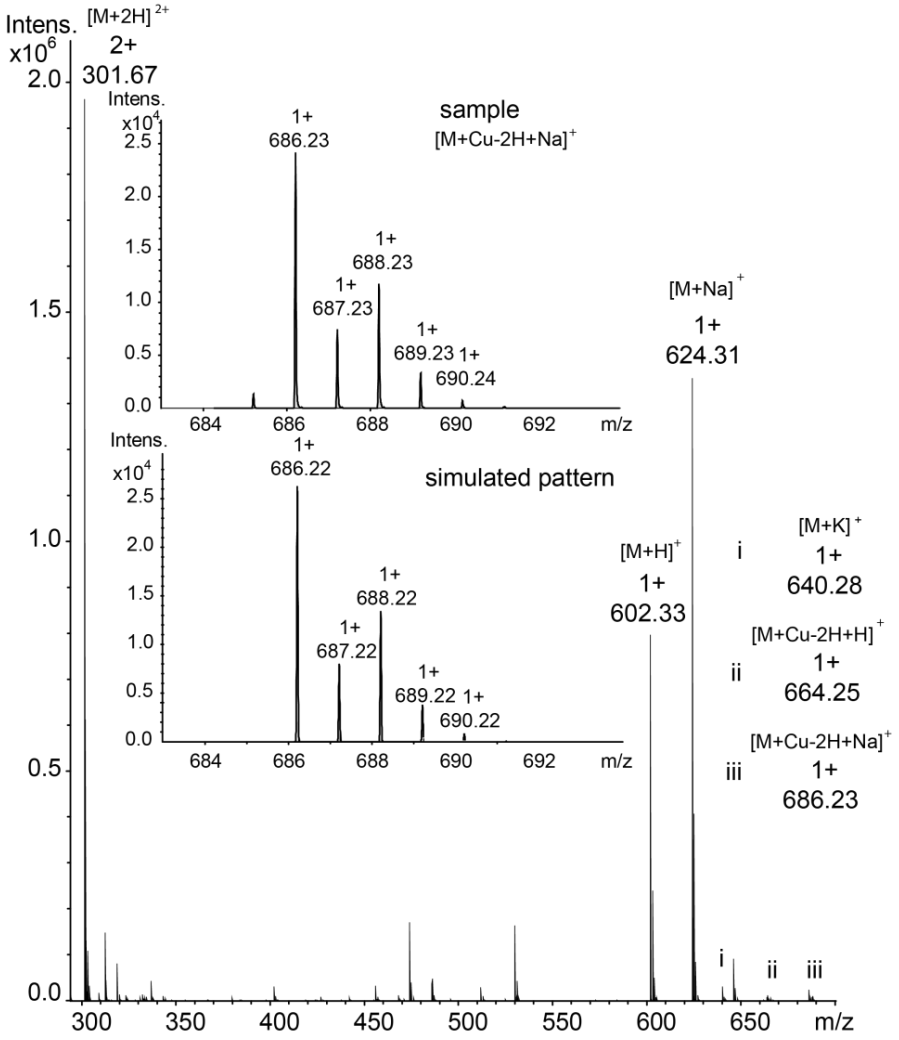

SI Figure 20. MS of peptide 1-Cu(II) complex

Species	Calculated m/z	Measured m/z
$[M+H^+]^+$ ($M = C_{25}H_{43}N_7O_{10}$)	602.31	602.33
$[M+2H^+]^{2+}$	301.66	301.67
$[M+Na^+]^+$	624.64	624.31
$[M+K^+]^+$	640.75	640.28
$[M-2H+Cu+H^+]^+$	664.19	664.25
$[M-2H+Cu+Na^+]^+$	686.17	686.23

SI Table 4. MS of peptide 1-Cu(II) complex. Calculated and measured m/z

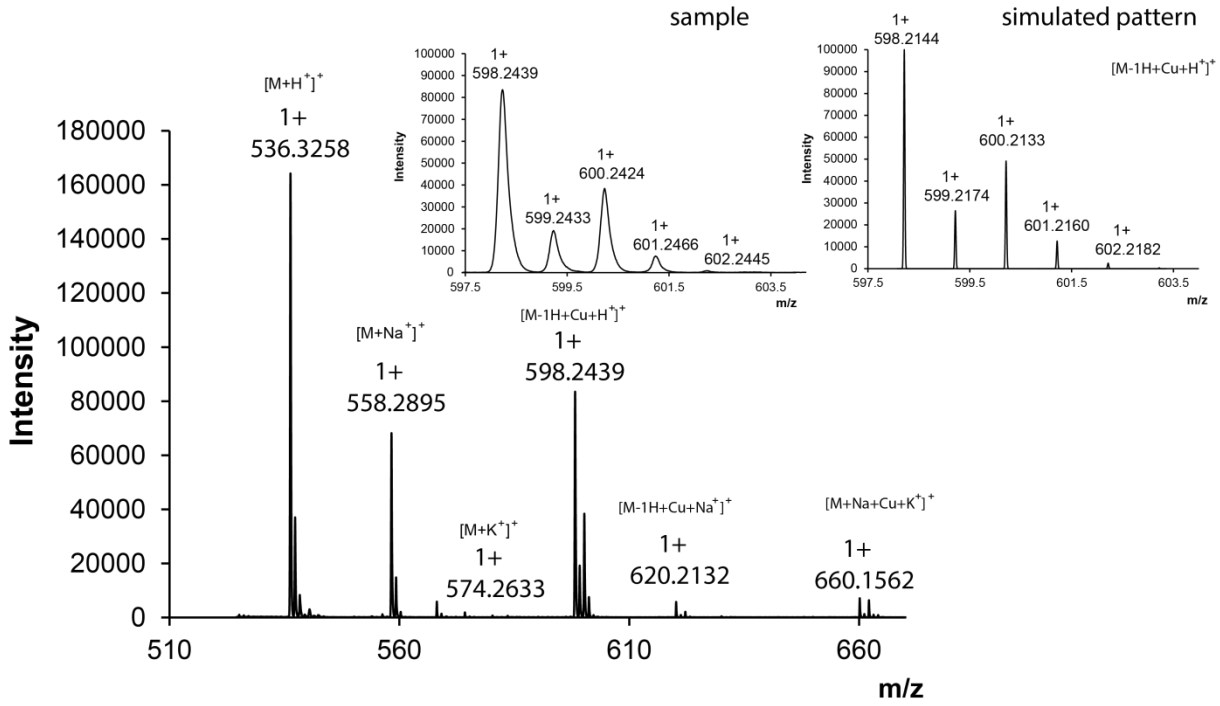

SI Figure 21. MS of peptide 2-Cu(II) complex

The following table shows the calculated and measured masses for species shown in this figure.

Species	Calculated m/z	Measured m/z
$[M+H^+]^+$ ($M = C_{22}H_{41}N_5O_{10}$)	536.2926	536.3258
$[M+Na^+]^+$	558.2746	558.2895
$[M+K^+]^+$	574.2485	574.2633
$[M\text{-}H+Cu+H^+]^+$	598.2144	598.2439
$[M\text{-}H+Cu+Na^+]^+$	620.1960	620.2132
$[M+Na+Cu+K^+]^+$	660.1679	660.1562

SI Table 5. MS of peptide 2-Cu(II) complex. Calculated and measured masses (m/z)

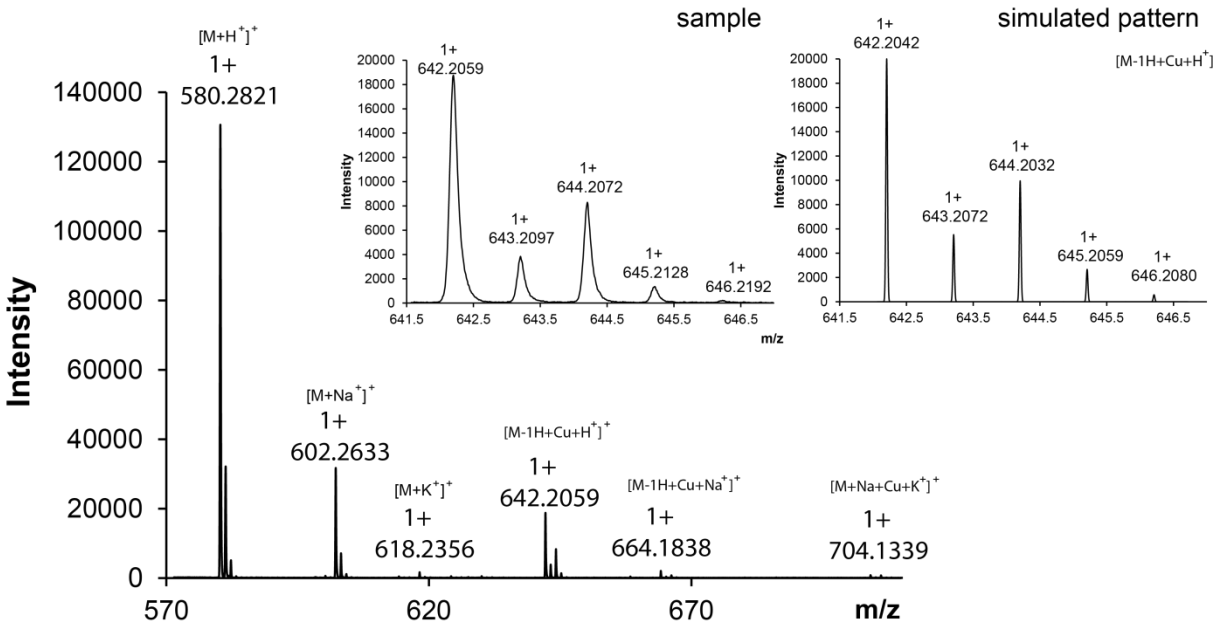

SI Figure 22. MS of peptide 3-Cu(II) complex

The following table shows the calculated and measured masses for species shown in this figure.

Species	Calculated m/z	Measured m/z
$[M+H^+]^+$ ($M = C_{23}H_{41}N_5O_{12}$)	580.2824	580.2821
$[M+Na^+]^+$	602.2644	602.2633
$[M-H+Cu+H^+]^+$	642.2042	642.2059
$[M-H+Cu+Na^+]^+$	664.1862	664.1838
$[M+Na+Cu+K^+]^+$	704.1577	704.1339

SI Table 6. MS of peptide 3-Cu(II) complex. Calculated and measured masses (m/z)

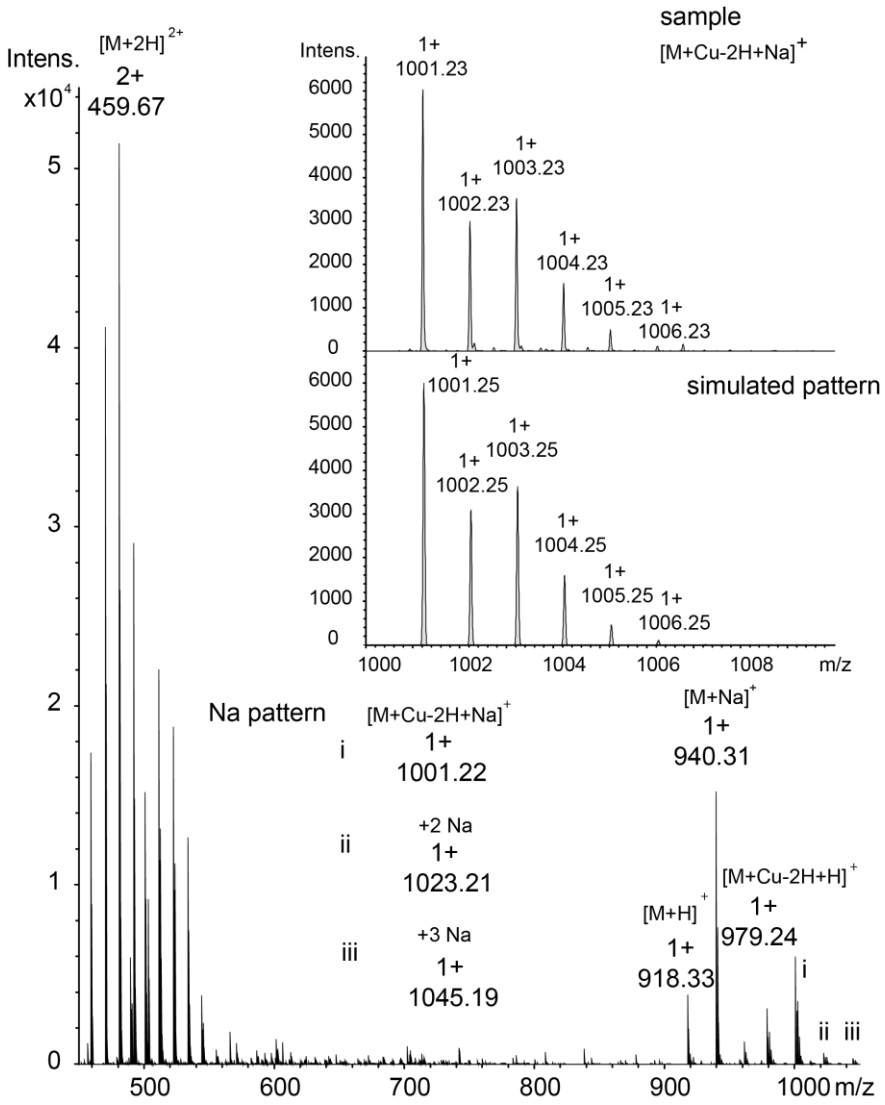

SI Figure 23. MS of peptide 4-Cu(II) complex

Species	Calculated m/z	Measured m/z
$[M+H^+]^+$ ($M = C_{44}H_{51}N_7O_{15}$)	918.35	918.33
$[M+Na^+]^+$	940.90	940.31
$[M+2H^+]^{2+}$	459.68	459.67
$[M\text{-}3H+Cu+H^+]^+$	979.42	979.24
$[M\text{-}3H+Cu+Na^+]^+$	1001.25	1001.22
$[M\text{-}4H+Na+Cu+Na^+]^+$	1023.41	1023.21
$[M\text{-}5H+2Na+Cu+Na^+]^+$	1049.39	1045.19

SI Table 7. MS of peptide 4-Cu(II) complex. Calculated and measured masses m/z

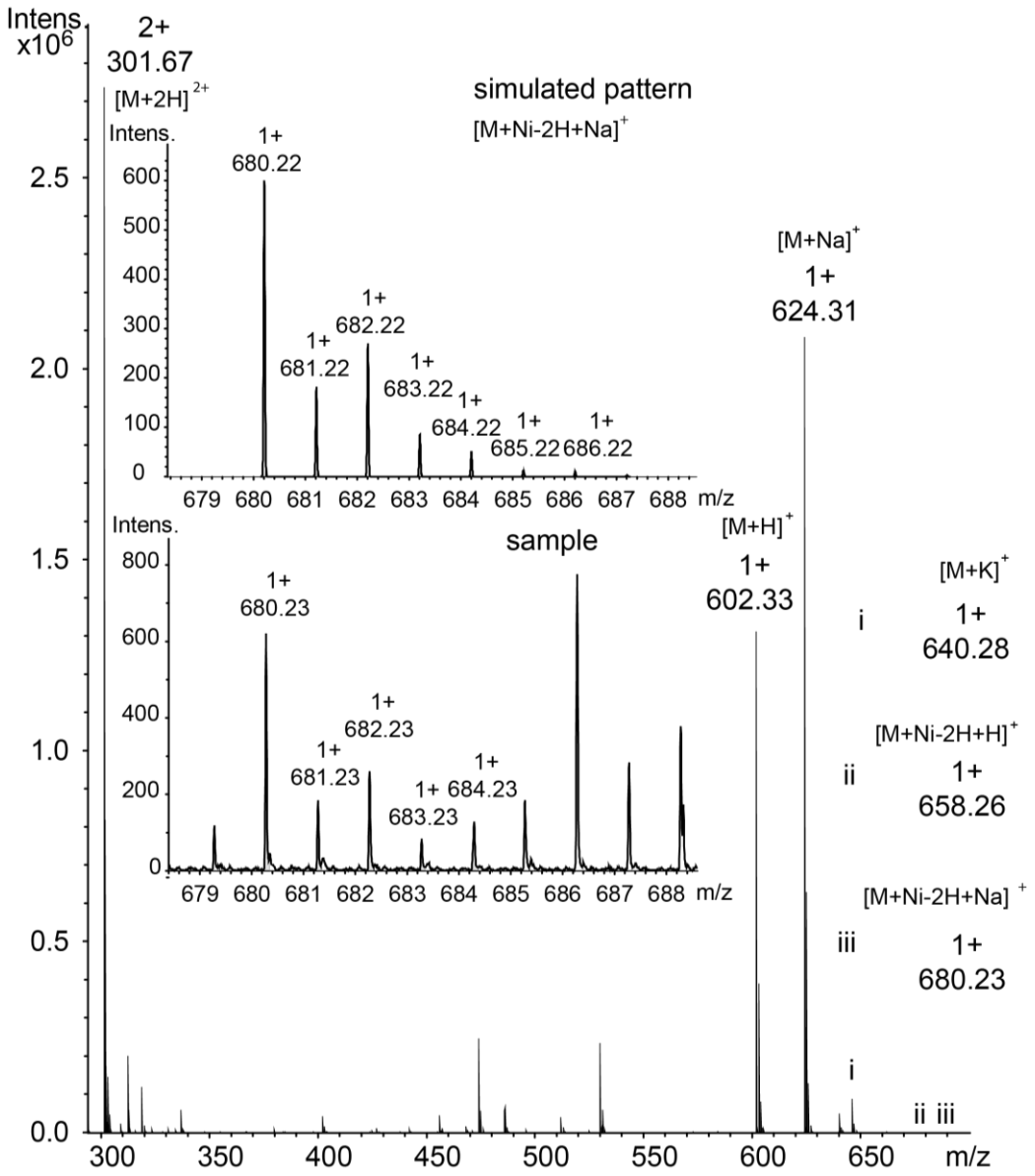

SI Figure 24. MS of peptide 1-Ni(II) complex

Species	Calculated m/z	Measured m/z
$[M+H^+]^+$ ($M = C_{25}H_{43}N_7O_{10}$)	602.31	602.33
$[M+Na^+]^+$	624.64	624.31
$[M+K^+]^+$	640.75	640.28
$[M+2H^+]^{2+}$	301.66	301.67
$[M-H+Ni+H^+]^+$	658.33	658.26
$[M-H+Ni+Na^+]^+$	680.22	680.23

SI Table 8. MS of peptide 1-Ni(II) complex. Calculated and measured masses m/z

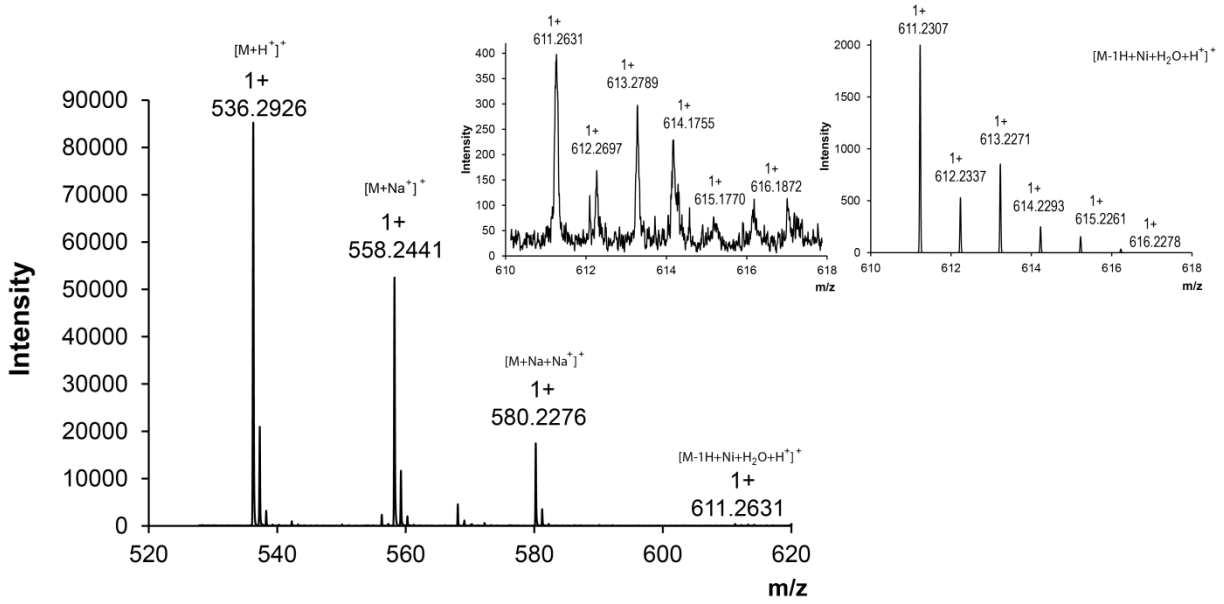

SI Figure 25. MS of peptide 2-Ni(II) complex

The following table shows the calculated and measured masses for species shown in this figure.

Species	Calculated m/z	Measured m/z
$[M+H^+]^+$ ($M = C_{22}H_{41}N_5O_{10}$)	536.2926	536.2661
$[M+Na^+]^+$	558.2746	558.2441
$[M-H+Na+Na^+]^+$	580.2565	580.2276
$[M-H+Ni+H_2O+H^+]^+$	611.2307	611.2631

SI Table 9. MS of peptide 2-Ni(II) complex. Calculated and measured masses (m/z)

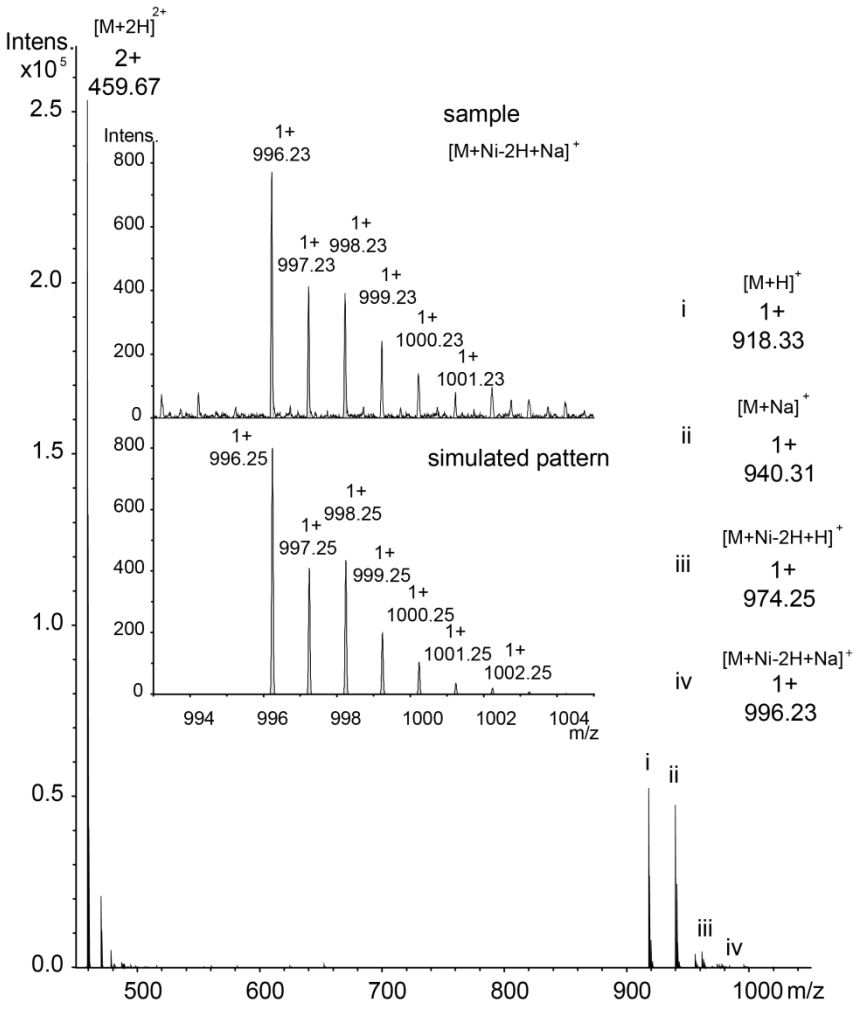

SI Figure 26. MS of peptide 4-Ni(II) complex

Species	Calculated m/z	Measured m/z
$[M+H^+]^+$ ($M = C_{44}H_{51}N_7O_{15}$)	918.35	918.33
$[M+Na^+]^+$	940.90	940.31
$[M+2H^+]^{2+}$	459.68	459.67
$[M\text{-}2H+Ni+H^+]^+$	974.59	974.25
$[M\text{-}2H+Ni+Na^+]^+$	996.25	996.23

SI Table 10. MS of peptide 4-Ni(II) complex. Calculated and measured masses m/z

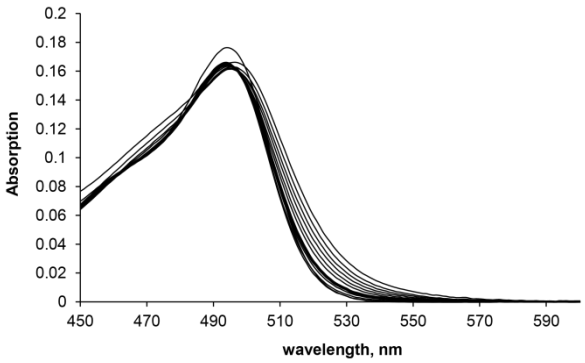

SI Figure 27. UV VIS spectra of Cu(II) titration to peptide 4 in MES buffer pH 6.5

The absorption maximum of the peptide-copper complex is determined to be at around 550 nm. As seen in the figure, the absorption of the fluorophore, 5/6-FAM interferes with the absorption maximum of the complex. An accurate evaluation of the titration data is not given

(a) (b)

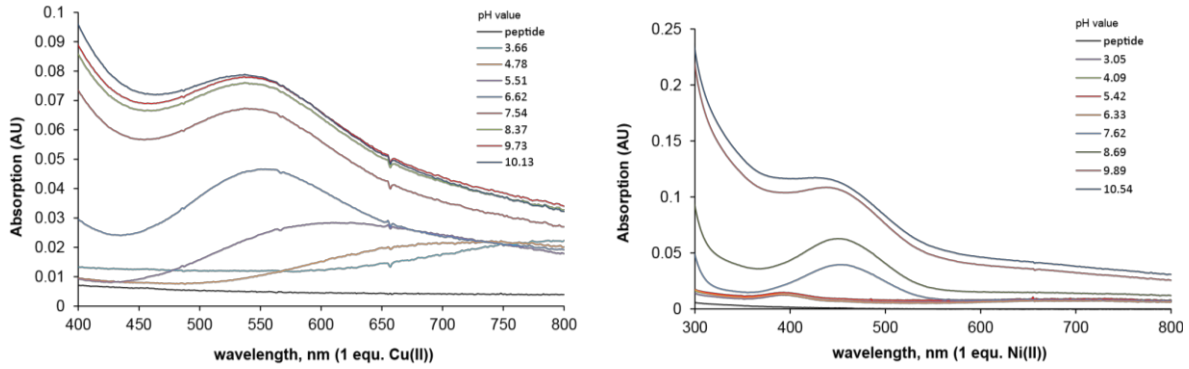

SI Figure 28. pH-dependent titration studies on peptide 1

(a) Absorption spectra for different pH values of 1 mM peptide 4 in water + 1 equ Cu(II). (b) Absorption spectra for different pH values of 1 mM peptide 1 in water + 1 equ Ni(II).

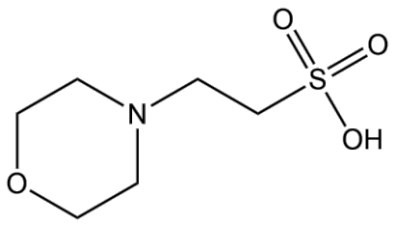

SI Figure 29. Structure of MES

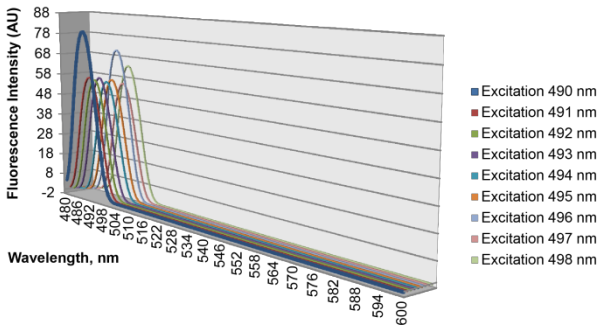

SI Figure 30. MES buffer pH 6.5 at different excitation wavelengths

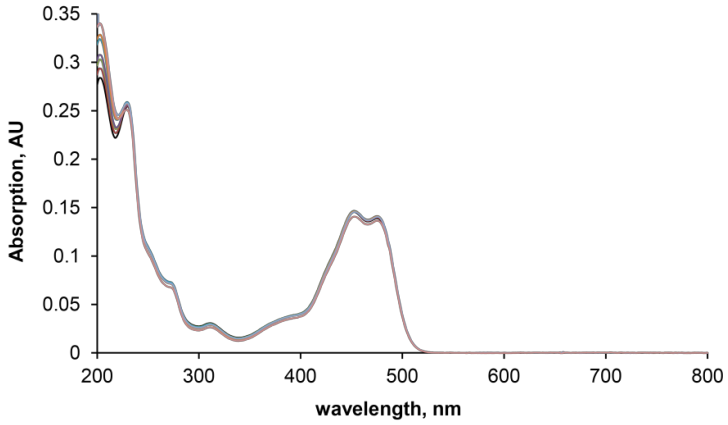

SI Figure 31. Copper titration to 5/6 FAM solution

1 µM 5/6-FAM in water, addition of equivalents of Cu(II) ($CuSO_4$, in water)

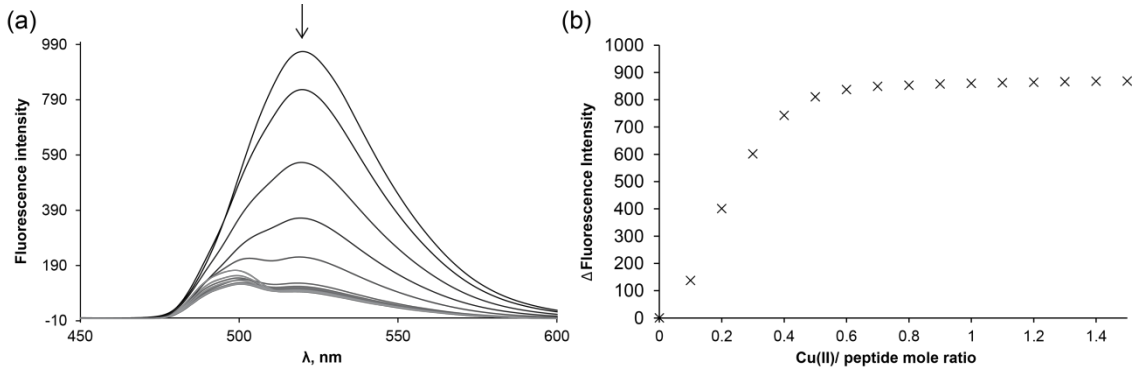

SI Figure 32. Fluorescence titration of copper to peptide 4 in PBS buffer pH 8.00

Fluorescence titration experiment of peptide (0.1 μM in PBS buffer pH 8.0) (a) decrease in fluorescence intensity upon the addition of Cu(II) to the peptide solution (b) change in fluorescence intensity vs. Cu(II) equivalents added to the peptide solution.

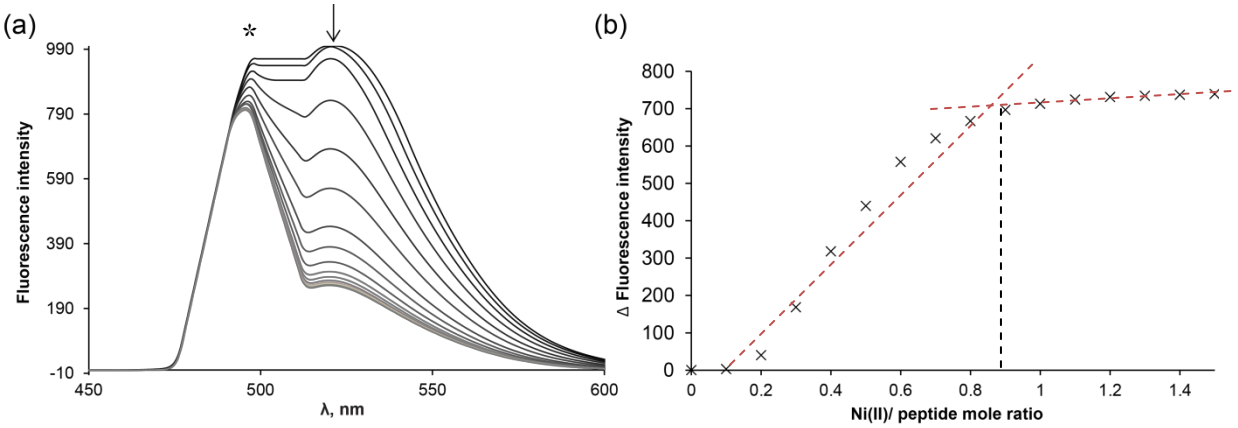

SI Figure 33. Fluorescence titration of nickel to peptide 4 in CAPS buffer pH 10.55

Fluorescence titration experiment of peptide 4 (0.025 μM in CAPS buffer pH 10.55) (a) decrease in fluorescence intensity upon the addition of Ni(II) to the peptide solution (b) change in fluorescence intensity vs. Ni(II) equivalents added to the peptide solution. *At the excitation of 494 nm, CAPS buffer absorbs , interfering the spectra

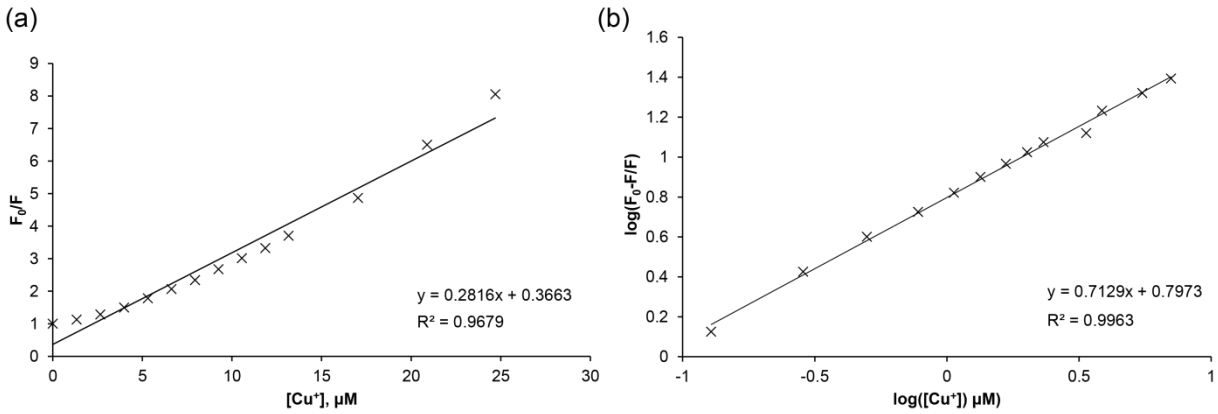

SI Figure 34. Stern-Volmer Plot of peptide 4 with Cu(II) at pH 6.5

(a) plot of F_0/F vs. concentration of Cu(II) to determine the quenching constant from the slope. (b) logarithmic plot to determine binding constant. Fluorescence titration was executed in 100 mM MES buffer pH 6.5 with an excitation at 494 nm and emission at 518 nm

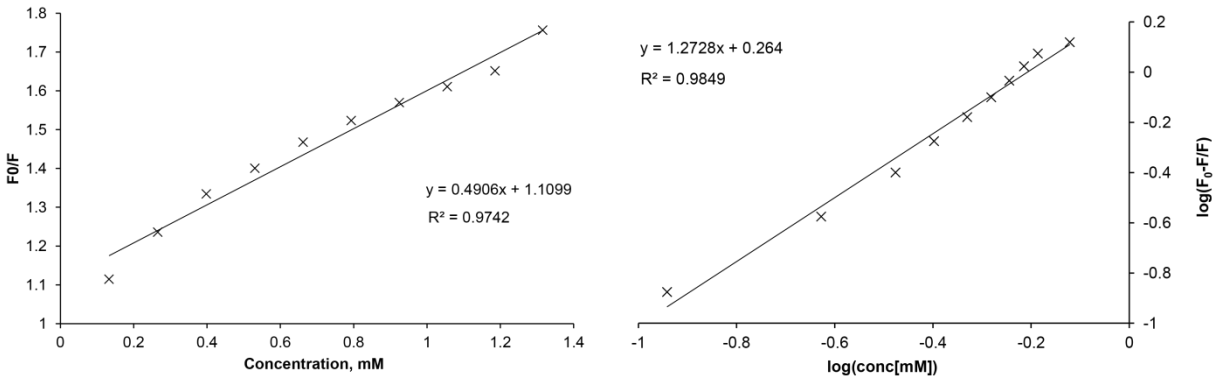

SI Figure 35. Stern-Volmer plot of peptide 4 with Ni(II) at pH 6.5

(a) plot of F_0/F vs. concentration of Ni(II) to determine the quenching constant from the slope. (b) logarithmic plot to determine binding constant. Fluorescence titration was executed in 100 mM MES buffer pH 6.5 with an excitation at 494 nm and emission at 518 nm

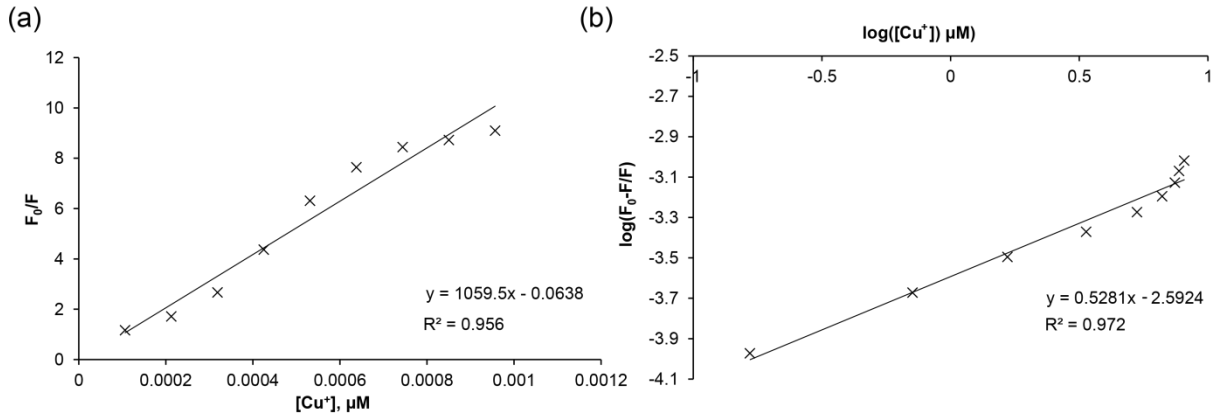

SI Figure 36. Stern-Volmer plot of peptide 1 with Cu(II) at pH 8.0

(a) plot of F_0/F vs. concentration of Cu(II) to determine the quenching constant from the slope. (b) logarithmic plot to determine binding constant. Fluorescence titration was executed in 100 mM PBS buffer pH 8.0 with an excitation at 494 nm and emission at 518 nm

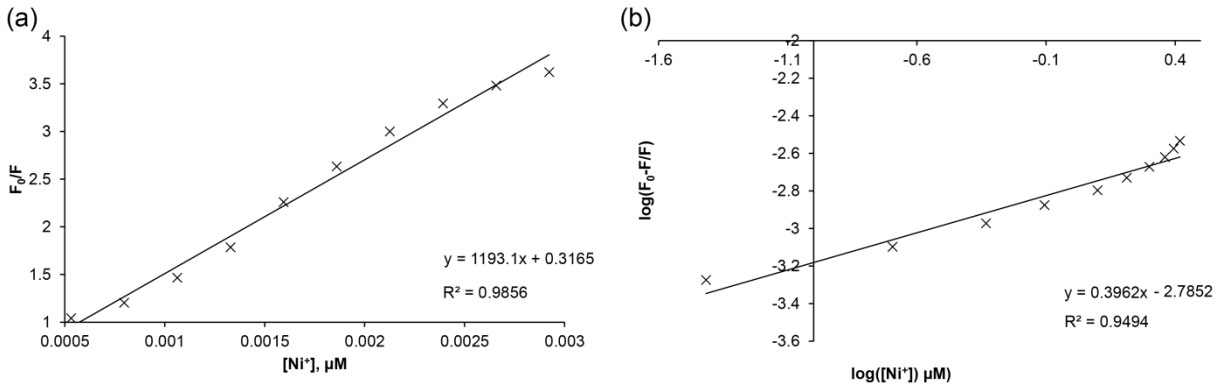

SI Figure 37. Stern-Volmer Plot of peptide 4 with Ni(II) at pH 10.55

(a) plot of F_0/F vs. concentration of Ni(II) to determine the quenching constant from the slope. (b) logarithmic plot to determine binding constant. Fluorescence titration was executed in 100 mM MES buffer pH 6.5 with an excitation at 494 nm and emission at 518 nm

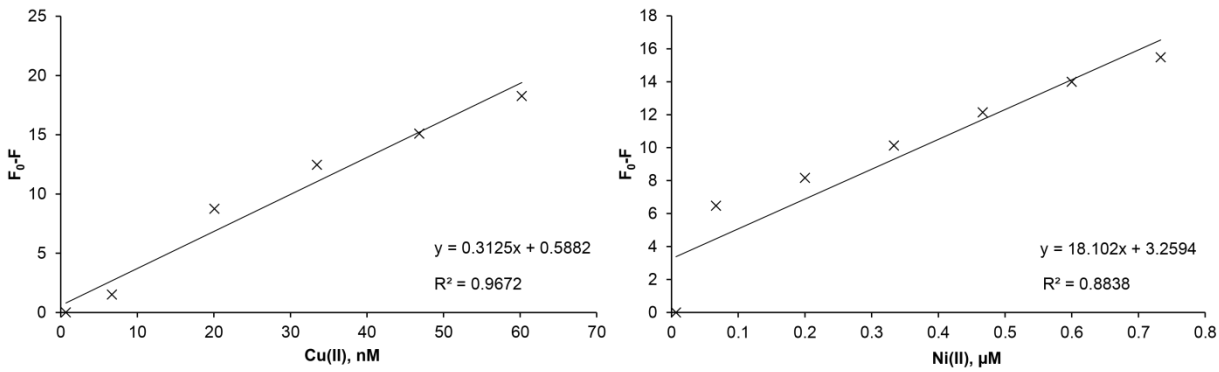

SI Figure 38. Limit of detection of Cu(II) and Ni(II)

To a 1 µM peptide 4 solution (100 mM MES pH 6.5) (a) copper is added in concentrations of 0.67 – 60.22 nM (b) nickel is added in concentrations of 6.67 – 733.33 nM.

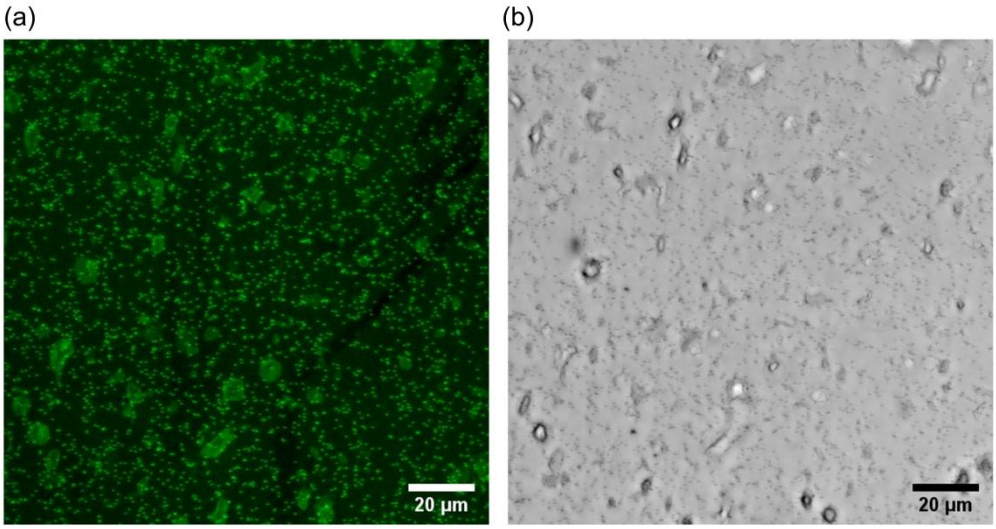

SI Figure 39. Fluorescence and brightlight image of cylindrical nanopores

(a) shows fluorescence image of a PET foil with cylindrical nanopores with a diameter of 200 µm and peptide 4 coupled. Laser details: Emission at 488 nm and excitation at 515 – 530 nm. (b) shows the brightlight image of the same foil section

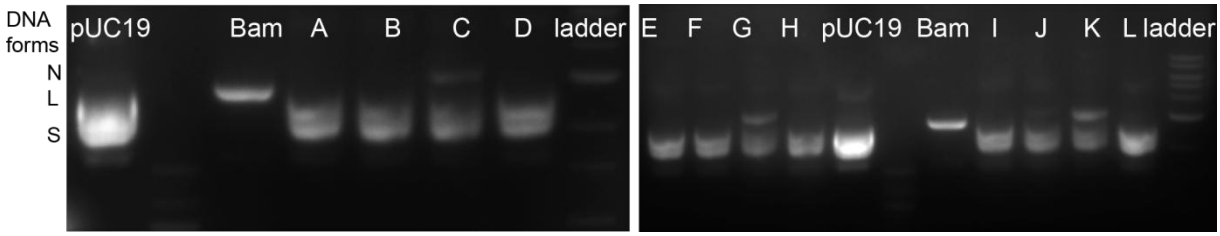

SI Figure 40. Negative samples of peptides 2 - 4 towards pUC19

Lane	**A**	**B**	**C**	**D**	**E**	**F**	**G**	**H**	**I**	**J**	**K**	**L**
Sample	pUC19 + peptide 1				pUC19 + Peptide 2				pUC 19 + Peptide 3			
Time		$+Cu^{2+}$	+Asc	$+Ni^{2+}$		$+Cu^{2+}$	+Asc	$+Ni^{2+}$		$+Cu^{2+}$	+Asc	$+Ni^{2+}$

SI Table 11. Negative samples of peptides 2 - 4 towards pUC19

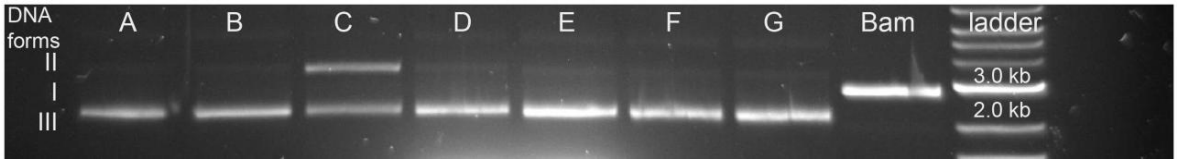

SI Figure 41. Scission of pUC19 using the peptide 4 – Ni(II) and peptide 1 – Ni(II) complexes and negative samples

Lane	**A**	**B**	**C**	**D**	**E**	**F**	**G**
Sample	pUC19	Ni^{2+}	Ni^{2+} Asc	P4 and Ni^{2+}		P1 and Ni^{2+}	
Time	6 h			0 h	6 h	0 h	6 h

SI Table 12. Negative samples and scission of pUC19 and peptide 4 – Ni(II) and peptide 1 – Ni(II) complexes

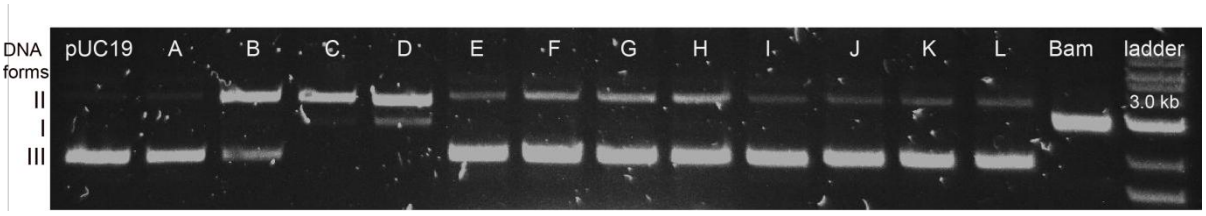

SI Figure 42. Scission of pUC19 using peptide 1-Cu(II)/-Ni(II) and peptide 4 –Ni(II)

Lane	**A**	**B**	**C**	**D**	**E**	**F**	**G**	**H**	**I**	**J**	**K**	**L**
Sample	Peptide 1 + Asc + Cu^{2+}				Peptide 1 + Asc + Ni^{2+}				Peptide 4 + Asc + Ni^{2+}			
Time	0 h	0.5 h	2 h	4 h	0 h	0.5 h	2 h	4 h	0 h	0.5 h	2 h	4 h

SI Table 13. Scission of pUC19 using 100 µM peptide 1 copper and nickel complexes and peptide 4 nickel complexes

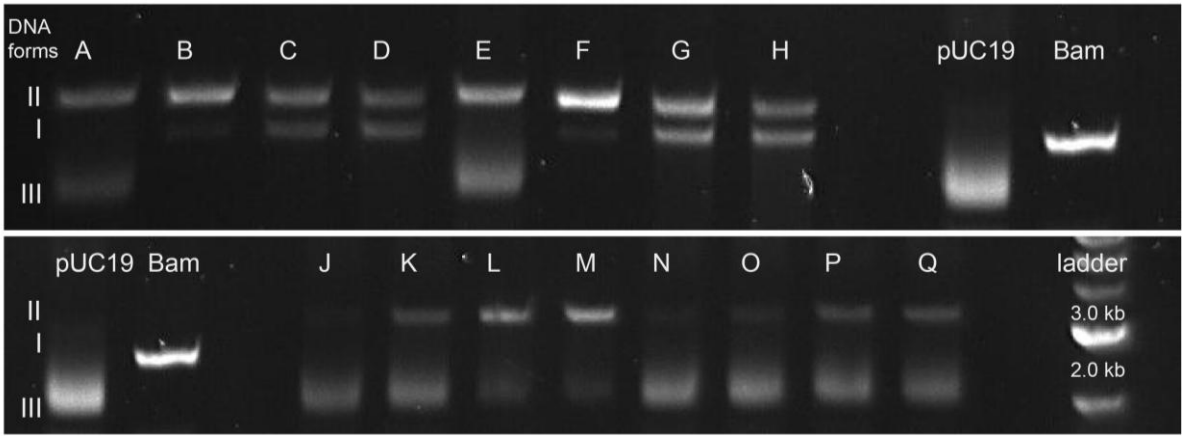

SI Figure 43. Scission of pUC19 using peptide 2-Cu(II)/-Ni(II) and peptide 3-Cu(II)/-Ni(II) complexes

Lane	**A**	**B**	**C**	**D**	**E**	**F**	**G**	**I**
Sample	Peptide 2 + Asc + Cu^{2+}				Peptide 3 + Asc + Cu^{2+}			
Time	0 h	0.5 h	2 h	4 h	0 h	0.5 h	2 h	4 h

Lane	**J**	**K**	**L**	**M**	**N**	**O**	**P**	**Q**
Sample	Peptide 2 + Asc + Ni^{2+}				Peptide 3 + Asc + Ni^{2+}			
Time	0 h	0.5 h	2 h	4 h	0 h	0.5 h	2 h	4 h

SI Table 14. Scission of pUC19 using peptide 2 and peptide 3 with Cu and Ni

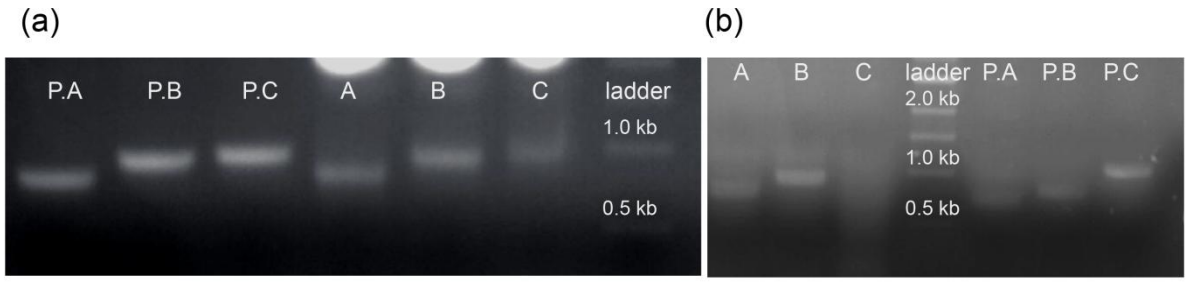

SI Figure 44. pUC19 segments ABC after linearization using peptide 2 and 3

(a) shows segmentation of linearized pUC19 after scission using peptide 2 with P.A/P.B and P.C representing the positive pUC19 samples where no linearization took place. (b) shows peptide 3 with positive samples, respectively.

Segment	**A**	**B**	**C**
Primer reverse	pUC A rv	pUC B rv	pUC C rv
Primer forward	pUC A fw	pUC B fw	pUC C fw

SI Table 15. Primers used for pCU19 segmentation

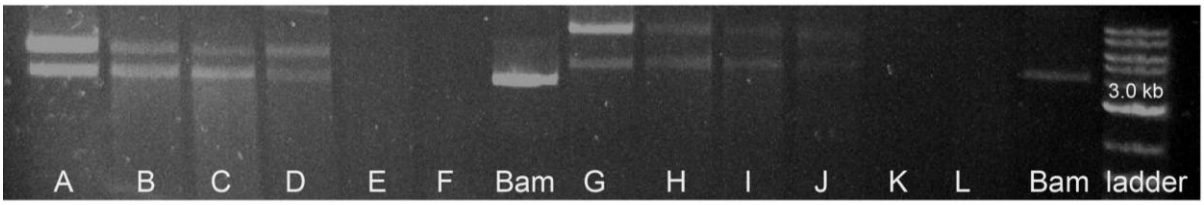

SI Figure 45. pASK and pACY scission with peptide 2-Cu(II) and peptide 3-Cu(II)

Lane	**A**	**B**	**C**	**D**	**E**	**F**	**G**	**H**	**I**	**J**	**K**	**L**
Sample	pASK, peptide 3 + Cu^{2+} + Asc			pASK, peptide 2 + Cu^{2+} + Asc			pACY, peptide 3 + Cu^{2+} + Asc			pACY, peptide 2 + Cu^{2+} + Asc		
Time	0.5 h	2 h	4 h	0.5 h	2 h	4 h	0.5 h	2 h	4 h	0.5 h	2 h	4 h

SI Table 16. pASK and pACY scission with peptide 2 and peptide 3

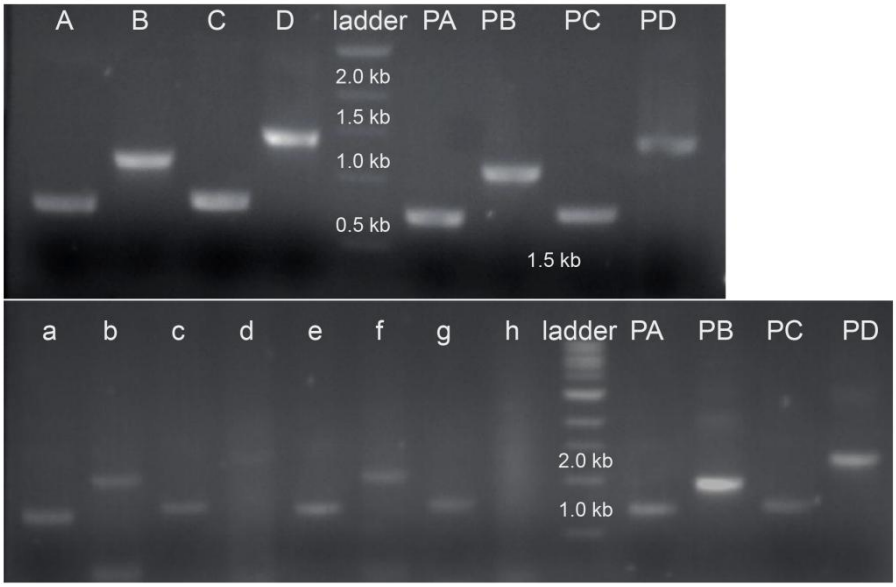

SI Figure 46. Segmentation of pASK using peptide 1 – 3 for DNA scission

A – D represent cutting of pASK prior to PCR using peptide 1, a – d peptide 2 and e – h peptide 3, PA – PD represents the positive sample with no cutting of plasmid DNA

	A (PA; a; e)	**B (PB; b; f)**	**C (PC; c; g)**	**D (PD; d; h)**
Primer reverse	pASK A rv	pASK B rv	pASK C rv	pASK D rv
Primer forward	pASK A fw	pASK B fw	pASK C fw	pASK D fw

SI Table 17. Reverse and forward primers used for segmentation pASK

13.2. List of Figures

13.3. List of SI figures

13.4. List of Tables

13.5. List of SI Tables

13.6. List of Equations

13.7. List of Abbreviations

5/6-FAM	5/6-Carboxyfluorescein
AAA	Amino acid analysis
AFM	Atomic force microscopy
AmpR	Ampicillin resistance
AQC	Aminoquinolyl-N-hydroxysuccinimidyl carbamate
Asc	Ascorbate
ATCUN	Amino terminal Cu(II)-and Ni(II)-binding motif
ATP	Adenosine triphosphate
Boc	butyloxycarbonyl
BOMI	(1H-benzotriazol-1-yloxy)-N,N-dimethyl methaniminium hexachloroantimonate
bp	Basepairs
BSA	Bovine serum albumin
CAPS	2-(Cyclohexylamino)-1-propanesulfonic acid
CD	Circular dichroism
CDI	Carbonyldiimidazole
CLSM	Confocal laser scanning microscopy
Cl-Trt	Chlorotrityl resin
CmR	Chloramphenicol resistance
Cryo-EM	Cryo-electron-microscopy
CuAAC	Cu(I)-catalyzed azide-alkyne [3 + 2] cycloadditions
Da	Dalton
DBU	1,8diazabicyclo[5.4.0]undec-7-ene
DCC	Carbodiimide
DCM	Dichloromethane
DDM	N-Dodecyl-beta-maltoside
DEAD	Diethyl azodicarboxylate
DHAP	2,5 – Dihydroxyacetophenone
DIEA	N-ethyl-N-(propan-2-yl)propan-2-amin

DMF	N,N-Dimethylformamide
DNA	Desoxyribonucleic acid
Dns	5-(dimethylamino)naphthalene-1-sulfonamide
DPC	Dodecylphosphocholine
DPPA	Diphenylphosporyl azide
DSA	Dog serum albumin
dsDNA	Double stranded DNA
EDA	Ethylenediamine
EDC	1-Ethyl-3-(3-dimethylaminoprpyl)carbodiimide
EDTA	Ethylenediaminetetraacetic acid
Equ	Equivalents
ESEM	Environmental scanning electron microscopy
ESI	Electron spray ionization
FA	Formic acid
FIB	Fast ion bombardment
Fmoc	Flouenylmethyloxycarbonyl
fw	forward
Gdn·HCl	Guanidinium hydrochloride
GPCR	G-protein coupled receptor
HATU	1-[Bis(dimethylamino)methylene]-1*H*-1,2,3-triazolo[4,5-*b*]pyridinium 3-oxid hexafluorophosphate
HBTU	(2-(1*H*-benzotriazol-1-yl)-1,1,3,3-tetramethyluronium hexafluorophosphate
HCCA	α-Cyano-4-hydroxycinnamic acid
HFIP	Hexafluoro-2-propanol
Hmp	2-hydroxy-3-thio-propanic acid
HOBt	Hydroxybenzotriazole
HR-FES-EM	High-resolution field-emission scanning electron microscopy
HSA	Human serum albumin
ISE	Ion-selective electrodes

kb	Kilobases
LC-MS	Liquid chromatography mass spectrometry
LOD	Limit of detection
LOQ	Limit of quantitation
LP	Linear positive
MALDI	Matrix assisted laser desorption ionization
MeOh	Methanol
MES	2-(N-morpholino)ethanesulfonic acid
MPAA	4-mercaptophenylacetic acid
MRA	Molecular recognition agents
MS	Mass Spectrometry
MspA	*Mycobacterim smegmatis*
NaOH	Sodium hydroxide
NCL	Native chemical ligation
NMP	1-Methyl-2pyrrolidinone
NMR	Nuclear magnetic resonance
NTP	Nucleoside triphosphate
OG	Octyl-beta-glucoside
pACY	pACYCT2
PAGE	Polyacryl gel electrophoresis
pASK	pASK-IBA3
PBS	Phosphate buffered saline
PC	Polycarbonate
PDA	Photo-diode array (detector)
PEG	Polyethylene glycol
PES	Polysulfone
PET	Polyethylene terephthalate
PFP	Pentafluorophenyl esters
pNB	p-nitrobenzyl

POPC	1-palmitoyl-2-oleoyl-*sn*-glycero-3-phosphocholine
PPh3	Triphenylphosphine
PS	Polystyrene
RAM	Rink amide resin
RNA	Ribonucleic acid
RP	Reflector positive
RP HPLC	Reverse phase high performance liquid chromatography
RSA	Rat serum albumin
RT	Room temperature
rv	reverse
SA	Sinapinic acid
SDS	Sodium dodecyl sulfate
SERT	Serotonine transporter
SGLT	Sodium dependent glucose transporter
SiN	Silicon nitride
SPPS	Solid phase peptide synthesis
SRI	Serotonine reuptake inhibitor
ssDNA	Single stranded DNA
TAcm	Trimethylacetamidomethyl
TCEP	Tris(2-carvoxyethyl)phosphine
TEM	Transmission electron microscope
TFA	Trifluoroacetic acid
TFE	Trifluoroethanol
TFFH	Tetramethylfluoroformamidium hexafluorophosphate
THF	Tetrahydrofuran
Thz	1,3-thiazolidine-4-carboxo
TIPS	Triisoporpylsilane
TM	Transmembrane
TOF	Time of flight

UNILAC	Universal linear accelerator
UV-Vis	Ultraviolet-visible
VA-022	2,2'-azobis(2-(2-imidazoline-2-yl)propane)dihydrochloride
α-HL	Alpha-hemolysine

14. References

1 Doyle, D. A. *et al.* The structure of the potassium channel: Molecular basis of K+ conduction and selectivity. *Science* **280**, 69-77, doi:DOI 10.1126/science.280.5360.69 (1998).

2 Catterall, W. A. Voltage-gated calcium channels. *Cold Spring Harbor perspectives in biology* **3**, a003947, doi:10.1101/cshperspect.a003947 (2011).

3 Rosenbaum, D. M., Rasmussen, S. G. & Kobilka, B. K. The structure and function of G-protein-coupled receptors. *Nature* **459**, 356-363, doi:10.1038/nature08144 (2009).

4 Allen, J. P. Recent innovations in membrane-protein structural biology. *F1000Research* **8**, doi:10.12688/f1000research.16234.1 (2019).

5 Overington, J. P., Al-Lazikani, B. & Hopkins, A. L. How many drug targets are there? *Nature reviews. Drug discovery* **5**, 993-996, doi:10.1038/nrd2199 (2006).

6 Hou, X., Guo, W. & Jiang, L. Biomimetic smart nanopores and nanochannels. *Chem Soc Rev* **40**, 2385-2401, doi:10.1039/c0cs00053a (2011).

7 Hou, X. & Jiang, L. Learning from nature: building bio-inspired smart nanochannels. *ACS nano* **3**, 3339-3342, doi:10.1021/nn901402b (2009).

8 Duznovic, I. D., M; Ali, M.; Stein, T.; Biesalski, M.; Ensinger, W. Automated measuring of mass transport through synthetic nanochannels functionalized with polyelectrolyte porous networkds. *Journal of Membrane Science* **591**, doi:https://doi.org/10.1016/j.memsci.2019.117344 (2019).

9 Sato, T. Chemical synthesis of transmembrane peptide and its application for research on the transmembrane-juxtamembrane region of membrane protein. *Biopolymers* **106**, 613-621, doi:10.1002/bip.22775 (2016).

10 Gonzalez, P. *et al.* N-Terminal Cu-Binding Motifs (Xxx-Zzz-His, Xxx-His) and Their Derivatives: Chemistry, Biology and Medicinal Applications. *Chem-Eur J* **24**, 8029-8041, doi:10.1002/chem.201705398 (2018).

11 Dasari, S. & Tchounwou, P. B. Cisplatin in cancer therapy: molecular mechanisms of action. *European journal of pharmacology* **740**, 364-378, doi:10.1016/j.ejphar.2014.07.025 (2014).

12 Harford, C. & Sarkar, B. Amino terminal Cu(II)- and Ni(II)-binding (ATCUN) motif of proteins and peptides: Metal binding, DNA cleavage, and other properties. *Accounts Chem Res* **30**, 123-130, doi:Doi 10.1021/Ar9501535 (1997).

13 Lee, K. *et al.* Recent Progress in Solid-State Nanopores. *Advanced materials* **30**, e1704680, doi:10.1002/adma.201704680 (2018).

14 Eglen, R. M., Hunter, J. C. & Dray, A. Ions in the fire: recent ion-channel research and approaches to pain therapy. *Trends in pharmacological sciences* **20**, 337-342 (1999).

15 Kasianowicz, J. J., Brandin, E., Branton, D. & Deamer, D. W. Characterization of individual polynucleotide molecules using a membrane channel. *Proceedings of the National Academy of Sciences of the United States of America* **93**, 13770-13773, doi:DOI 10.1073/pnas.93.24.13770 (1996).

16 Vercoutere, W. *et al.* Rapid discrimination among individual DNA hairpin molecules at single-nucleotide resolution using an ion channel. *Nature biotechnology* **19**, 248-252, doi:10.1038/85696 (2001).

17 Akeson, M., Branton, D., Kasianowicz, J. J., Brandin, E. & Deamer, D. W. Microsecond time-scale discrimination among polycytidylic acid, polyadenylic acid, and polyuridylic acid as homopolymers or as segments within single RNA molecules. *Biophys J* **77**, 3227-3233, doi:Doi 10.1016/S0006-3495(99)77153-5 (1999).

18 Dekker, C. Solid-state nanopores. *Nature nanotechnology* **2**, 209-215, doi:10.1038/nnano.2007.27 (2007).

19 Pitchford, W. H. *et al.* Synchronized optical and electronic detection of biomolecules using a low noise nanopore platform. *ACS nano* **9**, 1740-1748, doi:10.1021/nn506572r (2015).

20 Li, J. *et al.* Ion-beam sculpting at nanometre length scales. *Nature* **412**, 166-169, doi:Doi 10.1038/35084037 (2001).
21 Gokel, G. W. & Mukhopadhyay, A. Synthetic models of cation-conducting channels. *Chem Soc Rev* **30**, 274-286, doi:Doi 10.1039/B008667n (2001).
22 Fyles, T. M. Synthetic ion channels in bilayer membranes. *Chem Soc Rev* **36**, 335-347, doi:10.1039/b603256g (2007).
23 Dittmann, M. E., M. in *Chemical Ligation: Tools for Biomolecule Synthesis and Modification* (ed Alessandra Romanelli Luca D. D'Andrea) (John Wiley & Sons, Inc., 2017).
24 Achalkumar, A. S., Bushby, R. J. & Evans, S. D. Cholesterol-based anchors and tethers for phospholipid bilayers and for model biological membranes. *Soft Matter* **6**, 6036-6051, doi:10.1039/c0sm00030b (2010).
25 Li, J. B., Tang, S., Zheng, J. S., Tian, C. L. & Liu, L. Removable Backbone Modification Method for the Chemical Synthesis of Membrane Proteins. *Acc Chem Res* **50**, 1143-1153, doi:10.1021/acs.accounts.7b00001 (2017).
26 Yildirim, M. A., Goh, K. I., Cusick, M. E., Barabasi, A. L. & Vidal, M. Drug-target network. *Nature biotechnology* **25**, 1119-1126, doi:10.1038/nbt1338 (2007).
27 Mutschler, E. G., G.; Kroemer, H. K.; Ruth, P.; Schäfer-Korting, M. *Mutschler Arzneimittelwirkungen Lehrbuch der Pharmakologie und Toxikologie*. Vol. 9 (Wissenschaftliche Verlagsgesellschaft mbH Stuttgart, 2008).
28 Herdegen, T. B., R.; Cimin-Bredée, N., Culman, J.; Gohlke, P.; Ley, L.; Luippold, G.; Ufer, M.; Wätzig, V. *Kurzlehrbuch Pharmakologie und Toxikologie*. (Thieme, 2008).
29 Melnyk, R. A. *et al.* Polar residue tagging of transmembrane peptides. *Biopolymers* **71**, 675-685, doi:10.1002/bip.10595 (2003).
30 Shen, F., Huang, Y. C., Tang, S., Chen, Y. X. & Liu, L. Chemical Synthesis of Integral Membrane Proteins: Methods and Applications. *Isr J Chem* **51**, 940-952, doi:10.1002/ijch.201100076 (2011).
31 MacKinnon, R., Cohen, S. L., Kuo, A. L., Lee, A. & Chait, B. T. Structural conservation in prokaryotic and eukaryotic potassium channels. *Science* **280**, 106-109, doi:DOI 10.1126/science.280.5360.106 (1998).
32 Mackinnon, R. & Miller, C. Mutant Potassium Channels with Altered Binding of Charybdotoxin, a Pore-Blocking Peptide Inhibitor. *Science* **245**, 1382-1385, doi:DOI 10.1126/science.2476850 (1989).
33 Heginbotham, L., Lu, Z., Abramson, T. & Mackinnon, R. Mutations in the K+ Channel Signature Sequence. *Biophys J* **66**, 1061-1067, doi:Doi 10.1016/S0006-3495(94)80887-2 (1994).
34 Roux, B. Ion conduction and selectivity in K+ channels. *Annu Rev Bioph Biom* **34**, 153-171, doi:DOI 10.1146/annurev.biophys.34.040204.144655 (2005).
35 Pauling, L. *The Nature of the Chemical Bond*. 3rd ed. edn, (Cornell Universsity, Ithaca, NY, 1960).
36 Thiel, G., Moroni, A., Blanc, G. & Van Etten, J. L. Potassium ion channels: could they have evolved from viruses? *Plant physiology* **162**, 1215-1224, doi:10.1104/pp.113.219360 (2013).
37 Mackinnon, R. Determination of the Subunit Stoichiometry of a Voltage-Activated Potassium Channel. *Nature* **350**, 232-235, doi:Doi 10.1038/350232a0 (1991).
38 Hodgkin, A. L. & Keynes, R. D. The Potassium Permeability of a Giant Nerve Fibre. *J Physiol-London* **128**, 61-88, doi:DOI 10.1113/jphysiol.1955.sp005291 (1955).
39 MacKinnon, R. Potassium channels and the atomic basis of selective ion conduction (Nobel Lecture). *Angew Chem Int Ed Engl* **43**, 4265-4277, doi:10.1002/anie.200400662 (2004).
40 Zhou, Y., Morais-Cabral, J. H., Kaufman, A. & MacKinnon, R. Chemistry of ion coordination and hydration revealed by a K+ channel-Fab complex at 2.0 A resolution. *Nature* **414**, 43-48, doi:10.1038/35102009 (2001).

41 Kuang, Q., Purhonen, P. & Hebert, H. Structure of potassium channels. *Cellular and molecular life sciences : CMLS* **72**, 3677-3693, doi:10.1007/s00018-015-1948-5 (2015).
42 Ketchum, K. A., Joiner, W. J., Sellers, A. J., Kaczmarek, L. K. & Goldstein, S. A. A new family of outwardly rectifying potassium channel proteins with two pore domains in tandem. *Nature* **376**, 690-695, doi:10.1038/376690a0 (1995).
43 Kuo, A. *et al.* Crystal structure of the potassium channel KirBac1.1 in the closed state. *Science* **300**, 1922-1926, doi:10.1126/science.1085028 (2003).
44 Yang, J., Jan, Y. N. & Jan, L. Y. Determination of the subunit stoichiometry of an inwardly rectifying potassium channel. *Neuron* **15**, 1441-1447 (1995).
45 Gazzarrini, S. *et al.* Chlorella virus ATCV-1 encodes a functional potassium channel of 82 amino acids. *The Biochemical journal* **420**, 295-303, doi:10.1042/BJ20090095 (2009).
46 Pongs, O. & Schwarz, J. R. Ancillary Subunits Associated With Voltage-Dependent K+ Channels. *Physiol Rev* **90**, 755-796, doi:10.1152/physrev.00020.2009 (2010).
47 Sanguinetti, M. C. & Tristani-Firouzi, M. hERG potassium channels and cardiac arrhythmia. *Nature* **440**, 463-469, doi:10.1038/nature04710 (2006).
48 Kuang, Q., Purhonen, P., Jegerschold, C. & Hebert, H. The projection structure of Kch, a putative potassium channel in Escherichia coli, by electron crystallography. *Bba-Biomembranes* **1838**, 237-243, doi:10.1016/j.bbamem.2013.09.006 (2014).
49 Lesage, F. & Lazdunski, M. Molecular and functional properties of two-pore-domain potassium channels. *Am J Physiol-Renal* **279**, F793-F801 (2000).
50 Thiel, G. *et al.* Minimal art: or why small viral K(+) channels are good tools for understanding basic structure and function relations. *Biochimica et biophysica acta* **1808**, 580-588, doi:10.1016/j.bbamem.2010.04.008 (2011).
51 Braun, C. J. *et al.* Viral potassium channels as a robust model system for studies of membrane-protein interaction. *Biochimica et biophysica acta* **1838**, 1096-1103, doi:10.1016/j.bbamem.2013.06.010 (2014).
52 Rauh, O. *et al.* Identification of Intrahelical Bifurcated H-Bonds as a New Type of Gate in K+ Channels. *J Am Chem Soc* **139**, 7494-7503, doi:10.1021/jacs.7b01158 (2017).
53 Ogden, D. S., P. in *Microelectrode techniques: the Plymouth workshop handbook* (The Company of Biologists, Cambridge, 1987).
54 Braun, C. J., Baer, T., Moroni, A. & Thiel, G. Pseudo painting/air bubble technique for planar lipid bilayers. *Journal of neuroscience methods* **233**, 13-17, doi:10.1016/j.jneumeth.2014.05.031 (2014).
55 Brauser, A. *et al.* Modulation of enrofloxacin binding in OmpF by Mg2+ as revealed by the analysis of fast flickering single-porin current. *Journal of General Physiology* **140**, 69-82, doi:10.1085/jgp.201210776 (2012).
56 Mueller, P., Rudin, D. O., Tien, H. T. & Wescott, W. C. Reconstitution of cell membrane structure in vitro and its transformation into an excitable system. *Nature* **194**, 979-980, doi:10.1038/194979a0 (1962).
57 Morera, F. J., Vargas, G., Gonzalez, C., Rosenmann, E. & Latorre, R. Ion-channel reconstitution. *Methods in molecular biology* **400**, 571-585, doi:10.1007/978-1-59745-519-0_38 (2007).
58 Nature. *G-Protein-Coupled Receptors Play Many Different Roles in Eukaryotic Cell Signaling*, <www.nature.com/scitable/ebooks/essentials-of-cell-biology-14749010/122997540/> (2014).
59 Rahman, N., Buck, J. & Levin, L. R. pH sensing via bicarbonate-regulated "soluble" adenylyl cyclase (sAC). *Front Physiol* **4**, doi:Artn 343 doi: 10.3389/Fphys.2013.00343 (2013).
60 Soleimani, M. Receptor Protein Tyrosine Phosphatase gamma, CO2 Sensing in Proximal Tubule and Acid Base Homeostasis. *J Am Soc Nephrol* **27**, 2543-2545, doi:10.1681/Asn.2016030332 (2016).

61 Plugge, B. *et al.* A potassium channel protein encoded by chlorella virus PBCV-1. *Science* **287**, 1641-1644, doi:10.1126/science.287.5458.1641 (2000).
62 Gazzarrini, S., Van Etten, J. L., DiFrancesco, D., Thiel, G. & Moroni, A. Voltage-dependence of virus-encoded miniature K+ channel Kcv. *J Membrane Biol* **187**, 15-25, doi:10.1007/s00232-001-0147-5 (2002).
63 Perutz, M. F. Regulation of oxygen affinity of hemoglobin: influence of structure of the globin on the heme iron. *Annu Rev Biochem* **48**, 327-386, doi:10.1146/annurev.bi.48.070179.001551 (1979).
64 Outten, C. E. & O'Halloran, T. V. Femtomolar sensitivity of metalloregulatory proteins controlling zinc homeostasis. *Science* **292**, 2488-2492, doi:10.1126/science.1060331 (2001).
65 Baker, L. A. & Bird, S. P. Nanopores: a makeover for membranes. *Nature nanotechnology* **3**, 73-74, doi:10.1038/nnano.2008.13 (2008).
66 Stein, D., Li, J. L. & Golovchenko, J. A. Ion-beam sculpting time scales. *Physical review letters* **89**, doi:Artn 276106 doi:10.1103/Physrevlett.89.276106 (2002).
67 Chen, P. *et al.* Atomic layer deposition to fine-tune the surface properties and diameters of fabricated nanopores. *Nano letters* **4**, 1333-1337, doi:10.1021/nl0494001 (2004).
68 Harrell, C. C., Kohli, P., Siwy, Z. & Martin, C. R. DNA - Nanotube artificial ion channels. *J Am Chem Soc* **126**, 15646-15647, doi:10.1021/ja044948v (2004).
69 Ali, M. *et al.* Layer-by-Layer Assembly of Polyelectrolytes into Ionic Current Rectifying Solid-State Nanopores: Insights from Theory and Experiment. *J Am Chem Soc* **132**, 8338-8348, doi:10.1021/ja101014y (2010).
70 Li, N. C., Yu, S. F., Harrell, C. C. & Martin, C. R. Conical nanopore membranes. Preparation and transport properties. *Anal Chem* **76**, 2025-2030, doi:10.1021/ac035402e (2004).
71 Howorka, S. & Siwy, Z. Nanopore analytics: sensing of single molecules. *Chem Soc Rev* **38**, 2360-2384, doi:10.1039/b813796j (2009).
72 van den Hout, M. *et al.* Controlling nanopore size, shape and stability. *Nanotechnology* **21**, 115304, doi:10.1088/0957-4484/21/11/115304 (2010).
73 Harrer, S. *et al.* Electrochemical protection of thin film electrodes in solid state nanopores. *Nanotechnology* **22**, 275304, doi:10.1088/0957-4484/22/27/275304 (2011).
74 Kuan, A. T., Lu, B., Xie, P., Szalay, T. & Golovchenko, J. A. Electrical pulse fabrication of graphene nanopores in electrolyte solution. *Appl Phys Lett* **106**, doi:Artn 203109 10.1063/1.4921620 (2015).
75 Rollings, R. C., Kuan, A. T. & Golovchenko, J. A. Ion selectivity of graphene nanopores. *Nat Commun* **7**, doi:Artn 11408 10.1038/Ncomms11408 (2016).
76 Lee, S. B. & Martin, C. R. pH-switchable, ion-permselective gold nanotubule membrane based on chemisorbed cysteine. *Anal Chem* **73**, 768-775, doi:10.1021/ac0008901 (2001).
77 Jirage, K. B., Hulteen, J. C. & Martin, C. R. Effect of thiol chemisorption on the transport properties of gold nanotubule membranes. *Anal Chem* **71**, 4913-4918, doi:10.1021/ac990615i (1999).
78 Nishizawa, M., Menon, V. P. & Martin, C. R. Metal nanotubule membranes with electrochemically switchable ion-transport selectivity. *Science* **268**, 700-702, doi:10.1126/science.268.5211.700 (1995).
79 Yameen, B. *et al.* Single conical nanopores displaying pH-tunable rectifying characteristics. manipulating ionic transport with zwitterionic polymer brushes. *J Am Chem Soc* **131**, 2070-2071, doi:10.1021/ja8086104 (2009).
80 Sexton, L. T., Horne, L. P. & Martin, C. R. Developing synthetic conical nanopores for biosensing applications. *Mol Biosyst* **3**, 667-685, doi:10.1039/b708725j (2007).

81 Bayley, H. & Martin, C. R. Resistive-Pulse Sensing-From Microbes to Molecules. *Chemical reviews* **100**, 2575-2594 (2000).
82 Choi, Y., Baker, L. A., Hillebrenner, H. & Martin, C. R. Biosensing with conically shaped nanopores and nanotubes. *Physical chemistry chemical physics : PCCP* **8**, 4976-4988, doi:10.1039/b607360c (2006).
83 Zhang, H., Tian, Y. & Jiang, L. From symmetric to asymmetric design of bio-inspired smart single nanochannels. *Chem Commun (Camb)* **49**, 10048-10063, doi:10.1039/c3cc45526b (2013).
84 Sexton, L. T. *et al.* Resistive-pulse studies of proteins and protein/antibody complexes using a conical nanotube sensor. *J Am Chem Soc* **129**, 13144-13152, doi:10.1021/ja0739943 (2007).
85 Siwy, Z. *et al.* Protein biosensors based on biofunctionalized conical gold nanotubes. *J Am Chem Soc* **127**, 5000-5001, doi:10.1021/ja043910f (2005).
86 Mertz, W. The essential trace elements. *Science* **213**, 1332-1338, doi:10.1126/science.7022654 (1981).
87 Kim, B. E., Nevitt, T. & Thiele, D. J. Mechanisms for copper acquisition, distribution and regulation. *Nature chemical biology* **4**, 176-185, doi:10.1038/nchembio.72 (2008).
88 Georgopoulos, P. G., Roy, A., Yonone-Lioy, M. J., Opiekun, R. E. & Lioy, P. J. Environmental copper: its dynamics and human exposure issues. *Journal of toxicology and environmental health. Part B, Critical reviews* **4**, 341-394, doi:10.1080/10937400175314620 7 (2001).
89 Milne, D. B. Copper intake and assessment of copper status. *The American journal of clinical nutrition* **67**, 1041S-1045S, doi:10.1093/ajcn/67.5.1041S (1998).
90 Gaetke, L. M. & Chow, C. K. Copper toxicity, oxidative stress, and antioxidant nutrients. *Toxicology* **189**, 147-163 (2003).
91 WHO. Copper in Drinking-water. (World Health Organization, www.who.int).
92 Cempel, M. & Nikel, G. Nickel: A review of its sources and environmental toxicology. *Pol J Environ Stud* **15**, 375-382 (2006).
93 WHO. Chemical Fact Sheets - Nickel. (World Health Organization).
94 Wirth, P. L. & Linder, M. C. Distribution of copper among components of human serum. *Journal of the National Cancer Institute* **75**, 277-284 (1985).
95 Peters, T., Jr. Interaction of one mole of copper with the alpha amino group of bovine serum albumin. *Biochimica et biophysica acta* **39**, 546-547, doi:10.1016/0006-3002(60)90215-8 (1960).
96 Peters, T., Jr. & Blumenstock, F. A. Copper-binding properties of bovine serum albumin and its amino-terminal peptide fragment. *The Journal of biological chemistry* **242**, 1574-1578 (1967).
97 Harford, C. & Sarkar, B. Neuromedin-C Binds Cu(Ii) and Ni(Ii) Via the Atcun Motif - Implications for the Cns and Cancer Growth. *Biochem Bioph Res Co* **209**, 877-882, doi:DOI 10.1006/bbrc.1995.1580 (1995).
98 Camerman, N., Camerman, A. & Sarkar, B. Molecular Design to Mimic Copper(Ii) Transport Site of Human-Albumin - Crystal and Molecular-Structure of Copper(Ii) - Glycylglycyl-L-Histidine-N-Methyl Amide Monoaquo Complex. *Can J Chem* **54**, 1309-1316, doi:Doi 10.1139/V76-185 (1976).
99 Torrado, A., Walkup, G. K. & Imperiali, B. Exploiting polypeptide motifs for the design of selective Cu(II) ion chemosensors. *J Am Chem Soc* **120**, 609-610, doi:10.1021/Ja973357k (1998).
100 Imperiali, B. P., D. A.; Sohna Sohna, J.-E.; Walkup, G.; Torrado, A. Peptide platforms for metal ion sensing. *Proc. SPIE 3853 Advanced Materials and Optical Systems for Chemical and Biological Detection*, doi:10.1117/12.372909 (1999).
101 Choi, Y. A. *et al.* A novel copper-chelating strategy for fluorescent proteins to image dynamic copper fluctuations on live cell surfaces. *Chemical science* **6**, 1301-1307, doi:10.1039/c4sc03027c (2015).

102 Deng, D. H. *et al.* Electrochemical sensing devices using ATCUN-Cu(II) complexes as electrocatalysts for water oxidation. *Sensor Actuat B-Chem* **269**, 189-194, doi:10.1016/j.snb.2018.04.177 (2018).
103 Lottspeich, F. E., J. W. in *Bioanalytik* Vol. 3 Ch. 28.1, 739-748 (Springer Spektrum, 2012).
104 Chiou, S. H. DNA- and protein-scission activities of ascorbate in the presence of copper ion and a copper-peptide complex. *Journal of biochemistry* **94**, 1259-1267, doi:10.1093/oxfordjournals.jbchem.a134471 (1983).
105 Balasubramanian, B., Pogozelski, W. K. & Tullius, T. D. DNA strand breaking by the hydroxyl radical is governed by the accessible surface areas of the hydrogen atoms of the DNA backbone. *Proceedings of the National Academy of Sciences of the United States of America* **95**, 9738-9743, doi:10.1073/pnas.95.17.9738 (1998).
106 Sigman, D. S. Nuclease Activity of 1,10-Phenanthroline Copper-Ion. *Accounts Chem Res* **19**, 180-186, doi:Doi 10.1021/Ar00126a004 (1986).
107 Fang, Y. Y., Ray, B. D., Claussen, C. A., Lipkowitz, K. B. & Long, E. C. Ni(II)center dot Arg-Gly-His - DNA interactions: Investigation into the basis for minor-groove binding and recognition. *J Am Chem Soc* **126**, 5403-5412, doi:10.1021/ja049875u (2004).
108 Huang, X. F., Pieczko, M. E. & Long, E. C. Combinatorial optimization of the DNA cleaving Ni(II)center dot Xaa-Xaa-His metallotripeptide domain. *Biochemistry-Us* **38**, 2160-2166, doi:Doi 10.1021/Bi982587o (1999).
109 Umezawa, H., Maeda, K., Takeuchi, T. & Okami, Y. New Antibiotics Bleomycin a and B. *J Antibiot* **19**, 200-& (1966).
110 Chen, J. Y. & Stubbe, J. Bleomycins: Towards better therapeutics. *Nat Rev Cancer* **5**, 102-112, doi:10.1038/nrc1547 (2005).
111 Stubbe, J. & Kozarich, J. W. Mechanisms of Bleomycin-Induced DNA-Degradation. *Chemical reviews* **87**, 1107-1136, doi:Doi 10.1021/Cr00081a011 (1987).
112 Jordan, P. & Carmo-Fonseca, M. Molecular mechanisms involved in cisplatin cytotoxicity. *Cellular and Molecular Life Sciences* **57**, 1229-1235, doi:Doi 10.1007/Pl00000762 (2000).
113 Aparicio, S. & Caldas, C. The implications of clonal genome evolution for cancer medicine. *The New England journal of medicine* **368**, 842-851, doi:10.1056/NEJMra1204892 (2013).
114 Heather, J. M. & Chain, B. The sequence of sequencers: The history of sequencing DNA. *Genomics* **107**, 1-8, doi:10.1016/j.ygeno.2015.11.003 (2016).
115 Deamer, D. W. & Akeson, M. Nanopores and nucleic acids: prospects for ultrarapid sequencing. *Trends in biotechnology* **18**, 147-151, doi:10.1016/s0167-7799(00)01426-8 (2000).
116 Song, L. *et al.* Structure of staphylococcal alpha-hemolysin, a heptameric transmembrane pore. *Science* **274**, 1859-1866, doi:10.1126/science.274.5294.1859 (1996).
117 Schneider, G. F. & Dekker, C. DNA sequencing with nanopores. *Nature biotechnology* **30**, 326-328, doi:10.1038/nbt.2181 (2012).
118 Cherf, G. M. *et al.* Automated forward and reverse ratcheting of DNA in a nanopore at 5-A precision. *Nature biotechnology* **30**, 344-348, doi:10.1038/nbt.2147 (2012).
119 Derrington, I. M. *et al.* Nanopore DNA sequencing with MspA. *Proceedings of the National Academy of Sciences of the United States of America* **107**, 16060-16065, doi:10.1073/pnas.1001831107 (2010).
120 Manrao, E. A. *et al.* Reading DNA at single-nucleotide resolution with a mutant MspA nanopore and phi29 DNA polymerase. *Nature biotechnology* **30**, 349-U174, doi:10.1038/nbt.2171 (2012).
121 Wendell, D. *et al.* Translocation of double-stranded DNA through membrane-adapted phi29 motor protein nanopores. *Nature nanotechnology* **4**, 765-772, doi:10.1038/nnano.2009.259 (2009).

122 Kohli, P. *et al.* DNA-functionalized nanotube membranes with single-base mismatch selectivity. *Science* **305**, 984-986, doi:10.1126/science.1100024 (2004).
123 Iqbal, S. M., Akin, D. & Bashir, R. Solid-state nanopore channels with DNA selectivity. *Nature nanotechnology* **2**, 243-248, doi:10.1038/nnano.2007.78 (2007).
124 Merchant, C. A. *et al.* DNA translocation through graphene nanopores. *Nano letters* **10**, 2915-2921, doi:10.1021/nl101046t (2010).
125 Cadene, M. & Chait, B. T. A robust, detergent-friendly method for mass spectrometric analysis of integral membrane proteins. *Anal Chem* **72**, 5655-5658, doi:10.1021/Ac0008111 (2000).
126 Keller, B. O. & Li, L. Three-layer matrix/sample preparation method for MALDI MS analysis of low nanomolar protein samples. *Journal of the American Society for Mass Spectrometry* **17**, 780-785, doi:10.1016/j.jasms.2006.02.012 (2006).
127 Schagger, H. Tricine-SDS-PAGE. *Nature protocols* **1**, 16-22, doi:10.1038/nprot.2006.4 (2006).
128 Benesi, H. A. & Hildebrand, J. H. A Spectrophotometric Investigation of the Interaction of Iodine with Aromatic Hydrocarbons. *J Am Chem Soc* **71**, 2703-2707, doi:Doi 10.1021/Ja01176a030 (1949).
129 Wang, R. & Yu, Z. W. Validity and reliability of Benesi-Hildebrand method. *Acta Phys-Chim Sin* **23**, 1353-1359, doi: 10.1016/S1872-1508(07)60071-0 (2007).
130 Stern, O. V., Max. Über die Abklingungszeit der Fluoreszenz. *Physik. Z.* **20**, 183-188 (1919).
131 Lakowicz, J. R. & Weber, G. Quenching of Fluorescence by Oxygen - Probe for Structural Fluctuations in Macromolecules. *Biochemistry-Us* **12**, 4161-4170, doi:Doi 10.1021/Bi00745a020 (1973).
132 ICH. Validation of Analytical Procedures: Text and Methodology Q2(R1). (International conference on harmonisation of technical requirements for registration of pharmaceutivals for human use, 2005).
133 Haywood, D. G., Saha-Shah, A., Baker, L. A. & Jacobson, S. C. Fundamental studies of nanofluidics: nanopores, nanochannels, and nanopipets. *Anal Chem* **87**, 172-187, doi:10.1021/ac504180h (2015).
134 INSTRUCTIONS NHS and Sulfo-NHS. (Thermo Scientific, 2001).
135 Microsphere Coupling - Two-step EDC/Sulfo NHS Covalent Coupling Procedure for Estapor Carboxyl-modified Dyed Microspheres. (Merck Millipore, 2015).
136 *User manual Plasmid DNA purification*, 2019).
137 *User manual PCR clean-up Gel extraction*, 2017).
138 Braha, O. *et al.* Simultaneous stochastic sensing of divalent metal ions. *Nature biotechnology* **18**, 1005-1007, doi:10.1038/79275 (2000).
139 Ostroumova, O. S., Efimova, S. S. & Schagina, L. V. 5- and 4'-Hydroxylated flavonoids affect voltage gating of single alpha-hemolysin pore. *Biochimica et biophysica acta* **1808**, 2051-2058, doi:10.1016/j.bbamem.2011.04.005 (2011).
140 Haque, F., Li, J., Wu, H. C., Liang, X. J. & Guo, P. Solid-State and Biological Nanopore for Real-Time Sensing of Single Chemical and Sequencing of DNA. *Nano today* **8**, 56-74, doi:10.1016/j.nantod.2012.12.008 (2013).
141 Haugland, M. M., Borsley, S., Cairns-Gibson, D. F., Elmi, A. & Cockroft, S. L. Synthetically Diversified Protein Nanopores: Resolving Click Reaction Mechanisms. *ACS nano* **13**, 4101-4110, doi:10.1021/acsnano.8b08691 (2019).
142 Lee, J. & Bayley, H. Semisynthetic protein nanoreactor for single-molecule chemistry. *Proceedings of the National Academy of Sciences of the United States of America* **112**, 13768-13773, doi:10.1073/pnas.1510565112 (2015).
143 Baumruck, A. C., Tietze, D., Steinacker, L. K. & Tietze, A. A. Chemical synthesis of membrane proteins: a model study on the influenza virus B proton channel. *Chemical science* **9**, 2365-2375, doi:10.1039/c8sc00004b (2018).

144 Englebretsen, D. R. & Alewood, P. F. Boc SPPS of two hydrophobic peptides using a "solubilising tail" strategy: Dodecaalanine and chemotactic protein 10(42-55). *Tetrahedron Lett* **37**, 8431-8434, doi:Doi 10.1016/0040-4039(96)01910-7 (1996).
145 Zheng, J. S. *et al.* Expedient Total Synthesis of Small to Medium-Sized Membrane Proteins via Fmoc Chemistry. *J Am Chem Soc* **136**, 3695-3704, doi:10.1021/ja500222u (2014).
146 Sato, T., Saito, Y. & Aimoto, S. Synthesis of the C-terminal region of opioid receptor like 1 in an SDS micelle by the native chemical ligation: effect of thiol additive and SDS concentration on ligation efficiency. *Journal of peptide science : an official publication of the European Peptide Society* **11**, 410-416, doi:10.1002/psc.634 (2005).
147 Johnson, E. C. & Kent, S. B. Towards the total chemical synthesis of integral membrane proteins: a general method for the synthesis of hydrophobic peptide-thioester building blocks. *Tetrahedron Lett* **48**, 1795-1799, doi:10.1016/j.tetlet.2007.01.030 (2007).
148 Mutter, M. *et al.* Pseudo-Prolines (Psi-Pro) for Accessing Inaccessible Peptides. *Peptide Res* **8**, 145-153 (1995).
149 Mutter, M., Wohr, T., Gioria, S. & Keller, M. Pseudo-prolines: Induction of cis/trans-conformational interconversion by decreased transition state barriers. *Biopolymers* **51**, 121-128, doi: 10.1002/(Sici)1097-0282(1999)51:2<121::Aid-Bip2>3.0.Co;2-O (1999).
150 Wohr, T. *et al.* Pseudo-prolines as a solubilizing, structure-disrupting protection technique in peptide synthesis. *J Am Chem Soc* **118**, 9218-9227, doi:Doi 10.1021/Ja961509q (1996).
151 Bachem. Pseudoproline Dipeptides. (2017).
152 Liu, F. & Mayer, J. P. An Fmoc compatible, O to S shift-mediated procedure for the preparation of C-terminal thioester peptides. *J Org Chem* **78**, 9848-9856, doi:10.1021/jo4015112 (2013).
153 Miseta, A. & Csutora, P. Relationship between the occurrence of cysteine in proteins and the complexity of organisms. *Mol Biol Evol* **17**, 1232-1239, doi: 10.1093/oxfordjournals.molbev.a026406 (2000).
154 Leiro, V. *et al.* Design and preparation of biomimetic and bioinspired materials. *Woodh Publ Ser Biom* **121**, 1-44, doi:10.1016/B978-0-08-100741-9.00001-2 (2017).
155 Wan, Q. & Danishefsky, S. J. Free-radical-based, specific desulfurization of cysteine: a powerful advance in the synthesis of polypeptides and glycopolypeptides. *Angew Chem Int Ed Engl* **46**, 9248-9252, doi:10.1002/anie.200704195 (2007).
156 Lee, J. Y. & Bang, D. Challenges in the chemical synthesis of average sized proteins: sequential vs. convergent ligation of multiple peptide fragments. *Biopolymers* **94**, 441-447, doi:10.1002/bip.21379 (2010).
157 Fauvet, B., Butterfield, S. M., Fuks, J., Brik, A. & Lashuel, H. A. One-pot total chemical synthesis of human alpha-synuclein. *Chem Commun* **49**, 9254-9256, doi:10.1039/c3cc45353g (2013).
158 Bang, D. & Kent, S. B. H. A One-Pot Total Synthesis of Crambin. *Journal of Peptide Science* **10**, 93-93 (2004).
159 Villain, M., Vizzavona, J. & Rose, K. Covalent capture: a new tool for the purification of synthetic and recombinant polypeptides. *Chemistry & biology* **8**, 673-679, doi:Doi 10.1016/S1074-5521(01)00044-8 (2001).
160 Veber, D. F., Milkowski, J. D., Denkewalter, R. G. & Hirschmann, R. Synthesis of Peptides in Aqueous Medium .4. A Novel Protecting Group for Cysteine. *Tetrahedron Lett*, 3057-+ (1968).
161 Veber, D. F., Varga, S. L., Hirschma.R, Milkowsk.Jd & Denkewal.Rg. Acetamidomethyl - Novel Thiol Protecting Group for Cysteine. *J Am Chem Soc* **94**, 5456-&, doi:Doi 10.1021/Ja00770a600 (1972).

162 Fujii, N. *et al.* Silver Trifluoromethanesulfonate as an S-Deprotecting Reagent for the Synthesis of Cystine Peptides. *J Chem Soc Chem Comm*, 283-284, doi:Doi 10.1039/C39890000283 (1989).

163 Ste Marie, E. J. & Hondal, R. J. Reduction of cysteine-S-protecting groups by triisopropylsilane. *Journal of Peptide Science* **24**, doi:Unsp E3130 10.1002/Psc.3130 (2018).

164 Seddon, A. M., Curnow, P. & Booth, P. J. Membrane proteins, lipids and detergents: not just a soap opera. *Biochimica et biophysica acta* **1666**, 105-117, doi:10.1016/j.bbamem.2004.04.011 (2004).

165 Bogusz, S., Venable, R. M. & Pastor, R. W. Molecular dynamics simulations of octyl glucoside micelles: Dynamic properties. *J Phys Chem B* **105**, 8312-8321, doi:10.1021/jp004475o (2001).

166 Wang, H., Andersen, K. K., Vad, B. S. & Otzen, D. E. OmpA can form folded and unfolded oligomers. *Bba-Proteins Proteom* **1834**, 127-136, doi:10.1016/j.bbapap.2012.09.002 (2013).

167 Kochendoerfer, G. G. *et al.* Total chemical synthesis of the integral membrane protein influenza A virus M2: role of its C-terminal domain in tetramer assembly. *Biochemistry-Us* **38**, 11905-11913 (1999).

168 Dittmann, M., Sauermann, J., Seidel, R., Zimmermann, W. & Engelhard, M. Native chemical ligation of hydrophobic peptides in organic solvents. *Journal of peptide science : an official publication of the European Peptide Society* **16**, 558-562, doi:10.1002/psc.1285 (2010).

169 Dittmann, M., Sadek, M., Seidel, R. & Engelhard, M. Native chemical ligation in dimethylformamide can be performed chemoselectively without racemization. *Journal of peptide science : an official publication of the European Peptide Society* **18**, 312-316, doi:10.1002/psc.2401 (2012).

170 Gupta, R., Yadav, S. & Ahmad, F. Protein stability: urea-induced versus guanidine-induced unfolding of metmyoglobin. *Biochemistry-Us* **35**, 11925-11930, doi:10.1021/bi961079g (1996).

171 Valiyaveetil, F. I., MacKinnon, R. & Muir, T. W. Semisynthesis and folding of the potassium channel KcsA. *J Am Chem Soc* **124**, 9113-9120 (2002).

172 Hunter, C. L. & Kochendoerfer, G. G. Native chemical ligation of hydrophobic peptides in lipid bilayer systems (vol 15, pg 437, 2004). *Bioconjugate Chem* **15**, 948-948, doi:10.1021/bc04291r (2004).

173 Clayton, D. *et al.* Total chemical synthesis and electrophysiological characterization of mechanosensitive channels from Escherichia coli and Mycobacterium tuberculosis. *Proceedings of the National Academy of Sciences of the United States of America* **101**, 4764-4769, doi:10.1073/pnas.0305693101 (2004).

174 Zaima, N., Hayasaka, T., Goto-Inoue, N. & Setou, M. Matrix-assisted laser desorption/ionization imaging mass spectrometry. *International journal of molecular sciences* **11**, 5040-5055, doi:10.3390/ijms11125040 (2010).

175 Lottspeich, F. E., J. W. in *Bioanalytik* Ch. 12.3, 274-290 (Springer Spektrum, 2012).

176 BIORAD. Vol. Bulletin 6040 Ver C (Bio-Rad Laboratories, Inc.).

177 ThermoFisher. *Protein Gel Staining Methods*, <https://www.thermofisher.com/de/de/home/life-science/protein-biology/protein-biology-learning-center/protein-biology-resource-library/pierce-protein-methods/protein-gel-stains.html> (

178 Pagliuca, C. *et al.* Molecular properties of Kcv, a virus encoded K+ channel. *Biochemistry-Us* **46**, 1079-1090, doi:10.1021/bi061530w (2007).

179 Mandala, V. S., Liao, S. Y., Gelenter, M. D. & Hong, M. The Transmembrane Conformation of the Influenza B Virus M2 Protein in Lipid Bilayers. *Scientific reports* **9**, 3725, doi:10.1038/s41598-019-40217-1 (2019).

180 Winterstein, L. M. *et al.* Reconstitution and functional characterization of ion channels from nanodiscs in lipid bilayers. *The Journal of general physiology* **150**, 637-646, doi:10.1085/jgp.201711904 (2018).
181 Greenfield, N. J. Using circular dichroism spectra to estimate protein secondary structure. *Nature protocols* **1**, 2876-2890, doi:10.1038/nprot.2006.202 (2006).
182 Greenfield, N. J. Analysis of the kinetics of folding of proteins and peptides using circular dichroism. *Nature protocols* **1**, 2891-2899, doi:10.1038/nprot.2006.244 (2006).
183 Holzwarth, G. & Doty, P. The Ultraviolet Circular Dichroism of Polypeptides. *J Am Chem Soc* **87**, 218-228, doi:10.1021/ja01080a015 (1965).
184 Khan, S., Li, M., Muench, S. P., Jeuken, L. J. & Beales, P. A. Durable proteo-hybrid vesicles for the extended functional lifetime of membrane proteins in bionanotechnology. *Chem Commun (Camb)* **52**, 11020-11023, doi:10.1039/c6cc04207d (2016).
185 Beales, P. A., Khan, S., Muench, S. P. & Jeuken, L. J. Durable vesicles for reconstitution of membrane proteins in biotechnology. *Biochemical Society transactions* **45**, 15-26, doi:10.1042/BST20160019 (2017).
186 Sabatino, G., Mulinacci, B., Alcaro, M. C., Chelli, M., Rovero, P., Papini A. M. Assessment of new 6-Cl-HOBt based coupling reagents for peptide synthesis. Part 1: Coupling efficiency study. *Letters in Peptide Science* **9**, 119-123 (2002).
187 Valeur, E. & Bradley, M. Amide bond formation: beyond the myth of coupling reagents. *Chem Soc Rev* **38**, 606-631, doi:10.1039/b701677h (2009).
188 Albericio, F., Bofill, J. M., El-Faham, A. & Kates, S. A. Use of onium salt-based coupling reagents in peptide synthesis. *J Org Chem* **63**, 9678-9683, doi:Doi 10.1021/Jo980807y (1998).
189 Pedersen, S. L., Sorensen, K. K. & Jensen, K. J. Semi-automated microwave-assisted SPPS: Optimization of protocols and synthesis of difficult sequences. *Biopolymers* **94**, 206-212, doi:10.1002/bip.21347 (2010).
190 *Overcoming Aggregation in Solid-phase Peptide Synthesis*, <www.sigmaaldrich.com/technical-documents/articles/chemistry/overcoming-aggregation-in-spps.html> (
191 Pugh, K. C., York, E. J. & Stewart, J. M. Effects of Resin Swelling and Substitution on Solid-Phase Synthesis. *Int J Pept Prot Res* **40**, 208-213 (1992).
192 (ed Varian Inc.) (2008).
193 Zeng, W. G., Regamey, P. O., Rose, K., Wang, Y. Z. & Bayer, E. Use of Fmoc-N-(2-hydroxy-4-methoxybenzyl)amino acids in peptide synthesis. *J Pept Res* **49**, 273-279 (1997).
194 Carpino, L. A. *et al.* Synthesis of 'difficult' peptide sequences: application of a depsipeptide technique to the Jung-Redemann 10- and 26-mers and the amyloid peptide A beta(1-42). *Tetrahedron Lett* **45**, 7519-7523, doi:10.1016/j.tetlet.2004.07.162 (2004).
195 Coin, I. *et al.* Depsipeptide methodology for solid-phase peptide synthesis: Circumventing side reactions and development of an automated technique via depsidipeptide units. *J Org Chem* **71**, 6171-6177, doi:10.1021/jo060914p (2006).
196 Olschewski, D. & Becker, C. F. W. Chemical synthesis and semisynthesis of membrane proteins. *Mol Biosyst* **4**, 733-740, doi:10.1039/b803248c (2008).
197 Hojo, H. & Aimoto, S. Polypeptide-Synthesis Using the S-Alkyl Thioester of a Partially Protected Peptide Segment - Synthesis of the DNA-Binding Domain of C-Myb Protein (142-193)-Nh2. *B Chem Soc Jpn* **64**, 111-117, doi:Doi 10.1246/Bcsj.64.111 (1991).
198 Carr, D. (ed Advanced Chromatography Technologies).
199 Englebretsen, D. R. & Robillard, G. T. An N-terminal method for peptide solubilisation. *Tetrahedron* **55**, 6623-6634, doi:Doi 10.1016/S0040-4020(99)00309-9 (1999).

200 Zeng, Z. F. *et al.* On-Plate Selective Enrichment and Self-Desalting of Peptides/Proteins for Direct MALDI MS Analysis. *Anal Chem* **84**, 2118-2123, doi:10.1021/ac203378q (2012).
201 Bensalem, N. *et al.* High sensitivity identification of membrane proteins by MALDI TOF-MASS spectrometry using polystyrene beads. *J Proteome Res* **6**, 1595-1602, doi:10.1021/pr0606272 (2007).
202 Brailsford, J. A. *et al.* Total chemical synthesis of human thyroid-stimulating hormone (hTSH) beta-subunit: Application of arginine-tagged acetamidomethyl (Acm(R)) protecting groups. *Tetrahedron* **74**, 1951-1956, doi:10.1016/j.tet.2018.02.067 (2018).
203 Baumruck, A. C., Tietze, D., Stark, A. & Tietze, A. A. Reactions of Sulfur-Containing Organic Compounds and Peptides in 1-Ethyl-3-methyl-imidazolium Acetate. *J Org Chem* **82**, 7538-7545, doi:10.1021/acs.joc.7b01272 (2017).
204 Tietze, A. A., Heimer, P., Stark, A. & Imhof, D. Ionic liquid applications in peptide chemistry: synthesis, purification and analytical characterization processes. *Molecules* **17**, 4158-4185, doi:10.3390/molecules17044158 (2012).
205 Schmidt, M., Toplak, A., Quaedflieg, P. J. & Nuijens, T. Enzyme-mediated ligation technologies for peptides and proteins. *Current opinion in chemical biology* **38**, 1-7, doi:10.1016/j.cbpa.2017.01.017 (2017).
206 Hall, A. R. *et al.* Hybrid pore formation by directed insertion of alpha-haemolysin into solid-state nanopores. *Nature nanotechnology* **5**, 874-877, doi:10.1038/nnano.2010.237 (2010).
207 Jin, Y. & Cowan, J. A. DNA cleavage by copper-ATCUN complexes. Factors influencing cleavage mechanism and linearization of dsDNA. *J Am Chem Soc* **127**, 8408-8415, doi:10.1021/ja0503985 (2005).
208 Mal, T. K., Ikura, M. & Kay, L. E. The ATCUN domain as a probe of intermolecular interactions: application to calmodulin-peptide complexes. *J Am Chem Soc* **124**, 14002-14003, doi:10.1021/ja028109p (2002).
209 Pearce, D. A., Walkup, G. K. & Imperiali, B. Peptidyl chemosensors incorporating a FRET mechanism for detection of Ni(II). *Bioorganic & medicinal chemistry letters* **8**, 1963-1968, doi:10.1016/s0960-894x(98)00354-0 (1998).
210 Wende, C. & Kulak, N. Fluorophore ATCUN complexes: combining agent and probe for oxidative DNA cleavage. *Chem Commun* **51**, 12395-12398, doi:10.1039/c5cc04508h (2015).
211 Ganesh, N. V. *et al.* Surface-tethered iterative carbohydrate synthesis: a spacer study. *J Org Chem* **78**, 6849-6857, doi:10.1021/jo400095u (2013).
212 Veronese, F. M. & Pasut, G. PEGylation, successful approach to drug delivery. *Drug discovery today* **10**, 1451-1458, doi:10.1016/S1359-6446(05)03575-0 (2005).
213 Yamagishi, K., Sawaki, K., Murata, A. & Takeoka, S. A Cu-free clickable fluorescent probe for intracellular targeting of small biomolecules. *Chem Commun (Camb)* **51**, 7879-7882, doi:10.1039/c4cc09947h (2015).
214 Yang, G., Yuan, R. & Chai, Y. Q. A high-sensitive amperometric hydrogen peroxide biosensor based on the immobilization of hemoglobin on gold colloid/L-cysteine/gold colloid/nanoparticles Pt-chitosan composite film-modified platinum disk electrode. *Colloids and surfaces. B, Biointerfaces* **61**, 93-100, doi:10.1016/j.colsurfb.2007.07.014 (2008).
215 Lu, Y. *et al.* Impedance spectroscopy analysis of human odorant binding proteins immobilized on nanopore arrays for biochemical detection. *Biosensors & bioelectronics* **79**, 251-257, doi:10.1016/j.bios.2015.12.047 (2016).
216 Neupane, K. P., Aldous, A. R. & Kritzer, J. A. Metal-binding and redox properties of substituted linear and cyclic ATCUN motifs. *J Inorg Biochem* **139**, 65-76, doi:10.1016/j.jinorgbio.2014.06.004 (2014).

217 Gajda, T., Henry, B., Aubry, A. & Delpuech, J. J. Proton and metal ion interactions with glycylglycylhistamine, a serum albumin mimicking pseudopeptide. *Inorg Chem* **35**, 586-593, doi:Doi 10.1021/Ic950373e (1996).
218 (ed AppliChem) (2008).
219 Yu, Q., Kandegedara, A., Xu, Y. & Rorabacher, D. B. Avoiding interferences from Good's buffers: A contiguous series of noncomplexing tertiary amine buffers covering the entire range of pH 3-11. *Anal Biochem* **253**, 50-56, doi:10.1006/abio.1997.2349 (1997).
220 Good, N. E. & Izawa, S. Hydrogen ion buffers. *Methods in enzymology* **24**, 53-68 (1972).
221 Tietze, D., Seth, B. K., Brauser, M., Tietze, A. A. & Buntkowsky, G. Ni-II Complex Formation and Protonation States at the Active Site of a Nickel Superoxide Dismutase-Derived Metallopeptide: Implications for the Mechanism of Superoxide Degradation. *Chem-Eur J* **24**, 15879-15888, doi:10.1002/chem.201803042 (2018).
222 Zhang, Y., Akilesh, S. & Wilcox, D. E. Isothermal titration calorimetry measurements of Ni(II) and Cu(II) binding to His, GlyGlyHis, HisGlyHis, and bovine serum albumin: a critical evaluation. *Inorg Chem* **39**, 3057-3064 (2000).
223 Ferreira, C. M. H., Pinto, I. S. S., Soares, E. V. & Soares, H. M. V. M. (Un)suitability of the use of pH buffers in biological, biochemical and environmental studies and their interaction with metal ions - a review. *Rsc Adv* **5**, 30989-31003, doi:10.1039/c4ra15453c (2015).
224 Neupane, K. P., Aldous, A. R. & Kritzer, J. A. Macrocyclization of the ATCUN motif controls metal binding and catalysis. *Abstr Pap Am Chem S* **247** (2014).
225 Appleton, D. W. & Sarkar, B. The absence of specific copper (II)-binding site in dog albumin. A comparative study of human and dog albumins. *The Journal of biological chemistry* **246**, 5040-5046 (1971).
226 Lakowicz, J. R. in *Principles of Fluorescence Spectroscopy* Vol. 3 Ch. 8, (2006).
227 Pan, B. *et al.* Quantitative identification of dynamic and static quenching of ofloxacin by dissolved organic matter using temperature-dependent kinetic approach. *Environmental pollution* **161**, 192-198, doi:10.1016/j.envpol.2011.10.026 (2012).
228 AnaSpec. *5(6) - FAM UltraPure Grade Mixed Isomers*, <https://www.anaspec.com/products/product.asp?id=43485> (
229 Li, L., Guo, Q., Dong, J., Xu, T. & Li, J. DNA binding, DNA cleavage and BSA interaction of a mixed-ligand copper(II) complex with taurine Schiff base and 1,10-phenanthroline. *Journal of photochemistry and photobiology. B, Biology* **125**, 56-62, doi:10.1016/j.jphotobiol.2013.05.007 (2013).
230 Armbruster, D. A., Tillman, M. D. & Hubbs, L. M. Limit of detection (LQD)/limit of quantitation (LOQ): comparison of the empirical and the statistical methods exemplified with GC-MS assays of abused drugs. *Clin Chem* **40**, 1233-1238 (1994).
231 Haas, K. L., Putterman, A. B., White, D. R., Thiele, D. J. & Franz, K. J. Model peptides provide new insights into the role of histidine residues as potential ligands in human cellular copper acquisition via Ctr1. *J Am Chem Soc* **133**, 4427-4437, doi:10.1021/ja108890c (2011).
232 Zheng, Y., Gattas-Asfura, K. M., Konka, V. & Leblanc, R. M. A dansylated peptide for the selective detection of copper ions. *Chem Commun (Camb)*, 2350-2351 (2002).
233 Crouse, H. F. P., J.; Nejrabi, F.; Snyder, D. L.; chohan, B. S. Quenching of Tryptophan Fluorescence in Various Proteins by a Series of Small Nickel Complexes. *Susquehanna University Scholary Commons* (2014).
234 Garcia, R. & Perez, R. Dynamic atomic force microscopy methods. *Surf Sci Rep* **47**, 197-301, doi:Pii S0167-5729(02)00077-8 doi: 10.1016/S0167-5729(02)00077-8 (2002).
235 Cruz-Chu, E. R., Aksimentiev, A. & Schulten, K. Ionic Current Rectification through Silica Nanopores. *J Phys Chem C* **113**, 1850-1862, doi:10.1021/jp804724p (2009).

236 Miyamoto, T., Fukino, Y., Kamino, S., Ueda, M. & Enomoto, S. Enhanced stability of Cu(2+)-ATCUN complexes under physiologically relevant conditions by insertion of structurally bulky and hydrophobic amino acid residues into the ATCUN motif. *Dalton transactions* **45**, 9436-9445, doi:10.1039/c6dt01387b (2016).
237 Mlynarz, P. *et al.* How the alpha-hydroxymethylserine residue stabilizes oligopeptide complexes with nickel(II) and copper(II) ions. *J Chem Soc Dalton*, 1033-1038, doi: 10.1039/A909354k (2000).
238 Shearer, W. T., Bradshaw, R. A., Gurd, F. R. & Peters, T., Jr. The amino acid sequence and copper(II)-binding properties of peptide (1-24) of bovine serum albumin. *The Journal of biological chemistry* **242**, 5451-5459 (1967).
239 Zheng, Y. J. *et al.* Design of a membrane fluorescent sensor based on photo-cross-linked PEG hydrogel. *J Phys Chem B* **107**, 483-488, doi:10.1021/jp027119+ (2003).
240 Papp, S., Jagerszki, G. & Gyurcsanyi, R. E. Ion-Selective Electrodes Based on Hydrophilic Ionophore-Modified Nanopores. *Angew Chem Int Ed Engl* **57**, 4752-4755, doi:10.1002/anie.201800954 (2018).
241 Guo, Y. L., Jian, F. F. & Kang, X. F. Nanopore sensor for copper ion detection using a polyamine decorated beta- cyclodextrin as the recognition element. *Rsc Adv* **7**, 15315-15320, doi:10.1039/c7ra00454k (2017).
242 Zimmerman, L. Toxicity of copper and ascorbic acid to Serratia marcescens. *Journal of bacteriology* **91**, 1537-1542 (1966).
243 Li, Z. Y. & Grant, K. B. DNA photo-cleaving agents in the far-red to near-infrared range - a review. *Rsc Adv* **6**, 24617-24634, doi:10.1039/c5ra28102d (2016).
244 Bossu, F. P. & Margerum, D. W. Electrode-Potentials of Nickel(Iii,Ii)-Peptide Complexes. *Inorg Chem* **16**, 1210-1214, doi: 10.1021/Ic50171a047 (1977).
245 Jiang, Q., Xiao, N., Shi, P. F., Zhu, Y. G. & Guo, Z. J. Design of artificial metallonucleases with oxidative mechanism. *Coordin Chem Rev* **251**, 1951-1972, doi:10.1016/j.ccr.2007.02.013 (2007).
246 Uerpmann, C. *et al.* Design and DNA binding of an extended triple-stranded metallo-supramolecular cylinder. *Chem-Eur J* **11**, 1750-1756, doi:10.1002/chem.200401054 (2005).
247 Johnstone, T. C., Suntharalingam, K. & Lippard, S. J. The Next Generation of Platinum Drugs: Targeted Pt(II) Agents, Nanoparticle Delivery, and Pt(IV) Prodrugs. *Chemical reviews* **116**, 3436-3486, doi:10.1021/acs.chemrev.5b00597 (2016).
248 McGivern, T. J. P., Afsharpour, S. & Marmion, C. J. Copper complexes as artificial DNA metallonucleases: From Sigman's reagent to next generation anti-cancer agent? *Inorg Chim Acta* **472**, 12-39, doi:10.1016/j.ica.2017.08.043 (2018).
249 Traversi, F. *et al.* Detecting the translocation of DNA through a nanopore using graphene nanoribbons. *Nature nanotechnology* **8**, 939-945, doi:10.1038/Nnano.2013.240 (2013).
250 Kaya, D., Dinler, A., San, N. & Kececi, K. Effect of Pore Geometry on Resistive-Pulse Sensing of DNA Using Track-Etched PET Nanopore Membrane. *Electrochim Acta* **202**, 157-165, doi:10.1016/j.electacta.2016.04.014 (2016).

15. Acknowledgements

First of all I would like to express my deep gratitude to my supervisor Asst. Prof. Alesia Tietze for her guidance throughout my time within her lab group. Thank you for motivating me everytime I got upset with Kcv and supporting me with every idea I had. I would also like to thank you for giving me the opportunities to travel to national and international conferences and to the new lab team in Sweden. I had a great time within you team and with you, whether it was during jogging in the forests of Darmstadt or at conferences in Cologne and Gothenburg. I wish you and your family all the best in your new home.

I would also like to thank various departments at the Technical University of Darmstadt. First off the MS department: thank you Christiane for measuring my rather difficult MS samples. Your patience, support and your ideas were always very much appreciated. Of course, a huge thanks also to Gül for all the MALDI TOF measurements especially of Kcv, which were very challenging. Thank you to Alex for you support and ideas.
I would like to thank Christian Dietz for introducing Ivana and me to the world of AFM and for measuring our samples.
I'm grateful for having had the possibility to use the CEM synthesizer at Prof. Thiele's lab, different instruments at Prof. Kolmar's lab and being welcome at Buntkowsky's lab. Thank you Daniel, for guiding me through titration set-ups and experiments, for your support and ideas and measuring of NMR samples.
Thank you Susanne for the introduction of the synthesizer and you invitations to the FEM meetings and Julia for helping me with the CD measurements.
A huge "thank you" to the whole iNAPO family, for the mutual support, all the PhD meetings and retreats. Special thanks to Viktor Stein for letting me conduct the DNA experiments and to all lab members: to Wadim for all your dedication to get the perfect CLSM images, to Alex for helping me and introducing me to primers, sequencing and PCR and to Jan for your ideas… and for the coffee. Thanks to Prof. Thiel, Tobias and Indra for your support in synthesis of Kcv_{NTS}, for lipid bilayer experiments and for letting me use the Fluorimeter.
Without the iNAPO project I would have never met Ivana. I am so very grateful that we became great friends. Thank you for enormous amounts of coffee, sushi, laughter and other extracurricular activities as well as the conduction of numerous I/V measurements and for introducing me to the solid-state nanopore world! A huge thanks to Prof. Ensinger and the whole lab for having me there as a plus one in many activities.

To the old and the new lab team: thank you! Special thanks to Andreas for your support and our conversations from chemistry to trash TV shows and to my bachelor student Joshua who worked on the topic of DNA scission. Additionaly a great thank you to the Swedish lab team, for all the cakes, food and talks in Gothenburg.

Thank you to all my friends who supported my during my PhD studies.
I would like to express gratefulness to my family. They are always there to help me, build me up and motivate me. Thank you for letting me have the opportunity to always follow my dreams and supporting me in my ideas.
Finally, I would like to thank my husband Thorsten. Thank you for your continuous support and for pushing and empowering me.

16. Affirmations

Erklärung

Ich erkläre hiermit, dass ich meine Dissertation selbstständig und nur mit den angegebenen Hilfsmitteln angefertigt und noch keinen Promotionsversuch unternommen habe.

_____

Lena Müller

Erklärung der Übereinstimmung

Ich erkläre hiermit, dass die elektronische Version der Doktorarbeit mit der schriftlichen Version übereinstimmt. Die elektronische Version liegt dem Prüfungssekretariat vor.

_____

Lena Müller